JOINT INSTITUTE FOR NUCLEAR RESEARCH

Bogoliubov Laboratory of Theoretical Physics

4^{th} South Africa - JINR SYMPOSIUM

"Few to Many Body Systems: Models, Methods and Applications"

Proceedings

Dubna, Moscow region
September 21-25, 2015

Composed by A.V. Malykh

Title page design: O.A. Koval

Proceedings of the 4^{th} South Africa - JINR SYMPOSIUM "Few to Many Body Systems: Models, Methods and Applications" (Dubna, September 21-25, 2015) / Eds.F. Šimkovic and coveners of sessions. -Dubna: JINR, 2015.-256p.;2 photo.

The 4^{th} South Africa - JINR SYMPOSIUM "Few to Many Body Systems: Models, Methods and Applications" was organized by the Bogoliubov Laboratory of Theoretical Physics of the the Joint Institute for Nuclear Research in the period September 21-25, 2015. It was dedicated to the celebration of the 60th anniversary of the JINR and 10th anniversary of signing the Memorandum of Understanding between the Government of the Republic of South Africa and the Joint Institute for Nuclear Research. The Symposium discussed the scope, success and prospective of experimental, theoretical and applied physics at the JINR and in South Africa institutions and a special attention was devoted to scientific facilities on both sides. The goal of the meeting was to present main results of the SA-JINR collaboration, to extend the scientific and technological cooperation among the JINR and South Africa institutions and to attract young scientists from both sides to running joined research projects. The Symposium program covered new developments in the field of particle physics, nuclear physics, applied nuclear physics, condensed matter physics, bio-monitoring project and physics of underground laboratories. Symposium initiated opportunities to establish new areas scientific cooperation and to extend the existing cooperation among physicists from South Africa and the JINR.

The financial support was provided by the Joint Institute for Nuclear Research and the National Research Foundation of South Africa.

Organizing Committee

Co-chairmen:

V. Voronov (JINR)
R. Adam (SKA)

Vice-chairmen:

F. Šimkovic (JINR)
S. Wyngaardt (Uni-Stellenbosch)

Members of the organizing committee:

D. Kamanin (JINR)
J. Cleymans (Uni-Cape Town)
N. Mkaza (Uni-Stellenbosch)
S. Pakuliak (JINR)
S. Rakityansky (Uni-Pretoria)
R. Newman (Uni-Stellenbosch)
E. Kolganova (JINR)
S. Nedelko (JINR)
O. Matyukhina, secretary (JINR)

Contents

SESSION "NUCLEAR REACTIONS (FISSION AND CLUSTERING)"

Conveners: D. Kamanin, S. Mullins

SESSION "CONDENSED MATTER PHYSICS"

Conveners: Yu. Shukrinov, A.E. Botha

SESSION "NICA"
Conveners: A. Sorin, J. Cleymans

SESSION "PHYSICS AT UNDERGROUND LABORATORY"
Conveners: F. Šimkovic, S. Wyngaardt

STUDENT SESSION
Conveners: S. Pakuliak, N. Mkaza

PREFACE

BACKGROUND: The Republic of South Africa is an associated member of the JINR already for 10 years. Currently, scientists from the RSA participate in different themes of the Topical Plan for JINR Research and International Cooperation including theory of nuclear structure and reactions, experimental elementary particle physics, relativistic nuclear physics, synthesis and properties of nuclei at the stability limits, accelerator complex of ion beams of stable and radioactive nuclides, investigations in the field of nuclear physics with neutrons, investigations of condensed matter by modern neutron scattering methods, networking, computing, computational physics, educational programme etc. On the initiative of the JINR and South Africa institutions three South Africa-JINR Symposiums were already organized, namely the 1st Symposium at Skukuza, Kruger National Park, in February 2007, the 2nd Symposium at JINR Dubna, in September 2010; the 3rd Symposium at Blaauwklippen wine farm, Stellenbosch, in November 2012. These successful scientific meetings have established new and fruitful collaborations between both physical communities.

PRESENT MEETING: The Joint Institute for Nuclear Research hosted the 4th South Africa-JINR Symposium in Dubna in the period September 21-25, 2015. This Symposium was dedicated to the celebration of the 60th anniversary of the JINR and 10th anniversary of signing the Memorandum of Understanding between the Government of the Republic of South Africa and the Joint Institute for Nuclear Research. The Symposium discussed the scope, success and perspectives of experimental, theoretical and applied physics at the JINR and in South Africa institutions and a special attention was devoted to scientific facilities on both sides. The Symposium included three days of plenary and discussion sessions, namely September 21-23, 2015. On September 24, 2015 an excursion to Moscow was organized and on September 25, 2015 visit of the JINR Laboratories was organized.

This scientific meeting allowed to present main results of the SA-JINR collaboration, to extend the scientific and technological cooperation among the JINR and South Africa institutions and to attract young scientists from both sides to running joined research projects. The Symposium program covered new developments in the field of particle physics, nuclear physics, applied nuclear physics, condensed matter physics, bio-monitoring project and physics of underground laboratories. Speakers of each of 12 sessions were selected by the conveners of the session. The main idea was to have speakers from both South Africa and JINR and in particular cases, an expert from the field from other institute. Students from both sides was given an opportunity to make short presentations on their research during the student session. The symposium initiated opportunities to establish new areas scientific cooperation and extend the existing cooperation among physicists from South Africa and the JINR.

The Symposium program covered new experimental and theoretical developments in the field of nuclear physics.

Main topics:

- Dense matter in heavy ion collisions and astrophysics
- Nuclear reactions, beams and facilities, techniques and applications
- Nuclear structure, clusters, modern microscopical methods
- Reactor neutrons for fundamental and applied research
- Physics of few-body, atomic and molecular systems
- Computational and mathematical methods in many-body physics
- Nonlinear phenomena in condensed matter
- Physics at underground laboratories and particle astrophysics

IN MEMORY OF PROF. S.A. SOFIANOS AND V.B. BELYAEV

S.A. Rakityansky
Dept. of Physics, University of Pretoria, Pretoria, South Africa

The late Professors Sofianos and Belyaev were the main founders of the whole collaboration between Dubna and South Africa. They both passed away at the beginning of last year with just two months interval.

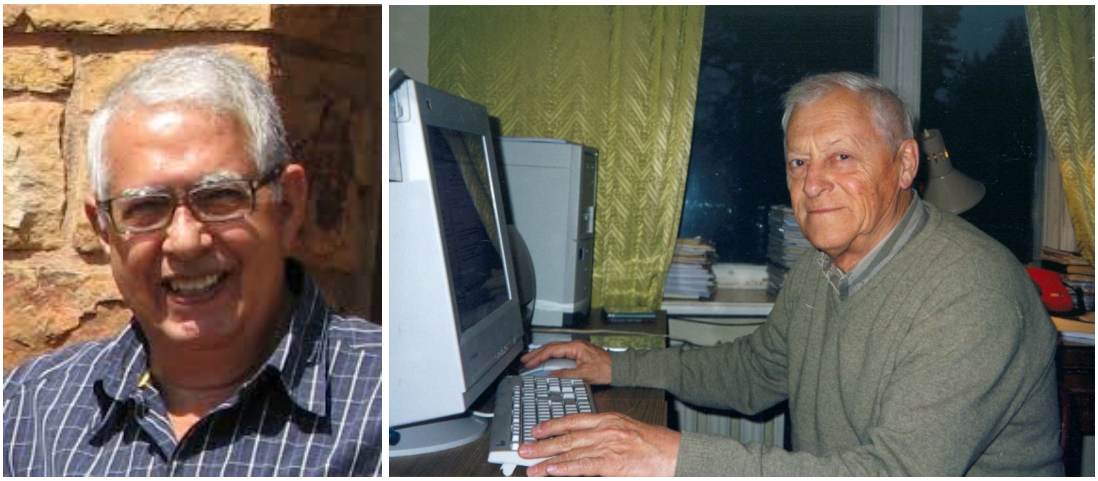

FIGURE 1. S.A. Sofianos (left) and V.B. Belyaev (right)

The story begun 25 years ago in 1991 when they met in Bonn university (in Germany), where Sofianos was spending his sabbatical and Belyaev was on a long-term visit. At that time it were no official relations between Russia and South Africa yet. So, when Prof. Belyaev visited Pretoria in 1991, he was one of the first Russian scientists in that part of the world.

Very soon after meeting, these two men became not only colleagues and collaborators, but very good friends. They were different, but something was in common for them - the passion for science. Belyaev always was an inexhaustible source of new ideas. Sofianos was a more practical and down-to-earth scientist. They perfectly complemented each other. A typical discussion between them would be that Belyaev very enthusiastically suggested to calculate something, and Sofianos skeptically pointed out all the difficulties. Then Belyaev would say: "OK, then I have a better idea". And the cycle repeated itself.

Sofianos used to jokingly call Belyaev the "Amakhozi". In Zulu language, this means the chief or leader of a tribe. Of course he put sincere and great respect in that joke. They were not dry, absentminded scientists. Both of them were full of life and enjoyed all aspects of life. They drank wine (when in Pretoria) or vodka (when in Dubna). Belyaev had passion for mountain ski and classical music. Sofianos loved to watch wild animals in a game reserve and to read history books.

Both these men were internationally renowned and highly respected scientists. Each of them published more than a hundred papers and presented talks at numerous conferences.

In 1995, they initiated the signing of the first treaty of collaboration between the University of South Africa (UNISA) and the JINR. And 10 years later, in 2005, this treaty evolved into a full-fledged collaboration, involving not only UNISA, but all South African research institutions. I think, we should be thankful to these two good men and always remember them.

In South Africa, we are planning to organize in October next year an international workshop dedicated to the memory of Prof. Sofianos. Of course it would be impossible to invite all the people with whom he collaborated. But we hope to see at that workshop many people who knew him very well. I know that similar idea is now under discussion here in Dubna. The colleagues of Prof. Belyaev want to organize a symposium dedicated to the memory of him.

Sofianos and Belyaev were close friends and left our world almost together. When I think about them, I cannot separate them. In my mind, they are sitting together somewhere in Heaven next to a blackboard full of equations. I will always remember them like that.

SESSION

"FEW-BODY SYSTEMS"

Conveners: A. Motovilov, S. Rakityansky

Nuclear fusion $d + {}^6\mathrm{Li} \to {}^8\mathrm{Be}^*$ induced by X-rays in Lithium-Deuteride crystal

V.B. Belyaev[a] [1], M.B. Miller[b], J. Otto[c], S.A. Rakityansky[c] [2]

[a] *Joint Institute for Nuclear Research, Dubna, Russia*
[b] *Institute for Physical and Technical Problems, Dubna, Russia*
[c] *Dept. of Physics, University of Pretoria, Pretoria, South Africa*

Abstract. Exposing to the X-rays the solid compound LiD (lithium-deuteride) for the duration of 111 hours, we have detected 88 events of the nuclear fusion $d + {}^6\mathrm{Li} \to {}^8\mathrm{Be}^*$. Our theoretical estimate agrees with what we observed.

Keywords: nuclear fusion, X-rays, Coulomb barrier, CR-39 track detector, lithium deuteride, master equation
PACS: 25.10.+s; 25.70.Jj; 29.40.Gx

The nuclei that constitute a crystalline lattice, oscillate relative to each other with a very low energy that is not sufficient to penetrate through the Coulomb barriers separating them. An additional energy, which is needed to tunnel through the barrier and fuse, can be supplied by external electromagnetic waves (X-rays or the synchrotron radiation), which can shake the crystalline lattice. The nuclei swayed around their equilibrium positions, acquire kinetic energy relative to each other. As a result, the original Boltzmann distribution of the nuclei over the oscillation levels is changing and the higher levels are populated. From these higher energy levels the nuclei can tunnel through the Coulomb barrier and fuse. This is what we observed when irradiated the LiD crystal with the X-rays. The rate of such a fusion turned out to be very low (one event every half an hour), but still easily measurable.

The nuclei we want to fuse, are the isotopes of hydrogen and lithium, namely, ${}^2\mathrm{H}$ and ${}^6\mathrm{Li}$. Their compound nucleus, ${}^8\mathrm{Be}$, has no stable states. The d-${}^6\mathrm{Li}$ threshold lies 22.2808 MeV above the ground state (which is also unstable). At this energy, the compound system has a wide resonance state with $\Gamma \sim 800\,\mathrm{keV}$[1], and it is above the thresholds for all the other two-body channels, namely, $t\,{}^5\mathrm{Li}$, ${}^3\mathrm{He}\,{}^5\mathrm{He}$, $n\,{}^7\mathrm{Be}$, $p\,{}^7\mathrm{Li}$, and $\alpha\,\alpha$. When sitting at the nodes of a crystalline lattice, the nuclei can be considered as being at rest relative to each other. In other words, the nuclear pair $d\,{}^6\mathrm{Li}$ in a crystal is practically at this threshold energy.

If d and ${}^6\mathrm{Li}$ in the crystal, overcome the Coulomb barrier and fuse, then there is no way back for them. Indeed, for the resulting excited (resonant) state ${}^8\mathrm{Be}^*$ to decay back into the channel $d + {}^6\mathrm{Li}$, the deuteron and lithium nuclei must overcome the same huge Coulomb barrier, while they have practically zero relative kinetic energy. It is much

[1] Passed away in March 2015
[2] e-mail: rakitsa@up.ac.za

more easier to decay into one of the channels whose thresholds are below and where the kinetic energy is above the Coulomb barrier. For example, in the lowest channel $\alpha+\alpha$ (which lies 0.0918 MeV below the ground state of the compound nucleus) the relative kinetic energy is greater than in the $d\,^6$Li channel by the amount of $22.2808\,\mathrm{MeV} + 0.0918\,\mathrm{MeV} = 22.3726\,\mathrm{MeV}$, i.e. is always well above the barrier (which is $\sim 1\,\mathrm{MeV}$).

Recent analysis of experimental data, based on the R-matrix parametrization [2], showed that at the near-threshold energies the inelastic collision of d and ^{6}Li leads to the $\alpha\alpha$-channel, $d + {}^6\mathrm{Li} \longrightarrow \alpha + \alpha + 22.3726\,\mathrm{MeV}$, with the probability of $\gamma_\alpha = 0.96$. Ignoring the remaining 4%, we can assume that, if the fusion of our d and ^{6}Li happens, almost the only outcome is the $\alpha\alpha$ pair, where the energy and momentum are equally shared between the α-particles. Therefore the fusion event could be identified by detecting at least one of the two α-particles moving in the opposite directions with the energies of 11.1863 MeV.

Nuclear reactions at extremely low energies ($E \sim 10\,\mathrm{keV}$) are significantly suppressed by the repelling Coulomb forces. The probability $T(E)$ that the colliding nuclei tunnel through the Coulomb barrier can be estimated as (see Eq. (134.10) of Ref. [3]) $T(E) = 2\pi\eta/(\exp(2\pi\eta)-1) \underset{E\to 0}{\longrightarrow} 2\pi\eta\exp(-2\pi\eta)$, where $\eta = (Z_1 Z_2 e^2/\hbar)\sqrt{\mu/(2E)}$ is the Sommerfeld parameter that involves the nuclear charges, Z_1 and Z_2, and the reduced mass μ of the nuclear pair.

In our problem, the nuclei are confined to finite volumes of space in the crystal. Within its cell, a nucleus moves to and fro, periodically colliding with the barriers. Each of these collisions is an attempt to tunnel through. If the size of the cell is D and velocity of the nucleus is v, then the attempts are repeated with the period $2D/\mathsf{v}$, i.e. with the frequency $\nu = \mathsf{v}/2D$. Therefore, the number of transitions through the barrier per second (i.e. the transition rate) is $T\nu$. If a deuteron in the crystal oscillates with the energy E, the fusion happens with the rate $W_d(E) = T(E)\gamma_\alpha/(2D)\sqrt{2E/\mu_d}$, where μ_d is the mass of deuteron. Apparently, the same is valid for the tunneling of a lithium nucleus, and the corresponding reaction rate $W_{\mathrm{Li}}(E)$ can be obtained in the same way.

Lithium hydride is an ionic crystal with simple cubic structure. In each pair of Li and D atoms, one electron is transferred from the lithium to the deuterium. As a result, the crystal consists of positive ions of lithium and negative ions of deuterium. The extra electron is loosely bound to the deuterium, which makes the radius of the ion D^- approximately twice as much as the radius of Li^+ (see, for example, Ref. [4]). Schematically, the structure of lithium deuteride crystal is depicted in Fig. 1(a).

If we consider just bare nuclei sitting at the nodes of the lattice, they repel each other with the Coulomb forces and at short distances attract each other with the strong forces. The surrounding electrons make the configuration stable and partly screen the Coulomb repulsion. For a deuteron nucleus, the neighbouring ^{6}Li nuclei create the potential profile schematically shown in Fig. 1(b). There are three orthogonal axes along which the deuteron moves in such a potential. In order to fuse with ^{6}Li, the deuteron has to tunnel through one of the six potential barriers surrounding it.

The height $V_{\max}$ of the barrier can be estimated as the Coulomb repulsion energy of the charges $Z_1 = 1$ and $Z_2 = 3$ at the distance $r_1 + r_2$, where $r_1 = 2.1424\,\mathrm{fm}$ [5] and $r_2 = 2.5432\,\mathrm{fm}$ [6] are the nuclear radii of the deuteron and ^{6}Li, respectively. This gives $V_{\max} \approx Z_1 Z_2 e^2/(r_1+r_2) \approx 0.922\,\mathrm{MeV}$. If $R_0 = 2.04\ \mathring{\mathrm{A}}$ is the distance between the nuclei

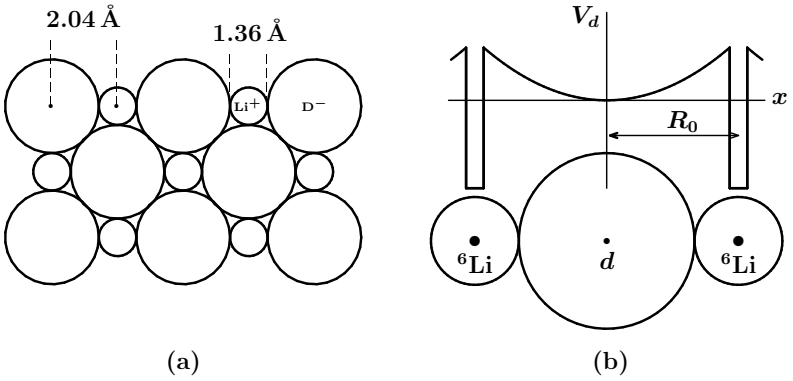

FIGURE 1. **(a)** Schematic picture of one layer of LiD crystal. The indicated distances are taken from Ref. [4]. **(b)** Schematic picture of the potential energy of a deuteron nucleus in the Coulomb and nuclear fields of the two neighbouring lithium atoms. The potential energy is considered along the line connecting the centers of these atoms.

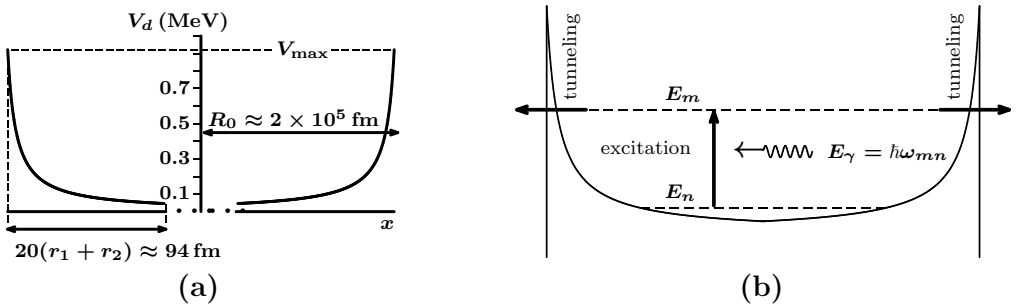

FIGURE 2. **(a)** The potential energy of a deuteron nucleus in the Coulomb fields of the two neighbouring lithium nuclei. The potential energy is considered along the line connecting the centers of these nuclei. There are shown only the leftmost and rightmost segments of this line. The central part (which is three orders of magnitude longer) is cut out because it is practically flat. **(b)** The deuteron gets the energy from the X-rays and tunnels through the Coulomb barrier towards the ^{6}Li nucleus.

d and ^{6}Li in the crystal [4], and x is the shift of the deuteron from its equilibrium position, then the Coulomb forces acting on it from the neighbouring lithium nuclei, generate the potential energy $V_d(x) = Z_1 Z_2 e^2/(R_0 - x) + Z_1 Z_2 e^2/(R_0 + x)$.

The deuteron sitting in the central well of the potential shown in Fig. 1(b), oscillates around its equilibrium point. In order to estimate the fusion rate, we need to know the energy levels (spectrum) of its oscillations, as well as the distribution of the statistical ensemble of the deuterons over these levels. For the estimation purpose, this problem can be simplified if we approximate the central well by another potential for which both the spectrum and wave functions are known analytically.

Looking at Fig. 1(b), one might guess that the best approximation would be a parabola, i.e. a harmonic oscillator potential. This however is wrong because the curve shown in that figure is schematic. Actually, if we accurately plot this potential on the interval $-R_0 + (r_1 + r_2) \le x \le R_0 - (r_1 + r_2)$, it is practically flat everywhere except for the left and right ends of this interval, where it quickly raises to $V_{\max}$ as is shown in Fig. 2(a).

Of course, in addition to the Coulomb fields generated by the nuclei, there are also electric fields due to the electron shells of the ions. However, these fields are weak as compared to the height $V_{\max} \approx 0.922\,\mathrm{MeV}$ of the Coulomb barriers. The reason of relative weakness of the electron field in the crystal is that, in contrast to the nuclei, the electrons act not as point-like charges but as a space charge of the electron cloud distributed within a volume of few Angstrom size. In other words, the bottom of the potential shown in Fig. 2(a), is not exactly flat. It can be shown that at the centre, it has an additional shallow "dent" (potential well) of the depth $\sim 30\,\mathrm{eV}$, which is spherically spread to a distance of ~ 1.36 Å.

Therefore, a good approximation for the potential $V_d(x)$ is a square well. Moreover, we can replace it with an infinitely deep square well, because the excitations that we are going to consider ($E \leq 100\,\mathrm{keV}$) are very small as compared to $V_{\max} \sim 1\,\mathrm{MeV}$. The advantage of using the infinite square well is that we know both the spectrum E_n and wave functions $\psi_n(x)$ for such a potential analytically. Apparently, everything that was said about the potential well for the deuteron, is valid for the lithium nucleus as well. The ground-state energies for both nuclei in the corresponding potential wells are very low, namely, $E_1(d) \approx 0.6\,\mathrm{meV}$ and $E_1(\mathrm{Li}) \approx 0.2\,\mathrm{meV}$. The excitation levels are very dense. On the interval $E \in [0, 100]\,\mathrm{keV}$ there are 12,746 and 22,030 levels for the deuteron and ^{6}Li, respectively.

The main idea of our experiment is to irradiate the crystal with X-rays, which may excite the oscillations of the nuclei (near their equilibrium positions) to such a level where they could tunnel through the Coulomb barrier as is shematically shown in Fig. 2(b).

Under the influence of an electromagnetic wave, the nuclei jump up and down over the ladder of the energy levels. The stimulated excitation (and de-exitation) rate p_{mn} as well as the rate of spontaneous de-excitations p^{sp}_{mn} can be found analytically in the dipole approximation by calculating the matrix elements $\langle \psi_m | x | \psi_n \rangle$ [7] over the simple square-well wave functions.

The statistical ensemble of deuterons (or ^{6}Li) in the crystal is in the thermodynamical equilibrium, and thus the population P_n of each level (i.e. the probability that a particular deuteron occupies the level n) can be found using the Boltzmann distribution. At the room temperature, $T = 300\,^\circ\mathrm{K}$, this distribution gives the average energies $\langle E \rangle_d = \sum_{n=1}^{\infty} E_n P_n \approx 14.2\,\mathrm{meV}$ for the deuterons and $\langle E \rangle_{\mathrm{Li}} \approx 13.6\,\mathrm{meV}$ for ^{6}Li. These small values are obtained because only a couple of dozens of the lowest levels are populated with appreciable probabilities.

When the crystal is exposed to X-rays, the statistical ensemble of deuterons (or similarly ^{6}Li nuclei) is not in the thermodynamical equilibrium anymore. If the flux of external photons is steady, a new dynamical equilibrium is formed with constant population $P_m(t) = \mathrm{const}$ for each level $m = 1, 2, 3, \ldots$. The time-evolution of the populations can be described by the so called master equation (see, for example, Ref.[8]),

$$\frac{dP_m}{dt} = \sum_{n \neq m} p_{mn} P_n - \sum_{n \neq m} p_{nm} P_m + \sum_{n > m} p^{\mathrm{sp}}_{mn} P_n - \sum_{n < m} p^{\mathrm{sp}}_{nm} P_m \,.$$

We only need the stationary distribution, when all $P_n(t)$ reach their constant values and their derivatives on the left hand sides of these equations become zero. This gives a ho-

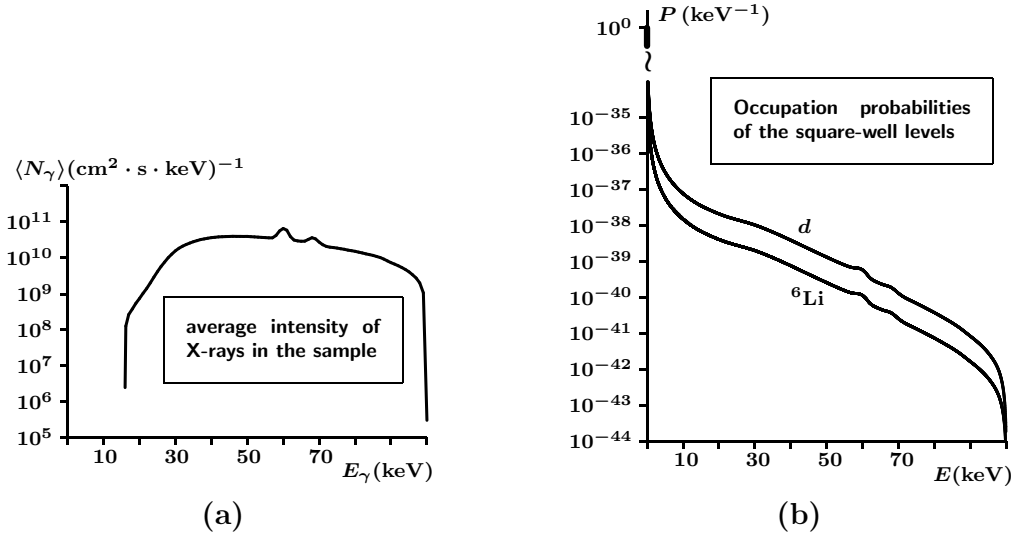

FIGURE 3. **(a)** Number of photons in the unit energy interval, bombarding $1\,\mathrm{cm}^2$ of the target cross section during one second. The number is averaged over the thickness of the sample. **(b)** Probabilities (per unit energy interval) of populating the levels in the square-well potential for the deuteron and ^{6}Li nuclei, when the crystal is exposed to the X-rays with the spectrum shown in Fig. 3(a).

mogeneous system of linear equations, $\sum_n A_{mn} P_n = 0$, with the normalisation condition $\sum_n P_n = 1$, where the matrix A_{mn} is composed of the transition rates. This homogeneous linear system can be transformed to an equivalent non-homogeneous system, which can be numerically solved using the Gauss-Seidel iterative procedure. An algorithm for such a solution can be found in Ref. [9].

In our experiment, we irradiated the sample with the X-rays whose spectrum covered the energy interval of $[15, 100]\,\mathrm{keV}$. In calculations, we used the intensity averaged over the depth of the sample. The averaged spectrum of X-rays is shown in Fig. 3(a). It is given in terms of the number N_γ of photons in the unit energy interval falling on the area of $1\,\mathrm{cm}^2$ per second. This density is needed in finding the stimulated transition rates. Using them, we found the stationary probability distribution for occupying various energy levels in the potential square-well. This was done for both the deuteron and ^{6}Li nuclei. The resulting distributions are shown in Fig. 3(b).

The observable fusion rate, corresponding to these distributions, is the following average $\langle W_i \rangle = \sum_n W_i(E_n^{(i)}) P_i(E_n^{(i)})$, where i stands for either d or Li.

Each deuteron has six neighbouring lithium nuclei and similarly each lithium nucleus has six hydrogen isotopes surrounding it. However, the crystal is not pure D^{6}Li compound. In some nodes of the lattice it can be a proton (instead of d) or ^{7}Li (instead of ^{6}Li). In our experiment, it was used a sample containing $M = 0.61\,\mathrm{g}$ of lithium hydride powder with natural isotope composition of lithium (mass fractions of ^{6}Li and ^{7}Li being $f_6 = 0.0759$ and $f_7 = 0.9241$, respectively) and enriched with the hydrogen isotope ^{2}H ($f_1 = 0.02$ and $f_2 = 0.98$). Therefore, if you find a hydrogen atom in the crystal, it is a deuterium with the probability of f_2. And a lithium atom has in its centre the ^{6}Li isotope with the probability of f_6. Therefore, a deuteron can find around itself a ^{6}Li nucleus with the probability of $6f_6$, and for a ^{6}Li isotope the probability to find a

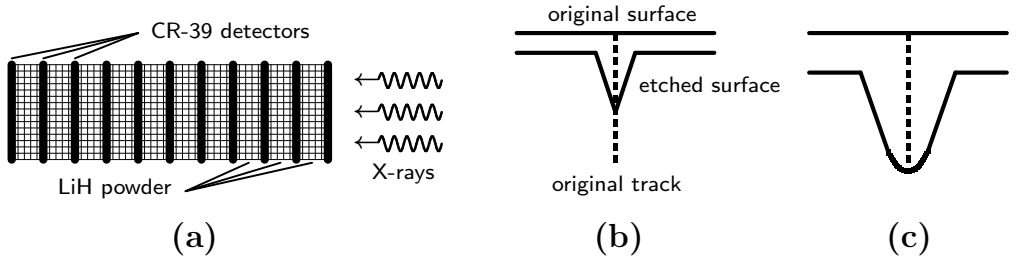

FIGURE 4. **(a)** Schematic picture of a sample unit composed of alternating layers of lithium-deuteride powder and the plastic detectors (CR-39). Whole assembly includes several units like this, placed parallel to each other inside a hermetic PVC container. The distance between the detector plates is 1 cm. The total number of the detectors in whole assembly is 85. Each detector plate is a square of the area 1cm×1cm with 1 mm thickness. The X-rays are directed perpendicular to the plates. **(b) (c)** Schematic representation of the etching process for two different durations: (b) Etching time is not sufficient to reach the bottom of the original track; (c) Rounding of the bottom of the pit after the track end has been reached.

deuteron nearby is $6f_2$. Since there are two possibilities for the same fusion event to happen: either the deuteron or the lithium gets through the barrier, the total ("bulk") fusion rate for the whole crystal can be found as a sum of the corresponding contributions: $R = 6f_6 N_d \langle W_d \rangle + 6f_2 N_{\rm Li} \langle W_{\rm Li} \rangle$, where N_d and $N_{\rm Li}$ are the numbers of available deuterons and ^{6}Li nuclei. The effective molar mass m of our crystal-powder is $m = f_1 1\,{\rm g} + f_2 2\,{\rm g} + f_6 6\,{\rm g} + f_7 7\,{\rm g}$. The number of hydrogen and lithium atoms (any isotopes) is the same, namely, $(M/m)N_A$, where N_A is the Avogadro number. This gives $N_d = (M/m)N_A f_2$, $N_{\rm Li} = (M/m)N_A f_6$, and therefore $R = 6(M/m)N_A f_2 f_6 \Big(\langle W_d \rangle + \langle W_{\rm Li} \rangle \Big)$. Numerical calculations with the X-ray spectrum shown in Fig. 3(a), give the following results for the single-nucleus rates: $\langle W_d \rangle \approx 2.4 \times 10^{-26}\,{\rm s}^{-1}$, $\langle W_{\rm Li} \rangle \approx 4.6 \times 10^{-27}\,{\rm s}^{-1}$. The corresponding "bulk" rate for the whole sample is $R \approx 5.2 \times 10^{-4}\,{\rm s}^{-1}$. For the total exposure time in our experiment, $t = 111.466$ hours, we therefore should have expected to register $N \sim 207$ fusion events.

Each fusion event results in a pair of α-particles moving in the opposite directions with the same energy of 11.1863 MeV. To register them, we used the polymer track detectors CR-39 in direct contact with the active material (lithium hydride). The particles leave tracks in the polymer material, which can be identified after the experiment is completed. The background tracks left by other charged particles, can be easily excluded using specific properties of the tracks belonging to the α-particles from the fusion events.

Lithium hydride (LiH) is a solid crystalline compound, usually available in the form of chunks or powder. It is extremely hygroscopic, absorbing water from the air. For our experiment, this is a destructive process and therefore we avoided the contacts of LiH with atmospheric air by all available means.

The crystalline chunks were ground into powder form. This powder was placed between square plates (1 cm^2 each) of the plastic detectors (CR-39), as is schematically shown in Fig. 4(a). We put in parallel several units like the one shown in this Figure, and the whole assembly was enclosed in a hermetic PVC container. The total number of the detector plates was 85. The length of our sample was 13.2 cm.

To generate the X-rays, we used a XYLON Y.TU 225-D02 tube. The tube was operated with a potential difference of 100 kV and the current of 30 mA. The spectrum

of X-rays in our sample is shown in Fig. 3(a).

Original tracks in the detectors are very narrow channels where the structure of the plastic material is damaged by the particle. These channels become much wider and visible under a microscope magnification, after etching. For etching, we used a 6.25 mol/ℓ solution of NaOH at 70 °C. This solution removes the plastic material not only from the channels, but from all the surfaces. However the rate of etching at the damages is higher. There are certain empirical formulae that enable one to calculate the etching rates at various conditions (see Ref. [10] and the references therein). It is therefore possible to numerically model the shapes of the tracks for different etching times. For such a modelling, we used the standard code TRACK_TEST developed by the authors of Ref. [11].

Depending on its kinetic energy, the α-particle penetrates into the plastic material and damages it to a certain depth (typically a dozen of microns). When etched, such a track forms a pit in the shape of a sharp cone, as is shown in Fig. 4(b). The longer we etch it, the deeper and wider this cone becomes. This goes on until the depth of the pit becomes equal to the penetration length. After that the pit only becomes wider and retains practically the same depth. As a result, the bottom of the pit transforms from a sharp cone to a smooth spherically concave surface, as is schematically shown in Fig. 4(c).

The sharp cone and concave shapes have different optical properties. A smooth concave surface reflects the light and even focus it to a small dot, which is not possible for a sharp cone. Therefore just looking into the etched tracks, we can distinguish "finished" (track end has been reached) and "unfinished" tracks. Using the TRACK_TEST software, we can calculate the length of the track for any given energy E_α of the α-particle as well as calculate the depth of the pit for a given etching time t. Therefore we can choose t such that all the tracks for E_α higher than certain threshold $E_{\min}$, form sharp cone pits, while for $E_\alpha < E_{\min}$ the pits reflect the light.

In order to exclude all possible background events, we only counted the tracks left by the α-particles with the energy greater than $E_{\min} = 6\,\text{MeV}$. This corresponds to etching time $t = 8\,\text{hours}$. After the etching, we looked for completely dark pits (sharp cones) with certain diameter of the opening. These tracks could not be done by anything else but the α-particles from the fusion reaction.

It should be noted that we cannot register all the fusion events that occur in the sample. First of all, the α-particles from the reactions that take place far away from a detector plate, cannot reach the detector because the distance they can go through in any solid medium is very short. Moreover, even if they reach a detector surface from afar, they loose a significant part of the kinetic energy and thus cannot be registered if the remaining energy is less than $E_{\min} = 6\,\text{MeV}$.

Our calculations show that in the lithium-hydride the original energy of 11.1 MeV of the α-particle is reduced to the minimally acceptable energy of 6 MeV on the distance of $x_{\max} = 0.095\,\text{mm}$. This means that, when we count the events, we can only register the events happening within a thin layer of the lithium-hydride of 0.095 mm thickness, which is in contact with the detector. Since in total we have 85 detectors, and for each of them the surface area in contact with LiH is $0.95 \times 0.95\,\text{cm}^2$ (most of them have LiH on both sides), the total volume of LiH, from which we register the α-particles, is $0.77\,\text{cm}^3$ and the corresponding mass is 0.61 g. This effective mass of the active material was used

in our theoretical estimate of the fusion rate.

This is not the end of the story. The efficiency of the detection is reduced further by the fact that the α-particles are emitted isotropically in all directions. For example, if the fusion event happens at the maximal acceptable distance from the detector and the α-particle moves at a non-zero angle relative to the normal to the detector surface, the actual distance it has to pass in LiH is greater than the $x_{\max}$ and thus it looses too much energy. Similar losses take place at any distance within the thin layer, when the angle is too large. Moreover, the tracks with the angle to the normal greater that 45° cannot be identified using our simple method. Estimating all possible losses, we conclude that we can only register of about 40% of the events happening in 0.61 g of the material.

The sample was exposed to the X-ray radiation for the duration of 111.466 hours. Then, after the etching of the detectors, we identified (in total on all 85 plates) 88 tracks that belonged to the α-particles from the fusion reaction. Since we could not register all the fusion events, actual number N of the events (happened in 0.61 g of LiH) is greater, $N > 88$. Taking into account that the substance we used was not pure lithium-deuteride, we conclude that under the used electromagnetic radiation the fusion rate for a single $d - {}^6\mathrm{Li}$ pair is $R_{d^6\mathrm{Li}} > 1.19 \times 10^{-26}\,\mathrm{s}^{-1}$. This result is of the same order of magnitude as was predicted by our theoretical estimate.

Apparently, the fusion rate turned out to be too low for any possible applications of this process in the energy production. However, the electromagnetically induced nuclear reactions in crystals can be used in a different way. In principle, this offers a new way of measuring the cross sections (or the astrophysical S-factors) of such reactions (not only fusion) at extremely low energies, which are not accessible in the direct collision experiments.

REFERENCES

1. D. R. Tilley, J. H. Kelley, J. L. Godwin, D. C. Millener, J. E. Purcell, C. G. Sheu, H. R. Weller, *"Energy levels of light nuclei $A = 8,9,10$"*, Nucl. Phys., **A745**, pp. 155-362 (2004).
2. J. Grineviciute, L. Lamia, A.M. Mukhamedzhanov, C. Spitaleri, M. La Cognata, *"Low-energy R-matrix fits for the ${}^6\mathrm{Li}(d,\alpha)^4\mathrm{He}$ S factor"*, Phys. Rev., **C91**, 014601 (2015).
3. L. D. Landau, E. M. Lifshitz, *"Quantum Mechanics"*, Pergamon Press, (1965).
4. D. Laplaze, *"Lattice dynamics of lithium hydride and lithium deuteride: effect of long-range tree-body forces"*, J.Phys.C: Solid State Phys., **C10**, pp. 3499-3520 (1977).
5. Table XLI of: P. J. Mohr, B. N. Taylor, D. B. Newell, *"CODATA recommended values of the fundamental physical constants: 2010"*, Rev.Mod.Phys., **84(4)**, pp. 1527-1605 (2012).
6. E. G. Nadjakov, K. P. Marinova, Yu. P. Gangrsky, *"Systematics of nuclear charge radii"*, Atomic Data and Nuclear Data Tables, **56**, pp. 133-157 (1994).
7. D. I. Blokhintsev, *"Quantum Mechanics"*, D. Reidel Publishing company, Dordrecht, Holland (1964).
8. N. G. Van Kampen, *"Stochastic Processes in Physics and Chemistry"*, Third Edition, NORTH-HOLLAND (2007).
9. http://www.mathpages.com/home/kmath175/kmath175.htm
10. A. A. Azooz, S. H. Al-NiaâĂŹemi, M. A. Al-Jubbori, *"A parameterization of nuclear track profiles in CR-39 detector"*, Computer Physics Communications, vol. 183, pp. 2470-2479 (2012).
11. D. Nikezic, K. N. Yu, *"Computer program TRACK_TEST for calculating parameters and plotting profiles for etch pits in nuclear track materials"*, Computer Physics Communications, vol. 174, pp. 160-165 (2006).

Universal Description Of Three Two-Species Particles

O. I. Kartavtsev and A. V. Malykh

JINR Dubna, 141980 Dubna, Moscow region, Russia.

Abstract. A system of two identical particles of mass m and a distinct particle of mass m_1 in the universal limit of zero-range interaction between different particles is studied in different L^P sectors of total angular momentum L and parity P. The states of odd L and P for two identical fermions and states of even L and P for two identical bosons are considered. It is shown that an additional three-body parameter b is needed for the unambiguous formulation of the three-body problem for mass ratio above some critical value $\mu_r(L^P)$ in each L^P sector. Within the framework of this formulation, the three-body bound-state energies are calculated in two limiting cases $b = 0$ and $b \to \infty$ for $m/m_1 > \mu_r(L^P)$ and $L \leq 5$.

Keywords: Few-body systems, ultracold trapped gases, universality, bound states
PACS: 67.85.-d, 03.65.Ge, 21.45.-v

INTRODUCTION

The low-energy dynamics of few two-species particles has attracted much interest in relation with the intensive experimental and theoretical investigations of ultra-cold binary quantum gases. It is of principal importance to describe the three-body systems: two identical fermions (or non-interacting bosons) of mass m, which interact with a distinct particle of mass m_1. In the low-energy limit, the few-body properties become independent of the particular form of the short-range two-body interaction, which can be taken as the contact or zero-range potential. The potential is defined by a single parameter, e. g., the two-body scattering length a, and for the properly chosen units the few-body properties depend on a single non-trivial parameter, the mass ratio m/m_1.

As it was shown in [1], for mass ratio above some critical value $\mu_c(L^P)$ it is necessary to introduce an additional parameter for the unambiguous formulation of the three-body problem for two-species particles in the zero-range interaction limit. This allows one to obtain the infinite number of the three-body bound states, which form the Efimov spectrum. The problem of the correct formulation exists also for smaller mass ratio values $\mu_r(L^P) < m/m_1 \leq \mu_c(L^P)$ as follows from the analyses of the wave function in the vicinity of the triple-collision point [2, 3, 4, 5]. The problem is connected with construction of the self-adjoint Hamiltonian as it was discussed in mathematical papers [6, 7, 8, 9]. Until now, in a number of reliable investigations of three two-component particles (for $m/m_1 \leq \mu_c(L^P)$) [2, 10, 11, 12, 13] it was explicitly or implicitly assumed the fastest decrease of the wave function near the triple-collision point.

The main aim of this report is to formulate the three-body problem in the mass-ratio region $\mu_r(L^P) < m/m_1 \leq \mu_c(L^P)$ in an arbitrary L^P sector by introducing the additional parameter b as it was done in [5] for $L^P = 1^-$ sector of two identical fermions and

distinct particle. Within the framework of this formulation, the bound-state energies are calculated for odd L and P if identical particles are fermions and for even L and P if identical particles are bosons. Two limiting cases of the three-body parameter $b = 0$ and $b \to \infty$ and the positive two-body scattering length a are considered throughout the report.

FORMULATION OF THREE-BODY PROBLEM

The Hamiltonian of two identical particles of mass m interacting with a distinct particle of mass m_1 in the centre-of-mass frame is defined as the six-dimensional kinetic-energy operator $H_0 = -\Delta_{\mathbf{x}} - \Delta_{\mathbf{y}}$ complimented by the boundary condition for the wave function Ψ imposed at zero distances between the distinct particle and either of identical ones. Here $\mathbf{x}$ and $\mathbf{y}$ are the scaled Jacobi coordinates and the units $\hbar = 2m/(1+m/m_1) = 1$ are used. The boundary condition represents the contact or zero-range two-body interaction and can be defined as

$$\lim_{r\to 0} \frac{\partial \ln(r\Psi)}{\partial r} = -\frac{1}{a}, \tag{1}$$

where r is the inter-particle distance and a is the two-body scattering length. Only one condition of the form (1) is necessary as the wave function is either antisymmetric or symmetric under permutation of identical fermions or bosons. The formal definition of the Hamiltonian does not obviously provide the unambiguous formulation of the three-body problem; at least, it is necessary to inspect the solution near the triple-collision point.

For qualitative analyses and numerical calculations it is convenient to expand the wave function $\Psi = \rho^{-5/2} \sum_{n=1}^{\infty} f_n(\rho)\Phi_n(\rho,\Omega)$ into a set of eigenfunctions $\Phi_n(\rho,\Omega)$ of the auxiliary problem on a hyper-sphere at fixed ρ, where $\rho = \sqrt{x^2+y^2}$ is a hyper-radius and Ω denotes a set of hyper-angular variables. This leads to an infinite set of coupled hyper-radial equations (HREs),

$$\left[\frac{d^2}{d\rho^2} - \frac{\gamma_n^2(\rho) - 1/4}{\rho^2} + E\right] f_n(\rho) - \sum_{m=1}^{\infty} \left[P_{nm}(\rho) - Q_{nm}(\rho)\frac{d}{d\rho} - \frac{d}{d\rho}Q_{nm}(\rho)\right] f_m(\rho) = 0, \tag{2}$$

where the eigenvalues of the auxiliary problem $\gamma_n^2(\rho)$ are enumerated in ascending order and can be obtained by a solution of transcendental equation [10, 11]. The coupling terms $Q_{nm}(\rho)$ and $P_{nm}(\rho)$ are expressed in the analytical form via $\gamma_n^2(\rho)$ and their derivatives [14, 15].

As discussed in [5] for $L^P = 1^-$, the wave function Ψ near the triple-collision point ($\rho \to 0$) is basically determined by the most singular diagonal term in HREs (2), i. e., by the lowest eigenvalue of the auxiliary problem $\gamma_1^2(\rho)$ and the corresponding channel function $f_1(\rho)$. Henceforth, for the sake of brevity denote $\gamma \equiv \gamma_1(0)$. As follows from HREs (2), in each L^P sector there are two square-integrable solutions at $\rho \to 0$ for the mass-ratio values corresponding $\gamma^2 < 1$. In this case, for unambiguous formulation of the three-body problem it is necessary to fix the linear combination of these solutions, which

requires the additional three-body parameter. If $\gamma^2 < 0$, the wave function oscillates near the triple-collision point and the Efimov spectrum takes place. Furthermore, one should consider the case $0 < \gamma^2 < 1$. The three-body boundary condition can be imposed on the channel function $f_1(\rho)$ by introducing the three-body parameter b,

$$f_1(\rho) \underset{\rho\to 0}{\longrightarrow} \rho^{1/2+\gamma} \mp |b|^{2\gamma}\rho^{1/2-\gamma}[1+q\rho/(1-2\gamma)] \ , \tag{3}$$

where $q = \left[\dfrac{d\gamma_1^2(\rho)}{d\rho}\right]_{\rho=0}$ and $\gamma \neq 1/2$. The last term in the square brackets ($\sim q\rho$) is necessary only for $1 > \gamma > 1/2$ and can be omitted for $1/2 > \gamma > 0$. In the specific case $\gamma = 1/2$ the boundary condition can be written

$$f_1(\rho) \underset{\rho\to 0}{\longrightarrow} \rho - b(1+q\rho\log\rho) \ . \tag{4}$$

One should note that for $\gamma^2 \geq 1$ only one solution is square-integrable for $\rho \to 0$ and the appropriate boundary condition is $f_1(\rho) \to 0$. As all other channel functions $f_n(\rho)$ tend to zero faster than $f_1(\rho)$ at $\rho \to 0$, the conditions $f_n(0) = 0$ are sufficient to complete the formulation. Two cases $b = 0$ and $b \to \infty$ represent two different limits of the channel function's dependence for $\rho \to 0$, namely, $f_1(\rho) \to \rho^{1/2+\gamma}$ and $f_1(\rho) \to \rho^{1/2-\gamma}[1+q\rho/(1-2\gamma)]$.

In each L^P sector, the lowest eigenvalue γ takes three specific values $\gamma = 1,\ 1/2$, and 0 for odd L and P if the identical particles are fermions and even L and P if the identical particles are bosons when mass ratio takes the values $\mu_r(L^P)$, $\mu_e(L^P)$, and $\mu_c(L^P)$. The values of the mass ratio μ_r, μ_e, and μ_c corresponding to $\gamma = 1,\ 1/2$, and 0 for few values of angular momentum $L = 1-5$ are presented in Tab. 1.

TABLE 1. The values $\mu_r(L^P)$, $\mu_e(L^P)$, and $\mu_c(L^P)$ corresponding to $\gamma = 1,\ 1/2$, and 0 for angular momentum L and parity P.

L^P	μ_r	μ_e	μ_c
1^-	8.6185769247	12.313099346	13.606965698
2^+	32.947611782	37.198932993	38.630158395
3^-	70.070774958	74.510074146	75.994494341
4^+	119.73121698	124.25484012	125.764635719
5^-	181.86643779	186.43468381	187.958355086

RESULTS OF CALCULATION

The mass-ratio dependence of the three-body energies were calculated for angular momentum $L \leq 5$, the positive two-body scattering length $a > 0$, and two values of the three-body parameter $b = 0$ and $b \to \infty$ ($L^P = 1^-, 3^-, 5^-$ or $L^P = 2^+, 4^+$ if two identical particles are fermions or bosons). The three-body bound-state energies are determined by numerical solution of the truncated system of HREs (2) complemented by boundary conditions (3) or (4). Solution of five - eight HREs provides five - six digits in the calculated energy. The mass-ratio dependence of the bound-state energies is shown in Fig. 1 for $L^p = 1^-, 3^-, 5^-$ states of two identical fermions and distinct particle.

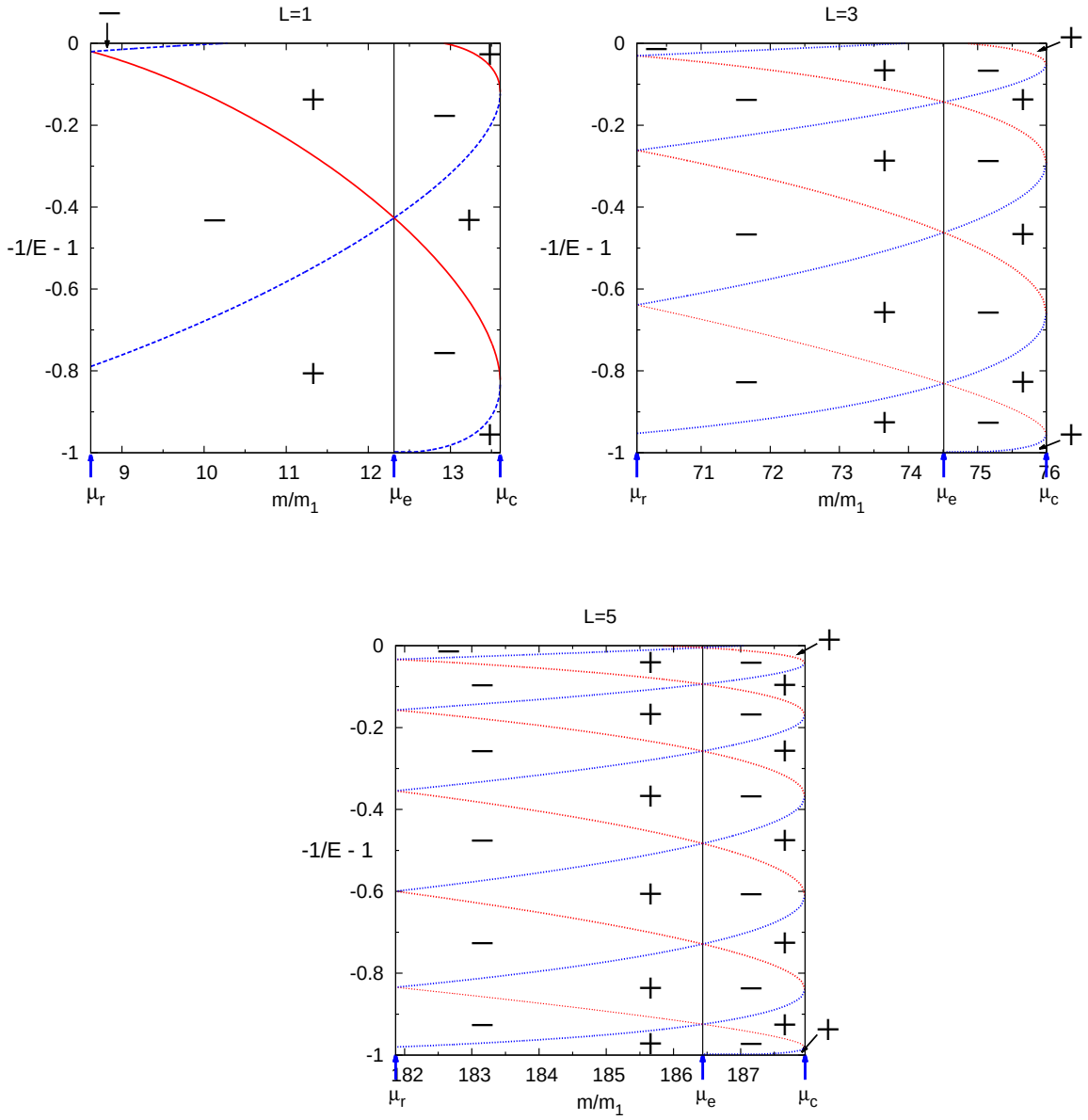

FIGURE 1. Bound-state energies E of the $L^p = 1^-, 3^-, 5^-$ states as a function of m/m_1 for two identical fermions and distinct particle. The energies for $b = 0$ and $b \to \infty$ are plotted by solid (red) and dashed (blue) lines. Plus and minus signs in the plots mark the regions corresponding to positive and negative b values. Vertical (black) line is plotted at $m/m_1 = \mu_e$. The energy axis is scaled to map the interval $(-\infty, -1)$ onto $(-1, 0)$.

Qualitatively, energy dependence on m/m_1, b is similar for different L, only distinction is increasing bound-state number with increasing L. With increasing mass ratio the three-body energies decrease for $b = 0$ and increase for $b \to \infty$ as illustrated in Fig. 1. When m/m_1 tends to either of specific values $\mu_r(L^P)$, $\mu_e(L^P)$, and $\mu_c(L^P)$, the three-body energies for $b = 0$ coincide with those for $b \to \infty$. Besides, for $b \to \infty$ there is the

ground state, which energy tends to the finite value as $m/m_1 \to \mu_r(L^P)$ and to minus infinity as $m/m_1 \to \mu_e(L^P)$. The calculated three-body energies in three limits $\mu_r(L^P)$, $\mu_e(L^P)$, and $\mu_c(L^P)$ are presented in Tab. 2.

TABLE 2. Three-body bound-state energies for three limiting values of mass ratio ($\mu_r(L^P)$, $\mu_e(L^P)$, and $\mu_c(L^P)$) for $L \leq 5$ ($L^P = 1^-, 3^-, 5^-$ or $L^P = 2^+, 4^+$ if two identical particles are fermions or bosons). All the entries represent the energy values both for $b = 0$ and $b \to \infty$, except the underlined numbers in the first line, which gives the ground state energies only for $b \to \infty$ in the limit $m/m_1 \to \mu_r$.

$m/m_1 \to \mu_r$				
1^-	2^+	3^-	4^+	5^-
<u>4.7473</u>	<u>11.3111</u>	<u>21.1146</u>	<u>34.1622</u>	<u>50.4592</u>
1.02090	1.68551	2.77004	4.22117	6.03404
-	1.02748	1.35435	1.85585	2.49935
-	-	1.03169	1.24191	1.54982
-	-	-	1.03374	1.18686
-	-	-	-	1.03485

$m/m_1 \to \mu_e$				
1^-	2^+	3^-	4^+	5^-
1.74397	3.42540	5.90130	9.17834	13.26233
-	1.27038	1.86005	2.66958	3.68670
-	-	1.16759	1.49716	1.93501
-	-	-	1.12596	1.34729
-	-	-	1.00088	1.10398
-	-	-	-	1.00503

$m/m_1 \to \mu_c$				
1^-	2^+	3^-	4^+	5^-
5.89543	12.67370	22.57676	35.67806	52.00787
1.13767	1.84445	2.93742	4.39267	6.20802
-	1.07220	1.41376	1.91816	2.56267
-	-	1.05497	1.27207	1.58177
-	-	-	1.04795	1.20485
-	-	-	-	1.04442

It is of interest to determine the critical mass-ratio values, for which the bound states arise. It happens when the bound-state energy coincides with the threshold $E = -1$. In fact, existence of bound states at the threshold energy follows from the power decay of the channel function $f_1(\rho) \sim \rho^{-L}$ for $\rho \to \infty$. The critical mass-ratio values are presented in Tab. 3 in the cases $b = 0$ and $b \to \infty$.

The bound-state energies and critical values of m/m_1 of this report are in agreement with results of [11, 12] for $b = 0$. The one-channel approximation of calculation in [11] is the reason of small discrepancies with the present results. The critical values of mass ratio for $b = 0$ are in accordance with those obtained by the solution of the integral equations in [12], except for the missed loosely bound 3^- state.

TABLE 3. The critical values of mass ratio, for which the bound L^P states arise in the cases $b = 0$ and $b \to \infty$ ($L^P = 1^-, 3^-, 5^-$ or $L^P = 2^+, 4^+$ if two identical particles are fermions or bosons).

$b = 0$				
1^-	2^+	3^-	4^+	5^-
8.17259	22.6369	43.3951	70.457	103.823
12.91742	31.5226	56.1652	87.027	124.155
-	37.7662	67.3352	102.488	143.664
-	-	74.8233	115.536	161.402
-	-	-	124.168	176.097
-	-	-	-	185.829
$b \to \infty$				
1^-	2^+	3^-	4^+	5^-
10.2948	35.9163	73.9853	124.3660	187.056

DISCUSSION

Universal description of three two species particles is given in different L^P sectors ($L \leq 5$). Similar to consideration the $L^P = 1^-$ states of two fermions and distinct particle [5], it was shown that the additional parameter b is needed for the mass ratio within the intervals $\mu_r(L^P) < m/m_1 < \mu_c(L^P)$ to provide the unambiguous formulation of the three-body problem in arbitrary L^P sector. In two limiting cases of the three-body parameter $b = 0$ and $b \to \infty$ and the two-body scattering length $a > 0$, the dependences of the three-body bound-state energy on m/m_1 are calculated for odd L and P if identical particles are fermions and for even L and P if identical particles are bosons. In the case of negative two-body scattering length $a < 0$, similar to the results of [5], one expects that one bound state should appear for $b \to \infty$ and $\mu_r(L^P) < m/m_1 < \mu_e(L^P)$. In the limit $a \to \infty$ the exact result of [5] is applicable, namely, the bound-state energy $E = -4b^{-2}\left[-\Gamma(\gamma)/\Gamma(-\gamma)\right]^{1/\gamma}$.

One should note that the wave function in the vicinity of the triple-collision point can be specified by imposing the three-body boundary condition for small ρ_0, i. e., by setting the dimensionless logarithmic derivative of the channel function, $\tan\delta = \rho\dfrac{d\log f}{d\rho}$ [16]. Thus, the two-parameter family of three-body problem is defined. As shown in [5] one can readily find the relation between two-parameters δ and ρ_0 and the three-body parameter b.

The described universal picture is generally expected in a number of problems. In this respect, one should mention scattering problems for three two-species particles [2, 10, 12, 13], the universal description of two-species $(3+1)$ and $(2+2)$ four-body systems [17, 18], the few-body problems in the presence of spin-orbit interaction [19, 20], and consideration of few particles in the mixed dimensions [21, 22].

REFERENCES

1. V. Efimov, Nucl. Phys. A **210**, 157 (1973).
2. D. S. Petrov, Phys. Rev. A **67**, 010703(R) (2003).
3. Y. Nishida, D. T. Son, and S. Tan, Phys. Rev. Lett. **100**, 090405 (2008).
4. O. I. Kartavtsev and A. V. Malykh, Phys. At. Nucl. **77**, 430 (2014), [Yad. Fiz. **77**, 458 (2014)].
5. O. I. Kartavtsev and A. V. Malykh, *Three two-component fermions with zero-range interactions: correct formulation and energy spectrum* (2015), arXiv:1512.06786.
6. R. A. Minlos, ISRN Math. Phys. **2012**, 230245 (2012).
7. R. A. Minlos, Mosc. Math. J. **14**, 617 (2014).
8. M. Correggi, G. Dell'Antonio, D. Finco, A. Michelangeli, and A. Teta, Rev. Math. Phys. **24**, 1250017 (2012).
9. M. Correggi, G. Dell'Antonio, D. Finco, A. Michelangeli, and A. Teta, Math. Phys. Analys. Geom. **18**, 32 (2015).
10. O. I. Kartavtsev and A. V. Malykh, J. Phys. B **40**, 1429 (2007).
11. O. I. Kartavtsev and A. V. Malykh, Pis'ma ZhETF **86**, 713 (2007), [JETP Lett. **86**, 625 (2007)].
12. S. Endo, P. Naidon, and M. Ueda, Few-Body Syst. **51**, 207 (2011).
13. K. Helfrich and H.-W. Hammer, J. Phys. B **44**, 215301 (2011).
14. O. I. Kartavtsev, Few-Body Syst. Suppl. **10**, 199 (1999).
15. O. I. Kartavtsev and A. V. Malykh, Phys. Rev. A **74**, 042506 (2006).
16. A. Safavi-Naini, S. T. Rittenhouse, D. Blume, and H. R. Sadeghpour, Phys. Rev. A **87**, 032713 (2013).
17. Y. Castin, C. Mora, and L. Pricoupenko, Phys. Rev. Lett. **105**, 223201 (2010).
18. S. Endo and Y. Castin, Phys. Rev. A **92**, 053624 (2015).
19. Z.-Y. Shi, X. Cui, and H. Zhai, Phys. Rev. Lett. **112**, 013201 (2014).
20. Z.-Y. Shi, H. Zhai, and X. Cui, Phys. Rev. A **91**, 023618 (2015).
21. Y. Nishida and S. Tan, Phys. Rev. Lett. **101**, 170401 (2008).
22. Y. Nishida and S. Tan, Few-Body Syst. **51**, 191 (2011).

Analysis of the partial Coulomb-nuclear interferences in the breakups of ^{11}Be and ^{15}C halo nuclei

B. Mukeru and M. L. Lekala

Department of Physics, University of South Africa, PO Box 392, Pretoria 0003

Abstract. We use the energy-integrated total, Coulomb and nuclear breakup cross sections taken from Ref.[9], to analyse the effects of the first-order and higher-order multipole interferences on the partial Coulomb-nuclear interferences. It is shown that the first-order interference decreases the Coulomb-nuclear interference, while it is increased owing to the higher-order interference. For the ^{11}Be projectile, the first-order interference changes the nature of the Coulomb-nuclear interference, whereas the higher-order interference has no effect on the nature of the Coulomb-nuclear interference. For the ^{15}C projectile, it is obtained that the first-order and higher-order interferences have no effect on the nature of the Coulomb-nuclear interference. We also show that the first-order and higher-order multipole transitions produce weak nuclear absorptions, while the first-order interference produces a strong nuclear absorption.

Keywords: Mutlipole transition, First-order and higher-order interferences, Coulomb-nuclear interference
PACS: $24.10.\mathrm{E_q}, 25.60.\mathrm{D_z}, 25.60.\mathrm{G_c}$

INTRODUCTION

In the attempt to eliminate the nuclear breakup in order to obtain a pure Coulomb breakup for Coulomb dominated reactions, the procedures adopted have been criticised due the significance of the Coulomb-nuclear interference [1]. This interference have been investigated in various works [2, 3, 4, 5, 6, 7, 8], where the common conclusion is that it can even be significant where the nuclear breakup contributes insignificantly. As a result, it is argued that the nuclear breakup contribution could not be simply disregarded in a Coulomb-dominated breakup reaction. However, the results in the literature still lack detailed analysis of this interference to confidently back up these conclusions. For instance, it is not clearly established how important is the Coulomb-nuclear interference in each partial wave retained in the breakup model space. Moreover, it is not well known how different multipole transitions affect the nature and magnitude of this interference. What is the role of the projectile binding energy on the nature and magnitude of the Coulomb-nuclear interference? Although we know that the breakup cross section increases with the decrease of the projectile binding energy, to the best of our knowledge, there is no clear answer to this question.

Recently we studied the first-order and higher-order interferences in the $^{11}\mathrm{Be} + ^{208}\mathrm{Pb}$ and $^{15}\mathrm{C} + ^{208}\mathrm{Pb}$ breakup reactions at the same incident energy [9]. We showed that already at the first-order, if the multipoles are summed incoherently, the nuclear breakup

cross sections are much more significant than their Coulomb breakup counterparts. We also obtained unlike what is commonly assumed that the higher-order interference plays a significant role in the breakup process of these reactions. Higher partial waves were found to contribute considerably to the overall breakup cross sections. However, these conclusions do not tell much about the effects of these first-order and higher-order interferences on the Coulomb-nuclear interference. In this paper, we employ the different energy-integrated total, Coulomb and nuclear breakup cross sections obtained in [9], to analyse the effects of the multipole transitions and first-order and higher-order interferences on the Coulomb-nuclear interferences. The angular momentum and impact parameter distributions total, Coulomb and nuclear breakup cross sections are also considered for a better understanding of the extention to larger angles behavior of the angular distributions differential total and nuclear breakup cross sections observed in that reference.

RESULTS AND DISCUSSION

The partial Coulomb-nuclear interferences presented in Table 1 and Table 2, for each multipole transition are derived from the energy-integrated total, Coulomb and nuclear breakup cross sections which are summarized in Table IV of Ref.[9] for the $^{11}\mathrm{Be}+{}^{208}\mathrm{Pb}$ and $^{15}\mathrm{C}+{}^{208}\mathrm{Pb}$ reactions. The CDCC formalism employed to obtain these breakup cross section is presented in that reference and references therein. Therefore, we do not repeat the details here. For both tables, λ represents a single multipole transition, $\lambda_{\max}=1$ represents the coherent sum of the zero-order and first-order multipole transitions and contains the effect of the first-order interference, while $\lambda_{\max}=4$ stands of the coherent sum all the different multiples and contains the effect of the all order interference. The Coulomb-nuclear interference in each partial wave and for each multipole transition is defined as

$$\sigma_I^{\ell}=\sigma_T^{\ell}-(\sigma_C^{\ell}+\sigma_N^{\ell}), \tag{1}$$

where $\sigma_C^{\ell},\sigma_N^{\ell}$ and σ_T^{ℓ} are the Coulomb, nuclear and total (coherent sum of Coulomb and nuclear) energy-integrated breakup cross sections, and $\sigma_C^{\ell}+\sigma_N^{\ell}$ is the Coulomb-nuclear incoherent sum. On the other hand, $\sigma_I^{\lambda_{\max}}$ is the Coulomb-nuclear interference obtained when the involved multipoles are summed coherently, and therefore serves to estimate the effects of the first-order and higher-order interferences on the Coulomb-nuclear interference. The symbol $S^{\lambda}=\sigma_I^s+\sigma_I^p+\sigma_I^d+\sigma_I^f+\sigma_I^{\mathrm{g}}$ is the incoherent sum of the partial Coulomb-nuclear interferences.

We analyze the nature and magnitude of the partial Coulomb-nuclear interferences, starting with the $^{11}\mathrm{Be}+{}^{208}\mathrm{Pb}$ reaction. Looking at the different multipole transitions, we observe from Table 1 that at zero-order transition, the *s*-wave Coulomb-nuclear interference is exclusively destructive, and is equal to the integrated Coulomb breakup cross section in magnitude. At the first-order, one notices that this interference is strongly constructive in the *s*-waves, followed by the *d*-waves, whereas it is weakly constructive in the *f*-waves. It is rather strongly destructive in the *p*-waves and weakly destructive in the g-waves. It is observed that $S^{\lambda}=655.76$ mb, reflecting a strongly constructive Coulomb-nuclear interference due mostly to its *s*-wave contribution. At the

TABLE 1. Partial wave Coulomb-nuclear interferences for the ^{11}Be + ^{208}Pb reaction.

	σ_I^{ℓ}				$\sigma_I^{\lambda_{\max}}$	
Part.	$\lambda=0$	$\lambda=1$	$\lambda=2$	$\lambda=3$	$\lambda_{\max}=1$	$\lambda_{\max}=4$
s	-12.42	620.69	-27.27	2.36	14.69	-131.36
p	-	-207.91	0.00	0.06	-471.46	-535.30
d	-	250.50	-54.37	-0.45	-33.86	-85.28
f	-	3.90	0.00	-0.33	-17.25	-53.99
g	-	-11.42	-8.91	1.36	-14.49	-10.25
S^{λ}	-12.42	655.76	-90.54	1.99	-522.37	-816.16

second-order on the other hand, this interference is seen to be exclusively destructive wherever is nonzero, owing to the fact that here, the nuclear breakup cross section prevails over the total breakup cross section in each partial wave. At the third-order however, it is noticed that the Coulomb-nuclear interference is weakly constructive in the *s*-, *p*- and g-waves, and weakly destructive in the *d*- and *f*-waves.

Let us now consider the effects of the first-order and higher-order interferences on the partial Coulomb-nuclear interferences. Looking at the first-order interference, one observes that it dramatically reduces the *s*-wave Coulomb-nuclear interference from 620.69 mb to 14.69 mb without affecting its nature, while the *p*-wave Coulomb-nuclear interference is substantially increased from -207.91 mb to -471.46 mb, keeping also its nature. Regarding the *d*-wave, it is noticed that the Coulomb-nuclear interference is substantially decreased from 250.50 mb to -33.86 mb and becomes destructive by nature. As for the *f*-waves, this interference is increased from 3.90 mb to -17.25 mb, becoming as well destructive, whereas in the g-waves, it is slightly increased from -11.42 mb to -14.49 mb. The sum $S^{\lambda} = -522.37$ mb serves to conclude that the first-order interference reduces around 18.80% of the Coulomb-nuclear interference, and changes its nature. Thus for this reaction the first-order interference does not affect considerably the magnitude of the Coulomb-nuclear interference, but changes its nature.

TABLE 2. Partial wave Coulomb-nuclear interferences for the ^{15}C + ^{208}Pb reaction.

	σ_I^{ℓ}				$\sigma_I^{\lambda_{\max}}$	
Part.	$\lambda=0$	$\lambda=1$	$\lambda=2$	$\lambda=3$	$\lambda_{\max}=1$	$\lambda_{\max}=4$
s	-14.03	197.80	-6.68	0.12	64.08	-4.71
p	-	-799.80	0.00	0.00	-364.95	-359.60
d	-	112.10	-6.03	0.01	-5.08	-24.47
f	-	73.84	0.00	0.03	12.76	-2.28
g	-	11.43	-1.53	0.02	1.94	1.72
S^{λ}	-14.03	-401.64	-14.25	0.46	-290.96	-389.32

As in Ref.[9], the higher-order interference effect is estimated by comparing the first-order and all order interference effects. The table shows that the s-wave Coulomb-nuclear breakup cross section is substantially increased from 14.69 mb to -131.36 becoming strongly destructive, owing to the higher-order interference. This interference in the other partial waves is increased without changing the nature, except in the g-waves where it is decreased from -14.49 mb to -10.25 mb. While one could expect the higher-order interference to have minor effect on the Coulomb-nuclear interference, the sum $S^{\lambda} = -816.16$ mb shows that this interference is significantly increased by 36.0%. It is interesting to see that the higher-order interference affects more the Coulomb-nuclear interference than the first-order interference. However, the results show that the higher-order interference does not have any effect on the nature of this interference. This shows the important of the higher-order effects in the breakup process of this reaction.

In order to get more insight into the conclusions above, and to assess the role of the binding energy on the nature and magnitude of the Coulomb-nuclear interference, we also consider the $^{15}C + ^{208}Pb$ reaction. We first analyze also the different multipole transition effects, where at zero-order one notices that the Coulomb-nuclear interference is again destructive and is equal in magnitude to the Coulomb breakup cross section. At first-order this interference is strongly destructive in the p-waves ($\sigma_I = -799.80$ mb), while is it constructive in all the other partial waves. This strong destructiveness in the p-waves is attenuated by the contribution of the other partial waves, such that $S^{\lambda} = -401.64$ mb $\ll -799.80$ mb. At second-order however, one sees that this interference is exclusively destructive wherever it is nonzero, where its overall magnitude is roughly equal to its zero-order magnitude. At third-order on the other hand, the Coulomb-nuclear interference is much weakly constructive. Looking at the first-order interference, we see that the Coulomb-nuclear interference is still destructive in the p-waves, but its magnitude is largely reduced to -364.95 mb, a reduction of 54.37%, while it is dramatically reduced by 95.47% in the d-waves, where it becomes very weakly destructive. The sum $S^{\lambda} = -290.96$ mb shows that the first-order interference reduces the overall Coulomb-nuclear interference by 27.56%, without affecting its nature. One observes on the other hand, that due to the higher-order interference, the Coulomb-nuclear becomes destructive in all partial waves expect in the g-waves, and is overall increased by 25.26%.

Let us now compare the effects of the first-order and higher-order interference on the partial Coulomb-nuclear interferences for the two reactions. To render this comparison easy, we plot in Fig.1, the partial Coulomb-nuclear interferences as functions of the partial waves. If we consider first the first-order transition, we find that in the s-waves, the Coulomb-nuclear interference is more strongly constructive for the $^{11}Be + ^{208}Pb$ reaction [Fig.1(a)] than for the $^{15}C + ^{208}Pb$ reaction [Fig.1(b)]. In the p-waves on the other hand, this interference is more strongly destructive for the $^{15}C + ^{208}Pb$ reaction. In the d-waves, we find that the interference is more destructive for the $^{11}Be + ^{208}Pb$ reaction. In the f-and g-waves however, the Coulomb-nuclear interference is more constructive for the $^{15}C + ^{208}Pb$ reaction, while it becomes destructive in the g-waves for the $^{11}Be + ^{208}Pb$ reaction. Considering the effects of the first-order interference, it is found that in the s-waves, the Coulomb-nuclear interference is substantially reduced but keeps

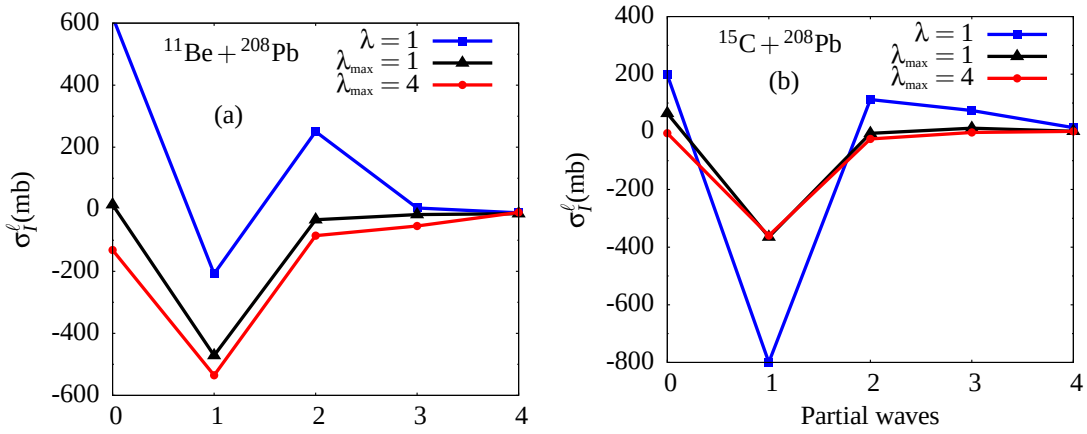

FIGURE 1. Comparison between the effects of the first-order and higher-order interferences on the Coulomb-nuclear interference for the two reactions

its nature for the $^{15}C + ^{208}Pb$ reaction, while it is dramatically reduced and becomes weakly destructive for the $^{11}Be + ^{208}Pb$ reaction. In the *p*-waves, this interference still substantially reduced and remains destructive for the $^{15}C + ^{208}Pb$ reaction. However, for the $^{11}Be + ^{208}Pb$ reaction, one notices that this interference is rather substantially increased without affecting its nature as well. This interference is largely reduced and becomes weakly destructive for both reactions in the *d*-waves. The variation of this interference in the *f*-and g-waves is small at this stage. Looking at both figures, we observe that the higher-order interference has a pronounced effect on the Coulomb-nuclear interference for the $^{11}Be + ^{208}Pb$ reaction than for the $^{15}C + ^{208}Pb$ reaction.

In Ref.[9], it was obtained that the first-order and higher-order angular distributions differential total and nuclear breakup cross sections are extended to larger angles. This extension behavior was found to be washed away, due largely to the first-order interference. Among other reasons, one may conclude that the extension to larger angles is a result of a weak nuclear absorption when the projectile approaches the target, al-

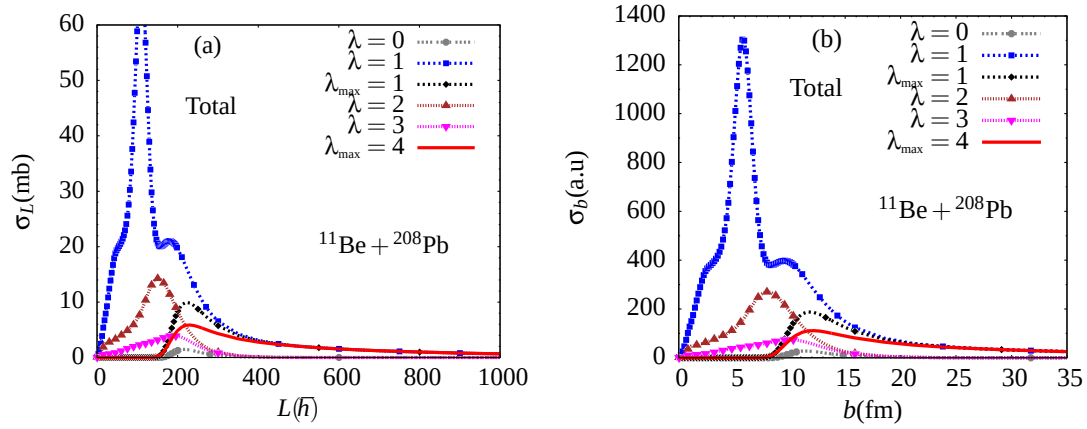

FIGURE 2. Angular momentum (a) and impact parameter (b) distributions for the total breakup.

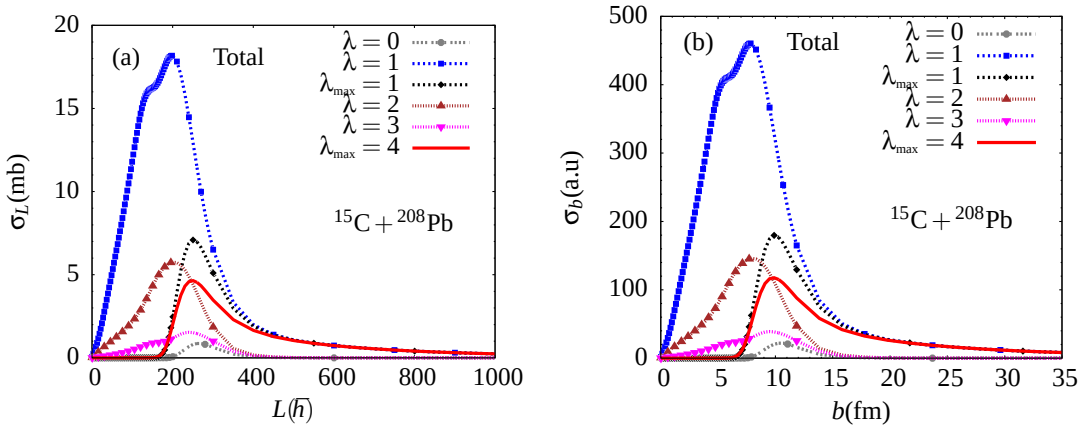

FIGURE 3. Angular momentum (a) and impact parameter (b) distributions for the total breakup.

lowing more projectile flux to penetrate the Coulomb barrier. On the other hand, the removal of this extension behavior owing to the first-order interference, is a reflection of the fact that this interference produces a stronger nuclear absorption at small impact parameters, such that more projectile flux is removed from the breakup channel to fuel probably other channels. Moreover, the non-negligible nuclear breakup cross sections even when the different multipoles are included coherently in such Coulomb-dominated reactions, shows that a considerable amount of nuclear flux survives the absorption and therefore is felt beyond the projectile-target relative distance. In order to get more insight into these conclusions, we consider the analysis of the impact parameter distributions breakup cross sections. Using the code FRESCO [10], with the inputs parameters described in Ref.[9], we obtain the angular momentum distributions breakup cross sections. These cross sections are converted into impact parameter distributions, by first writing the classical relation that relates the grazing impact parameter ($b_{\rm gr}$) to the grazing angle ($\theta_{\rm gr}$) and the grazing angular momentum ($L_{\rm gr}$), reading [11]

$$b_{\rm gr} = \frac{Z_p Z_t e^2}{2E_{\rm cm}\tan\left(\frac{\theta_{\rm gr}}{2}\right)}, \quad L_{\rm gr} = \sqrt{\frac{2\mu_{pt}(E_{\rm cm}+\varepsilon_0)}{\hbar^2}}\, b_{\rm gr}, \tag{2}$$

where Z_p, Z_t are the projectile and target charges, and μ_{pt} the projectile-target reduced mass, $E_{\rm cm}$ is the center of mass energy and ε_0 the projectile binding energy. We then convert the angular distributions cross sections into impact parameter distributions cross sections as

$$\frac{d\sigma_b}{db} = \sqrt{\frac{2\mu_{pt}(E_{\rm cm}+\varepsilon_0)}{\hbar^2}}\frac{d\sigma_L}{dL} \quad \Rightarrow \sigma_b = \sqrt{\frac{2\mu_{pt}(E_{\rm cm}+\varepsilon_0)}{\hbar^2}}\sigma_L. \tag{3}$$

For the ^{11}Be + ^{208}Pb reaction, we use $b_{\rm gr} = 1.25(11^{1/3} + 208^{1/3}) = 10.186$fm, corresponding to $\theta_{\rm gr} = 3.74^\circ$ and $L_{\rm gr} = 192.648\hbar$. F the ^{15}C + ^{208}Pb reaction we have, $b_{\rm gr} = 1.25(15^{1/3} + 208^{1/3}) \simeq 10.490$fm, implying $\theta_{\rm gr} = 4.06^\circ$ and $L_{\rm gr} = 266.04\hbar$.

We start with the $^{11}\mathrm{Be} + {}^{208}\mathrm{Pb}$ reaction, where the angular momentum and impact parameter distributions total breakup cross sections are given in Fig.2 (a) and (b). If we consider only the impact parameter distributions (although the same observations apply to both figures), we observe a largely dominating narrow first-order breakup cross section, with a peak at around the half of the grazing impact parameter ($b \simeq 5$ fm), meaning inside the Coulomb barrier. This shows a negligible nuclear absorption when the projectile is closest to the target. It is similarly observed for the higher-order breakup cross sections that they are significant at small impact parameters, but vanish rapidly beyond the grazing impact parameter ($b \leq 15$ fm). It follows that as the projectile moves away from the target, the higher-order effects become quickly irrelevant. These results allow one to conclude that single multipole transitions produce weak nuclear absorption, which among other reasons can explain the extension behavior of the first-order and higher-order differential total and nuclear breakup cross sections to larger angles.

Although the zero-order breakup cross section is negligible below the grazing impact parameter, we observe a strong effect of the first-order interference, such that the $\lambda_{\max} = 1$ breakup cross section is similarly negligible below the grazing impact parameter, after which it suddenly grows in the vicinity of the grazing impact parameter to be extended to larger impact parameters. This shows that the first-order interference produces a strong nuclear absorption, preventing more projectile flux to penetrate the Coulomb barrier. The figure also shows that when the projectile is far away from the target, where the nuclear effects are negligible, the first-order interference effect is negligible since the first-order and the $\lambda_{\max} = 1$ breakup cross section curves are hardly distinguishable. It follows that the extension of the first-order breakup cross sections to larger angles obtained in Ref.[9], is mainly due to the weak nuclear absorption, at the first-order multipole transition. One notices that the effect of the higher-order interference is to lower the magnitude of the breakup cross section in the vicinity of the grazing impact parameter.

The results obtained for the $^{15}\mathrm{C} + {}^{208}\mathrm{Pb}$ reaction are presented in Figs.3 (a) and (b). Qualitatively, we can draw similar conclusions as for the $^{11}\mathrm{Be} + {}^{208}\mathrm{Pb}$ reaction. However, here one observes more wider first-order breakup cross section, owing on one hand to the large $^{15}\mathrm{C}$ binding energy that $^{11}\mathrm{Be}$.

CONCLUSION

In this paper, we have investigated the effects of the first-order and higher-order interferences on partial Coulomb-nuclear interferences for the $^{11}\mathrm{Be},{}^{15}\mathrm{C} + {}^{208}\mathrm{Pb}$ breakup reactions. Considering the multipole transitions first, for the $^{11}\mathrm{Be} + {}^{208}\mathrm{Pb}$ reaction, at first-order, the Coulomb-nuclear interference is strongly constructive, owing to its s-wave contribution. It becomes destructive at second-order it becomes destructive, due mostly to its d-wave contribution, and weakly constructive at third-order. For the $^{15}\mathrm{C} + {}^{208}\mathrm{Pb}$ reaction on the other hand, at first-order, the Coulomb-nuclear interference is strongly destructive, due to its p-wave contribution, it becomes weakly destructive at second-order, while it is negligibly constructive at third-order.

It is obtained that for the ^{11}Be $+^{208}$ Pb reaction, the first-order interference slightly reduces the Coulomb-nuclear interference by 18.80%, and becomes destructive by nature. On the other hand, the higher-order interference is found to increase the Coulomb-nuclear interference by 36.0%, but has no effect on its nature. The conclusion is that the higher-order interference affects more the magnitude of the Coulomb-nuclear interference than the first-order interference. For the ^{15}C $+^{208}$ Pb reaction however, the first-order interference reduces the Coulomb-nuclear interference by 27.56% without affecting its nature, and it is increased by 25.26% due to the higher-order interference.

REFERENCES

1. M. S. Hussein, R. Lichtenthaler, F. M. Nunes, I. J. Thompson, Scaling and interference in the dissociation of halo nuclei, *Phys. Lett.* **B 640**, 91 (2006).
2. B. Mukeru, M. L. Lekala, A. S. Denikin, Study of the effects of nuclear and Coulomb interactions in the breakup of ^{19}C on ^{208}Pb, *J. Phys. G: Nucl. Part. Phys.* **42**,015109 (11pp) (2015).
3. R. Chatterjee, R. Shyam, Coulomb-nuclear interference in the breakup of ^{11}Be, *Phys. Rev*. **C 66**, 061601 (R) (2002).
4. R. Chatterjee, Beam energy dependence of the Coulomb-nuclear interference in the breakup of ^{11}Be, *Phys. Rev.* **C 75**,064604 (2007).
5. R. Chatterjee, Full quantal theory of one-neutron breakup reactions, *Phys. Rev.* **C 68**,044604 (2003).
6. T. Tarutina, M. S. Hussein, Interference effects in the Coulomb dissociation of ^{15,17,19}C, *Phys. Rev.* **C 70**,034603 (2004).
7. N. C. Summers and F. M. Nunes, Extracting (n,γ) direct capture cross section from Coulomb dissociation: Application to ^{14}C$(n,\gamma)^{15}$C, *Phys. Rev.* **C 78**,011601 (R) (2008).
8. B. Mukeru, M. L. Lekala and A. S. Denikin, Role of the diagonal and off-diagonal continuum-continuum couplings in the breakup of ^{8}B and ^{19}C on ^{58}Ni and ^{208}Pb targets, *N*ucl. Phys. **A 935**,18-27 (2015).
9. B Mukeru and M L Lekala, First-order and higher-order interferences in the ^{15}C $+^{208}$ Pb and ^{11}Be $+^{208}$ Pb reactions, *Phys. Rev.* **C 91**,064609 (2015).
10. www.fresco.org.uk
11. P. Fröbrich, P. Lipperheide, *Theory of Nuclear Reactions*, Oxford 1996
12. P. Capel, F. M. Nunes, Peripherality of breakup reactions, *Phys. Rev.* **C 75**,054609 (2007).

Tunneling of composite particles through repulsive barriers

S.I. Vinitsky*, A.A. Gusev*, O. Chuluunbaatar*, V.L. Derbov†, A. Góźdź** and P.M. Krassovitskiy‡

*Joint Institute for Nuclear Research, Dubna, Russia
†Saratov State University, Saratov, Russia
**University of M. Curie-Skłodowska, Lublin, Poland
‡Institute of Nuclear Physics, Almaty, Kazakhstan

Abstract. A method for calculating the quantum tunneling of composite systems comprizing a few identical particles through repulsive barriers is presented. The coupled-channel approximation in the new symmetrized-coordinate representation of the harmonic oscillator basis is used. In this approach the multichannel scattering problem for the Schrödinger equation is reduced to a set of coupled second-order ordinary differential equations with third-type boundary conditions and solved using the finite element method. The efficiency of the proposed approach and software are demonstrated by the analysis of metastable states of the composite systems of identical particles coupled by the harmonic oscillator potential in 1D-space. These states are shown to cause the quantum transparency of the barrier, depending on the number of identical particles in the tunneling cluster and the permutation symmetry type.

Keywords: coupled channel method, quantum tunnelling, system of identical particles, representation of symmetrized coordinates, metastable states, quantum transparency
PACS: 24.10.-i, 24.10.Eq, 21.45.-v, 21.60.Gx

INTRODUCTION

Quantum tunneling of composite systems through barriers is one of the problems most often occurring in nuclear physics, physics of solid state and semiconductor nanostructures. Usually, the theory is based on considering the penetration of a structureless particle through barriers within the effective mass approximation. However, the majority of important applications deal with tunneling of structured objects (clusters), e.g., atomic nuclei through Coulomb barrier, where the effects of structure (multiple particles) manifest themselves in anomalous behavior of nuclear reaction cross-sections below the Coulomb barrier. Indeed, when the cluster size is comparable with the spatial width of the barrier, the mechanisms arise that enhance the barrier transparency. The effect of quantum barrier transparency depending on the internal structure of the incident particles was revealed for a pair of coupled particles tunnelling through a repulsive barrier [1]. The effect was shown to be due to the barrier resonance formation under the condition that the potential energy of the compound system (cluster + barriers) possesses local minima, thus providing the appearance of metastable states of the moving cluster [2]. The manifestations and the underlying mechanisms of the effect were extensively studied in multiple quantum phenomena, e.g, the near-surface quantum diffusion of molecules [3, 4, 5, 6], the channelling and tunnelling of ions through multidimensional barriers

[7, 8, 9], the sub-barrier tunnelling of light nuclei [10], and the collinear ternary fission [11]. For studying these systems, as well as tetrahedral and octahedral-symmetric nuclei [12], it is urgent not only to consider the tunnelling of a more general quantum system of n identical particles[13, 14, 15, 16, 17], but also to develop efficient methods, algorithms [18] and software[19, 20, 21], implementing the appropriate numerical modelling.

Here we consider the cluster tunneling problem in symmetrized coordinates basing on the close-coupled channel method and the finite element method. The efficiency of the proposed approach and software are demonstrated by the example of metastable states in clusters of a few identical particles coupled by the harmonic oscillator potential in 1D-space. These metastable states are shown to be responsible for the quantum transmittance properties when the clusters penetrate thorugh Gaussian barriers, depending on the number of identical particles in the cluster and the permutation symmetry type of the state.

REPRESENTATION OF SYMMETRIZED COORDINATES

Consider n identical quantum particles having the mass m and the set of Cartesian coordinates $x_i \in \mathbf{R}^d$ in the d-dimensional Euclidean space, forming a vector $\tilde{\mathbf{x}} = (\tilde{x}_1, ..., \tilde{x}_n) \in \mathbf{R}^{n\times d}$ in the $n \times d$-dimensional configuration space. The particles form a cluster due to the coupling via the pair potential $\tilde{V}^{pair}(\tilde{x}_{ij})$ depending on the relative coordinates $\tilde{x}_{ij} = \tilde{x}_i - \tilde{x}_j$ in a way, similar to the potential of a harmonic oscillator $\tilde{V}^{hosc}(\tilde{x}_{ij}) = \frac{m\omega^2}{2}(\tilde{x}_{ij})^2$ with the frequency ω. The particles are considered to penetrate through the repulsive potential barrier $\tilde{V}(\tilde{x}_i)$. In the dimensionless coordinates $x_i = \tilde{x}_i/x_{osc}$, $x_{ij} = \tilde{x}_{ij}/x_{osc} = x_i - x_j$ and energy $E = \tilde{E}/E_{osc}$, $V(x_i) = \tilde{V}(x_i x_{osc})/E_{osc}$, $V^{hosc}(x_{ij}) = \tilde{V}^{hosc}(x_{ij}x_{osc})/E_{osc} = x_{ij}^2/n$, using the oscillator units $x_{osc} = \sqrt{\hbar/(m\omega\sqrt{n})}$, and $E_{osc} = \hbar\omega\sqrt{n}/2$ one can write the appropriate Schrödinger equation as

$$\left[-\frac{\partial^2}{\partial \mathbf{x}^2} + \sum_{i,j=1;i<j}^{n} \frac{(x_{ij})^2}{n} + U(\mathbf{x}) - E\right]\Psi(\mathbf{x}) = 0, \tag{1}$$

$$U(\mathbf{x}) = \sum_{i,j=1;i<j}^{n} U^{pair}(x_{ij}) + \sum_{i=1}^{n} V(x_i),$$

where $U^{pair}(x_{ij}) = V^{pair}(x_{ij}) - V^{hosc}(x_{ij})$, is the non-oscillator part of the coupling potential i.e., if $V^{pair}(x_{ij}) = V^{hosc}(x_{ij})$, then $U^{pair}(x_{ij}) = 0$, $\mathbf{x} = (x_1, ..., x_n) \in \mathbf{R}^{n\times d}$.

We seek the solutions $\Psi(\mathbf{x})$ of Eq. (1), totally symmetric or antisymmetric under the permutations of n particles that belong to the permutation group S_n. A permutation of particles is nothing but a permutation of the appropriate Cartesian coordinates $x_i \leftrightarrow x_j$, $i, j = 1, ..., n$.

The construction of states that keep the symmetry (antisymmetry) under the permutations of n initial Cartesian coordinates (below referred to as S (A) states), is most clearly implemented using the new symmetrized relative coordinates rather than the Jacobi ones.

One of the possible definitions for the symmetrized coordinates is [13]

$$\begin{pmatrix} \xi_0 \\ \xi_1 \\ \vdots \\ \xi_{n-1} \end{pmatrix} = \frac{1}{\sqrt{n}} \begin{pmatrix} 1 & 1 & 1 & \cdots & 1 \\ 1 & a_1 & a_0 & \cdots & a_0 \\ 1 & a_0 & a_1 & \cdots & a_0 \\ \vdots & \vdots & \vdots & \ddots & \vdots \\ 1 & a_0 & a_0 & \cdots & a_1 \end{pmatrix} \begin{pmatrix} x_1 \\ x_2 \\ \vdots \\ x_n \end{pmatrix}, \tag{2}$$

where $a_0 = 1/(1-\sqrt{n})$, $a_1 = a_0 + \sqrt{n}$. If $n = 2$, then the above symmetrized coordinates are similar to the symmetrized Jacobi coordinates, while for $n = 4$ they to a normalizing factor correspond to tetrahedral ones [22, 23].

In the symmetrized coordinates Eq. (1) takes the form

$$\left[-\frac{\partial^2}{\partial \xi_0^2} + \sum_{i=1}^{n-1} \left(-\frac{\partial^2}{\partial \xi_i^2} + \xi_i^2 \right) + U(\xi_0, \xi) - E \right] \Psi(\xi_0, \xi) = 0, \tag{3}$$

$$U(\xi_0, \xi) = \sum_{i,j=1; i<j}^{n} U^{pair}(x_{ij}(\xi)) + \sum_{i=1}^{n} V(x_i(\xi_0, \xi)),$$

$\xi_0 \in \mathbf{R}^d$ and $\xi = \{\xi_1, ..., \xi_{n-1}\} \in \mathbf{R}^{(n-1)\times d}$, which is invariant under the permutations $\xi_i \leftrightarrow \xi_j$ with $i, j = 1, ..., n-1$, i.e., the invariance of Eq. (1) under permutations $x_i \leftrightarrow x_j$ with $i, j = 1, ..., n$ survives the symmetrising coordinate transformation (2). This remarkable fact is one of the most prominent features of the proposed approach.

SYMMETRIZED OSCILLATOR BASIS

Let us restrict ourselves to considering the pair interactions in the form of harmonic oscillator potentials $V^{pair}(x_{ij}) = V^{hosc}(x_{ij})$ in the case of one-dimensional Euclidean space ($d = 1$). Let us define the set of cluster functions $\langle \xi \,|\, j \rangle^{S(A)} \equiv \Phi_j^{S(A)}(\xi) \in \mathbf{L}_2(\mathbf{R}^{n-1})$, symmetric (S) (antisymmetric (A)) under the permutations of n identical particles and the corresponding values of energy $\varepsilon_j^{S(A)}$ as the solutions of the eigenvalue problem for the equation

$$\left(\sum_{i=1}^{n-1} \left(-\frac{\partial^2}{\partial \xi_i^2} + \xi_i^2 \right) - \varepsilon_j^{S(A)} \right) \Phi_j^{S(A)}(\xi) = 0. \tag{4}$$

The desired solutions $\Phi_j^{S(A)}(\xi)$ are sought in the form of linear combinations of the known functions of the $(n-1)$-dimensional harmonic oscillator $\Phi^{osc}_{[i_1,...,i_{n-1}]}(\xi) \in \mathbf{L}_2(\mathbf{R}^{n-1})$

$$\Phi_j^{S(A)}(\xi) = \sum_{\{i_1,...,i_{n-1}\} \in \Delta_j} \alpha^{S(A)}_{j[i_1,...,i_{n-1}]} \Phi^{osc}_{[i_1,...,i_{n-1}]}(\xi), \tag{5}$$

$$\Phi^{osc}_{[i_1,...,i_{n-1}]}(\xi) = \prod_{k=1}^{n-1} \frac{\exp(-\xi_k^2/2) H_{i_k}(\xi_k)}{\sqrt[4]{\pi}\sqrt{2^{i_k}}\sqrt{i_k!}}.$$

Here $H_{i_k}(\xi_k)$ are the Hermite polynomials [24], the set of subscripts $\Delta_j \equiv \{i_1,...,i_{n-1}\}$, taking the natural number values, is defined by the condition

$$\Delta_j = \left\{ i_1,...,i_{n-1} \middle| 2\sum_{k=1}^{n-1} i_k + n - 1 = \varepsilon_j^{S(A)} \right\}, \tag{6}$$

of their belonging to the set of eigenfunctions $\Phi^{osc}_{[i_1,...,i_{n-1}]}(\xi)$, corresponding to the eigenvalue $\varepsilon^{osc}_{[i_1,...,i_{n-1}]} \equiv \varepsilon^{osc}_f = 2f + n - 1$, $f = \sum_{k=1}^{n-1} i_k$, of the $(n-1)$-dimensional oscillator, possessing the $p = (n+f-2)!/f!/(n-2)!$-fold degeneracy [25], which is chosen to equal the desired energy eigenvalue $\varepsilon_j^{S(A)} = \varepsilon^{osc}_{[i_1,...,i_{n-1}]}$.

The unknown coefficients $\alpha^{S(A)}_{j[i_1,...,i_{n-1}]}$ of the expansion (5) for the orthonormalised functions $\Phi_j^{S(A)}(\xi)$, symmetric (S) (or antisymmatric (A)) under the permutations of n identical particles, the corresponding eigenvalues $\varepsilon_j^{S(A)}$ and the multiplicity of their degeneracy $p^{S(A)} \ll p$ were calculated using the algorithm [13, 16] that consists of two steps:
1. The eigenfunctions symmetric (or antisymmetric) under the permutations $\xi_i \leftrightarrow \xi_j$ $(j = 1,...,n-1)$ are generated using the standard method [26]. These functions are also symmetric (or antisymmetric) under the permutations $x_i \leftrightarrow x_j$ $(i, j = 2,...,n)$, but possess no symmetry with respect to the permutations $x_1 \leftrightarrow x_j$ $(j = 2,...,n)$.
2. Using the eigenfunctions obtained at the previous step, the set of linearly-independent functions, symmetric (or antisymmetric) under the permutation $x_2 \leftrightarrow x_1$ is constructed, from which we get the desired orthonormalised basis (5) using the Gram-Schmidt procedure.

COUPLED CHANNEL EQUATIONS

The solution of the problem (3) in the symmetrized coordinates (2) is sought in the form of the expansion

$$\Psi^{S(A)}_{i_o}(\xi_0,\xi) = \sum_{j=1}^{N} \Phi_j^{S(A)}(\xi)\chi^{S(A)}_{ji_o}(\xi_0), \tag{7}$$

where $\chi^{S(A)}_{ji_o}(\xi_0)$ are the elements of the desired matrix function with the dimension $N \times N_o$, and $\Phi_j^{S(A)}(\xi)$ are the cluster basis functions (5). In the oscillator representation (5) the set of coupled ordinary differential equations for the functions depending on the center-of-mass variable ξ_0 has the form

$$\sum_{j=1}^{N} \left[\left(-\frac{d^2}{d\xi_0^2} - (E - \varepsilon_i^{S(A)}) \right) \delta_{ij} + V^{S(A)}_{ij}(\xi_0) \right] \chi^{S(A)}_{ji_o}(\xi_0) = 0, \tag{8}$$

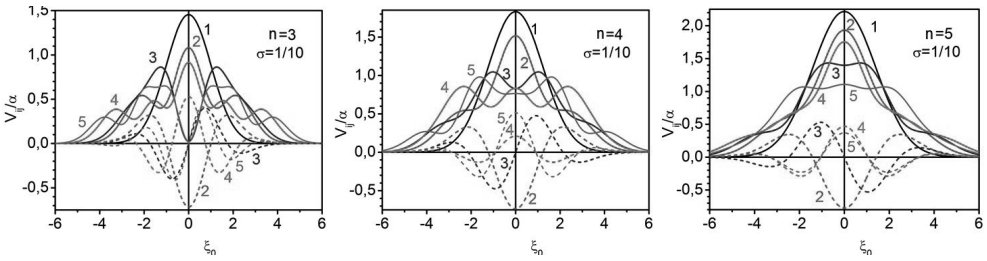

FIGURE 1. Diagonal V_{jj} (solid lines) and nondiagonal V_{j1} (dashed lines) effective potential matrix elements for S states for $n = 3$, $n = 4$, and $n = 5$ particles at $\sigma = 1/10$.

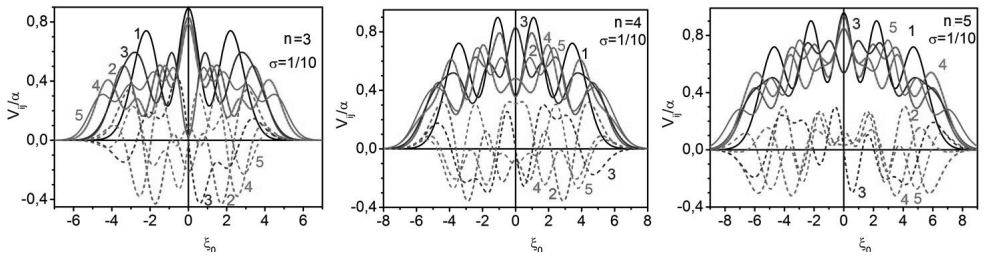

FIGURE 2. Diagonal V_{jj} (solid lines) and nondiagonal V_{j1} (dashed lines) effective potential matrix elements for A states for $n = 3$, $n = 4$, and $n = 5$ particles at $\sigma = 1/10$.

where $V_{ij}^{S(A)}(\xi_0) = V_{ji}^{S(A)}(\xi_0)$ are the elements of the symmetric matrix $\mathbf{V}^{S(A)}(\xi_0)$ of effective potentials with the dimension $N \times N$, expressed as the integrals

$$V_{ij}^{S(A)}(\xi_0) = \int d\xi \Phi_i^{S(A)}(\xi) \left(\sum_{k=1}^{n} V(x_k(\xi_0, \xi)) \right) \Phi_j^{S(A)}(\xi). \tag{9}$$

For Gaussian potentials $V(x_i) = \frac{\alpha}{\sqrt{2\pi}\sigma} \exp(-\frac{x_i^2}{\sigma^2})$ the integrals are calculated analytically and presented in Figs. 1, 2.

Multichannel scattering problem. Consider the scattering problem with the homogeneous boundary conditions of the third kind with respect to the variable ξ_0 at $\xi_0 = \xi_0^{\min} \ll 0$ and $\xi_0 = \xi_0^{\max} \gg 0$:

$$\left.\frac{d\mathbf{F}(\xi_0)}{d\xi_0}\right|_{\xi_0=\xi_0^{\min}} = \mathscr{R}(\xi_0^{\min})\mathbf{F}(\xi_0^{\min}), \quad \left.\frac{d\mathbf{F}(\xi_0)}{d\xi_0}\right|_{\xi_0=\xi_0^{\max}} = \mathscr{R}(\xi_0^{\max})\mathbf{F}(\xi_0^{\max}). \tag{10}$$

Here $\mathscr{R}(\xi_0)$ is an unknown $N \times N$ matrix function, $\mathbf{F}(\xi_0) = \{\chi^{(j)}(\xi_0)\}_{j=1}^{N_o}$ is the desired $N \times N_o$ matrix solution and N_o is the number of open channels, $N_o = \max_{2E \geq \varepsilon_j} j \leq N$. The matrix solution $\mathbf{F}_\nu(\xi_0) \equiv \mathbf{F}_\nu(\xi_0, E)$, describing the incidence of the particle and its

scattering, with the asymptotic form "incident wave + outgoing waves" is written as

$$\mathbf{F}_v^{\rm as}(\xi_0\to\pm\infty)=\left\{\begin{array}{ll}\left\{\begin{array}{ll}\mathbf{X}^{(+)}(\xi_0)\mathbf{T}_v, & \xi_0>0,\\ \mathbf{X}^{(+)}(\xi_0)+\mathbf{X}^{(-)}(\xi_0)\mathbf{R}_v, & \xi_0<0,\end{array}\right. & v=\!\!\rightarrow,\\ \left\{\begin{array}{ll}\mathbf{X}^{(-)}(\xi_0)+\mathbf{X}^{(+)}(\xi_0)\mathbf{R}_v, & \xi_0>0,\\ \mathbf{X}^{(-)}(\xi_0)\mathbf{T}_v, & \xi_0<0,\end{array}\right. & v=\!\!\leftarrow,\end{array}\right. \tag{11}$$

where $\mathbf{R}_v$ and $\mathbf{T}_v$ are the reflection and transmission $N_o\times N_o$ matrices, $v=\!\!\rightarrow$ and $v=\!\!\leftarrow$ denotes the initial direction of the particle motion along the ξ_0 axis. The leading term of the asymptotic rectangular matrix functions $\mathbf{X}^{(\pm)}(\xi_0)$ has the form

$$X_{ij}^{(\pm)}(\xi_0)\to p_j^{-1/2}\exp\left(\pm\imath\left(p_j\xi_0-\frac{Z_j}{p_j}\ln(2p_j|\xi_0|)\right)\right)\delta_{ij}, \tag{12}$$
$$p_j=\sqrt{2E-\varepsilon_j},\quad i=1,\ldots,N,\quad j=1,\ldots,N_o,$$

where $Z_j=Z_j^+$ at $\xi_0>0$ and $Z_j=Z_j^-$ at $\xi_0<0$, i.e., when the effective charges are located to the left or to the right of the repulsive long-range Coulomb potential barrier [8]. The matrix solution $\mathbf{F}_v(\xi_0,E)$ is normalized by the condition

$$\int_{-\infty}^{\infty}\mathbf{F}_{v'}^{\dagger}(\xi_0,E')\mathbf{F}_v(\xi_0,E)d\xi_0=2\pi\delta(E'-E)\delta_{v'v}\mathbf{I}_{oo}, \tag{13}$$

where $\mathbf{I}_{oo}$ is the unit $N_o\times N_o$ matrix. Let us rewrite Eq. (11) in the matrix form at $\xi_0^+\to+\infty$ and $\xi_0^-\to-\infty$ as

$$\left(\begin{array}{ll}\mathbf{F}_{\rightarrow}(\xi_0^+) & \mathbf{F}_{\leftarrow}(\xi_0^+)\\ \mathbf{F}_{\rightarrow}(\xi_0^-) & \mathbf{F}_{\leftarrow}(\xi_0^-)\end{array}\right)=\left(\begin{array}{ll}\mathbf{0} & \mathbf{X}^{(-)}(\xi_0^+)\\ \mathbf{X}^{(+)}(\xi_0^-) & \mathbf{0}\end{array}\right)+\left(\begin{array}{ll}\mathbf{0} & \mathbf{X}^{(+)}(\xi_0^+)\\ \mathbf{X}^{(-)}(\xi_0^-) & \mathbf{0}\end{array}\right)\mathbf{S}, \tag{14}$$

where the unitary and symmetric scattering matrix $\mathbf{S}$

$$\mathbf{S}=\left(\begin{array}{ll}\mathbf{R}_{\rightarrow} & \mathbf{T}_{\leftarrow}\\ \mathbf{T}_{\rightarrow} & \mathbf{R}_{\leftarrow}\end{array}\right),\qquad \mathbf{S}^{\dagger}\mathbf{S}=\mathbf{S}\mathbf{S}^{\dagger}=\mathbf{I} \tag{15}$$

is composed of the reflection and transmission matrices. So, the logarithmic derivative matrices $\mathscr{R}(\xi_0)$ are constructed using the asymptotic solutions of the multichannel scattering problem in both open and closed channels. The detailed calculation of the matrix solution $\mathbf{F}_v(\xi_0)$ using a variational functional of (8)–(10) is presented in Ref. [14, 21, 17].

Metastable states. For metastable states the eigenfunctions obey the boundary conditions of the third kind (10), where the matrices $\mathscr{R}(\xi_0^t)=\mathrm{diag}(\mathscr{R}(\xi_0^t))$ depend on the desired complex energy eigenvalue $E\equiv E_m=\Re E_m+\imath\Im E_m$, $\Im E_m<0$ and are expressed as

$$\mathscr{R}_{i_oi_o}(\xi_0^{\max})=\left\{\begin{array}{ll}\imath p_m, & \Re E_m\geq\varepsilon_j^{S(A)},\\ \imath q_m, & \Re E_m<\varepsilon_j^{S(A)}\end{array}\right\},\quad \mathscr{R}_{i_oi_o}(\xi_0^{\min})=-\mathscr{R}_{i_oi_o}(\xi_0^{\max})$$
$$p_m=\sqrt{E_m-\varepsilon_{i_o}^{S(A)}},\quad q_m=\imath\sqrt{\varepsilon_{i_o}^{S(A)}-E_m}, \tag{16}$$

TABLE 1. The sets of the first resonance energy values $E_l^{S(A)}$, at which the maximum of the transmission coefficient $|T|_{11}^2$ is achieved, the complex energy eigenvalues $E_m^M = \Re E_m^M + \imath \Im E_m^M$ of the metastable states, and their approximations E_l^{D21} for symmetric S (antisymmetric A) states of $n = 3$ particles at $\sigma = 1/10$, $\alpha = 20$.

l	E_l^S	$\lvert T\rvert_{11}^2$	m	E_m^M	E_l^{D21}
1	8.175	0.775	1	8.175$-\imath$5.1(–3)	8.19
	8.306	0.737	2	8.306$-\imath$5.0(–3)	
2	11.111	0.495	3	11.110$-\imath$5.6(–3)	11.09
	11.229	0.476	4	11.229$-\imath$5.5(–3)	
3	12.598	0.013	5	12.598$-\imath$6.4(–3)	12.51
			6	12.599$-\imath$6.3(–3)	
4	13.929	0.331	7	13.929$-\imath$4.5(–3)	13.86
	14.003	0.328	8	14.004$-\imath$4.6(–3)	
5	14.841	0.014	9	14.841$-\imath$3.5(–3)	14.74
	14.877	0.008	10	14.878$-\imath$3.5(–3)	
6	15.794	0.246	11	15.788$-\imath$6.0(–3)	15.67
			12	15.799$-\imath$6.3(–3)	
7	16.670	0.065	13	16.666$-\imath$2.9(–3)	16.53
			14	16.669$-\imath$4.3(–3)	
8	16.731	0.361	15	16.730$-\imath$7.0(–3)	16.59
	16.775	0.404	16	16.775$-\imath$5.2(–3)	

l	E_l^A	$\lvert T\rvert_{11}^2$	m	E_m^M	E_l^{D21}
1	11.551	1.000	1	11.551$-\imath$1.8(–3)	11.52
	11.610	1.000	2	11.610$-\imath$2.0(–3)	
2	14.459	0.553	3	14.459$-\imath$2.9(–3)	14.42
	14.564	0.480	4	14.565$-\imath$2.7(–3)	
3	16.176	0.855	5	16.176$-\imath$4.7(–3)	16.11
	16.254	0.824	6	16.254$-\imath$4.2(–3)	

since the asymptotic solutions of this problem contain only outgoing waves in the open channels. In this case the eigenfunctions obey the orthogonality and normalization conditions

$$(\mathbf{F}_{m'}|\mathbf{F}_m)=(E_m-E_{m'})\left[\int_{\xi_0^{\min}}^{\xi_0^{\max}}(\mathbf{F}_{m'}(\xi_0))^T\mathbf{F}_m(\xi_0)f_B(\xi_0)d\xi_0-\delta_{m'm}\right]+C_{m'm}=0, \tag{17}$$

$$C_{m'm}=\sum_{t=\min,\max}\mp f_A(\xi_0^t)(\mathbf{F}_{m'}(\xi_0^t))^T[\mathscr{R}_{i_oi_o}(\xi_0^t,E_m)-\mathscr{R}_{i_oi_o}(\xi_0^t,E_{m'})]\mathbf{F}_m(\xi_0^t),$$

where $+$ or $-$ corresponds to $t = \min$ or $t = \max$, respectively.

TABLE 2. The same as presented in Table 1, but for $n = 4$ particles.

l	E_l^S	$\lvert T\rvert_{11}^2$	m	E_m^M	E_l^{D31}	E_l^{D22}
1	10.121	0.321	1	10.119$-\imath$4.0(–3)	10.03	
			2	10.123$-\imath$4.0(–3)		
2	11.896	0.349	3	11.896$-\imath$6.3(–5)		11.76
3	12.713	0.538	4	12.710$-\imath$4.5(–3)	12.60	
	12.717	0.538	5	12.720$-\imath$4.5(–3)		
4	14.858	0.017	6	14.857$-\imath$4.3(–3)	14.71	
			7	14.859$-\imath$4.3(–3)		
5	15.188	0.476	8	15.185$-\imath$3.9(–3)	15.04	
			9	15.191$-\imath$3.9(–3)		
6	15.405	0.160	10	15.405$-\imath$1.4(–5)		15.21
7	15.863	0.389	11	15.863$-\imath$5.3(–5)		15.64

l	E_l^A	$\lvert T\rvert_{11}^2$	m	E_m^M	E_l^{D31}	E_l^{D22}
1	19.224	0.177	1	19.224$-\imath$4.0(–4)	19.03	
			2	19.224$-\imath$4.0(–4)		
2	20.029	0.970	3	20.029$-\imath$3.3(–7)		19.24

TABLE 3. The same as presented in Table 1, but for $n = 5$ particles.

l	E_l^S	$\lvert T\rvert_{11}^2$	m	E_m^M	E_l^{D41}	E_l^{D32}
1	11.794	1.6(–4)	1	11.794$-\imath$1.3(–3)	11.61	
			2	11.794$-\imath$1.3(–3)		
2	14.166	0.014	3	14.166$-\imath$1.1(–3)	13.94	
			4	14.166$-\imath$1.1(–3)		
3	14.764	0.666	5	14.764$-\imath$6.6(–6)		14.42
	14.774	0.666	6	14.774$-\imath$5.6(–6)		
4	16.429	0.005	7	16.429$-\imath$3.3(–3)	16.16	
			8	16.429$-\imath$3.3(–3)		

QUANTUM TRANSPARENCY INDUCED BY METASTABLE STATES

Below we consider the application of the above calculation scheme to the tunneling problem for the cluster consisting of three, four and five identical particles in symmetric (S) and antisymmetric (A) oscillator states.

We start from the solution of the scattering problem with fixed energy $E = \Re E$ using the KANTBP 3.0 program [19]. The discretization of the solutions of the BVPs (8)–(10) was carried out on the finite-element grid $\Omega_h = (-11(11)11)$ for $n = 3$, $\Omega_h = (-13(13)13)$ for $n = 4$, and $\Omega_h = (-15(15)15)$ for $n = 5$ with the number of Lagrange elements of the twelfth order $p' = 12$ given in brackets. The boundary points

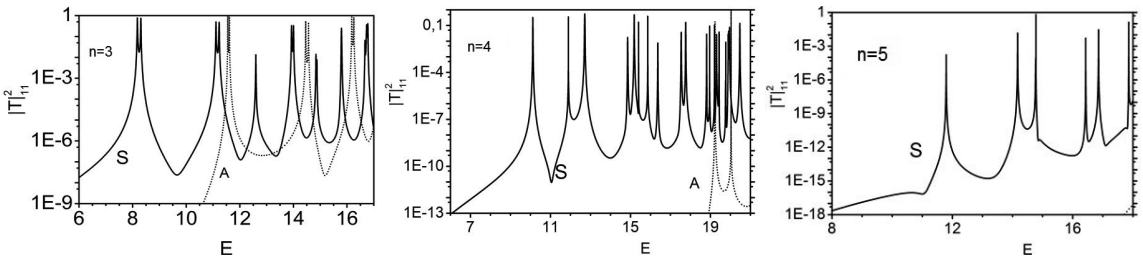

FIGURE 3. The total probability $|T|^2_{11}$ of transmission through the repulsive Gaussian barrier versus the energy E (in oscillator units) at $\sigma = 1/10$, $\alpha = 20$ for the system of three ($n = 3$), four ($n = 4$), and five ($n = 5$) identical particles initially being in the in the ground symmetric (S) state (solid lines) and ground antisymmetric (A) state (dashed lines).

of the interval ξ_0^t were chosen in correspondence with the required accuracy of the approximate solution $\max\{|V_{ij}(\xi_0^t)/\alpha|; i,j = 1,...,N\} < 10^{-8}$. The number N of the cluster basis functions in the expansion (7) of the solutions of the original problem (3) and, correspondingly, the number of equations (8) for S-states at $n = 3,4,5$ was chosen equal to $N = 21,39,37$ and for A-states at $n = 3,4$ was chosen equal to $N = 16,15$. The results of the calculations are presented in Tables 1–3 and Fig. 3. The resonance values of energy $E = E_l^{S(A)}$ and the corresponding maximal values of the transmission coefficient $|\mathbf{T}|^2_{11}$ clearly seen in Fig. 3 are presented in Table 1–3. For metastable states the eigenfunctions obey the boundary conditions of the third kind (10), where the matrices $\mathscr{R}(\xi_0^t) = \mathrm{diag}(\mathscr{R}(\xi_0^t))$ depend on the sought complex energy eigenvalue $E \equiv E_m^M = \Re E_m^M + \imath \Im E_m^M$, $\Im E_m^M < 0$, since the asymptotic solutions of this problem contain only outgoing waves in the open channels. In this case the eigenfunctions obey the orthogonality and normalization conditions (17). The discretisation of the solutions of the boundary problem was implemented on the above finite-element grid. The algebraic eigenvalue problem was solved using the FORTRAN version of program KANTBP 4M [21] applying Newton method with the optimal choice of the iteration step [27] using the additional condition $\Xi_h(\mathbf{F}_m, E_m, \xi_0^{\min}, \xi_0^{\max}) = 0$, obtained as a result of the discretisation of a variational functional and providing the upper estimates for the approximate eigenvalue. As the initial approximation the real eigenvalues and the eigenfunctions, orthonormalised by the condition that the expression in square brackets in Eq. (17) is zero were used. They were found using program KANTBP 3.0, as a result of solving the bound-state problem with a variational functional at $\mathscr{R}(\xi_0^t) = 0$ on the grid $\Omega_h = (-5(5)5)$. The results of the calculations performed in the interval $[\xi_0^{\min}, \xi_0^{\max}]$, for the complex values of energy of the metastable states $E_m^M \equiv E_m = \Re E_m^M + \imath \Im E_m^M$ for $n = 3$, $n = 4$, and $n = 5$ are presented in Tables 1–3. *These metastable states are responsible for the resonance values of energy, corresponding to the maximal values of the transmission coefficient, i.e., the quantum transparency of the barriers.* The position of peaks presented in Fig. 3 is seen to be in quantitative agreement with the real part $\Re E_m^M$, and the halfwidth of the $|\mathbf{T}(E_l)|^2_{11}$ peaks agrees by the order of magnitude with the imaginary part $\Gamma = -2\Im E_m^M$ of the complex energy eigenvalues $E_m^M = \Re E_m^M + \imath \Im E_m^M$ of the metastable states.

Classification of metastable states. Since the potential barriers $V(x_i)$, $i = 1,...,n$ were chosen to be narrow Gaussian peaks $V(x_i) = \frac{\alpha}{\sqrt{2\pi}\sigma}\exp(-\frac{x_i^2}{\sigma^2})$, for the approximate calculation of the real part ${E_l}^D \approx \Re E_m$ of the energy eigenvalues for symmetric (S) and antisymmetric (A) metastable states we restrict ourselves to the solution of the problem (1) with $d = 1$, using the approximation of the potential barriers $V(x_i)$ by infinitely high non-penetrable walls. In this approach we seek the approximate solution in one of the potential wells, neglecting the tunneling through the barriers that separate the adjacent wells. Thus, we are not able to calculate the splitting inherent in the exact eigenvalues of the S-symmetric and A-antisymmetric metastable states. Nevertheless, me can explain the mechanism of their appearance and give their classification, which is an important characteristic of the spectrum.

For the case of $n = 2,3,...,$ identical particles there are $2^n - 2$ potential wells. For odd n there are groups $D(n-k)(k)$, $k = 1,...,(n-1)/2$, each including $2n!/k!/(n-k)!$ wells, separated by barriers, and in this case only doublet states exist (for $n = 3$ see Table 1). For example, if $n = 5$, then there are four groups of wells: five D41 wells and ten D32 wells, corresponding to the case when one or two particles are to the left of the barrier, and two similar groups, corresponding to one or two particles being located to the right of the barrier. This is analogous to the case of the four-well symmetric potential, in which two central wells are different from the two peripheral ones. For example, if $n = 5$ (see. Table 3), then the complex energies of the doubled D41 states are close to each other (the separation between them being 10^{-4}), and the individual maxima of the transmission coefficient are not resolved, while for doublet D32 states the separation between the levels is greater than their width, so that double peaks are observed. For even n, in addition to the groups $D(n-k)(k)$, $k = 1,...,(n-2)/2$ there is a group of $n!/((n/2)!)^2$ wells located in the vicinity of the coordinate frame origin, i.e., $n/2$ particles are on one side of the barrier and $n/2$ are on the other side, which yields singlet states (see. Table 2). In this case, the separation between the complex energy values in the doublets for a fixed number n of particles in the cluster grows as the number k of particles located on one side of the barrier increases, because the number of barriers separating the groups of wells decreases. The level width decreases because of the increasing number of barriers separating the wells from the domain of "free motion" of the entire cluster of n particles, and the singlet levels have the minimum width. In particular, from Tables 1–3 it is seen that the energy level widths for the corresponding doublet states D21, D31, and D41 with $n = 3,4,5$, respectively, which are separated from the domain of free motion by a single barrier only, are nearly similar and amount to $\sim 10^{-3}$.

As expected, for $n = 3$, $n = 4$, and $n = 5$ for the considered narrow and high barrier, the approximation by impermeable walls yields an estimate with the error smaller than 2% for the calculated resonance energies $E_l^{S(A)}$ and the real part of the energy E_m^M of metastable states presented in Tables 1–3.

FUTURE APPLICATIONS

The developed approach, algorithms and programs can be adapted and applied to the calculations of waveguide modes of a planar optical waveguide, channeling of ions

through thin films, near-surfaces quantum diffusion of molecules and micro-clusters, and the study of fragmentation mechanism in producing very neutron-rich light nuclei and the collinear ternary fission.

ACKNOWLEDGMENTS

The work was partially supported by the Russian Foundation for Basic Research (project 14-01-00420), the Bogolyubov-Infeld program and the grant 0333/GF4 MES RK.

REFERENCES

1. F.M. Pen'kov, *JETP* **91**, 698–705 (2000).
2. F.M. Pen'kov, *Phys. Rev. A* **62**, 044701 (2000).
3. G.L. Goodvin and M.R.A. Shegelski, *Phys. Rev. A* **72**, 042713 (2005).
4. E. Pijper and A. Fasolino *J. Chem. Phys.* **126**, 014708 (2007).
5. P.M. Krassovitskiy and F.M. Pen'kov, *J. Phys. B* **47**, 225210 (2014).
6. S.I. Vinitsky et al, *Lecture Notes in Computer Science* **8660**, 472–490 (2014).
7. O. Chuluunbaatar et al *Phys. Atom. Nucl.* **72**, 768–778 (2009).
8. A.A. Gusev et al, *Lecture Notes in Computer Science* **6885**, 175–191 (2011).
9. S. Petrović et al, *Phys. Rev. A* **85**, 032901 (2012).
10. A.C. Shotter and M.D. Shotter, *Phys. Rev. C* **83**, 054621 (2011).
11. R.B. Tashkhodjaev et al, *Phys. Rev. C* **91**, 054612 (2015).
12. A. Dobrowolski et al *Int. J. Mod. Phys. E* **20**, 500–506 (2011).
13. A. Gusev et al, *Lecture Notes in Computer Science* **8136**, 155–168 (2013).
14. A. Gusev et al, *Lecture Notes in Computer Science* **8136**, 427–442 (2013).
15. A.A. Gusev et al, *Phys. Scr.* **89** 054011 (2014).
16. A.A. Gusev et al,*Phys. Atom. Nucl.* **77**, 389–413 (2014).
17. A. Gusev et al, *Theor. Math. Phys.* **186**, 21–40 (2016).
18. A. Gusev et al, *Lecture Notes in Computer Science* **9301**, 182–197 (2015).
19. A.A. Gusev et al, *Comput. Phys. Commun.* **185** 3341–3343 (2014).
20. A.A. Gusev et al, *Comput. Phys. Commun.* **185** 2636–2654 (2014).
21. A.A. Gusev, L. Le Hai, O. Chuluunbaatar, S.I. Vinitsky, http://wwwinfo.jinr.ru/programs/jinrlib/kantbp4m/
22. P. Kramer and M. Moshinsky, *Nucl. Phys.* **82**, 241–274 (1966).
23. P. Kramer and T. Kramer, *Phys. Scr.* **90**, 074014 (2015).
24. M. Abramovits and I.A. Stegun, *Handbook of Mathematical Functions*, Dover, New York (1972).
25. G. A. Baker Jr., *Phys. Rev.*, **103**, 1119–1120 (1956).
26. V.A. Fock, *Zs. Phys.* **61**, 126–148 (1930).
27. T. Zhanlav, O. Chuluunbaatar, and V. Ulziibayar, *Appl. Math. Comput.* **236**, 239-246 (2014).

SESSION
"NUCLEAR STRUCTURE"

Conveners: R. Nazmitdinov, W.D. Heiss

Symmetry effects in mesoscopic systems

R. G. Nazmitdinov

Laboratory of Theoretical Physics, JINR Dubna, 141980 Dubna, Moscow region, Russia
Departament de Física, Universitat de les Illes Balears, 07122 Palma de Mallorca, Spain

Abstract. An interplay between regular and chaotic dynamics of particles, confined by effective potentials of various shapes, are discussed. It is demonstrated that dynamical symmetries emerging from this interplay in classical and quantum systems are related to existence of conserved quantities of the dynamics and integrability. Important role of these symmetries are illustrated on a broad class of mesoscopic systems that include octupole deformed nuclei and two-electron quantum dots in a magnetic field.

Keywords: chaos, nuclear shell structure, quantum dots
PACS: 05.45.-a, 21.60.-n,73.21.La

INTRODUCTION

Symmetries are important ingredients of natural science, since they lie very often at the heart of fundamental laws of nature or/and serve as important tools to understand properties of complex systems. They are equally useful in classical and quantum physics. In mesoscopic physics, when there is an interplay between classical and quantum dynamics, symmetries become apparent in a dominance of order over chaos in classical limit, providing most probable realization of quantum equilibrium configurations of finite systems.

A remarkable example of symmetry manifestaion is shell phenomenon in finite Fermi systems such as nuclei, metallic clusters, and quantum dots (for a review see [1]). The quantisation of a system of fermions moving in a common potential leads to a bunching of levels in the single–particle spectrum, known as shells. Quantum mechanically shell structure yields the degeneracy of quantum states for the most stable configurations, producing "magic numbers". Consequently, spherical symmetry leads to very strong shell effects that are exhibited in the stability of the noble gases, nuclei and metallic clusters. However, when a spherical shell is only partially filled, the higher degeneracy in the single-particle spectrum of a deformed mean field can lead to a breaking of spherical symmetry, and it, therefore, gives rise to a deformed equilibrium shape. Among most exciting examples is the prediction of the superdeformed high-spin states [2, 3] which have been discovered 10 years later by the group of P.J. Twin [4]. The underlying mechanism is a bunching of single-particle levels at large deformation (2 : 1 axes ratio of a system) which give rise to strong shell effects. Another example is a prediction of shell structure in small quantum dots (QDs) [5, 6, 7]. Indeed, it was found experimentally [8] that the energy needed to place the extra electron (addition energy) into a vertical QD at zero magnetic field has characteristic maxima which correspond to the sequence of magic numbers (due to a complete filling of shells) of a two-dimensional (2D) harmonic

oscillator.

In classical picture there are not discrete states like in quantum mechanics for closed system. The energy of a m-fold degenerate bound system can be described as a multiple Fourier series with fundamental frequencies that obey the condition

$$\sum_{i=1}^{f} n_i^{(k)} \omega_i = 0, \quad k = 1, \ldots, m \quad (1 \leq m < f-1). \tag{1}$$

with integer n_i, when there are f degrees of freedom (see [9] and references therein). At complete degeneracy ($m = f-1$), all frequencies are rational fractions of each other. In this case the motion is simply periodic, and the frequencies are given by

$$\omega_i = \partial H / \partial J_i \,, \tag{2}$$

where H is the Hamiltonian and the J_i are the action variables

$$J_i = \oint p_i dq_i \,, \tag{3}$$

where the integration is done over one complete cycle of q_i. Thus, a separable multiply periodic system is degenerate if the Hamiltonian can be expressed only through a linear combination of these action variables with integer coefficients. The most famous examples of these systems are the non-relativistic Coulomb (Kepler) problem and three-dimensional (3D) isotropic oscillator (see, for example, [10]). In fact, a Coulomb system and a 3D harmonic oscillator with frequencies in rational ratios (RHO) are benchmarks for the hidden symmetries which account for the accidental degeneracies of their quantum spectra. The classical and semiclassical treatment of the RHO (see, e.g., [11, 12, 13, 14]) provide invaluable insight into quantum properties of this system. It is especially noteworthy that the harmonic oscillator model is used quite often as a simplest mean field model for various many-body finite quantum systems. For example, basic features of quantum dots and Bose condensates have been understood within models with a parabolic confinement (see, e.g., [1]). In this contribution we will consider octupole deformed nuclei and quantum dots. For nuclei effective confining potentials are modelled by a parabolic potential with higher multipoles. For two-electron QDs we consider the interplay between the parabolic confinement and the Coulomb interaction. Our major goal is to demonstrate how the analysis of a classical dynamics of a corresponding quantum mechanical problem enables to us to understand quantum properties of these mesoscopic systems.

SHELL STRUCTURE AND CHAOS IN OCTUPOLE DEFORMED POTENTIALS

Depending on the particular mean field potential a deviation from spherical symmetry can lead to chaotic motion in the corresponding classical problem, and the shell structure of the corresponding quantum spectrum is affected or even destroyed depending on the degree of chaos (see, e.g., [15, 16, 17, 18]). On the other hand, the need for multipole

deformations higher than the quadrupole has been recognized in nuclei and metallic clusters in numerous calculations to explain experimental data. The most important ones are the octupole and hexadecapole terms. For example, the hexadecapole deformation is essential for the understanding of equilibrium shapes and the fission process of super- and hyperdeformed nuclei and the interpretation of experimental data for metallic clusters. The study of octupole deformations could shed light on the tendency for the system on the way towards fission to avoid superdeformation [19]. However, as it was stressed above, inclusion of the octupole and hexadecapole deformations leads to a nonintegrable problem. A natural question arises: can we bring into coincidence the presence of higher multipoles, that are responsible for chaotic dynamics in mean field potentials, with experimental data ?

In many cases analysis of classical analogy of quantum mechanically system provide a useful insight into understanding its shell structure. As an example, we consider the case of an axial octupole potential

$$V(\rho,z)=\frac{m}{2}\omega^2\left(\rho^2+\frac{z^2}{b^2}+\lambda\frac{2z^2-3z\rho^2}{\sqrt{\rho^2+z^2}}\right). \tag{4}$$

For $b>1 (b<1)$ this is an axially-symmetric harmonic oscillator of prolate (oblate) shape with an additional octupole term. The term proportional to λ is $r^2P_3(\cos\theta)$ with P_3 the third -order Legendre polynomial. We use cylindrical coordinates z and $\rho=\sqrt{x^2+y^2}$. For $\lambda\neq 0$ this is a two degrees of freeedom system which is nonintegrable. With the aid of this example, we will discuss basic ideas of our approach [20] that is enable to answer on the above question. More examples can be found in [21, 22].

Adiabatic approach

To understand the occurrence of shell structure in the corresponding quantum-mechanical problem we present a classical analysis in which it becomes obvious that, for the prolate case, the problem is approximately equivalent to an integrable problem even for finite values of λ. In fact, it was shown that, within the approximation used, the motion in the z and ρ direction becomes uncoupled whereby the motion in the z direction depends on λ. In this way frequencies in either directions can be clearly defined with the effect that the corresponding winding number, i.e., the ratio ω_ρ/ω_z becomes a simple function of λ. This provides the basic mechanism for the occurrence of shell structures for the quantum-mechanical problem; in fact it provides classical evidence for the quantum-mechanical finding that the spectrum for specific values of λ is nearly equivalent to a spectrum with $\lambda=0$ but with larger value of the quadrupole parameter b.

The method employed consists of averaging the Hamilton function over the fastest angle of the unperturbed motion ($\lambda=0$) after rewriting the momenta and coordinates in terms of action-angle variables

$$q_i=\sqrt{\frac{2J_i}{m\omega_i}}\sin\theta_i\,,\quad p_i=\sqrt{2J_im\omega_i}\cos\theta_i,\theta_i=\omega_it\,,\quad i=\rho,z\,. \tag{5}$$

This method called the "removal of resonances" method (RRM) is widely used in classical problems of nonlinear dynamics and in celestial mechanics [23].

The complete Hamilton function written in terms of the angle and action variables of the unperturbed problem reads

$$H(J_\rho, J_z, \theta_\rho, \theta_z) = \omega \left[J_\rho + \frac{1}{b} J_z + \lambda \frac{\sqrt{bJ_z} \sin\theta_z (2bJ_z \sin^2\theta_z - 3J_\rho \sin^2\theta_\rho)}{\sqrt{bJ_z \sin^2\theta_z + J_\rho \sin^2\theta_\rho}} \right]. \quad (6)$$

The frequencies $\omega_{\rho,z}$ are given by Eq.(2). Obviously, the winding number of a trajectory is essentially equal to b when λ is small. This means that for b sufficiently far from unity, there will always be a fast and a slow moving phase, i.e., the averaging could be performed over the corresponding fast angle.

For prolate deformation the fast phase is θ_ρ. Averaging the Hamilton function over θ_ρ, we are led to a new averaged Hamiltonian H_{av}, which is independent of θ_ρ. This means that the corresponding action J_ρ becomes a constant of motion in this approximation: $J_\rho = J_\rho(0)$. Introducing the notation $\zeta^2 = 2J_\rho(0)/(m\omega) = \rho^2 + p_\rho^2/(m\omega)$ we obtain the effective potential

$$U_{eff} = \frac{m\omega^2}{2} \left\{ \frac{z^2}{b^2} + \lambda \zeta^2 \frac{sgn(z)}{2\pi} \times \left[8 \frac{z^2}{\zeta^2} K\left(-\frac{\zeta^2}{z^2} \right) - 3\pi \, {}_2F_1\left(\frac{1}{2}, \frac{3}{2}, 2; -\frac{\zeta^2}{z^2} \right) \right] \right\}. \quad (7)$$

Her, K and ${}_2F_1$ are the complete elliptic function of the first kind and the hypergeometric function, respectively. In this way, the problem is effectively reduced to two uncoupled one-dimensional cases: ρ and z motions. A remainder of the actual coupling is the fact that, through ζ, the z motion still depends on the initial conditions of the ρ motion. The frequency ω_z is given by $\omega_z = 2\pi/T$ where

$$T = \sqrt{2m} \int_{z_{min}}^{z_{max}} \frac{dz}{\sqrt{E_z - U_{eff}}}. \quad (8)$$

with $E_z = E - E_\rho = E - m\omega^2\zeta^2/2$. Once we choose the initial condition $\zeta = 0$, i.e., the total energy is associated with z motion only, the integral can be evaluated analytically, and we obtain for the winding numbers

$$\frac{\omega_\rho}{\omega_z} = \frac{b}{2} \left(\frac{1}{\sqrt{1 + \lambda/\lambda_{cr}}} + \frac{1}{\sqrt{1 - \lambda/\lambda_{cr}}} \right). \quad (9)$$

For the prolate case $\lambda_{cr} = 1/(2b^2)$ (see a complete definition of λcr in [20]).

In virtue of the formula (9) one can evaluate the quadrupole deformation parameter b and the octupole strength λ at which the quadrupole+octupole deformations could produce a pronounced shell structure. For instance, in the superdeformed case $(b = 2)$, according to formula (9), the winding number becomes equal to $5:2$ at $\lambda = 0.66\lambda_{cr}$. As a result, the quantum mechanical spectrum exhibits a periodic structure of the same kind as of a pure quadrupole deformation with winding numbers $5:2$. Quantum mechanical spectra obtained with the aid of this formula for axial case and the extended analysis for nonaxial octupole deformations are presented in [20, 21, 22].

TWO-ELECTRON QUANTUM DOTS IN A MAGNETIC FIELD

Two-electron quantum dots provide a prospective experimental platform for quantum communications in solid-state environment and allow the study of various aspects of quantum correlations with a high accuracy (see, e.g., [24]). For small QDs with a few electrons an effective trapping potential is quite well approximated by a parabolic confinement (see discussion in [1]). Note, if the harmonic oscillator and the Coulomb potential are combined like in a QD, most of the symmetries are expected to be broken. In the general case of an axially symmetric 3D quantum dot we have nonintegrable motion. However, it was discovered that the transition from chaotic to regular dynamics and vice versa can be controlled with aid of the magnetic field [25, 26]. This result has been investigated thoroughly one decade later [27] and rederived using Killing tensors (see discussion in [14]).

The system Hamiltonian for the case of a magnetic field B along a symmetry axis z reads

$$H = \sum_{i=1}^{2} \left[\frac{1}{2m^*} \left(\mathbf{p}_i - \frac{e}{c} \mathbf{A}_i \right)^2 + U(\mathbf{r}_i) \right] + V_C + H_{spin} \,. \tag{10}$$

Here the term $V_C = \alpha / |\mathbf{r}_1 - \mathbf{r}_2|$ with $\alpha = e^2 / 4\pi\varepsilon_0\varepsilon_r$ describes the Coulomb repulsion between electrons and $H_{spin} = g^* \mu_B (\mathbf{s}_1 + \mathbf{s}_2)\mathbf{B}$ is the Zeeman term, where $\mu_B = |e|\hbar/2m_e c$ is the Bohr magneton. For the magnetic field we choose the vector potential with gauge $\mathbf{A}_i = \frac{1}{2}\mathbf{B} \times \mathbf{r}_i = \frac{1}{2}B(-y_i, x_i, 0)$. The confining potential is approximated by a 2D circular HO in xy-plane and the vertical confinement V_z: $U(\mathbf{r}_i) = m^* \omega_0^2 \rho_i^2 / 2 + V_z(z_i)$; $r_i^2 = \rho_i^2 + z_i^2$, $\rho_i^2 = x_i^2 + y_i^2$ and $\hbar\omega_0$ is the energy scale of confinement in the xy-plane. By introducing the relative and center-of-mass (CM) coordinates $\mathbf{r} = \mathbf{r_1} - \mathbf{r_2}$, $\mathbf{R} = (\mathbf{r_1} + \mathbf{r_2})/\mathbf{2}$, the Hamiltonian (10) is separated into the CM and relative motion terms: $H = H_{\rm CM} + H_{\rm rel}$. Here, we focus on the relative motion Hamiltonian which contains the Coulomb interaction (see details in [1]). In this contribution we consider only a vertical parabolic confinement V_z, while different forms for the vertical confinement are analysed as well in [28].

For our analysis it is convenient to use cylindrical *scaled* coordinates, $\tilde{\rho} = \rho / l_0$, $\tilde{p}_\rho = p_\rho l_0 / \hbar$, $\tilde{z} = z/l_0$, $\tilde{p}_z = p_z l_0 / \hbar$, where $l_0 = (\hbar / \mu\omega_0)^{1/2}$ is the characteristic length of the confinement potential with the reduced mass $\mu = m^*/2$. The strength parameter α of the Coulomb repulsion goes over to $\lambda = 2\alpha / (\hbar\omega_0 l_0)$. Using the effective mass $m^* = 0.067 m_e$, the dielectric constant $\varepsilon = 12$, which are typical for GaAs, and the confining frequency $\hbar\omega_0$=3 meV, we obtain $\lambda \approx 3$. Hereafter, for the sake of simplicity, we drop the tilde, i.e. for the scaled variables we use the same symbols as before scaling.

In these variables the Hamiltonian for the relative motion takes a particular simple form (in units of $\hbar\omega_0$)

$$\varepsilon \equiv \frac{H_{\rm rel}}{\hbar\omega_0} = \frac{1}{2} \left[p_\rho^2 + \frac{m^2}{\rho^2} + p_z^2 + \left(\frac{\omega_\rho}{\omega_0} \right)^2 \rho^2 + \left(\frac{\omega_z}{\omega_0} \right)^2 z^2 + \frac{\lambda}{\sqrt{\rho^2 + z^2}} \right] - \frac{\omega_L}{\omega_0} m \,, \tag{11}$$

where $m = l_z/\hbar$, $\omega_L = eB/2m^*c$ is the Larmor frequency and $\omega_\rho = (\omega_L^2 + \omega_0^2)^{1/2}$ is the effective confinement frequency in the ρ-coordinate which depends through ω_L on the magnetic field.

Semiclassical analysis

For the parameters we have chosen the contribution of the Coulomb interaction to the total energy is comparable to the confinement energy at zero magnetic field and it becomes for small m even more important with increasing magnetic field. In this case, the standard perturbation theory is not valid, since the Coulomb interaction prevails over the confinement energy. Therefore, we make use of the fact that in real samples the confining potential in the z direction is much stronger than in the (x,y) plane that allows us to analyze the 3D nonintegrable system with the RRM. The original coordinates of the 3D axially symmetric HO read in terms of action-angle variables (for a derivation, see Appendix [25]):

$$\rho^2 = \frac{\omega_0}{\omega_\rho}\left(2j_\rho + |m| - 2\sqrt{j_\rho(j_\rho+|m|)}\cos 2\theta_\rho\right), \quad z^2 = \frac{2j_z\omega_0}{\omega_z}\sin^2\theta_z, \tag{12}$$

and $p_\rho = \dot{\rho}/\omega_0$, $p_z = \dot{z}/\omega_0$. Here, $j_z = J_z/\hbar$ and $j_\rho = J_\rho/\hbar$. If $\omega_z > \omega_\rho$ one averages over the angle $\theta_z = \omega_z t$. As a result, the motion effectively decouples into an unperturbed motion in the z-coordinate governed by the potential $(\omega_z/\omega_0)^2 z^2/2$ and into the relative motion in the ρ-coordinate governed by the effective potential (see details in [25, 28])

$$V_{\rm eff}(\rho, j_z) = \frac{1}{2}\left(\frac{\omega_\rho}{\omega_0}\right)^2\rho^2 + \frac{m^2}{2\rho^2} + \frac{\lambda}{\pi\rho}K\left(-2\frac{\omega_0}{\omega_z}\frac{j_z}{\rho^2}\right), \tag{13}$$

where $K(x)$ is the first elliptic integral. Hence, the effective Hamiltonian reads

$$\varepsilon = \frac{p_\rho^2}{2} + V_{\rm eff} - \frac{\omega_L}{\omega_0}m + \frac{\omega_z}{\omega_0}j_z. \tag{14}$$

Applying a WKB quantization

$$I_\rho(\varepsilon) = \frac{\hbar}{2\pi}\oint p_\rho\, d\rho = \frac{\hbar}{\pi}\int_{\rho_{\rm min}}^{\rho_{\rm max}} |p_\rho|\, d\rho, = \hbar\,(n_\rho + \tfrac{1}{2}), \quad j_z = n_z + \tfrac{1}{2},$$
$$n_\rho, n_z = 0,1,2,..., \quad m = 0,\pm1,\pm2,..., \tag{15}$$

we can calculate the action integral numerically and determine the energy levels. The momentum p_ρ is determined from Eq.(14) and the turning points $\rho_{\rm min}$, $\rho_{\rm max}$ are as usual the (positive) roots of the equation $p_\rho(\rho) = 0$. The semiclassical result, although not exact (the error is less than 1%), reproduces very well the quantum mechanical results (see details in [25]).

The integrable cases

In order to understand the role of the magnetic field, one can analyse the Hamiltonian (11) for the relative motion by using the Poincaré sections technique (see Fig.1). Examination of the Poincaré sections by varying the parameter ω_z/ω_ρ in the interval

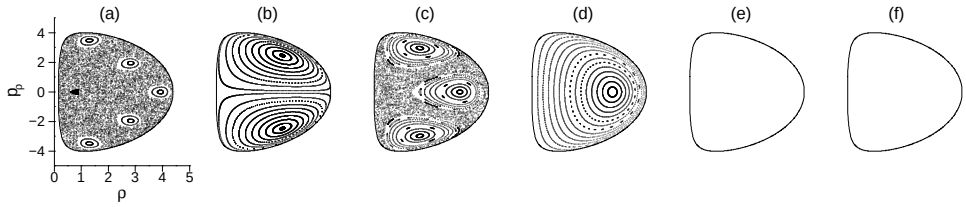

FIGURE 1. Poincaré surfaces of sections $z = 0$, $p_z > 0$ of the relative motion for the axially symmetric 3D two-electron quantum dot ($\lambda = 1.5$, $\varepsilon = 10$, $m = 0$) with: (a) $\omega_z/\omega_\rho = 5/2$, (b) $\omega_z/\omega_\rho = 2$, (c) $\omega_z/\omega_\rho = 3/2$, (d) $\omega_z/\omega_\rho = 1$, (e) $\omega_z/\omega_\rho = 2/3$ and (f) $\omega_z/\omega_\rho = 1/2$. The sections (b), (d) and (f) indicate that for the corresponding ratios ω_z/ω_ρ the system is integrable.

$(1/10, 10)$ with a small step indicates that there are five integrable cases. The trivial cases are $\omega_z/\omega_\rho \to 0$ and $\omega_z/\omega_\rho \to \infty$, which correspond to 1D vertical and 2D circular QDs, respectively. The nontrivial cases are $\omega_z/\omega_\rho = 1/2, 1, 2$. These results hold for any strength of the Coulomb interaction. Below we discuss the nontrivial cases only.

At the value $\omega_L' = (\omega_z^2 - \omega_0^2)^{1/2}$ the magnetic field gives rise to the spherical symmetry $(\omega_z/\omega_\rho = 1)$ in an axially symmetric QD (with $\omega_z > \omega_0$) [25]. In this case the Hamiltonian (11) is separable in (scaled) spherical coordinates (see Fig. 1d)

$$h = \frac{p_r^2}{2} + \frac{(\mathbf{l}/\hbar)^2}{2r^2} + \frac{\tilde{\omega}_z^2 r^2}{2} + \frac{\lambda}{r} - \tilde{\omega}_L' m \tag{16}$$

and the dynamics is integrable. The additional integral of motion is the square of the total angular momentum $\mathbf{l}^2$.

The integrable case $\omega_z/\omega_\rho = 2$ occurs for an axially symmetric QD (with $\omega_z > 2\omega_0$) by tuning the magnetic field to the value $\omega_L'' = (\omega_z^2/4 - \omega_0^2)^{1/2}$ (see Fig. 1b). The use of the parabolic coordinates (ξ, η, φ), where $\xi_1 = r + z$, $\xi_2 = r - z$, immediately leads to the separability of classical motion. In these coordinates we have discovered a third integral of motion $c_z = a_z - \omega_\rho{}^2 \rho^2 z$ (see details in [26]). Here $a_z = (z p_\rho - \rho p_z) p_\rho + \left(\frac{m^2}{\rho^2} + \frac{\kappa}{r}\right) z$ is the z-component of the Laplace-Runge-Lenz vector $\mathbf{a} = \mathbf{p} \times \mathbf{l} + \kappa \mathbf{r}/r$ in (scaled) cylindrical coordinates. The vector $\mathbf{a}$ is a constant of motion for the pure Coulomb system (i.e. when $\omega_\rho = \omega_z = 0$) [10]). Note that for a two-electron QD the constant of motion c_z includes a space contribution as well.

At the magnetic field $\omega_L''' \equiv (4\omega_z^2 - \omega_0^2)^{1/2}$ (see Fig.1f) the Hamiltonian (11) is separable in the coordinates $\xi_1' = r + \rho$, $\xi_2' = r - \rho$ for $m = 0$. Note that for $m = 0$ the cases $\omega_z/\omega_\rho = 1/2$ and 2 are equivalent if we exchange the ρ and z coordinates and, hence, the additional integral of motion is $|a_\rho - \omega_z{}^2 z^2 \rho|$. However, for $m \neq 0$ the Hamiltonian (11) for $m \neq 0$ cannot be separated in these coordinates due to the term m^2/ρ^2. In this case the desired integral of motion

$$C = [(a_\rho - \omega_z{}^2 z^2 \rho)^2 + a_\varphi^2 + 4m^2 \omega_z^2 r^2]^{1/2}. \tag{17}$$

Due to existence of three independent integrals of motion, h, m and C, which are in involution, the dynamics for $m \neq 0$, although non-separable, is integrable.

SUMMARY

Using the classical RRM, we were able to reduce effectively the non-integrable problems of octupole deformed potentials and two electrons in the parabolic potential under the perpendicular magnetic field to integrable cases. Under these circumstances we obtain that the classical analysis enables to provide a set of deformation parameters that could be used in the corresponding quantum-mechanical problem to find stable configurations with octupole deformed shapes. In virtue of the classical analysis we have found the magnetic field strengths at which the classical dynamics becomes integrable in the 3D two-electron QD. Quantum spectra of such QDs exhibit hidden symmetries at certain values of the magnetic field. This fact has been overlooked in a plain quantum-mechanical models.

ACKNOWLEDGEMENT

I am grateful for fruitful collaboration to W.D. Heiss and N. S. Simonović. This work was supported in part by Russian Foundation for Basic Research Grant No.14-03-00723.

REFERENCES

1. J. L. Birman, R. G. Nazmitdinov, and V. I. Yukalov, *Phys. Rep.* **526**, 1 (2013).
2. R. Bengtsson, et al., *Phys. Lett.* **B57**, 301 (1975).
3. K. Neergard and V. V. Pashkevich, *Phys. Lett.* **B59**, 218 (1975).
4. P. J. Twin, et al., *Phys. Rev. Lett.* **57**, 811 (1986).
5. M. Macucci, K. Hess, and G.J. Iafrate, *J. Appl. Phys.* **77**, 3267 (1995).
6. W. D. Heiss and R. G. Nazmitdinov, *Phys. Lett.* **A222**, 309 (1996).
7. A. Wojs, P. Hawrylak, S. Fafard, and L. Jacak, *Rhys. Rev.* **B54**, 5604. (1996).
8. S. Tarucha, et al., *Phys. Rev. Lett.* **77**, 3613 (1996).
9. P. Stehle and M. Y. Han, *Phys. Rev.* **159**, 1076 (1967).
10. L. D. Landau and E. M. Lifshitz *Quantum Mechanics* (Pergamon, Oxford, 1977)
11. J.-P. Amiet and S. Weigert, *J. Math. Phys.* **43**, 4110 (2002).
12. R. Doll and G.-L. Ingold, *Am. J. Phys.* **75**, 208 (2006).
13. M. S. Kumar and B. Datta-Roy, *J. Phys. A: Math. Theor.* **41**, 075306 (2008).
14. M. Cariglia, *Rev. Mod. Phys.* **86**, 1283 (2014).
15. R. Arvieu, et al., *Rhys. Rev.* **A35**, 2389 (1987).
16. W. D. Heiss, R. G. Nazmitdinov, and S. Radu, *Phys. Rev. Lett.* **72**, 2351 (1994).
17. W. D. Heiss and R. G. Nazmitdinov, *Phys. Rev. Lett.* **73**, 1235 (1994).
18. W. D. Heiss and R. G. Nazmitdinov, *Physica* **D118**, 134 (1998).
19. A. Bohr and B. R. Mottelson, *Nuclear Structure* vol. 2 (World Scientific, Singapore, 1999)
20. W. D. Heiss, R. G. Nazmitdinov, and S. Radu, *Phys. Rev.* **B51**, 1874 (1995).
21. W. D. Heiss, R. G. Nazmitdinov, and S. Radu, *Phys. Rev.* **C52**, R1179 (1995).
22. W. D. Heiss, R. G. Nazmitdinov, and R. A. Lynch, *Pis'ma v ZhETP* **69**, 525 (1999); *Phys. Rev.* **C60**, 034303 (1999).
23. A. J. Lichtenberg and M. A. Lieberman, *Regular and Chaotic Dynamics*, Second Edition (Springer-Verlag, New York, 1992)
24. N. S. Simonović and R. G. Nazmitdinov, *Phys. Rev.* **A92**, 052332 (2015).
25. R. G. Nazmitdinov, N. S. Simonović, and J.-M. Rost, *Phys. Rev.* **B65**, 155307 (2002).
26. N. S. Simonović and R. G. Nazmitdinov, *Phys. Rev.* **B67**, 041305R (2003).
27. P.-M. Zhang, L.-P. Zou, P. A. Horvathy, and G. W. Gibbons, *Ann. Rhys.* **341**, 94 (2014).
28. N. S. Simonović and R. G. Nazmitdinov, *Phys. Rev.* **A78**, 032115 (2008).

Deformation effects in giant dipole resonance: wavelet analysis

V.O. Nesterenko*, W. Kleinig*, J. Kvasil† and P.-G. Reinhard**

*Laboratory of Theoretical Physics, JINR Dubna, 141980 Dubna, Moscow region, Russia
†Institute of Particle and Nuclear Physics, Charles University, CZ-18000, Prague 8, Czech Republic
**Institute of Theoretical Physics II, University Erlangen, D-91058, Erlangen, Germany

Abstract. The deformation effects in the giant dipole resonance (GDR) in ^{150}Nd are analyzed within the self-consistent separable random-phase approximation (SRPA) model based on the Skyrme functional. The Skyrme parametrization SV-bas is used. The fine structure of the GDR strength function, including the deformation-induced splitting into branches with K=0 and 1, is inspected. The characteristic scales are considered using the wavelet Morlet transforms.

Keywords: QRPA, giant dipole resonance, nuclear deformation, wavelet
PACS: 21.60.Jz; 24.30.Cz; 27.90.B+b

INTRODUCTION

Giant resonances (GR) represent prominent and well studied excitation modes of atomic nuclei [1]. Despite a long history of investigations of GR, some their features are not yet clear and deserve a further exploration. In particular, this concerns the fine structures (FS) of GR and characteristic scales/widths (CSW). The FS and CSW take place in both spherical and deformed nuclei. However in deformed nuclei these features are complicated by the deformation K-splitting of GR.

The present interest on FS/CSW in GR is stimulated by the appearance of new high-resolution experimental data. A great step forward was provided by (p,p') experiments in iThemba facility (South Africa) [2, 3, 4, 5]. The iThemba experiments covered the isoscalar giant quadrupole resonance (ISGQR) in ^{208}Pb [2, 3] and Nd isotopes [4], and the isovector giant dipole resonance (IVGDR) in Nd [5]. An analysis of the experiments for ISGQR [4] and IVGDR [5] in Nd isotopes is in progress [4, 5].

The second aspect stimulating investigation of FS/CSW is that these high-resolution data allow to apply the powerfull wavelet analysis [2, 3]. The wavelet can be viewed as a specific modification of the Fourier transformation [6]. As compared to the Fourier method, the wavelet has an important advantage: it allows to investigate the scales of interest locally. For atomic nuclei, this means that we can get not only the set of CSW but also localize intervals in the energy spectrum where the CSW are most pronounced. The wavelet analysis has been recently performed for ISGQR in ^{208}Pb [2, 3]. Implementation of the wavelet to the ISGQR [4] and IVGDR [5] in Nd isotopes is in progress.

Note that the wavelet analysis still has subtle open points. In particular, it is not very clear which GR features are actually highlighted by the wavelet: level spacings, widths or both them. The effect of the deformation is unclear. The difference between

the wavelet results for ISGQR and IVGDR should yet be understood. Dependence of the results on the parameters of the Morlet wavelet function is not well established. We do not know well, at least for IVGDR, how much the wavelet results depend on the model describing nuclear structure. The dependence on the nuclear mass region is also unclear.

In this connection, we present here the self-consistent results for IVGDR in deformed ^{238}U. The nuclear spectrum is obtained within the Skyrme separable random-phase-approximation (SRPA) method [7] using the Skyrme parametrization SV-bas [8]. To study the role of the residual interaction, the strength functions and wavelet powers are given for both two-quasiparticle (2qp) and SRPA cases. To discriminate the deformation effects, the results for the total strength and IVGDR branches with K=0 and K=1 are compared. Unlike the spherical nuclei where the coupling to complex configurations is often important, in deformed nuclei the SRPA exploration should be relevant. The nucleus ^{238}U is chosen to see the wavelet results in the new (actinide) mass region. This should supplement the studies [2, 3, 4, 5] for ^{208}Pb and Nd isotopes and to check the dependence of the results on the nuclear mass.

THE MODEL

As mentioned above, the calculations of the strength functions were performed within the SRPA approach [7]. The method is fully self-consistent since both the mean field and residual interaction are derived from the same Skyrme functional. The residual interaction includes all the functional contributions as well as the Coulomb direct and exchange terms. The self-consistent factorization of the residual interaction crucially reduces the computational effort for deformed nuclei and simultaneously maintains high accuracy of the calculations [7, 9]. The recent Skyrme parametrization SV-bas [8] is used. The axial quadrupole deformation β=0.275 close to the experimental value $\beta_{\rm exp}$=0.286 [10] is determined by minimization of the total energy. The pairing is treated at BCS level using a zero-range pairing interaction. A large two-quasiparticle basis up to $\sim$100 MeV is taken into account. This guarantees that the energy-weighted sum rule is fully exhausted.

The calculated strength function has the form

$$S(\mathrm{E1K;E}) = \sum_{\nu} \mathrm{E}_{\nu} |\, \langle \nu | \hat{\mathrm{M}}(\mathrm{E1K}) | 0 \rangle |^2 \, \xi_{\mathrm{D}}(\mathrm{E} - \mathrm{E}_{\nu}) \tag{1}$$

where $\hat{M}(\mathrm{E1K}) = \mathrm{e}[\mathrm{N/A}\sum_{\mathrm{i}}^{\mathrm{Z}}(\mathrm{rY_{1K}})_{\mathrm{i}} - \mathrm{Z/A}\sum_{\mathrm{i}}^{\mathrm{N}}(\mathrm{rY_{1K}})_{\mathrm{i}}]$ is the E1(T=1) transition operator, $|0\rangle$ the ground state wave function, $|\nu\rangle$ and E_ν are SRPA states and energies. The strength function includes a Lorentz smoothing $\xi_D(E-E_\nu) = D/[2\pi[(E-E_\nu)^2 - D^2/4]]$ with the averaging parameter D. Here the small energy step d=2 keV and smoothing D=10 keV are used to exhibit the IVGDR fine structures.

We consider a wavelet transformation C using the complex Morlet function ψ [2, 3, 6]

$$C(E,\Delta) = \frac{1}{\sqrt{\Delta}} \int dE_x S(E_x) \; \psi\left(\frac{E_x - E}{\Delta}\right), \tag{2}$$

$$\psi_(x) = \pi^{-1/4} e^{\mathrm{i}kx} e^{-x^2/2}, \tag{3}$$

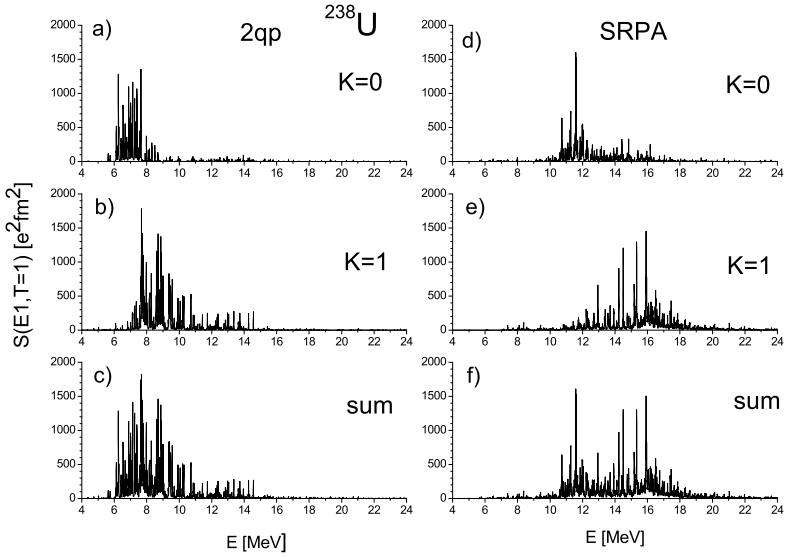

FIGURE 1. The 2qp (left) and SRPA (right) strength functions for E1(T=1) transitions in ^{238}U, calculated with the Skyrme force SV-bas. The strengths for K=0 (upper plots) and K=1 (middle plots) branches as well as the total strength (bottom plots) are exhibited.

$$P(\Delta) \;=\; \int dE\, |C(E,\Delta)|^2, \tag{4}$$

where $S(E)$ is the strength function to be analyzed, $x = (E_x - E)/\Delta$ is the argument of the Morlet function, $P(\Delta)$ is the wavelet power. The Morlet function exhibits oscillations with the frequency k, modulated by the Gaussian function with the width Δ. The parameter k=5 is chosen to satisfy the admissibility condition [6]. The wavelet transform $C(E,\Delta)$ depends on E (energy localization) and Δ (widths and scales). For the sake of brevity, the detailed $C(E,\Delta)$ is not considered in the present study. Instead we consider the power $P(\Delta)$ which delivers information on the most significant CWS ignoring their localization in the energy spectrum.

RESULTS AND DISCUSSION

Results of the calculations for the IVGDR in the deformed nucleus ^{238}U are presented in Figs. 1 and 2. Figure 1 exhibits the unperturbed (2qp) and SRPA strength functions for the IVGDR branches K=0,1 and the total (summed) strengths. It is seen that the IVGDR embraces a huge number of states and displays a rich fine structure. In both 2qp and SRPA cases, there is a significant deformation splitting between K=0 and K=1 branches. The residual interaction upshifts the strength and enlarges the splitting.

The powers $P(\Delta)$ for the IVGDR are shown in Fig. 2. The maxima of the powers mark significant scales/widths Δ. The figure demonstrates three groups of the scales: (I) narrow at low-energy 0-0.3 MeV, (II) broad at middle energy 0.3-1-MeV, and (III) even broader at 1-3 MeV. It is remarkable that in general the maxima arise already in 2qp case. The SRPA residual interaction collects the maxima I-II into a more narrow interval

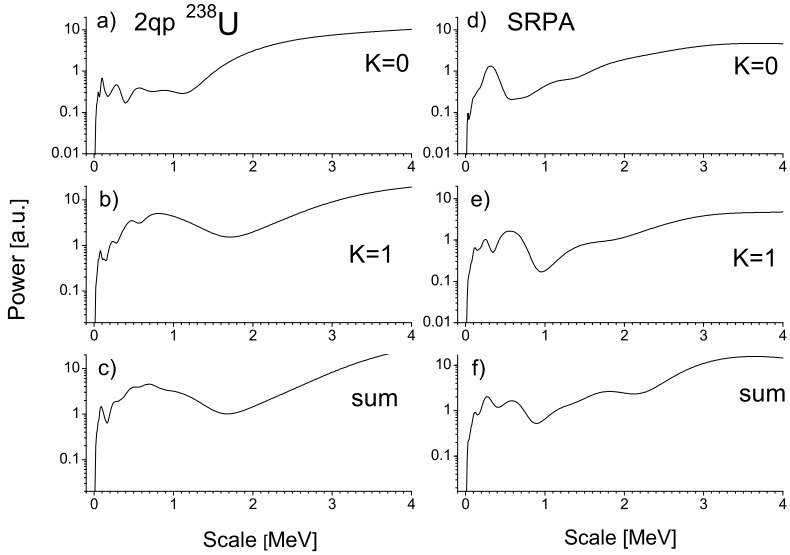

FIGURE 2. The same as in Fig. 1 but for the wavelet powers as a function of the scale Δ.

0-1 MeV and make the maxima II more pronounced. This is related to the appearance in SRPA of the collective states separated by the intervals 0.5-1 MeV (compare left and right plots in Fig. 1). All the powers have a distinct minimum at 1-2 MeV. The minimum for K=1 lies at a higher energy and is dipper than for K=0. So just the K=1 minimum mainly determines the minimum in the summed power. The vague maxima III take place only in SRPA case. Perhaps they are overtones (double values) of the maxima II. In general it seems that the powers represent rather level spacings than the physical widths determined by the interaction and decay channels.

SUMMARY

The structure of the isovector giant dipole resonance (IVGDR) was investigated in detail within the Skyrme self-consistent random-phase-approximation (SRPA) model in axially deformed ^{238}U. The strength functions and wavelet powers were determined for both unperturbed (2qp) and RPA cases. The results for the separate branches K=0 and K=1 as well as for the sum of the branches were compared.

The calculation demonstrate a clear deformation splitting of the IVGDR into K=0 and K=1 branches. Both branches exhibit a rich fine structure. The wavelet powers allow to highlight the relevant scales (level spacings) pertinent to the IVGDR. Similar results were earlier obtained for IVGDR in Nd isotopes (with the Skyrme force SLy6) [5].

ACKNOWLEDGEMENT

The work was partly supported by the Heisenberg-Landau (Germany-BLTP JINR) and Votruba-Blokhincev (Czech Republic-BLTP JINR) grants. P.-G.R. is grateful for the

BMBF support under Contracts No, 06 DD 9052D and 06 ER 9063. The support of the Czech Science Foundation (P203-13-07117S) is appreciated.

REFERENCES

1. M. N. Harakeh and A. van der Woude, *Giant Resonances* (Oxford: Clarendon, 2001).
2. A. Shevchenko, J. Carter, G.R.J. Cooper, R.W. Fearick, Y. Kalykov, P.von Neumann-Cosel, V.Yu. Ponomarev, A. Richter, I. Usman, and J. Wambach, *Phys. Rev. C* **77**, 024302 (2008).
3. A. Shevchenko et al, *Phys. Rev. C* **79**, 044305 (2009).
4. C.O. Kurebaa et al, private communication.
5. L.M. Donaldson et al, private communication.
6. D.T.L. Lee and A. Yamamoto, *Hewlett-Packard Journal*, p.44 (1994).
7. V.O. Nesterenko, W. Kleinig, J. Kvasil, P. Vesely, P.-G. Reinhard, and D.S. Dolci, *Phys. Rev. C* **74**, 064306 (2006).
8. P. Kluepfel, P.-G. Reinhard, T.J. Buervenich, and J.A. Maruhn, *Phys. Rev. C* **79**, 034310 (2009).
9. W. Kleinig, V. O. Nesterenko, J. Kvasil, P.-G. Reinhard, and P. Vesely, *Phys. Rev. C* **78**, 044313 (2008).
10. S. Raman, *At. Data Nucl. Data Tables* **36**, 1 (1987).

Nuclear polarizability: the sleeping beauty of nuclear physics

J. N. Orce

Department of Physics and Astronomy, University of the Western Cape, P/B X17, Bellville, ZA-7535 South Africa

Abstract. I present two different approaches to determine the (-2) moment of the photo-absorption cross section, σ_{-2}, which involve: 1) the latest 1988 photoneutron cross-section evaluation, and 2) the mass dependency of the symmetry energy, $a_{sym}(A)$. These two methods converge for heavy nuclei with $A \geq 70$ and are additionally supported by theoretical calculations. These approaches yield new polarization potentials which affect the quadrupole collectivity of light nuclei, mainly. A solution to the long-standing discrepancy between $B(E2;0_1^+ \rightarrow 2_1^+)$ values determined in ^{18}O by several Coulomb-excitation studies and a high-precision lifetime measurement is provided in favor of the latter.

Keywords: Photo-absorption cross section, second-order perturbation, $E1$ polarizability, reduced transition probability, spectroscopic quadupole moment
PACS: 21.10.Ky; 25.70.De; 25.20.-x; 25.20.Dc; 24.30.Cz

INTRODUCTION

Virtual excitations are responsible for the polarization of atoms and molecules and give rise to the well-known van der Waals forces between two neutral atoms or molecules, which are far enough apart for the overlap between the wave functions to be neglected [1]. In nuclei, electric-dipole virtual excitations via high-lying states in the giant dipole resonance, GDR [2], can also polarize the ground and excited states of nuclei [3, 4, 5]. This polarization phenomenon is the so-called $E1$ *polarizability* and is directly related to the static nuclear polarizability, α.

The ability for a nucleus to be polarized is driven by the dynamics of the GDR, i.e., the inter-penetrating motion of proton and neutron fluids out of phase [6]. Following the Bethe-Weizsäcker semi-empirical mass formula [7, 8], this motion results in the nuclear symmetry energy, $a_{sym}(A)(\rho_n - \rho_p)^2/\rho$, acting as a restoring force [6, 9]. The nuclear symmetry energy parameter, $a_{sym}(A)$, is key to understanding the elusive equation of state of neutron-rich matter, which impacts three-nucleon forces [10], neutron skins [11, 12], neutron stars and supernova cores [13, 14, 15, 16]. The macroscopic hydrodynamic model connects α and $a_{sym}(A)$ by [9, 17, 18],

$$\alpha = \frac{e^2 R^2 A}{40\, a_{sym}(A)} \mathrm{fm}^3. \quad (1)$$

In nuclear reactions, the induction of an electric dipole moment **p** in the nucleus can be generated by the time-dependent electric field **E** of the partner. The nuclear polarizability

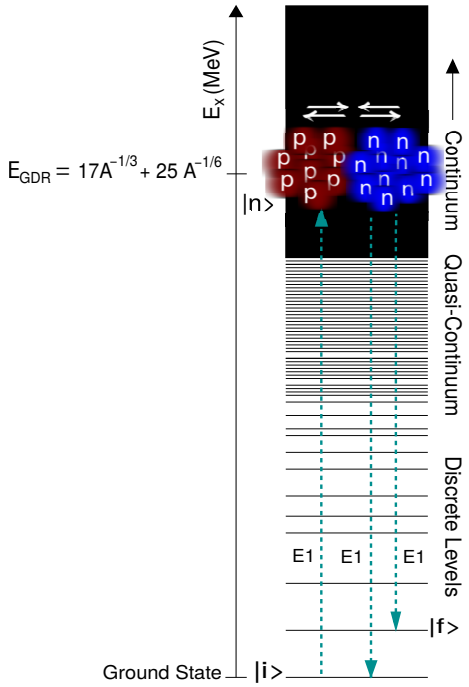

FIGURE 1. (Color online) Sketch of the $E1$ polarizability. Virtual $E1$ excitations via the GDR of the type $|i\rangle \rightarrow |n\rangle \rightarrow |i\rangle$ and $|i\rangle \rightarrow |n\rangle \rightarrow |f\rangle$ may polarize the ground $|i\rangle$ and excited $|f\rangle$ states, respectively. The excitation energy of the GDR, E_{GDR}, is given by $17A^{-1/3} + 25A^{-1/6}$ MeV [21].

$\alpha = \frac{\mathbf{p}}{\mathbf{E}}$ can also be determined using second-order perturbation theory,

$$\alpha = 2e^2 \sum_n \frac{\langle i \parallel \hat{E1} \parallel n \rangle \langle n \parallel \hat{E1} \parallel i \rangle}{E_\gamma} = \frac{\hbar c}{2\pi^2} \sigma_{-2}, \tag{2}$$

where σ_{-2} (in units of μb/MeV) is the (-2) moment of the total electric-dipole photoabsorption cross section [5, 19], defined as,

$$\sigma_{-2} = \int_{E_{threshold(\gamma,n)}}^{E_{\gamma max}} \frac{\sigma_{total}(E_\gamma)}{E_\gamma^2} \, dE_\gamma, \tag{3}$$

and is generally integrated between the neutron threshold and the upper limit available for E_γ, $E_{\gamma max} \approx 20 - 50$ MeV. As suggested by von Neumann-Cosel the low-energy contributions to σ_{-2} caused by the pygmy dipole resonance (PDR) should provide a systematic upward correction that needs to be quantified [20]. The sum rule in Eq. 2 indicates that large $E1$ matrix elements via virtual excitations of the GDR [21] may polarize, as illustrated in Fig. 1, the shape of the ground $|i\rangle$ and excited $|f\rangle$ states.

INDEPENDENT METHODS TO EXTRACT σ_{-2}

In Ref. [18], I used two independent methods to derive σ_{-2}: 1) from a fit to the extensive photoneutron evaluation published in 1988 by Dietrich and Berman [22], and 2) from

the mass dependence of the symmetry energy extracted from a global fit to the binding energies of isobaric nuclei with $A \geq 10$ [23] given by the 2012 mass evaluation [24].

1. Photoneutron data

In 1988, Dietrich and Berman evaluated the photoneutron cross-section data [22] using the preferred method of monochromatic photon beams generated by in-flight annihilation of positrons. This evaluation included $(\gamma,n)+(\gamma,pn)+(\gamma,2n)+(\gamma,3n)+(\gamma,F)$ data from studies at Livermore, Giessen, Saclay and other laboratories and shows overall agreement and consistency between measurements. Figure 2 shows the σ_{-2} data (in μb/MeV) from this evaluation (circles) [22], where Eq. 3 was integrated between the (γ,n) threshold and an upper limit of $E_{\gamma_{max}} \approx 20-50$ MeV. These integration limits include the GDR but do not take into consideration $\sigma(\gamma,p)$ contributions, the PDR and the rise of $\sigma(E_\gamma)$ at around 140 MeV due to pion exchange currents [25]. Because of the $1/E_\gamma^2$ factor, σ_{-2} is less sensitive to the high-energy contributions, which account for less than 10% of the total σ_{-2} value [17, 25, 26, 27]. The mean value of σ_{-2} was used when several measurements were available for the same isotope and data from natural samples excluded unless one single isotope dominated the isotopic abundance. These data follow a power-law,

$$\sigma_{-2} = 2.4\kappa\, A^{5/3}\ \mu\text{b/MeV}, \tag{4}$$

with a RMS deviation of 30% for $\kappa = 1$. For $A > 50$, on excluding the ^{58}Ni data point which has a large $\sigma(\gamma,p)$ contribution [28, 29], the agreement is even better, as shown in Fig. 2, with a RMS deviation of 6%. This formula agrees with the one published by Berman and Fultz in their 1975 review paper for $A > 60$: $\sigma_{-2} = 2.39(20)A^{5/3}\mu$b/MeV [28] and with Migdal's calculation of $\sigma_{-2} = 2.25\ A^{5/3}\mu$b/MeV based on the hydrodynamic model and the σ_{-2} sum rule. For $A < 50$, Fig. 2 presents large deviations from $\kappa = 1$ for $A = 4n$, $T_Z = 0$ nuclei ($\kappa < 1$) and loosely-bound light nuclei with $A < 20$ ($\kappa > 1$). The missing $\sigma(\gamma,p)$ contribution in the Dietrich and Berman compilation is the reason for the $\kappa < 1$ values observed for many $A < 50$ nuclei and ^{58}Ni. For heavier nuclei, neutron emission is the favorable decay mode due to the strong suppression of proton emission by the Coulomb barrier. Although the $\sigma(\gamma,p)$ data are scarce, the σ_{-2} sum rule [30] seems to be exhausted once the $\sigma(\gamma,p)$ contributions are included [31, 32, 33].

2. Mass dependence of the symmetry energy

The larger GDR effect ($\kappa > 1$) observed in Fig. 2 for light nuclei with $A < 20$ may be explained from the mass dependence of the symmetry energy coefficient. Migdal utilized a constant value of $a_{sym} = 23$ MeV to determine σ_{-2} in Eq. 1. Nevertheless, the mass dependence of $a_{sym}(A)$ has long been established in the liquid droplet model [34] and recognized as the fundamental parameter describing the GDR [28]. Its form has

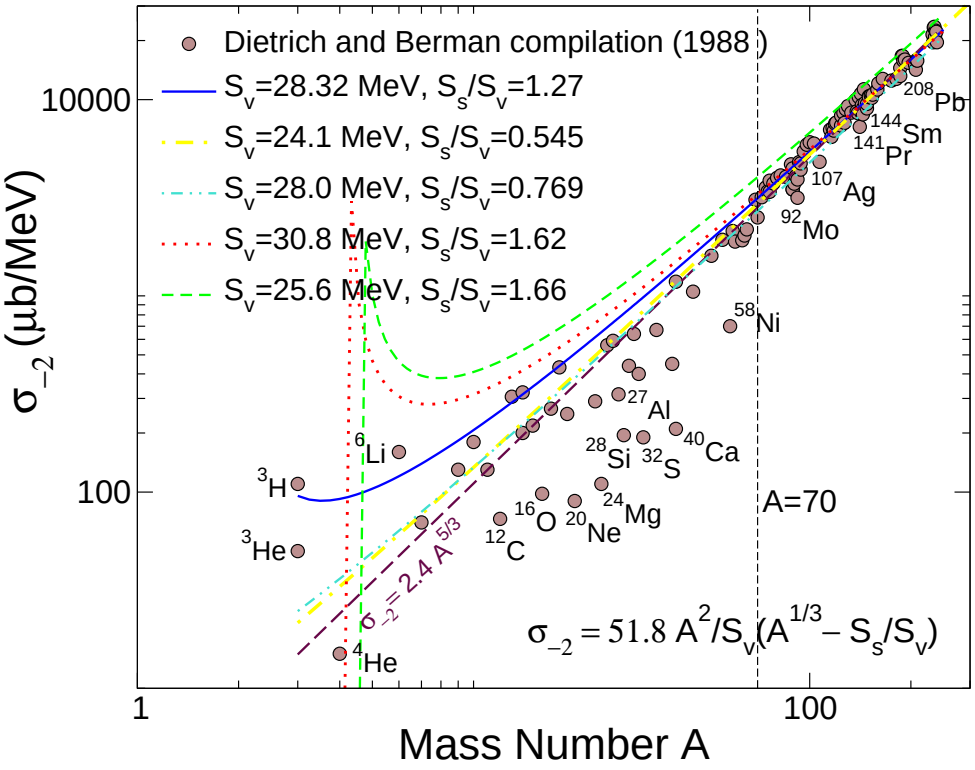

FIGURE 2. σ_{-2} plots for different sets of $(S_v, S_s/S_v)$ symmetry-energy parameters discussed in this work. The σ_{-2} data *vs* A on a log-log scale from the 1988 photo-neutron cross-section evaluation (circles) [22] are shown for comparison.

since been refined, despite its current model dependency [23], with the advent of high-precision mass measurements. From a global fit to the binding energies of isobaric nuclei with $A \geq 10$ [23], extracted from the 2012 atomic mass evaluation [24], Tian and co-workers determined $a_{sym}(A)$ as,

$$a_{sym}(A) = S_v \left(1 - \frac{S_s}{S_v\, A^{1/3}}\right), \tag{5}$$

with $S_v \approx 28.32$ MeV being the bulk symmetry energy coefficient and $\frac{S_s}{S_v} \approx 1.27$ the surface-to-volume ratio Within this approach, the extraction of $a_{sym}(A)$ only depends on the Coulomb-energy term in the Bethe-Weizsäcker semi-empirical mass formula and shell effects [35], which are both included [23].

After introducing this mass dependence in Eq. 1 and using Eq. 2, σ_{-2} can be given by,

$$\sigma_{-2} = \frac{1.8\, A^2}{A^{1/3} - 1.27}\ \mu\text{b/MeV}, \tag{6}$$

or, more generally,

$$\sigma_{-2} = \frac{51.8\, A^2}{S_v\left(A^{1/3} - S_s/S_v\right)}\ \mu\text{b/MeV}, \tag{7}$$

Equation 6 is plotted in Fig. 2 for $A \geq 10$ nuclides (solid line). Encouragingly, the increasing upbend observed as A decreases may provide an explanation for the large GDR effects observed in light nuclei.

Convergence of the two methods for $A > 70$

As shown in Fig. 2, most of the data points either fall below the predicted curve ($A < 70$) or merge with it for heavy nuclei where neutron emission is favorable ($A \geq 70$). These facts indicate that Eq. 6 could exhaust the σ_{-2} sum rule for both photoneutron and photoproton cross sections and, hence, incorporate the actual GDR effect to the nuclear polarizability. Consequently, the mass-dependent σ_{-2} curve may provide an estimate for the missing $\sigma(\gamma,p)$ contribution and Eq. 6 a means to evaluate nuclear polarizability without invoking a polarizability parameter. For example, the predicted value of σ_{-2} for ^{40}Ca is in agreement with the experimentally determined $\sigma(\gamma,p)/\sigma(\gamma,n)$ ratio [36]. No consistency in the photoneutron data is observed for lighter nuclei, which highlights the necessity for systematic studies of photoproton cross sections for $A < 70$ nuclei. This work should, preferably, be done in direct and simultaneous measurements of the partial photoneutron and photoproton cross sections, crucial to obtain reliable total photonuclear cross sections, as described in Ref. [37]. Many of these measurements could be done at the new Extreme Light Infrastructure - Nuclear Physics (ELI-NP) facility in Bucharest.

Additional theoretical evidence

Theoretical calculations have previously been done to calculate or constrain the symmetry energy parameters. Figure 2 shows σ_{-2} plots for the different sets of S_v and S_s/S_v coefficients discussed in this work. Additional support for the σ_{-2} relations discussed above arise from the various versions of the liquid droplet model. Using a modified liquid droplet model with six parameters, Steiner and collaborators [38] calculated $S_v = 24.1$ MeV, $S_s/S_v = 0.545$ after a χ^2 minimization that included nuclear masses with $A \geq 20$ from the 2003 atomic mass evaluation [39]. This set of parameters was favored by the authors and imply a neutron skin. As shown in Fig. 2, the curve fails to describe the σ_{-2} data for light nuclei, but it works where it is intended to, i.e., for heavy nuclei, where the excess neutrons can form a skin against a $N \approx Z$ core. The calculated σ_{-2} trend implying a neutron skin ($S_v = 24.1$ MeV, $S_s/S_v = 0.545$) also converges with the photoneutron data [22] and, for $A > 70$, with Eqs. 4 ($\sigma_{-2} = 2.4\kappa\, A^{5/3}\ \mu$b/MeV) and 6 ($S_v = 28.32$ MeV, $S_s/S_v = 1.27$). The model of Møller and co-workers based on the finite-range droplet macroscopic model and the folded-Yukawa single-particle microscopic model [40] yields values of ($S_v = 30.8$ MeV, $S_s/S_v = 1.62$) and also converges with the trends proposed in this work for heavy nuclei. Similar trends are determined by Dieperink and van Neck with the self-consistent Green function method [41] ($S_v = 28.0$ MeV, $S_s/S_v = 0.769$), although the trend has a slightly different slope.

Alternatively, from a free fit to available total nuclear photo-absorption data von Neumann-Cosel determined [20] the following symmetry-energy parameters (S_v = 25.6(8) MeV, $S_s/S_v = 1.66(5)$), similar to those also calculated by Steiner and collaborators. [38] ($S_v = 27.3$ MeV, $S_s/S_v = 1.68$). These theoretical parameters include the Coulomb interaction of protons but do not imply a neutron skin, later precisely measured in ^{208}Pb by Tamii and collaborators [42]. This last set of parameters misses the trend given by the photoneutron cross section data.

POLARIZABILITY IN COULOMB-EXCITATION STUDIES

New polarization potentials can be extracted based on Eqs. 4 and 6 [43], respectively. The magnitude of the first one is 54% stronger than the currently accepted polarization potential in modern Coulomb-excitation codes. The second one opens up the possibility for a parameter-free polarization potential. Consequently, both polarization potentials are essentially the same for heavy nuclei with $A > 70$.

Light nuclei present large polarizability parameters of $\kappa > 1$, which can enhance quadrupole collectivity. A remarkable case is the long-standing ≈12% discrepancy between the smaller $B(E2;0_1^+ \rightarrow 2_1^+)$ determined from seven Coulomb excitation measurements, 0.00421(9) e^2b^2 [44], and the larger one extracted from a high-precision lifetime measurement, 0.00476(11) e^2b^2, determined by Ball and co-workers in 1982 by fitting the Doppler-broadened γ-ray lineshapes [45]. The latter value nicely agrees with a similar lifetime measurement by Hermans and co-workers [46]. A half-way $B(E2;0_1^+ \rightarrow 2_1^+) = 0.00448(13)$ e^2b^2 is determined from an inelastic electron scattering measurement by Norum and collaborators in 1982 [47]. Using Eq. 4, a value of $\kappa \approx 1.8$ for the ground state of ^{18}O is determined from $\sigma_{-2} = 547$ μb/MeV [48]. This σ_{-2} value was determined from total photonuclear cross sections, which included $\sigma(\gamma,p)$, $\sigma(\gamma,n)$ + $\sigma(\gamma,np)$, and $\sigma(\gamma,2n)$, and was integrated from neutron threshold to 42 MeV. Using $\kappa = 1.8$ for the 2_1^+ state in ^{18}O, a GOSIA calculation of ^{18}O beams at a safe energy of 90 MeV scattered off a ^{208}Pb target with a [30°,60°] angular coverage yields an increase of ≈10% in the $B(E2;0_1^+ \rightarrow 2_1^+)$ value. This relative increase is independent of the $\langle 2_1^+ \,||\, \hat{E2} \,||\, 0_1^+ \rangle$ and $\langle 2_1^+ \,||\, \hat{E2} \,||\, 2_1^+ \rangle$ matrix elements. Finally, polarization effects in light nuclei also influence the determination of spectroscopic quadrupole moments in Coulomb-excitation measurements [49].

CONCLUSIONS

In conclusion, a more general treatment of nuclear polarizability may be achieved using $\sigma_{-2} = \frac{1.8\,A^2}{A^{1/3}-1.27}$ μb/MeV as extracted from the hydrodynamic model, the σ_{-2} sum rule and new volume and surface-to-volume coefficients of the symmetry energy [23]. The polarization effect on quadrupole collectivity is found to be more substantial than previously assumed for light nuclei [43]. A solution to the long-standing discrepancy between $B(E2;0_1^+ \rightarrow 2_1^+)$ values determined in ^{18}O by several Coulomb-excitation studies and a high-precision lifetime measurement is provided in favor of the latter.

Similar or larger enhancements of $B(E2)$ values can be expected for other light nuclei. Additional data are vital to pin down the mass dependence of σ_{-2} and the symmetry energy, especially for nuclei below $A \approx 70$.

ACKNOWLEDGEMENT

I acknowledge funding support by the South African National Research Foundation (NRF) under Grant 93500.

REFERENCES

1. N. F. Mott and I. N. Snedon, *Wave Mechanics and its Applications* (Clarendon Press, Oxford, 1948), Sec. 32.
2. K. A. Snover, Ann. Rev. Nucl. Part. Sci. **36**, 545 (1986).
3. J. Eichler, Phys. Rev. **133**, B1162 (1964).
4. K. Alder and A. Winther, *Electromagnetic Excitation* (North-Holland, Amsterdam, 1975).
5. J. S. Levinger, *Nuclear Photo-Disintegration* (Oxford University Press, Oxford, 1960).
6. A. B. Migdal, J. Phys. USSR **8**, 331 (1944).
7. C. F. von Weizsäcker, Z. Phys. **96**, 431 (1935).
8. H. A. Bethe and R. F. Bacher, Rev. Mod. Phys. **8**, 82 (1936).
9. A. B. Migdal, J. Exptl. Theoret. Phys. U.S.S.R. **15**, 81 (1945).
10. K. Hebeler and A. Schwenk, Eur. Phys. J. A **50**, 11 (2014).
11. M. Centelles, X. Roca-Maza, X. Viñas, and M. Warda, Phys. Rev. Lett. **102**, 122502 (2009).
12. J. Piekarewicz *et al.*, Phys. Rev. C **85**, 041302(R) (2012).
13. A. W. Steiner, M. Prakash, J. M. Lattimer and P. J. Ellis, Phys. Rep. **411**, 325 (2005).
14. J. M. Latimer, Nucl. Phys. A **928**, 276 (2014).
15. J. M. Latimer, and M. Prakash, Phys. Rep. **333-334**, 121 (2000).
16. J. M. Pearson, N. Chamel, A. F. Fantina and S. Goriely, Eur. Phys. J. A **50**, 43 (2014).
17. J. S. Levinger, Phys. Rev. **107**, 554 (1957).
18. J. N. Orce, Phys. Rev. C **91**, 064602 (2015).
19. A. B. Migdal, A. A. Lushnikov and D. F. Zaretsky, Nucl. Phys. A **66**, 193 (1965).
20. P. von Neumann-Cosel, to be published in Phys. Rev. C (2016).
21. J. J. Gaardhøje, Annu. Rev. Nucl. Part. Sci. **42**, 483 (1992).
22. S. S. Dietrich and B. L. Berman, Atom. Data Nucl. Data Tables **38**, 199-338 (1988).
23. J. Tian, H. Cui, K. Zheng, and N. Wang, Phys. Rev. C **90**, 024313 (2014).
24. M. Wang, G. Audi, A. H. Wapstra, F. G. Kondev *et al*., Chin. Phys. C **36**, 1603 (2012).
25. L. W. Jones and K. M. Terwilliger, Phys. Rev. **91**, 699 (1953).
26. D. W. Kerst and G. A. Price, Phys. Rev. **79**, 725 (1950).
27. J. Ahrens, H. Gimm, A. Zieger and B. Ziegler, Il Nuovo Cimento A, Vol. **32**, N. 3, 364 (1976).
28. B. L. Berman and S. C. Fultz, Rev. Mod. Phys. **47**, 713 (1975).
29. R. Bergere, Lecture Notes in Physics, *Photonuclear Reactions I*, (Springer-Verlag, 1977), p. 207.
30. J. S. Levinger and H. A. Bethe, Phys. Rev. **78**, 115 (1950).
31. S. A. E. Johansson, Phys. Rev. **97**, 1186 (1955).
32. H. Morinaga, Phys. Rev. **97**, 1185 (1955).
33. J. Halpern and A. K. Mann, Phys. Rev. **83**, 370 (1951).
34. W. M. Myers, W. J. Swiatecki, Ann. Phys. **55**, 395 (1969).
35. H. Koura, T. Tachibana, M. Uno, and M. Yamada, Prog. Theor. Phys. **113**, 305 (2005).
36. V. V. Balashov, Soviet Physics JETP **15**, 191 (1962).
37. R. Bergere, Lecture Notes in Physics, *Photonuclear Reactions I* (Springer-Verlag, 1977), Chapter II, p. 75.
38. A. W. Steiner, M. Prakash, J. M. Lattimer, and P. J. Ellis, Phys. Rep. **411**, 325 (2005).
39. G. Audi, A. H. Wapstra, C. Thibault, Nucl. Phys. A **729**, 337 (2003).

40. P. Møller, J.R. Nix, W.D. Myers, W.J. Swiatecki, At. Data and Nucl. Data Tables **59**, 185 (1995).
41. A. E. L. Dieperink and D. van Neck, J. Phys.: Conf. Series **20**, 160 (2005).
42. A. Tamii *et al.*, Phys. Rev. Lett. **107**, 062502 (2011).
43. J. N. Orce, submitted to Nucl. Phys. A (2016).
44. S. Raman, Jr. C. W. Nestor and P. Tikkanen, At. Data Nucl. Data Tables **78**, 1 (2001).
45. G. C. Ball, T. K. Alexander, W. G. Davies, J. S. Foster and I .V. Mitchell, Nucl. Phys. A**377**, 268 (1982).
46. J. A. J. Hermans *et al.*, Nucl. Phys. A **284**, 307 (1977).
47. B. E. Norum *et al.*, Phys. Rev. C **25**, 1778 (1982).
48. J. G. Woodworth *et al.*, Phys. Rev. C **19**, 1667 (1979).
49. J. N. Orce *et al.*, to be submitted to Phys. Rev. C (2016).

Self-Consistent RPA and the Time-dependent Density Matrix Approach

P. Schuck[1,2] and M. Tohyama[3]

[1] *Institut de Physique Nucléaire, F-91406 Orsay CEDEX, France*
[2] *Laboratoire de Physique et Modélisation des Milieux Condensés, CNRS and Université Joseph Fourier, 25 Avenue des Martyrs BP166, F-38042 Grenoble Cédex 9, France*
[3] *Kyorin University School of Medicine, Mitaka, Tokyo 181-8611, Japan*

Abstract. The time dependent density matrix (TDDM) or BBGKY (Bogoliubov, Born, Green, Kirkwood, Yvon) approach is decoupled and closed at the three-body level in finding a natural representation of the latter in terms of a quadratic form of two-body correlation functions. In the small amplitude limit an extended RPA coupled to an also extended second RPA is obtained. Since including two-body correlations means that the ground state cannot be a Hartree-Fock state, naturally the corresponding RPA is upgraded to Self-Consistent RPA (SCRPA) which was intoduced independently earlier and which is built on a correlated ground state. SCRPA conserves all the properties of standard RPA.

Keywords: Self-Consistent RPA, Lipkin and Hubbard models
PACS: 21.60.Jz; 31.15.Ne; 71.10-w

INTRODUCTION

Approaches to many body physics are many-fold. Only on the mean-field level there is consensus in practically all fields of physics. On the level of two body correlations, the approaches diverge. There are the Quantum Monte-Carlo methods with a reference state (usually a Slater determinant or a BCS state) on which a local two body operator in the exponential is applied [1], [2] which will have some relation with the Self-Consistent RPA (SCRPA) approach we will present here. There is the Coupled Cluster theory (CCT) [3], [4] most directly applicable for ground state energies. The Density Matrix Renormalisation Group (DRMG) method is very successful mostly in 1D systems [5], [6]. The correlated basis functions method is still another many body theory often applied to nuclear matter [7]. Many more attempts to tackle with the difficult many body problem, all taylored to specific problems, could be cited. In such a diversity, it may be worth to present recent progress with the equation of motion method where the hirarchy of time dependent density matrices is truncated at the three body level in approximating the latter by a quadratic form of two body correlation functions meeting in this way SCRPA as a sub-product of the theory. These equations are attractive in the sense that they are of the Schroedinger type still keeping all appreciated properties of standard RPA, as there are: conservation laws and sum rules are fullfilled. In the case of broken symmetries the Goldstone mode appears, Ward identities and gauge invariance are maintained. Ground state energies and excited states are obtained on the same footing. We will demonstrate these properties with applications to model cases.

This short review is organised as follows. In section 2, we will explain how we truncate and close the system of density matrix equations expressing the three body correlator by a quadratic form of the two body correlator. In section 3, we consider the small amplitude limit of those equations. In section 4 we give a reminder of Self-Consistent RPA (SCRPA) and in section, the relation of SCRPA with the Coupled Cluster Doubles (CCD) wave function [8] is outlined and it will be explained how to obtain the occupation numbers. In section 6, we present applications to the Lipkin and Hubbard models and in section 7 we give our conclusion.

TRUNCATION OF THE TIME-DEPENDENT DENSITY MATRIX EQUATIONS

General formalism

We start from the two body Hamiltonian for fermions in second quantisation

$$H = \sum_{\alpha} e_{\alpha} a^{+}_{\alpha} a_{\alpha} + \frac{1}{4} \sum_{\alpha\beta\gamma\delta} \bar{v}_{\alpha\beta\gamma\delta} a^{+}_{\alpha} a^{+}_{\beta} a_{\delta} a_{\gamma}. \tag{1}$$

where e_α are some single particle energies, a^+, a are the usual fermion creation and annihilation operators, and $\bar{v}_{\alpha\beta\gamma\delta} = \langle\alpha\beta|v|\gamma\delta\rangle - \langle\alpha\beta|v|\delta\gamma\rangle$ is the antisymmetrized matrix element of the two body interaction.

The coupled equations for the one-body and two-body density matrices are then of the following form [9]

$$i\dot{\rho}_{\alpha\alpha'} = \sum_{\lambda} (\varepsilon_{\alpha\lambda}\rho_{\lambda\alpha'} - \rho_{\alpha\lambda}\varepsilon_{\lambda\alpha'}) + \frac{1}{2} \sum_{\lambda_1\lambda_2\lambda_3} [\bar{v}_{\alpha\lambda_1\lambda_2\lambda_3} C_{\lambda_2\lambda_3\alpha'\lambda_1} - C_{\alpha\lambda_1\lambda_2\lambda_3} \bar{v}_{\lambda_2\lambda_3\alpha'\lambda_1}], \tag{2}$$

$$\begin{aligned} i\dot{C}_{\alpha\beta\alpha'\beta'} &= \sum_{\lambda} (\varepsilon_{\alpha\lambda} C_{\lambda\beta\alpha'\beta'} + \varepsilon_{\beta\lambda} C_{\alpha\lambda\alpha'\beta'} - \varepsilon_{\lambda\alpha'} C_{\alpha\beta\lambda\beta'} - \varepsilon_{\lambda\beta'} C_{\alpha\beta\alpha'\lambda}) \\ &+ B^0_{\alpha\beta\alpha'\beta'} + P^0_{\alpha\beta\alpha'\beta'} + H^0_{\alpha\beta\alpha'\beta'} + \frac{1}{2} \sum_{\lambda_1\lambda_2\lambda_3} [\bar{v}_{\alpha\lambda_1\lambda_2\lambda_3} C_{\lambda_2\lambda_3\beta\alpha'\lambda_1\beta'} \\ &+ \bar{v}_{\lambda_1\beta\lambda_2\lambda_3} C_{\lambda_2\lambda_3\alpha\alpha'\lambda_1\beta'} - \bar{v}_{\lambda_1\lambda_2\alpha'\lambda_3} C_{\alpha\lambda_3\beta\lambda_1\lambda_2\beta'} - \bar{v}_{\lambda_1\lambda_2\lambda_3\beta'} C_{\alpha\lambda_3\beta\lambda_1\lambda_2\alpha'}], \end{aligned} \tag{3}$$

where $C_{\alpha\beta\alpha'\beta'}$ is the correlated part of the two-body density matrix, that is

$$\rho_{\alpha\beta\alpha'\beta'} = \mathscr{A}(\rho_{\alpha\alpha'}\rho_{\beta\beta'}) + C_{\alpha\beta\alpha'\beta'}$$

and C_3 (in short hand notation) contained in the three-body density matrix

$$\rho_{\alpha\beta\gamma,\alpha'\beta'\gamma'} = \mathscr{A}S(\rho_{\alpha\alpha'}\rho_{\beta\beta'}\rho_{\gamma\gamma'} + \rho_{\alpha\alpha'}C_{\beta\gamma\beta'\gamma'}) + C_{\alpha\beta\gamma,\alpha'\beta'\gamma'} \tag{4}$$

is the fully correlated part of the three-body density-matrix in (4) which is neglected in the original version of TDDM [10]. In (4) and (4), $\mathscr{A}$ and $\mathscr{S}$ are the appropriate antisymmetrisers and symmetrisers. The energy (mean field) matrix $\varepsilon_{\alpha\alpha'}$ is given by

$$\varepsilon_{\alpha\alpha'} = e_\alpha \delta_{\alpha\alpha'} + \sum_{\lambda_1\lambda_2} \bar{v}_{\alpha\lambda_1\alpha'\lambda_2}\rho_{\lambda_2\lambda_1}. \tag{5}$$

The matrix $B^0_{\alpha\beta\alpha'\beta'}$ in Eq. (3) does not contain $C_{\alpha\beta\alpha'\beta'}$ and describes the $2p-2h$ and $2h-2p$ excitations:

$$\begin{aligned} B^0_{\alpha\beta\alpha'\beta'} &= \sum_{\lambda_1\lambda_2\lambda_3\lambda_4} \bar{v}_{\lambda_1\lambda_2\lambda_3\lambda_4}[(\delta_{\alpha\lambda_1}-\rho_{\alpha\lambda_1})(\delta_{\beta\lambda_2}-\rho_{\beta\lambda_2})\rho_{\lambda_3\alpha'}\rho_{\lambda_4\beta'} \\ &\quad -\rho_{\alpha\lambda_1}\rho_{\beta\lambda_2}(\delta_{\lambda_3\alpha'}-\rho_{\lambda_3\alpha'})(\delta_{\lambda_4\beta'}-\rho_{\lambda_4\beta'})]. \end{aligned} \tag{6}$$

Particle - particle ($p-p$) and hole-hole ($h-h$) correlations are taken care of by $P^0_{\alpha\beta\alpha'\beta'}$

$$\begin{aligned} P^0_{\alpha\beta\alpha'\beta'} &= \frac{1}{2}\sum_{\lambda_1\lambda_2\lambda_3\lambda_4} \bar{v}_{\lambda_1\lambda_2\lambda_3\lambda_4}[(\delta_{\alpha\lambda_1}\delta_{\beta\lambda_2}-\delta_{\alpha\lambda_1}\rho_{\beta\lambda_2}-\rho_{\alpha\lambda_1}\delta_{\beta\lambda_2})C_{\lambda_3\lambda_4\alpha'\beta'} \\ &\quad -(\delta_{\lambda_3\alpha'}\delta_{\lambda_4\beta'}-\delta_{\lambda_3\alpha'}\rho_{\lambda_4\beta'}-\rho_{\lambda_3\alpha'}\delta_{\lambda_4\beta'})C_{\alpha\beta\lambda_1\lambda_2}]. \end{aligned} \tag{7}$$

$H^0_{\alpha\beta\alpha'\beta'}$ contains the $p-h$ correlations.

$$\begin{aligned} H^0_{\alpha\beta\alpha'\beta'} &= \sum_{\lambda_1\lambda_2\lambda_3\lambda_4} \bar{v}_{\lambda_1\lambda_2\lambda_3\lambda_4}[\delta_{\alpha\lambda_1}(\rho_{\lambda_3\alpha'}C_{\lambda_4\beta\lambda_2\beta'}-\rho_{\lambda_3\beta'}C_{\lambda_4\beta\lambda_2\alpha'}) \\ &+ \delta_{\beta\lambda_2}(\rho_{\lambda_4\beta'}C_{\lambda_3\alpha\lambda_1\alpha'}-\rho_{\lambda_4\alpha'}C_{\lambda_3\alpha\lambda_1\beta'})-\delta_{\alpha'\lambda_3}(\rho_{\alpha\lambda_1}C_{\lambda_4\beta\lambda_2\beta'}-\rho_{\beta\lambda_1}C_{\lambda_4\alpha\lambda_2\beta'}) \\ &- \delta_{\beta'\lambda_4}(\rho_{\beta\lambda_2}C_{\lambda_3\alpha\lambda_1\alpha'}-n_{\alpha\lambda_2}C_{\lambda_3\beta\lambda_1\alpha'})]. \end{aligned} \tag{8}$$

In Eq. (3), the last four terms contain the correlated part C_3 of the three body density matrix. In the past, usually C_3 was neglected. We here want to keep it, approximating it by a quadratic form of C_2's what sums up an important sub-class of correlations contained in C_3. Inspecting (3), we see that the C_3's have a^+aa attached to the interaction. Therefore, the C_3's are of the 2particle-1hole (2p-1h) or 2h-1p type. Such type of correlations enter, e.g., the single particle self-energy of the Dyson equation [11]. An important subclass of Feynman diagrams in C_3 are the one-line reducible ones where the 2p-1h states collaps into 1p ones (as this is, e.g., the case in first order perturbation theory).This class of correlations we want to incorporate in our approach. They are graphically represented from a second order T-matrix approach of the three body Faddeev series in Fig.1.

This quadratic form of the three-body correlation matrix is most systematically and straightforwardly obtained from the identity between three-body and four-body density matrices:

$$\rho_{\alpha\beta\gamma\alpha'\beta'\gamma'} = \frac{1}{N-3}\sum_\lambda \rho_{\alpha\beta\gamma\lambda\alpha'\beta'\gamma'\lambda}. \tag{9}$$

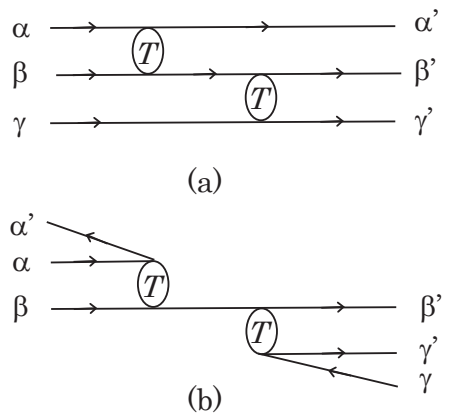

FIGURE 1. Second order T-matrix contribution to the Faddeev series of the three body correlation function.

The above identity is written in terms of correlation matrices as

$$\begin{aligned} C_{\alpha\beta\gamma\alpha'\beta'\gamma'} &= \frac{1}{3}\sum_{\lambda}(\rho_{\alpha\lambda}C_{\lambda\beta\gamma\alpha'\beta'\gamma'}+\rho_{\beta\lambda}C_{\alpha\lambda\gamma\alpha'\beta'\gamma'}+\rho_{\gamma\lambda}C_{\alpha\beta\lambda\alpha'\beta'\gamma'}+\rho_{\lambda\alpha'}C_{\alpha\beta\gamma\lambda\beta'\gamma'} \\ &+ \rho_{\lambda\beta'}C_{\alpha\beta\gamma\alpha'\lambda\gamma'}+\rho_{\lambda\gamma'}C_{\alpha\beta\gamma\alpha'\beta'\lambda}-C_{\alpha\beta\alpha'\lambda}C_{\gamma\lambda\beta'\gamma'}-C_{\alpha\beta\gamma'\lambda}C_{\gamma\lambda\alpha'\beta'} \\ &- C_{\alpha\beta\lambda\beta'}C_{\gamma\lambda\alpha'\gamma'}-C_{\alpha\gamma\alpha'\lambda}C_{\lambda\beta\beta'\gamma'}-C_{\alpha\gamma\beta'\lambda}C_{\beta\lambda\alpha'\gamma'}-C_{\alpha\gamma\lambda\gamma'}C_{\beta\lambda\alpha'\beta'} \\ &- C_{\alpha\lambda\alpha'\beta'}C_{\beta\gamma\gamma'\lambda}-C_{\alpha\lambda\alpha'\gamma'}C_{\beta\gamma\lambda\beta'}-C_{\alpha\lambda\beta'\gamma'}C_{\beta\gamma\alpha'\lambda}-C_{\alpha\beta\gamma\lambda\alpha'\beta'\gamma'\lambda}), \quad (10) \end{aligned}$$

where $C_{\alpha\beta\gamma\lambda\alpha'\beta'\gamma'\lambda}$ is a four-body correlation matrix. Under the assumptions that $\rho_{\alpha\alpha'} = \delta_{\alpha\alpha'}n_\alpha$ and $C_{\alpha\beta\gamma\lambda\alpha'\beta'\gamma'\lambda} = 0$, that is the fully correlated part, C_4, is neglected, the above relation is given as

$$\begin{aligned} C_{\alpha\beta\gamma\alpha'\beta'\gamma'} &= \frac{1}{3-n_\alpha-n_\beta-n_\gamma-n_{\alpha'}-n_{\beta'}-n_{\gamma'}}\sum_{\lambda}(-C_{\alpha\beta\alpha'\lambda}C_{\gamma\lambda\beta'\gamma'}-C_{\alpha\beta\gamma'\lambda}C_{\gamma\lambda\alpha'\beta'} \\ &- C_{\alpha\beta\lambda\beta'}C_{\gamma\lambda\alpha'\gamma'}-C_{\alpha\gamma\alpha'\lambda}C_{\lambda\beta\beta'\gamma'}-C_{\alpha\gamma\beta'\lambda}C_{\beta\lambda\alpha'\gamma'}-C_{\alpha\gamma\lambda\gamma'}C_{\beta\lambda\alpha'\beta'} \\ &- C_{\alpha\lambda\alpha'\beta'}C_{\beta\gamma\gamma'\lambda}-C_{\alpha\lambda\alpha'\gamma'}C_{\beta\gamma\lambda\beta'}-C_{\alpha\lambda\beta'\gamma'}C_{\beta\gamma\alpha'\lambda}). \quad (11) \end{aligned}$$

The correlated part of the occupation numbers in (11) may induce correlations of four body type which we want to neglect. Therefore, we will replace in (11) the n_α by their Hartree-Fock (HF) values zero or one. In principle the system of equations is now closed and, given initial conditions, one could start a time dependent solution. However, also a static equilibrium solution and small amplitude solutions around equilibrium are of particular interest. We want to elaborate those cases next.

Static limit. Restriction to particles and holes.

In the static limit, the first equation (12) becomes a generalised HF equation (6) where the single particle basis couples back to the ground state correlations

$$0 = \sum_{\lambda}(\varepsilon_{\alpha\lambda}\rho_{\lambda\alpha'} - \rho_{\alpha\lambda}\varepsilon_{\lambda\alpha'}) + \frac{1}{2}\sum_{\lambda_1\lambda_2\lambda_3}[\bar{v}_{\alpha\lambda_1\lambda_2\lambda_3}C_{\lambda_2\lambda_3\alpha'\lambda_1} - C_{\alpha\lambda_1\lambda_2\lambda_3}\bar{v}_{\lambda_2\lambda_3\alpha'\lambda_1}], \quad (12)$$

Such equation have been considered in the past [12]. The static equation for the two body correlation function, for convenience, is written in the basis where the mean field energies (5) are diagonal

$$0 = (\varepsilon_\alpha + \varepsilon_\beta - \varepsilon_{\alpha'} - \varepsilon_{\beta'})C_{\alpha\beta\alpha'\beta'} + B^0_{\alpha\beta\alpha'\beta'} + P^0_{\alpha\beta\alpha'\beta'} + H^0_{\alpha\beta\alpha'\beta'} + T_{\alpha\beta\alpha'\beta'} \quad (13)$$

As above the three body part is given by

$$\begin{aligned} T_{\alpha\beta\alpha'\beta'} &= \frac{1}{2}\sum_{\lambda_1\lambda_2\lambda_3}[\bar{v}_{\alpha\lambda_1\lambda_2\lambda_3}C_{\lambda_2\lambda_3\beta\alpha'\lambda_1\beta'} + \bar{v}_{\lambda_1\beta\lambda_2\lambda_3}C_{\lambda_2\lambda_3\alpha\alpha'\lambda_1\beta'} \\ &- \bar{v}_{\lambda_1\lambda_2\alpha'\lambda_3}C_{\alpha\lambda_3\beta\lambda_1\lambda_2\beta'} - \bar{v}_{\lambda_1\lambda_2\lambda_3\beta'}C_{\alpha\lambda_3\beta\lambda_1\lambda_2\alpha'}]. \end{aligned} \quad (14)$$

Again, approximating the C_3's by the quadratic form (11) yields a closed set of equations. However, it may be useful to solve those equations in the (generalised) HF basis which defines particle (p) states above the Fermi sea and hole (h) states below. One easily imagines then that correlation function with an odd number of $p(h)$-indices are suppressed with respect to those with an even number. We, therefore, will only consider the following four index combinations of the C_2's

$$C_{pp'hh'}; C_{p_1h_1p_2h_2}; C_{p_1p_2p_3p_4}; C_{h_1h_2h_3h_4},$$

That those combinations are the most important ones, may also be warranted by the fact that the 2p-2h states are the only ones which enter the B^0 matrix in the HF limit implying that among the four correlation functions, again $C_{pp'hh'}$ is the most important one. From the three body correlation functions the following are the dominant ones (as long as one is not close to a macroscopic phase transition or to systems with a Goldstone (zero) mode) (please note that in the following the denominator of (11) is equal to -1)

$$C_{p_1h_1h_2,p_2h_3h_4} \simeq \sum_p C_{p_1ph_3h_4}C_{h_1h_2p_2p} \quad (15)$$

that is the product of two correlation functions with $2p-2h$ indices is the most important one as argued above. There exists only one further 3-body correlation function which has this specific product property

$$C_{h_1p_1p_2,h_2p_3p_4} \simeq \sum_h C_{p_1p_2h_2h}C_{hh_1p_3p_4}. \quad (16)$$

Respecting this approximation scheme, we obtain for the four possible three body terms

$$\begin{aligned} T_{p_1p_2h_1h_2} &= \frac{1}{2}\sum_{pp'hh'}[\bar{v}_{p_1phh'}C_{p_2p'h_1h_2}C_{hh'pp'} - (p_1 \leftrightarrow p_2)] \\ &+ \frac{1}{2}\sum_{hh'pp'}[\bar{v}_{pp'h_1h}C_{p_1p_2h_2h'}C_{h'hpp'} - (h_1 \leftrightarrow h_2)], \end{aligned} \tag{17}$$

$$\begin{aligned} T_{p_1h_1p_2h_2} &= \frac{1}{2}\sum_{pp'hh'}\bar{v}_{p_1hh'p}C_{p'ph_2h}C_{h_1h'p_2p'} + \frac{1}{2}\sum_{pp'p''h}\bar{v}_{p_1pp'p''}C_{p'p''hh_2}C_{h_1hp_2p} \\ &- \frac{1}{2}\sum_{pp'hh'}\bar{v}_{ph'p_2h}C_{hh_1pp'}C_{p_1p'h'h_2} - \frac{1}{2}\sum_{pp'p''h}\bar{v}_{p'p''p_2p}C_{p_1ph_2h}C_{hh_1p'p''} \\ &- \frac{1}{2}\sum_{pp'hh'}\bar{v}_{h_1pp'h}C_{h'hp_2p}C_{p'p_1h'h_2} + \frac{1}{2}\sum_{phh'h''}\bar{v}_{h_1hh'h''}C_{h'h''p_2p}C_{pp_1hh_2} \\ &+ \frac{1}{2}\sum_{pp'hh'}\bar{v}_{ph'h_2p'}C_{p_1p'hh'}C_{h_1hp_2p} - \frac{1}{2}\sum_{phh'h''}\bar{v}_{h'h''hh_2}C_{pp_1h'h''}C_{h_1hp_2p}. \end{aligned} \tag{18}$$

The exchange matrix $T_{h_1p_1p_2h_2}$ of $T_{p_1h_1p_2h_2}$ is given not by changing p_1 and h_1 on the right-hand side of Eq. (18) but by using Eqs. (14), (15) and (16). Then the exchange property $T_{h_1p_1p_2h_2} = -T_{p_1h_1p_2h_2}$ is satisfied. Furthermore, we have

$$\begin{aligned} T_{p_1p_2p_3p_4} &= \frac{1}{2}\sum_{phh'h''}[\bar{v}_{p_1hph'}C_{pp_2hh''}C_{h''h'p_3p_4} - (p_1 \leftrightarrow p_2)] \\ &- \frac{1}{2}\sum_{phh'h''}[\bar{v}_{ph'p_3h}C_{p_1p_2hh''}C_{h''h'pp_4} - (p_3 \leftrightarrow p_4)]. \end{aligned} \tag{19}$$

$$\begin{aligned} T_{h_1h_2h_3h_4} &= \frac{1}{2}\sum_{pp'p''h}[\bar{v}_{h_1pp'h}C_{hh_2p''p}C_{p'p''h_3h_4} - (h_1 \leftrightarrow h_2)] \\ &- \frac{1}{2}\sum_{pp'p''h}[\bar{v}_{p'hh_3p}C_{h_1h_2p''p'}C_{pp''hh_4} - (h_3 \leftrightarrow h_4)]. \end{aligned} \tag{20}$$

For the numerical solution of those static correlation functions several possibilities exist. They are explained in [13]. The coupled set of equations for the four C_2's will be used in the TDDM applications presented below.

Above coupled equations have a number of appealing properties. They are totally antisymmetric and they are number and energy conserving.

We next want to elaborate on the small amplitude limit of TDDM.

THE SMALL AMPLITUDE LIMIT

Derivation of STDDM* with non-linear terms

Time dependent Hartree-Fock (TDHF) leads in the small amplitude limit, as is well known, to RPA with exchange (we will keep the acronym RPA including exchange as this is used in nuclear physics). Therefore, the corresponding ground state is a Slater determinant. Including two body correlations, the ground state cannot be a Slater determinant any longer. It must also contain correlations. The small amplitude limit of TDDM will lead to an eigenvalue problem connecting the one body sector with the two body one. It will be interesting to see in which way the one body sector will be modified with respect to RPA including the ground state correaltions.
Let us, therefore, take the small amplitude limit of our coupled equations derived above. With

$$\rho_1 = \rho_1^{(0)} + \delta\rho_1; \quad C_2 = C_2^{(0)} + \delta C_2$$

and

$$\delta\rho_1 = \sum_\nu [\tilde{\chi}^\nu e^{-i\Omega_\nu t} + \tilde{\chi}^{\nu,+} e^{i\Omega_\nu t}];$$
$$\delta C_2 = \sum_\nu [\tilde{\mathscr{X}}^\nu e^{-i\Omega_\nu t} + \tilde{\mathscr{X}}^{\nu,+} e^{i\Omega_\nu t}]$$

we obtain coupled equations for the one-body and two-body transition amplitudes $\tilde{\chi}^\nu_{\alpha\alpha'} = \langle\nu| : a^+_{\alpha'} a_\alpha : |0\rangle$ and $\tilde{\mathscr{X}}^\nu_{\alpha\beta\alpha'\beta'} = \langle\nu| : a^+_{\alpha'} a^+_{\beta'} a_\beta a_\alpha : |0\rangle$:

$$\begin{pmatrix} a & b \\ c & \tilde{d} \end{pmatrix} \begin{pmatrix} \tilde{\chi}^\nu \\ \tilde{\mathscr{X}}^\nu \end{pmatrix} = \Omega_\nu \begin{pmatrix} \tilde{\chi}^\nu \\ \tilde{\mathscr{X}}^\nu \end{pmatrix}. \tag{21}$$

where $: a^+_\lambda a_{\lambda'} := a^+_\lambda a_{\lambda'} - \rho_{\lambda\lambda'}$ and $: a^+_{\lambda_1} a^+_{\lambda_2} a_{\lambda_2'} a_{\lambda_1'} := a^+_{\lambda_1} a^+_{\lambda_2} a_{\lambda_2'} a_{\lambda_1'} - [\rho_{\lambda_1\lambda_1'}\rho_{\lambda_2\lambda_2'} - \rho_{\lambda_1\lambda_2'}\rho_{\lambda_2\lambda_1'}]$. The matrix $\tilde{d}$ is written as $\tilde{d} = d + \Delta d$ where d stems from variation of the linear terms of the two-body correlation matrix whereas Δd comes from the variation of the three-body correlation matrix when it is approximated as, e.g., in Eq. (15) and (16) by quadratic forms of C_2's (that is the leading contributions). The matrices c and Δd include the two-body correlation matrix. The matrices in Eq. (21) are given in Appendix. Equations (21) with $\Delta d = 0$ have been called in the past STDDM (small TDDM) equations [14]. With inclusion of the nonlinear terms Δd, we want to call those STDDM* equations.
Inspection of a, b matrices tells us that the matrix in (21) is highly non-symmetric. This stems from the fact that the amplitudes $\tilde{\chi}$ and $\tilde{\mathscr{X}}$ are linearly dependent. In the next section, we will clarify this point and introduce a rotation of the vector which makes the corresponding matrix essentially symmetric.

STDDM and STDDM* from an Extended Second RPA (ESRPA). Relation with SCRPA

In this section we will make a connection with Eq. (21) coming from a seemingly quite different side of attack. Let us, therefore, consider the Equation of Motion (EOM) approach [15] with one and two body sectors included without restriction of indices. We, thus, define the following generalised RPA operator

$$\mathcal{Q}_\nu^+ = \sum [\chi^\nu_{\lambda\lambda'} : a^+_\lambda a_{\lambda'} : + \mathcal{X}^\nu_{\lambda_1\lambda_2\lambda_1'\lambda_2'} : a^+_{\lambda_1} a^+_{\lambda_2} a_{\lambda_2'} a_{\lambda_1'} :] \tag{22}$$

As usual with EOM for such an ansatz, we suppose

$$\mathcal{Q}_\nu^+ |0\rangle = |\nu\rangle \quad \text{and} \quad \mathcal{Q}_\nu |0\rangle = 0.$$

Minimising the corresponding energy weighted sum rule
$2\Omega_\nu = \langle 0|[\mathcal{Q}_\nu, [H, \mathcal{Q}_\nu{}^+]]|0\rangle / \langle 0|[\mathcal{Q}, \mathcal{Q}^+]|0\rangle$,
see Sect. 4, we obtain the following eigenvalue problem

$$\begin{pmatrix} \mathscr{S} & \mathscr{B} \\ \mathscr{C} & \mathscr{D} \end{pmatrix} \begin{pmatrix} \chi \\ \mathscr{X} \end{pmatrix} = \Omega \begin{pmatrix} \mathscr{N}_1 & \mathscr{T} \\ \mathscr{T}^+ & \mathscr{N}_2 \end{pmatrix} \begin{pmatrix} \chi \\ \mathscr{X} \end{pmatrix}, \tag{23}$$

where the various matrix elements are given in an obvious way by the corresponding double commutators (lhs) and commutators (rhs) which correspond to the ones contained in the sum-rule for Ω_ν. The one body sector $\mathscr{S}\chi = \Omega\mathscr{N}_1\chi$ will be given explicitly below in Section 4.

The matrices in Eq. (23) are given in [16] where this equation was coined ERPA (Extended RPA). However, a more appropriate name is 'Extended Second RPA' (ESRPA) because it includes the two body sector and reduces to the standard second RPA in the limit where the expectation values are evaluated with the HF state. It has been shown in the past that, under certain approximations, this ESRPA is equivalent to the STDDM equation [17]. Let us sketch this again. For this, in ESRPA, we neglect everywhere C_3 (and C_4). This concerns $\mathscr{B}, \mathscr{C}, \mathscr{D}$, and $\mathscr{N}_2$. In $\mathscr{D}$ we additionally neglect the terms which are named in [18] the $\mathscr{T}_{32}$ terms. Those $\mathscr{T}_{32}$ terms correspond to the expectation values of the commutator between two-body and three-body operators [18]. Then we arrive at the following structure of above eigenvalue equation (23)

$$\begin{pmatrix} a\mathscr{N}_1 + b\mathscr{T}^+ & a\mathscr{T} + b\mathscr{N}_2 \\ c\mathscr{N}_1 + d\mathscr{T}^+ & c\mathscr{T} + d\mathscr{N}_2 \end{pmatrix} \begin{pmatrix} \chi \\ \mathscr{X} \end{pmatrix} = \Omega \begin{pmatrix} \mathscr{N}_1 & \mathscr{T} \\ \mathscr{T}^+ & \mathscr{N}_2 \end{pmatrix} \begin{pmatrix} \chi \\ \mathscr{X} \end{pmatrix}, \tag{24}$$

where the matrices a, b, c, d are as in (21) (see App. B) containing at most C_2's.

Equation (24) is intimately related to the STDDM equation as we will show now. Defining

$$\begin{pmatrix} \tilde{\chi} \\ \tilde{\mathscr{X}} \end{pmatrix} = \begin{pmatrix} \mathscr{N}_1 & \mathscr{T} \\ \mathscr{T}^+ & \mathscr{N}_2 \end{pmatrix} \begin{pmatrix} \chi \\ \mathscr{X} \end{pmatrix} \tag{25}$$

we obtain the following modified eigenvalue equation

$$\begin{pmatrix} a & b \\ c & d \end{pmatrix} \begin{pmatrix} \tilde{\chi} \\ \tilde{\mathscr{X}} \end{pmatrix} = \Omega \begin{pmatrix} \tilde{\chi} \\ \tilde{\mathscr{X}} \end{pmatrix}. \tag{26}$$

The remarkable fact is that this equation is also obtained in linearising around equilibrium the coupled EOM's for n_α and C_2 as is seen from Eq. (21) without Δd. With the use of Eq. (25) the STDDM* equation (Eq. (21) with Δd included can also be expressed as

$$\begin{pmatrix} a\mathscr{N}_1 + b\mathscr{T}^+ & a\mathscr{T} + b\mathscr{N}_2 \\ c\mathscr{N}_1 + \tilde{d}\mathscr{T}^+ & c\mathscr{T} + \tilde{d}\mathscr{N}_2 \end{pmatrix} \begin{pmatrix} \chi \\ \mathscr{X} \end{pmatrix} = \Omega \begin{pmatrix} \mathscr{N}_1 & \mathscr{T} \\ \mathscr{T}^+ & \mathscr{N}_2 \end{pmatrix} \begin{pmatrix} \chi \\ \mathscr{X} \end{pmatrix}. \tag{27}$$

Notice that with respect to (24) the matrix d is changed into $\tilde{d}$ in (27). With respect to (21), we want to call the set of equations (27), the STDDM*-b equations (or STDDM-b when Δd is neglected). Since $\mathscr{T}$, $\mathscr{N}_2$ and Δd contain C_2, the [21] and [22] elements of Eq. (27) have additional quadratic terms of C_2 that correspond to C_3. Thus, STDDM*-b is, in principle, a better approximation to ESRPA than STDDM.

Let us remark that in the left matrix the elements [12] and [21] are hermitian conjugates to one another. This stems from the fact that already in (23) the matrices $\mathscr{C}$ and $\mathscr{B}$ are the hermitian conjugates of one another under the condition that they are evaluated at equilibrium, see [17],[19] for a discussion of this point. The [11] element of the left matrix is also symmetric because at equilibrium we have $i\dot{\rho} = 0$. The one body sector of Eq.(24) corresponds to Self-Consistent RPA (SCRPA), see below, which was derived independently earlier [15]. So, in including correlations, the standard RPA has been upgraded to SCRPA. This is natural because, as mentioned, with correlations the corresponding ground state cannot be the HF state any longer. Therefore SCRPA has now found its natural place when the time-dependent HF equations are extended in a consistent way to include two body correlations. We will come back to SCRPA in Sect.4 and Sect.5. The [22] element is not hermitian because at this level of our theory we do not fullfill that 3-body and 4-body density matrices are stationary.

As already mentioned, in above STDDM equation $b \neq c^+$ and thus the corresponding matrix is strongly non-symmetric. One, therefore, has to define left and right eigenvectors. How this goes in detail is explained in [17] where also applications with good success are presented. On the other hand, (24) and (27) are much more symmetric versions of STDDM and STDDM*. The remaining non-hermiticity in the [22] element of the interaction matrix in STDDM* may be eliminated by the prescription of Rowe [20] who explicitly symmetrised the matrix. If the two versions (26) and (24) of STDDM (STDDM*, if Δd is included as in (27)) are solved in full, the results will be the same. However, the fact to transform the non-symmetric form of STDDM in (26) to the more symmetric STDDM one in (24) has apparently transferred a lot of correlations from the 2-body sector to the one body sector (standard RPA vs SCRPA). This may be of importance if in STDDM (or in STDDM*) further approximations are applied. An extreme approximation is to neglect the 2-body amplitudes in both cases where the difference clearly shows up. On the other hand, a non hermitian eigenvalue problem may also entail some problems concerning spurious solutions or non positive definite spectral functions. However, in the past applications [21, 17, 22], this has never caused any serious problems. In a way, the situation is rather similar to the difference which

exists between the Dyson boson expansion which leads to a non-hermitian problem and, e.g., the Holstein-Primakoff (Belyaev-Zelevinsky) boson expansion leading to a hermitian matrix [11]. The basic difference between both methods is, as here, the treatment of the norm matrix.

In summary of the present section, we can say that the linearisation of the TDDM equations has lead to a type of extended second RPA (ESRPA) equation which we coined STDDM*-b which contains an important part of the three body correlations (contained in the Δd matrix). The one body part of this equation is equivalent to what is known as SCRPA in the literature. It also contains already a good part of the three body correlations as shown in [13]. The structure of SCRPA is not affected by the inclusion or not of Δd. So, SCRPA is already contained in STDDM-b, that is without inclusion of the three body correlations. SCRPA takes into account a correlated ground state as it should be in a theory which goes beyond TDHF. Before elaborating on SCRPA in the next sections, let us shortly explain how to claculate occupation numbers and correlation energies from ESRPA, STDDM-b, or STDDM*-b.

Occupation numbers and correlation energy

We shall now consider how the occupation probabilities n_α are expressed by the transition amplitudes in ESRPA, STDDM-b, or STDDM*-b. We assume the following relation for the diagonal occupation matrix $\rho_{\alpha\alpha'} = n_\alpha \delta_{\alpha\alpha'}$

$$\begin{aligned}
\sum_\nu \tilde{\chi}^\nu_{\alpha\alpha'} \tilde{\chi}^{\nu *}_{\beta'\beta} &= \sum_\nu \langle 0| : a^+_{\alpha'} a_\alpha : |\nu\rangle\langle\nu| : a^+_{\beta'} a_\beta : |0\rangle \\
&= \delta_{\alpha\beta'} \langle 0| a^+_{\alpha'} a_\beta |0\rangle + \langle 0| : a^+_{\alpha'} a^+_{\beta'} a_\beta a_\alpha : |0\rangle \\
&= \delta_{\alpha\beta'}\delta_{\beta\alpha'} n_\beta \bar{n}_\alpha + C_{\alpha\beta\alpha'\beta'}, \qquad (28)
\end{aligned}$$

where $\bar{n}_\alpha = 1 - n_\alpha$. From Eq. (28) we obtain

$$\sum_\nu \tilde{\chi}^\nu_{\alpha\alpha} \tilde{\chi}^{\nu *}_{\alpha\alpha} = n_\alpha(1-n_\alpha) + C_{\alpha\alpha\alpha\alpha} = n_\alpha - n^2_\alpha. \qquad (29)$$

The above equation gives for the occupation numbers

$$n_\alpha = \frac{1}{2}\left(1 \pm \sqrt{1 - 4\sum_{\nu\neq 0} \tilde{\chi}^\nu_{\alpha\alpha} \tilde{\chi}^{\nu *}_{\alpha\alpha}}\right). \qquad (30)$$

In RPA and SCRPA there is no diagonal one-body amplitude such as $\chi^\nu_{\alpha\alpha}$, whereas in ESRPA, STDDM-b, or STDDM*-b $\chi^\nu_{\alpha\alpha}$ can couple to $\mathscr{X}^\nu_{\alpha\beta\alpha'\beta'}$ which has the same quantum numbers as the ground state. Thus the occupation probabilities in ESRPA, STDDM-b, or STDDM*-b are determined by two-phonon states expressed by $\mathscr{X}^\nu_{\alpha\beta\alpha'\beta'}$, which is in contrast with SCRPA. We use Eq. (30) to calculate the occupation probabilities in ESRPA, etc. Let us notice that relation (30) has the same structure as the occupation numbers obtained from BCS theory when expressed via the BCS amplitudes

$v_i u_i = \kappa_i$ [11].

The correlation energy is usually defined as the difference of the total correlated energy minus the Hartree-Fock energy. In this work, we thought it more appropriate to consider what one could call the 2-body correlation energy (for example in the case of BCS theory, this would reduce to the pairing energy) $E_{\rm 2bcor}$ defined by

$$E_{\rm 2bcor} = \frac{1}{4} \sum_{\alpha\beta\alpha'\beta'} \bar{v}_{\alpha\beta\alpha'\beta'} C_{\alpha'\beta'\alpha\beta}. \tag{31}$$

The equation for $\tilde{\chi}^{\nu}_{\alpha\alpha'}$ in STDDM, $a\tilde{\chi}^{\nu} + b\tilde{\mathscr{X}}^{\nu} = \Omega_\nu \tilde{\chi}^{\nu}$, gives

$$\begin{aligned} \Omega_\nu \tilde{\chi}^{\nu}_{\alpha\alpha'} &= (\varepsilon_\alpha - \varepsilon_{\alpha'})\tilde{\chi}^{\nu}_{\alpha\alpha'} + (n_{\alpha'} - n_\alpha) \sum_{\lambda\lambda'} \bar{v}_{\alpha\lambda'\alpha'\lambda} \tilde{\chi}^{\nu}_{\lambda\lambda'} \\ &+ \frac{1}{2} \sum_{\lambda_1\lambda_2\lambda_3} (\bar{v}_{\alpha\lambda_1\lambda_2\lambda_3} \tilde{\mathscr{X}}^{\nu}_{\lambda_2\lambda_3\alpha'\lambda_1} - \bar{v}_{\lambda_1\lambda_2\alpha'\lambda_3} \tilde{\mathscr{X}}^{\nu}_{\alpha\lambda_3\lambda_1\lambda_2}) \end{aligned} \tag{32}$$

Multiplying by $\tilde{\chi}^{\nu *}_{\beta'\beta}$ and using

$$\begin{aligned} \sum_{\nu} \tilde{\mathscr{X}}^{\nu}_{\alpha\beta\alpha'\beta'} \tilde{\chi}^{\nu *}_{\gamma'\gamma} &= \delta_{\alpha\gamma} C_{\gamma\beta\alpha'\beta'} - \delta_{\beta\gamma} C_{\gamma\alpha\alpha'\beta'} + n_{\gamma\alpha'} C_{\alpha\beta\beta'\gamma'} - n_{\gamma\beta'} C_{\alpha\beta\alpha'\gamma'} \\ &- n_{\beta\gamma} C_{\alpha\gamma\alpha'\beta'} + n_{\alpha\gamma} C_{\beta\gamma\alpha'\beta'} + C_{\alpha\beta\gamma\alpha'\beta'\gamma'}, \end{aligned} \tag{33}$$

and (28), we obtain

$$\sum_{\mu\alpha} \Omega_\nu \tilde{\chi}^{\nu}_{\alpha\alpha} \tilde{\chi}^{\nu *}_{\alpha\alpha} = \sum_{\alpha\lambda\lambda'} \bar{v}_{\alpha\lambda\alpha\lambda'} C_{\alpha\lambda'\alpha\lambda} - \frac{1}{2} \sum_{\alpha\lambda\lambda'\lambda''} \bar{v}_{\lambda\lambda'\alpha\lambda''} C_{\alpha\lambda''\lambda\lambda'}. \tag{34}$$

The first term on the right-hand side has no contribution in the solvable models discussed below. In general, $C_{phph'}$, $C_{pp'pp''}$, $C_{hphp'}$ and $C_{hh'hh''}$ are smaller than $C_{pp'hh'}$ and $C_{hh'pp'}$ in a perturbative regime. Therefore, $E_{\rm 2bcor}$ can approximately be expressed as

$$E_{\rm 2bcor} \approx -\frac{1}{2} \sum_{\nu\alpha} \Omega_\nu \tilde{\chi}^{\nu}_{\alpha\alpha} \tilde{\chi}^{\nu *}_{\alpha\alpha}. \tag{35}$$

Equation (35) has only diagonal elements $\tilde{\chi}^{\nu}_{\alpha\alpha}$, what means that in ESRPA $E_{\rm 2bcor}$ is determined by two-phonon states similarly to the occupation probabilities (Eq. (30)). We calculate $E_{\rm 2bcor}$ in ESRPA, etc., using Eq. (35) in the applications below. It will also be the expression we use for the applications in Sect.6. Since with (30) we have the occupation numbers, we can also calculate the one body part of the energy and, thus, the total energy is given as well.

CONCLUSIONS

In this contribution, we outlined a new decoupling scheme of the Time Dependent Density Matrix (TDDM) approach. Instead of neglecting totally the genuine three body

correlations, we approximated them by keeping an important sub-class of diagrams. Since the three body correlations are of the 2p-1h or 2h-1p type, there exist contributions which are one fermion line *reducible*. The vertices for 2p-1h (2h-1p) to 1p(1h) transitions involve two body correlation functions. Since those transitions intervene twice, one has a quadratic form in C_2's for the three body correlations and, thus, the system of equations is closed on the level of C_2's. In applications to exactly solvable models, it turned out that the inclusion of this approximate form of three body correlations is very important. We further linearised the new equations around equilibrium. This gives rise to extended second RPA equations, coupling the one body sector to the two body one. We named those equations the STDDM*-b equations. The one body sector turns out to have the structure of the Self-Consistent RPA (SCRPA) which was derived independently earlier. SCRPA, contrary to standard RPA, is built on a correlated ground state. Since this correlated ground state contains RPA correlations, naturally, one ends up with a self-consistency problem. Of course, neglecting correlations in the ground state, the STDDM*-b equations reduce to the standard second RPA ones. As an important side product, we could show that SCRPA as well as STDDM*-b conserve all the appreciated properties of standard RPA, as there are, fullfillment of sum-rules, conservation laws, appearence of Goldstone (zero) modes in cases of spontaneously broken symmetries, and gauge invariance in the case of charged systems.

ACKNOWLEDGEMENT

Past collaborations on SCRPA with J. Dukelsky, D. Delion, M. Jemai are appriciated.

APPENDIX. MATRICES IN STDDM

The matrices $a =$, b, c, d and Δd in Eq. (21) are given below.

$$a(\alpha\alpha' : \lambda\lambda') = (\varepsilon_\alpha - \varepsilon_{\alpha'})\delta_{\alpha\lambda}\delta_{\alpha'\lambda'} + \sum_\beta (\bar{v}_{\alpha\lambda'\beta\lambda} n_{\beta\alpha'} - \bar{v}_{\beta\lambda'\alpha'\lambda} n_{\alpha\beta}),$$

$$b(\alpha\alpha' : \lambda_1\lambda_2\lambda_1'\lambda_2') = \frac{1}{2}(\bar{v}_{\alpha\lambda_2'\lambda_1\lambda_2}\delta_{\alpha'\lambda_1'} - \bar{v}_{\lambda_1'\lambda_2'\alpha'\lambda_2}\delta_{\alpha\lambda_1}), \tag{36}$$

$$
\begin{aligned}
&c(\alpha_1\alpha_2\alpha_1'\alpha_2' : \lambda\lambda') \\
&= -\delta_{\alpha_1\lambda}\{\sum_{\beta\gamma\delta}[(\delta_{\alpha_2\beta}-n_{\alpha_2\beta})n_{\gamma\alpha_1'}n_{\delta\alpha_2'}+n_{\alpha_2\beta}(\delta_{\gamma\alpha_1'}-n_{\gamma\alpha_1'})(\delta_{\delta\alpha_2'}-n_{\delta\alpha_2'})]\bar{v}_{\lambda'\beta\gamma\delta} \\
&+\sum_{\beta\gamma}[\frac{1}{2}\bar{v}_{\lambda'\alpha_2\beta\gamma}C_{\beta\gamma\alpha_1'\alpha_2'}+\bar{v}_{\lambda'\beta\alpha_1'\gamma}C_{\alpha_2\gamma\alpha_2'\beta}-\bar{v}_{\lambda'\beta\alpha_2'\gamma}C_{\alpha_2\gamma\alpha_1'\beta}]\} \\
&\quad+\delta_{\alpha_2\lambda}\{\sum_{\beta\gamma\delta}[(\delta_{\alpha_1\beta}-n_{\alpha_1\beta})n_{\gamma\alpha_1'}n_{\delta\alpha_2'}+n_{\alpha_1\beta}(\delta_{\gamma\alpha_1'}-n_{\gamma\alpha_1'})(\delta_{\delta\alpha_2'}-n_{\delta\alpha_2'})]\bar{v}_{\lambda'\beta\gamma\delta} \\
&+\sum_{\beta\gamma}[\frac{1}{2}\bar{v}_{\lambda'\alpha_1\beta\gamma}C_{\beta\gamma\alpha_1'\alpha_2'}+\bar{v}_{\lambda'\beta\alpha_1'\gamma}C_{\alpha_1\gamma\alpha_2'\beta}-\bar{v}_{\lambda'\beta\alpha_2'\gamma}C_{\alpha_1\gamma\alpha_1'\beta}]\} \\
&\quad+\delta_{\alpha_1'\lambda'}\{\sum_{\beta\gamma\delta}[(\delta_{\delta\alpha_2'}-n_{\delta\alpha_2'})n_{\alpha_1\beta}n_{\alpha_2\gamma}+n_{\delta\alpha_2'}(\delta_{\alpha_1\beta}-n_{\alpha_1\beta})(\delta_{\alpha_2\gamma}-n_{\alpha_2\gamma})]\bar{v}_{\beta\gamma|\nu|\lambda\delta} \\
&+\sum_{\beta\gamma}[\frac{1}{2}\bar{v}_{\beta\gamma\lambda\alpha_2'}C_{\alpha_1\alpha_2\beta\gamma}+\bar{v}_{\alpha_1\beta\lambda\gamma}C_{\alpha_2\gamma\alpha_2'\beta}-\bar{v}_{\alpha_2\beta\lambda\gamma}C_{\alpha_1\gamma\alpha_2'\beta}]\} \\
&\quad-\delta_{\alpha_2'\lambda'}\{\sum_{\beta\gamma\delta}[(\delta_{\delta\alpha_1'}-n_{\delta\alpha_1'})n_{\alpha_1\beta}n_{\alpha_2\gamma}+n_{\delta\alpha_1'}(\delta_{\alpha_1\beta}-n_{\alpha_1\beta})(\delta_{\alpha_2\gamma}-n_{\alpha_2\gamma})]\bar{v}_{\beta\gamma\lambda\delta} \\
+&\sum_{\beta\gamma}[\frac{1}{2}\bar{v}_{\beta\gamma\lambda\alpha_1'}C_{\alpha_1\alpha_2\beta\gamma}+\bar{v}_{\alpha_1\beta\lambda\gamma}C_{\alpha_2\gamma\alpha_1'\beta}-\bar{v}_{\alpha_2\beta\lambda\gamma}C_{\alpha_1\gamma\alpha_1'\beta}]\} \\
&+\sum_{\beta}[\bar{v}_{\alpha_1\lambda'\beta\lambda}C_{\beta\alpha_2\alpha_1'\alpha_2'}-\bar{v}_{\alpha_2\lambda'\beta\lambda}C_{\beta\alpha_1\alpha_1'\alpha_2'}-\bar{v}_{\beta\lambda'\alpha_2'\lambda}C_{\alpha_1\alpha_2\alpha_1'\beta}+\bar{v}_{\beta\lambda'\alpha_1'\lambda}C_{\alpha_1\alpha_2\alpha_2'\beta}],
\end{aligned}
\tag{37}
$$

$$
\begin{aligned}
d(\quad&\alpha_1\alpha_2\alpha_1'\alpha_2' : \lambda_1\lambda_2\lambda_1'\lambda_2') = (\varepsilon_{\alpha_1}+\varepsilon_{\alpha_2}-\varepsilon_{\alpha_1'}-\varepsilon_{\alpha_2'})\delta_{\alpha_1\lambda_1}\delta_{\alpha_2\lambda_2}\delta_{\alpha_1'\lambda_1'}\delta_{\alpha_2'\lambda_2'} \\
+\quad&\frac{1}{2}\delta_{\alpha_1'\lambda_1'}\delta_{\alpha_2'\lambda_2'}\sum_{\beta\gamma}(\delta_{\alpha_1\beta}\delta_{\alpha_2\gamma}-\delta_{\alpha_2\gamma}n_{\alpha_1\beta}-\delta_{\alpha_1\beta}n_{\alpha_2\gamma})\bar{v}_{\beta\gamma\lambda_1\lambda_2} \\
-\quad&\frac{1}{2}\delta_{\alpha_1\lambda_1}\delta_{\alpha_2\lambda_2}\sum_{\beta\gamma}(\delta_{\alpha_1'\beta}\delta_{\alpha_2'\gamma}-\delta_{\alpha_2'\gamma}n_{\beta\alpha_1'}-\delta_{\alpha_1'\beta}n_{\gamma\alpha_2'})\bar{v}_{\lambda_1'\lambda_2'\beta\gamma} \\
+\quad&\delta_{\alpha_2\lambda_2}\delta_{\alpha_2'\lambda_2'}\sum_{\beta}(\bar{v}_{\alpha_1\lambda_1'\beta\lambda_1}n_{\beta\alpha_1'}-\bar{v}_{\beta\lambda_1'\alpha_1'\lambda_1}n_{\alpha_1\beta}) \\
+\quad&\delta_{\alpha_2\lambda_2}\delta_{\alpha_1'\lambda_1'}\sum_{\beta}(\bar{v}_{\alpha_1\lambda_2'\beta\lambda_1}n_{\beta\alpha_2'}-\bar{v}_{\beta\lambda_2'\alpha_2'\lambda_1}n_{\alpha_1\beta}) \\
+\quad&\delta_{\alpha_1\lambda_1}\delta_{\alpha_1'\lambda_1'}\sum_{\beta}(\bar{v}_{\alpha_2\lambda_2'\beta\lambda_2}n_{\beta\alpha_2'}-\bar{v}_{\beta\lambda_2'\alpha_2'\lambda_2}n_{\alpha_2\beta}) \\
+\quad&\delta_{\alpha_1\lambda_1}\delta_{\alpha_2'\lambda_2'}\sum_{\beta}(\bar{v}_{\alpha_2\lambda_1'\beta\lambda_2}n_{\beta\alpha_1'}-\bar{v}_{\beta\lambda_1'\alpha_1'\lambda_2}n_{\alpha_2\beta}).
\end{aligned}
\tag{38}
$$

We now give the expression for Δd which arises from the quadratic forms in C_2's of the 3-body correlation functions. We use Eqs. (15) and (16) for the three-body correlation

matrix.

$$
\begin{aligned}
\Delta d(\quad & \alpha\beta\alpha'\beta' : \lambda_1\lambda_2\lambda_1'\lambda_2') = -\frac{1}{2}\bar{v}_{\alpha(h)\lambda_1'(h)\lambda_1(p)\lambda_2(p)} \\
\times \quad & C_{\lambda_2'(h)\beta(h)\alpha'(p)\beta'(p)} \\
+ \quad & \frac{1}{2}\bar{v}_{\alpha(p)\lambda_1'(p)\lambda_1(h)\lambda_2(h)} C_{\lambda_2'(p)\beta(p)\alpha'(h)\beta'(h)} \\
- \quad & \frac{1}{2}\delta_{\beta\lambda_2}\delta_{\alpha'\lambda_1'}\delta_{\beta'\lambda_2'} \sum_{\lambda(h)\lambda'(p)\lambda''(p)} \bar{v}_{\alpha\lambda\lambda'\lambda''} C_{\lambda'\lambda''\lambda\lambda_1(h)} \\
- \quad & \frac{1}{2}\delta_{\beta\lambda_1}\delta_{\alpha'\lambda_1'}\delta_{\beta'\lambda_2'} \sum_{\lambda(p)\lambda'(h)\lambda''(h)} \bar{v}_{\alpha\lambda\lambda'\lambda''} C_{\lambda'\lambda''\lambda\lambda_2(p)} \\
+ \quad & \frac{1}{2}\bar{v}_{\beta(h)\lambda_1'(h)\lambda_1(p)\lambda_2(p)} C_{\lambda_2'(h)\alpha(h)\alpha'(p)\beta'(p)} \\
- \quad & \frac{1}{2}\bar{v}_{\beta(p)\lambda_1'(p)\lambda_1(h)\lambda_2(h)} C_{\lambda_2'(p)\alpha(p)\alpha'(h)\beta'(h)} \\
+ \quad & \frac{1}{2}\delta_{\alpha\lambda_2}\delta_{\alpha'\lambda_1'}\delta_{\beta'\lambda_2'} \sum_{\lambda(h)\lambda'(p)\lambda''(p)} \bar{v}_{\beta\lambda\lambda'\lambda''} C_{\lambda'\lambda''\lambda\lambda_1(h)} \\
+ \quad & \frac{1}{2}\delta_{\alpha\lambda_1}\delta_{\alpha'\lambda_1'}\delta_{\beta'\lambda_2'} \sum_{\lambda(p)\lambda'(h)\lambda''(h)} \bar{v}_{\beta\lambda\lambda'\lambda''} C_{\lambda'\lambda''\lambda\lambda_2(p)} \\
+ \quad & \frac{1}{2}\bar{v}_{\lambda_1'(p)\lambda_2'(p)\alpha'(h)\lambda_2(h)} C_{\alpha(p)\beta(p)\beta'(h)\lambda_1(h)} \\
- \quad & \frac{1}{2}\bar{v}_{\lambda_1'(h)\lambda_2'(h)\alpha'(p)\lambda_2(p)} C_{\alpha(h)\beta(h)\beta'(p)\lambda_1(p)} \\
+ \quad & \frac{1}{2}\delta_{\alpha\lambda_1}\delta_{\beta\lambda_2}\delta_{\beta'\lambda_1'} \sum_{\lambda(p)\lambda'(p)\lambda''(h)} \bar{v}_{\lambda\lambda'\alpha'\lambda''} C_{\lambda_2'(h)\lambda''\lambda\lambda'} \\
- \quad & \frac{1}{2}\delta_{\alpha\lambda_1}\delta_{\beta\lambda_2}\delta_{\beta'\lambda_1'} \sum_{\lambda(h)\lambda'(h)\lambda''(p)} \bar{v}_{\lambda\lambda'\alpha'\lambda''} C_{\lambda_2'(p)\lambda''\lambda\lambda'} \\
- \quad & \frac{1}{2}\bar{v}_{\lambda_1'(p)\lambda_2'(p)\beta'(h)\lambda_2(h)} C_{\alpha(p)\beta(p)\alpha'(h)\lambda_1(h)} \\
+ \quad & \frac{1}{2}\bar{v}_{\lambda_1'(h)\lambda_2'(h)\beta'(p)\lambda_2(p)} C_{\alpha(h)\beta(h)\alpha'(p)\lambda_1(p)} \\
- \quad & \frac{1}{2}\delta_{\alpha\lambda_1}\delta_{\beta\lambda_2}\delta_{\alpha'\lambda_1'} \sum_{\lambda(p)\lambda'(p)\lambda''(h)} \bar{v}_{\lambda\lambda'\beta'\lambda''} C_{\lambda_2'(h)\lambda''\lambda\lambda'} \\
+ \quad & \frac{1}{2}\delta_{\alpha\lambda_1}\delta_{\beta\lambda_2}\delta_{\alpha'\lambda_1'} \sum_{\lambda(h)\lambda'(h)\lambda''(p)} \bar{v}_{\lambda\lambda'\beta'\lambda''} C_{\lambda_2'(p)\lambda''\lambda\lambda'}
\end{aligned}
\tag{39}
$$

The terms with and without summation describe self-energy corrections and vertex corrections, respectively, and indices p (h) mean that the corresponding single-particle state is a particle (hole) state.

REFERENCES

1. M. P. Nightingale, C. J. Umrigar, (Eds.) *Quantum Monte Carlo Methods in Physics and Chemistry*, (Springer, Berlin, 1999).
2. M. Holzmann, B. Bernu, C. Pierleoni, J. Mc Minis, D. M. Ceperly, V. Olevano, L. Delle Site, Phys. Rev. Lett. **107**,110402 (2011).
3. P. J. Knowles, C. Hampel, H.-J. Werner, J. Chem. Phys. **99**, 5219 (1993).
4. R. F. Bishop, Theor. Chim. Acta, **80**, 95 (1991).
5. I. Peschel, X. Wang, M. Kaulke, K. Hallberg (Eds.), *Density-Matrix Renormalisation, A new Numerical Method in Physics*, (Springer, Berlin, 1999).
6. U. Schollwoeck, Ann. Physics **326**, 96 (2011) *and* Rev. Mod. Phys. **77**, 259 (2005).
7. J. W. Clark, P. Westhaus, Phys. Rev. **141**, 833 91966).
8. G. E. Scuseria, C. L. Janssen, H. F. Schaefer, J. Chem. Phys. **89**, 7382 (1988).
9. M. Tohyama, P. Schuck, Eur. Phys. J. A **50**, 77 (2014).
10. S. J. Wang and W. Cassing: Ann. Phys. **159**, 328 (1985).
11. P. Ring and P. Schuck, *The nuclear many-body problem*, (Springer-Verlag, Berlin, 1980).
12. J. Dukelsky, P. Schuck, Nucl. Phys. A **512**, 466 (1990).
13. P. Schuck, M. Tohyama, Phys. Rev. B **93**, 165117 (2016).
14. M. Gong and M. Tohyama: Z. Phys. A**335**, 153 (1990).
15. J. Dukelsky, G. Roepke, P. Schuck, Nucl. Phys. A **628**, 17 (1998).
16. M. Tohyama, P. Schuck, Eur. Phys. J. A **45**, 257 (2010).
17. M. Tohyama, P. Schuck, Eur. Phys. J. A **19**, 215 (2004).
18. M. Tohyama, S. Takahara, P. Schuck, Eur. Phys. J. A **21**, 217 (2004).
19. M. Tohyama, P. Schuck, Eur. Phys. J. A **32**, 139 (2007).
20. D. J. Rowe, Rev. Mod. Phys. **40**, 153 (1968); D. J. Rowe, *Nuclear Collective Motion, Models and Theory*, World Scientific 2010.
21. S. Takahara, M. Tohyama, P. Schuck, Phys. Rev. C **70**, 057307 (2004).
22. M. Tohyama, Phys. Rev. C **75**, 044310 (2007).

QRPA with a novel form of phonon operator

Fedor Šimkovic[1,2,3], Adam Smetana[3] and Miroslav Macko[2,3]

[1] *Laboratory of Theoretical Physics, JINR Dubna, 141980 Dubna, Moscow region, Russia*
[2] *Department of Nuclear Physics and Biophysics, Comenius University, Mlynska dolina, SK-84248 Bratislava, Slovakia*
[3] *Czech Technical University in Prague, 128-00 Prague, Czech Republic*

Abstract. The quasiparticle random phase approximation with a new form of the phonon operator, which includes non-linear terms, is proposed. We show that the suggested modification of the phonon operator allows to calculate states of multiphonon origin. Numerical analysis are performed with the simplest non-linear extension of a phonon operator within the proton-neutron Lipkin model. A good agreement is found both for energies and beta transition amplitudes with those obtained by a diagonalization of the bosonic Hamiltonian.

Keywords: double beta decay, nuclear matrix element, QRPA
PACS: 23.10.-s; 21.60.-n; 23.40.Bw; 23.40.Hc

INTRODUCTION

The random phase approximation (RPA) and its quasiparticle generalization (QRPA) have been, for a long time, very important theoretical tools in investigating the collective degrees of freedom of many-fermion systems. They have been extensively used in various branches of physics from metals in bulk to atomic nuclei.

The QRPA is the method of choice for a consistent description of nuclear excitations, in particular for understanding low-lying collective states and giant resonances. However, the standard QRPA with linear phonon operator is unable to account for correlations of higher order like 2p-2h, 3p-3h, etc. and to describe states of multi-phonon origin. These states are usually considered within the multi-phonon approach [1].

The goal of this contribution is to present a novel QRPA approach, namely QRPA with non-linear phonon operator (nlQRPA), which directly describes also the states of multiphonon origin. This modification of the QRPA is applied to the proton-neutron Lipkin model and we shall review it briefly.

THE SCHEMATIC MODEL

For the sake of simplicity we consider the proton-neutron monopole Lipkin Hamiltonian which is exactly solvable [2]

$$H_F = \varepsilon C + \lambda_1 A^\dagger A + \lambda_2 (A^\dagger A^\dagger + AA)\,. \tag{1}$$

where C and $A^\dagger$ are the number (proton and neutron) and proton-neutron pair quasiparticle operators, respectively. They form the SU(2) algebra $[A,A^\dagger] = 1 - C/(2\Omega)$, $[C,A^\dagger] = 2A^\dagger$ and $[C,A] = 2A$. The spaces of single-particle states associated with the

proton and neutron systems are restricted to a single j-shell. The model Hamiltonian in Equation 1 is obtained from the Hamiltonian in [2] which, in particle representation, apart from a pairing interaction for like nucleons, consists of a monopole-monopole proton-neutron two-body interaction of particle-hole and particle-particle types, whose strengths are parametrized by χ and κ, respectively. Their relation to the parameters $\lambda_{1,2}$ is

$$\lambda_1 = 4\Omega[\chi(u_p^2 v_n^2 + v_p^2 u_n^2) - \kappa(u_p^2 u_n^2 + v_p^2 v_n^2)], \quad \lambda_2 = 4\Omega(\chi + \kappa) u_p v_p u_n v_n \tag{2}$$

with $\Omega = j + 1/2$. $u_{p,n}$ and $v_{p,n}$ are the coefficients of the Bogoliubov-Valatin transformation. Hamiltonian H_F is exactly solvable by a diagonalization in the basis $(A^\dagger)^n|0\rangle$ where $n = 0, \ldots, 2\Omega$. Here $|0\rangle$ denotes quasiparticle vacuum. As the model Hamiltonian does not allow to mix even and odd basis states, the even (odd) eigenstates are mixture of the even (odd) basis states. As the β-transitions are linear in A and $A^\dagger$ (in the approximation of neglecting the scattering terms), only those connecting ground state with the odd excited states are nonzero.

We consider the boson mapping of H_F following the Marumori recipe up to quadratic terms in bosonic operators:

$$H_B = (2\varepsilon + \lambda_1) B^\dagger B + \lambda_2 (B^\dagger B^\dagger + BB)\,, \tag{3}$$

where $B^\dagger$ (B) is a creation (annihilation) boson operator satisfying $[B, B^\dagger] = 1$. The Hamiltonian H_B exhibits the main features of a realistic Hamiltonian used in the standard QRPA calculation of single and double beta decay nuclear transitions.

THE QRPA WITH NONLINEAR OPERATORS

Within the QRPA, an excited state $|Q\rangle$ is created by applying a phonon creation operator $Q^\dagger$ on the RPA ground state $|\mathrm{RPA}\rangle$ having the properties $|Q\rangle = Q^\dagger|\mathrm{RPA}\rangle$ and $Q|\mathrm{RPA}\rangle = 0$. The new form of the QRPA phonon operator which we propose contains nonlinear terms in the boson operators B and $B^\dagger$ as follows:

$$Q^{m\dagger} = X_1^m B^\dagger - Y_1^m B + X_3^m B^\dagger B^\dagger B^\dagger - Y_3^m BBB\,. \tag{4}$$

In the limit $X_3^m, Y_3^m = 0$ we recover the standard QRPA phonon operator. In this case the QRPA equation give an approximate solution to the first excited state $|1\rangle$ of the schematic Hamiltonian. With an additional degree of freedom given by variational amplitudes X_3^m, Y_3^m the dimension of the RPA equation is doubled. That allows to reproduce both the first $|1\rangle$ and third $|3\rangle$ excited states of Hamiltonian H_B. Corresponding set of variational amplitudes is

$$X^m = \begin{pmatrix} X_1^m \\ X_3^m \end{pmatrix}, \quad Y^m = \begin{pmatrix} Y_1^m \\ Y_3^m \end{pmatrix}, \quad \text{for } m = 1, 3, \tag{5}$$

The RPA ground state, which is a solution of equation $Q^m|\mathrm{RPA}\rangle = 0$, can be written as

$$|\mathrm{RPA}\rangle = \mathscr{N} \sum_{n=0}^{\infty} a_{2n} (B^\dagger B^\dagger)^n |0\rangle\,, \quad a_0 = 1\,. \tag{6}$$

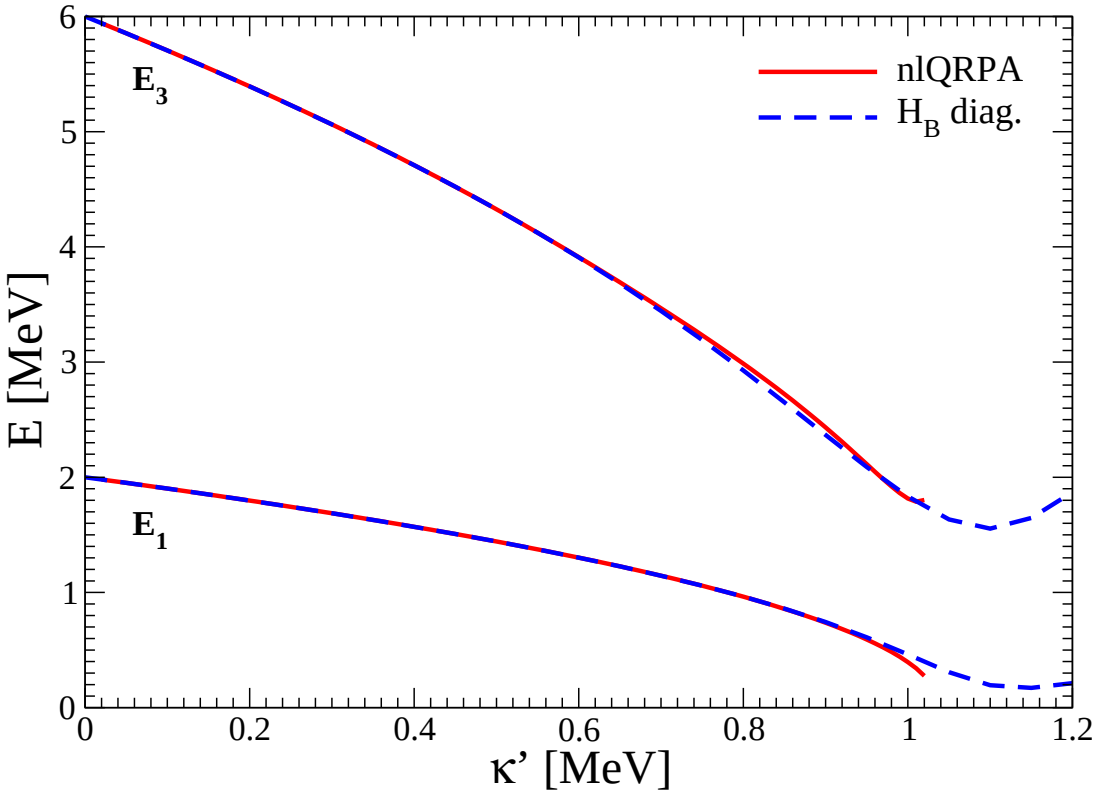

FIGURE 1. Comparison of the first and third excitation energies resulting from the diagonalization of H_B (dashed line) with the nlQRPA values (solid lines).

Here, the normalization factor $\mathcal{N}$ takes the form $\mathcal{N}^{-2} = \sum_{n=0}^{\infty}(2n)!\ a_{2n}^2$. The coefficients a_{2n} are functions of the RPA variational amplitudes. Below, for the sake of numerical calculation, we restrict ourselves only to work with the coefficients a_2, a_4, and a_6.

By using the machinery of the equation of motion, we get the RPA eigenvalue equation

$$\begin{pmatrix} A & B \\ B & A \end{pmatrix} \begin{pmatrix} X^m \\ Y^m \end{pmatrix} = E_m \begin{pmatrix} U & 0 \\ 0 & -U \end{pmatrix} \begin{pmatrix} X^m \\ Y^m \end{pmatrix}, \tag{7}$$

where elements of RPA matrices are given by

$$A = \langle \mathrm{RPA}| \begin{pmatrix} [B,H_B,B^\dagger] & [B,H_B,B^\dagger B^\dagger B^\dagger] \\ [B,H_B,B^\dagger B^\dagger B^\dagger] & [BBB,H_B,B^\dagger B^\dagger B^\dagger] \end{pmatrix} |\mathrm{RPA}\rangle \tag{8}$$

$$B = -\langle \mathrm{RPA}| \begin{pmatrix} [B,H_B,B] & [B,H_B,BBB] \\ [B,H_B,BBB] & [BBB,H_B,BBB] \end{pmatrix} |\mathrm{RPA}\rangle \tag{9}$$

$$U = \langle \mathrm{RPA}| \begin{pmatrix} [B,B^\dagger] & [B,B^\dagger B^\dagger B^\dagger] \\ [BBB,B^\dagger] & [BBB,B^\dagger B^\dagger B^\dagger] \end{pmatrix} |\mathrm{RPA}\rangle. \tag{10}$$

Here, the double commutators are defined as $[A,B,C] = \frac{1}{2}[A,[B,C]] + \frac{1}{2}[[A,B],C]$. The RPA Equation 7 must be solved iteratively as all elements of the participating matrices

depend on the RPA ground state parameters a_{2n}.

We transform the RPA Equation 7 to the standard form, which guarantees the completeness and orthonormality of the RPA $m = 1$ and $m = 3$ states. This is achieved by diagonalization of the matrix U. We have $\mathscr{O} U \mathscr{O}^{-1} = \varepsilon$, where

$$\mathscr{O} \equiv \begin{pmatrix} \cos\theta & \sin\theta \\ -\sin\theta & \cos\theta \end{pmatrix} \text{ and } \varepsilon \equiv \begin{pmatrix} \varepsilon_1 & 0 \\ 0 & \varepsilon_3 \end{pmatrix}, \quad \text{so that} \quad 1 = \varepsilon^{-1/2} \mathscr{O}^{-1} U \mathscr{O} \varepsilon^{-1/2}. \tag{11}$$

Here, $\tan 2\theta = 2a/(1-b)$ and ε_1 and ε_3 are eigenvalues of U. We introduce new RPA matrices and amplitudes as follows:

$$\begin{aligned} \bar{A} &= \varepsilon^{-1/2} \mathscr{O}^{-1} A \mathscr{O} \varepsilon^{-1/2}, \quad \bar{B} = \varepsilon^{-1/2} \mathscr{O}^{-1} B \mathscr{O} \varepsilon^{-1/2}, \\ \bar{X}^m &= \varepsilon^{1/2} \mathscr{O}^{-1} X^m, \quad \bar{Y}^m = \varepsilon^{1/2} \mathscr{O}^{-1} Y^m. \end{aligned} \tag{12}$$

Finally, we end up with RPA equation of the standard form

$$\begin{pmatrix} \bar{A} & \bar{B} \\ \bar{B} & \bar{A} \end{pmatrix} \begin{pmatrix} \bar{X}^m \\ \bar{Y}^m \end{pmatrix} = E_m \begin{pmatrix} 1 & 0 \\ 0 & -1 \end{pmatrix} \begin{pmatrix} \bar{X}^m \\ \bar{Y}^m \end{pmatrix}. \tag{13}$$

By solving the RPA Equation (13) we get eigenvalues $E_{1,3}$ and amplitudes $\bar{X}$ and $\bar{Y}$. The amplitudes are then used to calculate the RPA ground state parameters a_{2n} of the next iteration.

The RPA ground state parameters a_{2n} are determined by the "linearization" of phonon operator, which can be written as

$$Q^{m\dagger} = \bar{X}_1^m F_1^\dagger - \bar{Y}_1^m F_1 + \bar{X}_3^m F_3^\dagger - \bar{Y}_3^m F_3 \,. \tag{14}$$

where operators $F_{1,3}$ and $F_{1,3}^\dagger$ are given by

$$\begin{pmatrix} F_1 \\ F_3 \end{pmatrix} = \varepsilon^{-1/2} \mathscr{O} \begin{pmatrix} B \\ BBB \end{pmatrix}, \quad \begin{pmatrix} F_1^\dagger \\ F_3^\dagger \end{pmatrix} = \varepsilon^{-1/2} \mathscr{O} \begin{pmatrix} B^\dagger \\ B^\dagger B^\dagger B^\dagger \end{pmatrix}. \tag{15}$$

We introduce quasiboson approximation for these operators:

$$[F_i, F_j^\dagger] \simeq \langle \mathrm{RPA} | [F_i, F_j^\dagger] | \mathrm{RPA} \rangle = \delta_{ij}, \quad [F_i, F_j] \simeq \langle \mathrm{RPA} | [F_i, F_j] | \mathrm{RPA} \rangle = 0 \tag{16}$$

This step allows us to approximate the RPA ground state and its parameters a_{2n} by means of the standard Ansatz (which is exact in the standard QRPA defined with bosonic operators). We have

$$\begin{aligned} |\mathrm{RPA}\rangle &= \mathscr{N} (1 + a_2 B^\dagger B^\dagger + a_4 (B^\dagger B^\dagger)^2 + a_6 (B^\dagger B^\dagger)^3 + \ldots) \\ &\approx \mathscr{N}' \mathrm{e}^{\frac{1}{2} \sum_{ij} d_{ij} F_i^\dagger F_j^\dagger}, \quad \text{where} \quad d_{ij} = (\bar{Y} \bar{X}^{-1})_{ij}. \end{aligned} \tag{17}$$

The Equation 17 provides the prescription for the RPA ground state parameters of the next iteration as $a_{2n} = a_{2n}(\varepsilon_{1,3}, \theta, d_{ij})$. We restrict our consideration to the first four

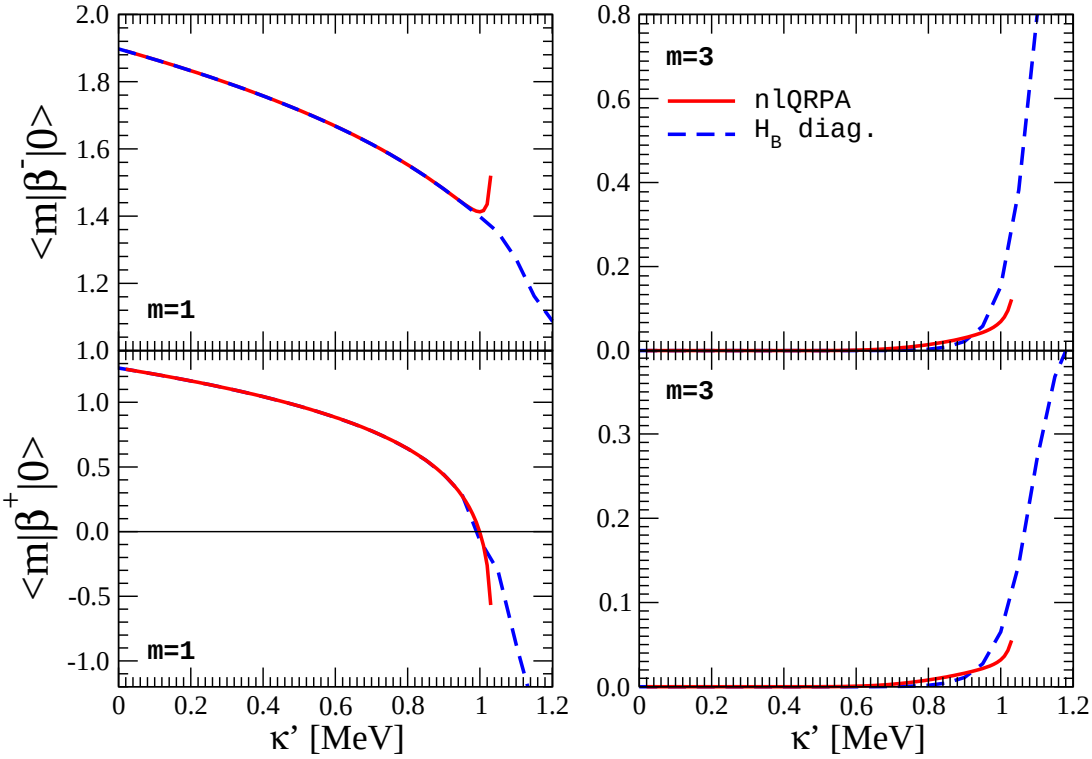

FIGURE 2. The $\beta^{\pm}$-transition amplitudes between the ground state and $|1\rangle$ or $|3\rangle$ excited state. (Same conventions as in Figure 1)

terms of the Equation 17. We continue iterating until the solution given by E_1, E_3, X and Y converges and fulfils the required accuracy.

It is straightforward to generalize the phonon operator in (4) for the phonon operator, which allows to describe also higher excited odd states of the original fermionic Hamiltonian (1). By assuming quasiboson approximation we have

$$\begin{aligned} Q^{m\dagger} &= X_1^m B^\dagger + X_3^m (B^\dagger)^3 + X_5^m (B^\dagger)^5 + \cdots \\ &\quad - Y_1^m B - Y_3^m (B)^3 - Y_5^m (B)^5 - \cdots \end{aligned} \tag{18}$$

Here, $m = 1,\ 3,\ 5,\ \cdots$ denotes the odd excited states. The RPA equation can be constructed by following the presented scheme above.

RESULTS

The numerical application is performed for a system of four protons and six neutrons moving in a $j = 9/2$ shell ($\Omega = 5$). Hence the model has 10 excited states out of which 9 are of multiphonon origin. We set $\varepsilon = 1\,\mathrm{MeV}$. The number of protons and neutrons determine the BCS amplitudes entering the $\lambda_{1,2}$ parameters of the model Hamiltonian H_B. We redefine the parameters κ and χ as in Ref. [2]:

$$\kappa \to \kappa' = 2\Omega\kappa, \qquad \chi \to \chi' = 2\Omega\chi. \tag{19}$$

The value $\chi' = 0$ is adopted while the particle-particle strength κ' is allowed to vary in the interval $0 \leq \kappa' \leq 1.2$. Comparing the schematic calculations with the realistic ones of the standard QRPA approach, a value for κ' close to unity is expected. In what follows we shall present the numerical results for the nlQRPA approach described in the previous section and compare them with the values provided by diagonalizing H_B.

In Figure 1 we present a dependence of energies E_1 and E_3 on the parameter κ', which follows from the iterative numerical solution of the nlQRPA, and compare it with the exact solution given by diagonalization of H_B. We see very good agreement up to the point, where the nlQRPA collapses at $\kappa' \doteq 1.03\,\mathrm{MeV}$.

In Figure 2 we show the $\beta^{\pm}$-transition amplitudes for the first and the third excited states. The β^{-}-amplitude is given by

$$\begin{aligned} \langle m|\beta^{-}|\mathrm{RPA}\rangle &= \sqrt{2\Omega}\left(u_p v_n[\sqrt{\varepsilon_1}\cos\theta\bar{X}_1^m - \sqrt{\varepsilon_3}\cos\theta\bar{X}_3^m]\right. \\ &\quad \left. + u_n v_p[\sqrt{\varepsilon_1}\cos\theta\bar{Y}_1^m - \sqrt{\varepsilon_3}\cos\theta\bar{Y}_3^m]\right) \quad \text{for} \quad m = 1,3. \end{aligned} \tag{20}$$

By mutually replacing p and n indices we get the β^{+} transition amplitudes. From Figure 2 we see that the $\beta^{\pm}$-transitions to the first excited states are reproduced accurately again up to the point of of the QRPA collapse, the same way as the standard QRPA does it. The $\beta^{\pm}$-transitions to the third excited state are reproduced quite well. An improved description might be achieved by adding higher nonlinear terms to the phonon operator and by a more accurate description of the RPA ground state. We note that the nlQRPA fulfils exactly the Ikeda sum rule even by the considered approximation scheme like the standard QRPA does.

CONCLUSIONS

In summary, we proposed a novel extension of the QRPA approach, namely the nlQRPA, which can describe also states of multiphonon origin. The obtained results within a schematic model are promising. There is straightforward way to extend this approach also for a realistic nuclear structure calculations. Our ultimate goal is to proceed in this direction.

ACKNOWLEDGMENTS

This work is supported in part by the VEGA Grant Agency of the Slovak Republic under Contract No. 1/0922/16, by Slovak Research and Development Agency under Contract No. APVV-14-0524, and by the Ministry of Education, Youth and Sports of the Czech Republic under Contract No. LM2011027.

REFERENCES

1. F. Andreozzi, F. Knapp, N. Lo Iudice, A. Porrino, and J. Kvasil, *Phys. Rev. C* **75**, 044312 (2007).
2. J.G. Hirsch, P. Hess, and O. Civitarese, *Phys. Rev. C* **54**, 1976 (1996).

Complex configuration effects on properties of pygmy resonance

N. N. Arsenyev*, A. P. Severyukhin*, V. V. Voronov* and Nguyen Van Giai†

*Laboratory of Theoretical Physics, JINR Dubna, 141980 Dubna, Moscow region, Russia
†Institut de Physique Nucléaire, CNRS-IN2P3, Université Paris-Sud, F-91406 Orsay Cedex, France

Abstract. Starting from the Skyrme interaction SLy4 we study the effects of phonon-phonon coupling (PPC) on the low-energy electric dipole response in $^{130-134}$Sn. Our calculations are performed within the finite-rank separable approximation, which enables one to perform quasiparticle random phase approximation calculations in very large two-quasiparticle configuration spaces. It is shown that the pygmy dipole resonance properties are correlated with the neutron skin thickness. The PPC effect gives a considerable contribution to the low-lying $E1$ strength.

Keywords: QRPA, Pygmy resonance, Nuclear skin
PACS: 21.60.Jz; 27.60.+j

INTRODUCTION

Using radioactive beams to explore nuclei far from the β-stability line has sparked intensive experimental and theoretical studies of neutron-rich nuclei during recent years [1, 2]. In addition to this much attention has been devoted to effects of varying the ratio of proton Z and neutron N numbers on different nuclear structure characteristics as nuclei deviate from their valley of β-stability. One of the phenomena associated with the change in N/Z ratios is the pygmy dipole resonance (PDR). The PDR leads to the enhancement of dipole strength below the region of the usual giant dipole resonance (GDR). The structure and dynamics of the PDR is one of the hot topics in nuclear physics. There are two major reasons in the case of the PDR. There is a special structure of the PDR which appears as a new collective motion in neutron-rich nuclei [2]. The other reason is the role of the PDR in nucleosynthesis. The PDR also induces noticeable effects on (γ,n) cross section and on the r-process [3].

The quasiparticle random phase approximation (QRPA) with a self-consistent mean-field derived from Skyrme energy density functionals (EDF) is one of the most successful methods for studying the low-energy dipole strength, see e.g., [4, 5, 6, 7, 8]. Such an approach describes the properties of the low-lying states less accurately than more phenomenological ones, but the results are in a reasonable agreement with experimental data. On the other hand, due to the anharmonicity of vibrations there is a coupling between one-phonon and more complex states [9, 10]. The main difficulty is that the complexity of calculations beyond standard QRPA increases rapidly with the size of the configuration space, so that one has to work within limited spaces. Using a finite-rank separable approximation (FRSA) [11, 12, 13, 14] for the residual interaction resulting

from Skyrme forces one can overcome this difficulty. Alternative schemes to factorize the particle-hole interaction have also been considered in Refs. [15, 16]. The so-called FRSA was thus used to study the electric low-energy excitations and giant resonances within and beyond the QRPA [13, 14, 17, 18]. In particular, we applied the FRSA approach for the PDR strength distribution [7, 19, 20]. The nuclei near the neutron magic number N=82 are quite suitable for studying the dependence of the PDR on neutron excess. In the present report we analyze the effects of the phonon-phonon coupling (PPC) on the $E1$ response for $^{130-134}$Sn, focusing on the emergence and the properties of the PDR. Properties of the PDR are investigated in terms of their relation with the neutron skin thickness.

BRIEF OUTLINE OF THE METHOD

The FRSA approach has been discussed in detail in Refs. [11, 14] and it is presented here briefly for completeness. The Hartree–Fock-BCS (HF-BSC) calculations are performed by using the SLy4 [21] EDF in the particle-hole (p-h) channel and a density-dependent zero-range interaction in the particle-particle (p-p) channel. This parametrization was proposed for describing isotopic properties of nuclei from the stability line to the drip lines. Spherical symmetry is assumed for the ground states. The continuous part of the single-particle spectrum is discretized by diagonalizing the HF hamiltonian in a harmonic oscillator basis. The strength of the surface-peaked zero-range pairing force is taken equal to -940 MeV·fm^3 in connection with the soft cutoff at 10 MeV above the Fermi energy as introduced in Ref. [14]. This value of the pairing strength is fitted to reproduce the experimental proton and neutron pairing energies of near nucleus ^{132}Sn.

The residual interaction in the p-h channel $V_{\rm res}^{\rm ph}$ and in the p-p channel $V_{\rm res}^{\rm pp}$ can be obtained as the second derivative of the energy density functional with respect to the particle density and the pair density, accordingly. Following Ref. [11] we simplify $V_{\rm res}^{\rm ph}$ by approximating it by its Landau–Migdal form. Moreover, we neglect the l=1 Landau parameters (Landau parameters with $l>1$ are equal to zero in the case of Skyrme interactions). The Landau parameters F_0, G_0, $F_0^{'}$, $G_0^{'}$ expressed in terms of the Skyrme force parameters depend on the Fermi momentum $k_{\rm F}$ for the nuclear matter [22]. In this work we study only normal parity states and one can neglect the spin-spin terms since they play a minor role [12]. The two-body Coulomb and spin-orbit residual interactions are also dropped.

We take into account the coupling between the one- and two-phonon components in the wave functions of excited states. Thus, in the simplest case one can write the wave functions of excited states as [9, 10]

$$\Psi_\nu(JM)=\left(\sum_i R_i(J\nu)Q^+_{JMi}+\sum_{\lambda_1 i_1\lambda_2 i_2} P^{\lambda_1 i_1}_{\lambda_2 i_2}(J\nu)\left[Q^+_{\lambda_1\mu_1 i_1}Q^+_{\lambda_2\mu_2 i_2}\right]_{JM}\right)|0\rangle\,, \qquad (1)$$

where $\mid 0\rangle$ is the phonon vacuum, $Q^+_{\lambda\mu i}$ is the phonon creation operator and ν labels the excited states. The coefficients $R_i(J\nu)$, $P^{\lambda_1 i_1}_{\lambda_2 i_2}(J\nu)$ and energies of the excited states E_ν are determined from the variational principle which leads to a set of linear equations [13].

The equations have the same form as in the quasiparticle-phonon model (QPM) [9, 10], but the single-particle spectrum and the parameters of the residual interaction are obtained from the chosen Skyrme forces without any further adjustments. We take into account all two-phonon terms that are constructed from the phonons with multipolarities $\lambda \leq 5$ [7, 19, 20]. All dipole excitations with energies below 35 MeV and 15 most collective phonons of the other multipolarities are included in the wave function (1). In addition, we have checked that extending the configurational space plays a minor role in our calculations.

RESULTS AND DISCUSSION

As the first step in the present analysis, we pay special attention to the neutron skin thickness. The simple hydrodynamical picture of the PDR [23] is a collective oscillation of neutron skin against the core part, from which the correlation between skin thickness and PDR is expected. The neutron skin thickness $\Delta R_{\rm np}$ is defined by the difference of root-mean-square radii of neutrons and protons, as

$$\Delta R_{\rm np} = \sqrt{\langle r^2 \rangle_{\rm n}} - \sqrt{\langle r^2 \rangle_{\rm p}}. \tag{2}$$

In Fig. 1, we show the neutron skin thickness of Sn isotopes as a function of neutron number. The proton-neutron root-mean-square differences become larger when the number of the neutrons is increased. As seen in Fig. 1 from ^{120}Sn to ^{132}Sn the neutron skin thickness is accompanied by a 7% increase since there is the occupation of the $1h_{11/2}$ intruder orbit in the neutron subsystem. A 13% increase of $\Delta R_{\rm np}$ is found at $^{132}\mathrm{Sn} \rightarrow {}^{134}$Sn. For ^{132}Sn, an extremely thick neutron skin is building up leading to a sudden jump in the neutron root-mean-square radii (the neutron $2f_{7/2}$ subshells become populated). Thus, the increase is directly related to the shell structure in the heavy tin isotopes. The same evolution has been obtained with other the Skyrme EDF [24, 25]. The available experimental data [26, 27, 28] are reasonably well reproduced.

Next, let us examine the correlation between the PDR and the neutron skin thickness $\Delta R_{\rm np}$ in $^{130-134}$Sn. Obviously, the crucial point of such an investigation is the determination of the energy region of the GDR. To quantify the low-lying $E1$ strength in a systematic analysis, we use the summed energy-weighted $E1$ strengths in the low-energy region below 11 MeV [7, 20]. The ratio of this to the classical Thomas–Reiche–Kuhn (TRK) sum rule

$$f_{\rm PDR} = \frac{\sum\limits_{k}^{E_k \leq 11\ \mathrm{MeV}} E_k \cdot B(E1; 0^+_{g.st.} \rightarrow 1^-_k)}{14.8 \cdot NZ/A\ e^2\mathrm{fm}^2 \cdot \mathrm{MeV}}, \tag{3}$$

is referred to as "PDR fraction", hereafter.

Figure 2 shows the PDR fraction as a function of the neutron skin thickness $\Delta R_{\rm np}$. The QRPA results indicate that the PDR strength is related with the neutron skin thickness. The closure of the neutron subshell $1h_{11/2}$ leads to a reduction of the strength of the PDR. In addition, the GDR becomes more collective with increasing neutron number,

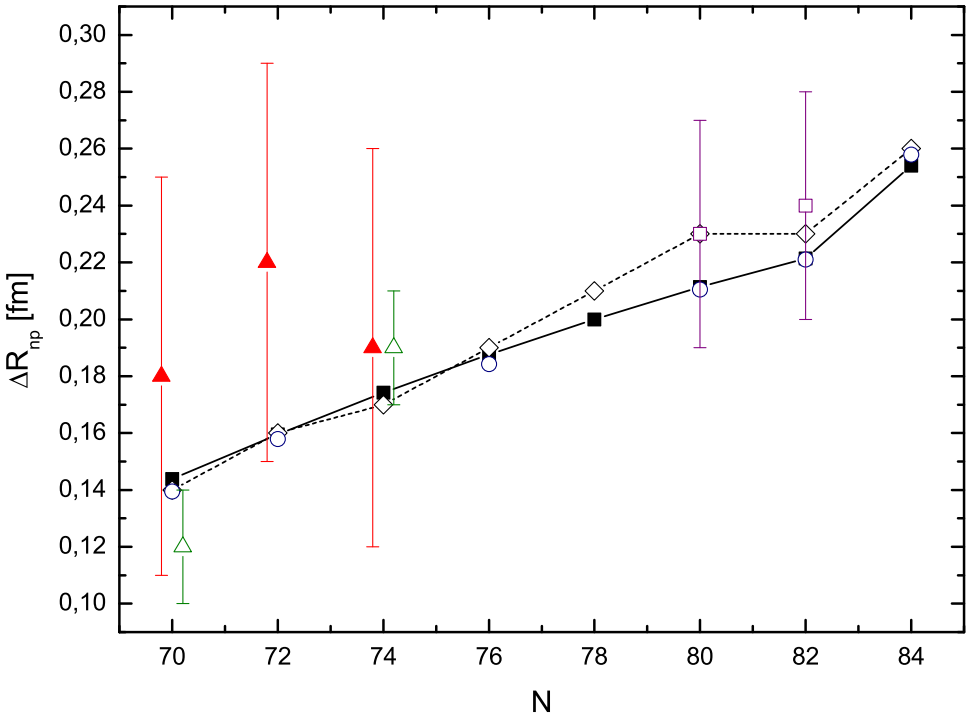

FIGURE 1. The neutron skin thickness $\Delta R_{\rm np}$ of the tin isotopes calculated within the HF-BCS with the SLy4 EDF (filled square symbols). Experimental data of the neutron skin thickness are derived from charge-exchange reactions [26] (filled triangle symbols), from the antiprotonic x-ray data [27] (open triangle symbols) and from observed pygmy dipole strength [28] (open square symbols).

the fraction of the energy-weighted sum rule (EWSR) contained in the PDR actually goes down as the neutron skin continues to increase. In contrast, there is an abrupt jump of the PDR fraction between N=82 and 84. This seems to be caused by the occupation of the neutron $2f_{7/2}$ subshell. In the Sn isotopic chain the local minima in the PDR fraction are obtained at N=82 due to the neutron-shell closure. Thus, the QRPA results indicate the shell-closure impact on the PDR strength. A similar behavior for Sn isotopes was observed in other self-consistent calculations with the Skyrme EDF [25].

Let us now discuss the extension of the space to one and two-phonon configurations in the FRSA model. As can be seen from Fig. 2, we can see that the two-phonon contribution is noticeable for the PDR fraction and its quantitative value is clearly increased. There is the redistribution of the $E1$ strength and a shift toward lower energies; see, e.g., Refs. [7, 19]. In particular, for ^{130}Sn, the QRPA and the calculations with the inclusion of the two-phonon terms give a PDR fraction of about 3.0% and 4.0%, respectively. The experimental data suggest the value of 7±3% [29]. For ^{132}Sn, the experimental data give an integrated strength of the PDR of about 4±3% of the TRK sum rule [29], while the calculations with and without the two-phonon configurations lead to 3.0% and 2.7%, respectively. Our calculations [19] show that the inclusion of the two-phonon terms results in an increase of the pygmy $E1$-resonance width from 1.2 to 2.0 MeV. An upper limit of experimental PDR width is 2.5 MeV [29]. Thus, we find that the impact of the phonon-phonon coupling on the correlation between the neutron skin

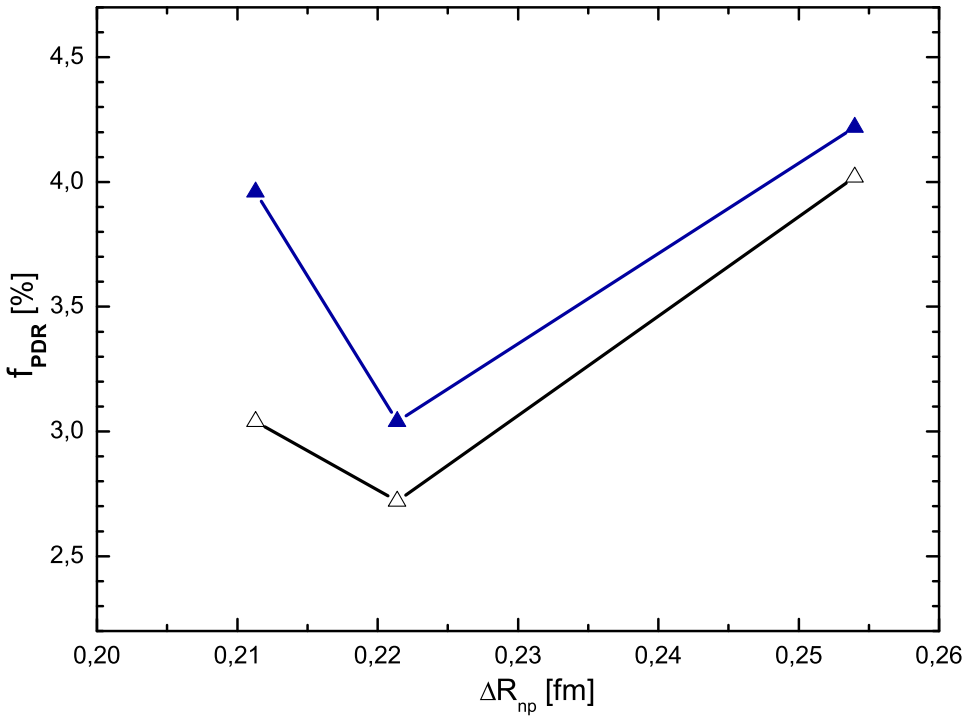

FIGURE 2. The PDR fraction of $^{130-134}$Sn isotopes as a function of the neutron skin thickness. Open and filled triangle symbols indicate the QRPA results and the calculation taking into account the two-phonon configurations, respectively.

thickness and the PDR strength.

CONCLUSION AND OUTLOOK

Starting from the Skyrme mean-field calculations, the properties of the electric dipole strength in neutron-rich Sn isotopes are studied by taking into account the coupling between one- and two-phonons terms in the wave functions of excited states. The finite-rank separable approach for the QRPA calculations enables one to reduce remarkably the dimensions of the matrices that must be inverted to perform nuclear structure calculations in very large configuration spaces.

Neutron excess effects on the PDR excitation energies and transition strengths have been investigated for the even-even nuclei $^{130-134}$Sn. We study the evolution of the PDR strength as a function of the neutron skin thickness. The strong enhancement of the PDR strengths are studied by taking into account the two-phonon configurations.

ACKNOWLEDGEMENT

N.N.A., A.P.S., and V.V.V. thank the hospitality of INP-Orsay where a part of this work was done. This work was partly supported by the IN2P3-RFBR agreement No. 16-52-

150003 and the IN2P3-JINR agreement.

REFERENCES

1. D. Savran, T. Aumann, and A. Zilges, *Prog. Part. Nucl. Phys.* **70**, 210 (2013).
2. N. Paar, D. Vretenar, E. Khan, and G. Colò, *Rep. Prog. Phys.* **70**, 691 (2007).
3. M. Arnould, S. Goriely, and K. Takahashi, *Phys. Rep.* **450**, 97 (2007).
4. D. Sarchi, P. F. Bortignon, and G. Colò, *Phys. Lett. B* **601**, 27 (2004).
5. D. Tarpanov, Ch. Stoyanov, N. V. Giai, and V. V. Voronov, *Phys. At. Nucl.* **70**, 1402 (2007).
6. A. Avdeenkov, S. Goriely, S. Kamerdzhiev, and S. Krewald *Phys. Rev. C* **83**, 064316 (2011).
7. N. N. Arsenyev, A. P. Severyukhin, V. V. Voronov, and N. V. Giai, *Eur. Phys. J. Web Conf.* **38**, 17002 (2012).
8. A. Repko, P.-G. Reinhard, V. O. Nesterenko, and J. Kvasil *Phys. Rev. C* **87**, 024305 (2013).
9. V. G. Soloviev, *Theory of atomic nuclei: quasiparticles and phonons*, Institute of Physics, Bristol and Philadelphia, 1992.
10. N. Lo Iudice, V. Yu. Ponomarev, Ch. Stoyanov, A. V. Sushkov, and V. V. Voronov, *J. Phys. G: Nucl. Part. Phys.* **39**, 043101 (2012).
11. N. V. Giai, Ch. Stoyanov, and V. V. Voronov, *Phys. Rev. C* **57**, 1204 (1998).
12. A. P. Severyukhin, Ch. Stoyanov, V. V. Voronov, and N. V. Giai, *Phys. Rev. C* **66**, 034304 (2002).
13. A. P. Severyukhin, V. V. Voronov, and N. V. Giai, *Eur. Phys. J. A* **22**, 397 (2004).
14. A. P. Severyukhin, V. V. Voronov, and N. V. Giai, *Phys. Rev. C* **77**, 024322 (2008).
15. T. Suzuki, and H. Sagawa, *Prog. Theor. Phys.* **65**, 565 (1981).
16. V. O. Nesterenko, J. Kvasil, and P.-G. Reinhard, *Phys. Rev. C* **66**, 044307 (2002).
17. A. P. Severyukhin, N. N. Arseniev, V. V. Voronov, and N. V. Giai, *Phys. At. Nucl.* **72**, 1149 (2009).
18. A. P. Severyukhin, N. N. Arsenyev, and N. Pietralla, *Phys. Rev. C* **86**, 024311 (2012).
19. N. N. Arsenyev, A. P. Severyukhin, V. V. Voronov, and N. V. Giai, *Acta Phys. Pol. B* **46**, 517 (2015).
20. N. N. Arsenyev, A. P. Severyukhin, V. V. Voronov, and N. V. Giai, *Eur. Phys. J. Web Conf.* **107**, 05006 (2016).
21. E. Chabanat, E. Bonche, E. Haensel, J. Meyer, and R. Schaeffer, *Nucl. Phys. A* **635**, 231 (1998).
22. N. V. Giai, and H. Sagawa, *Phys. Lett. B* **106**, 379 (1981).
23. Y. Suzuki, K. Ikeda, and H. Sato, *Prog. Theor. Phys.* **83**, 180 (1990).
24. F. Hofmann, and H. Lenske, *Phys. Rev. C* **57**, 2281 (1998).
25. S. Ebata, T. Nakatsukasa, and T. Inakura, *Phys. Rev. C* **90**, 024303 (2014).
26. A. Krasznahorkay, M. Fujiwara, P. van Aarle, H. Akimune, I. Daito, H. Fujimura, Y. Fujita, M. N. Harakeh, T. Inomata, J. Jänecke, S. Nakayama, A. Tamii, M. Tanaka, H. Toyokawa, W. Uijen, and M. Yosoi, *Phys. Rev. Lett.* **82**, 3216 (1999).
27. A. Trzcińska, J. Jastrzębski, P. Lubiński, F. J. Hartmann, R. Schmidt, T. von Egidy, and B. Kłos, *Phys. Rev. Lett.* **87**, 082501 (2001).
28. A. Klimkiewicz, N. Paar, P. Adrich, M. Fallot, K. Boretzky, T. Aumann, D. Cortina-Gil, U. Datta Pramanik, Th. W. Elze, H. Emling, H. Geissel, M. Hellström, K. L. Jones, J. V. Kratz, R. Kulessa, C. Nociforo, R. Palit, H. Simon, G. Surówka, K. Sümmerer, D. Vretenar, and W. Waluś (LAND Collaboration), *Phys. Rev. C* **76**, 051603(R) (2007).
29. P. Adrich, A. Klimkiewicz, M. Fallot, K. Boretzky, T. Aumann, D. Cortina-Gil, U. Datta Pramanik, Th. W. Elze, H. Emling, H. Geissel, M. Hellström, K. L. Jones, J. V. Kratz, R. Kulessa, Y. Leifels, C. Nociforo, R. Palit, H. Simon, G. Surówka, K. Sümmerer, and W. Waluś (LAND-FRS Collaboration), *Phys. Rev. Lett.* **95**, 132501 (2005).

Reorientation-effect measurements in ^{12}C

M. Kumar Raju[*,†], J. N. Orce [*,**], C. V. Mehl [*], N. Erasmus[*], T. E. Drake[‡], M. K. Djongolov[**], P. Navrátil[§], G. C. Ball[**], S. Triambak[*,†], K. J. Abrahams[*], E. H. Akakpo[*], H. Al Falou[**], R. Churchman[**], D. S. Cross[¶], P. Finlay[‖], A. B. Garnsworthy[**], P. E. Garrett[‖], G. Hackman[**], R. Kshetri[**], K. G. Leach[‖], D. L. Mavela[*], M. J. Mokgolobotho[*], C. J. Pearson[**], E. T. Rand[‖], F. Sarazin [††], S. K. L. Sjue[**], C. S. Sumithrarachchi [‖], C. E. Svensson [‖], E. R. Tardiff [**], S. J. Williams [**] and C. Y. Wu [§]

[*]*Department of Physics & Astronomy, University of the Western Cape, Bellville 7535, South Africa*
[†]*iThemba LABS, National Research Foundation, P.O. Box 722, Somerset-West 7129, South Africa*
[**]*TRIUMF, 4004 Wesbrook Mall, Vancouver, British Columbia V6T 2A3, Canada*
[‡]*Department of Physics, University of Toronto, Toronto, Ontario M5S 1A7, Canada*
[§]*Lawrence Livermore National Laboratory, Livermore, California 94550, USA*
[¶]*Department of Chemistry, Simon Fraser University, British Columbia V5A 1S6, Canada*
[‖]*Department of Physics, University of Guelph, Guelph, Ontario N1G 2W1, Canada*
[††]*Physics Department, Colorado School of Mines, Golden, Colorado 80401, USA*

Abstract. A safe Coulomb-excitation experiment was performed at TRIUMF to determine the spectroscopic quadrupole moment of the first 2^+ state, $Q_s(2_1^+)$, at 4.439 MeV in ^{12}C using the TIGRESS γ-ray array and a CD-type silicon detector setup. This is the first Coulomb-excitation particle-γ coincidence that allows an accurate determination of the $Q_s(2_1^+)$ value in ^{12}C.

Keywords: Coulomb excitation, nuclear shapes, diagonal matrix elements
PACS: 25.70.De; 23.20.Lv; 23.40.Hc; 21.60.De

INTRODUCTION

Reorientation effect (RE) in Coulomb-excitation measurements plays a vital role in nuclear structure physics as it facilitates information about the shape of even-even nuclei by determining the diagonal matrix elements $\langle 2_1^+ \,||\, \hat{E2} \,||\, 2_1^+ \rangle$, which are, in turn, proportional to the spectroscopic quadrupole moment, $Q_s(2_1^+)$ [1],

$$\begin{aligned} Q_S(2_1^+) &= \sqrt{\frac{16\pi}{5}} \frac{1}{\sqrt{2J+1}} \langle JJ20 \,|\, JJ \rangle \, \langle 2_1^+ \,||\, E2 \,||\, 2_1^+ \rangle \\ &= 0.75793 \, \langle 2_1^+ \,||\, E2 \,||\, 2_1^+ \rangle. \end{aligned} \quad (1)$$

Safe Coulomb-excitation measurements [2], i.e., when the bombarding energy is well below the Coulomb barrier and nuclear excitations can be considered negligible, selectively populate collective states with cross sections that are a direct measure of matrix elements. The RE is a time-dependent second-order perturbation effect in Coulomb-excitation theory which causes the hyperfine splitting of magnetic substates and influ-

ence their population according to the sign and magnitude of $Q_s(2_1^+)$ [3],

$$\sigma_{E2} = \sigma_R \, k_1(\vartheta_{c.m.}, \xi) B(E2) \left(1 + k_2(\vartheta_{c.m.}, \xi) Q_S(2_1^+)\right), \quad (2)$$

where $k_1(\vartheta_{c.m.}, \xi)$ and $k_2(\vartheta_{c.m.}, \xi)$ contain the dependence of σ_{E2} on the trajectory of the projectile. A positive sign of $Q_s(2_1^+)$ indicates an oblate shape in the intrinsic frame whereas a negative sign of it represents a prolate shape.

The ^{12}C nucleus with $Z = N = 6$ is expected to have a spherical shape in its ground state based on the shell model configurations. However, ^{12}C has long been predicted to have α cluster configurations composed of three α particles built on the 0_2^+ excited state. This was confirmed with the identification of the *Hoyle state* (0_2^+) [4] at 7.645 MeV which has been interpreted as arising from the coupling of three α cluster structures which account for the observed ^{12}C abundance in nature. This state has considerable mixing with the 0_1^+ ground state inferred from the reported electric monopole transition strength ($10^3 \times \rho^2$(E0) = 500(81)) from electron scattering experiments [5], and γ decays to it through the 2_1^+ excited state. Theoretically, the structure of ^{12}C has been investigated in number of studies such as isomorphic shell model, rotational models, and the α-particle model [4, 6, 7, 8], whose predictions are inconsistent with each other and suggest the ground state of ^{12}C to have a deformation ranging from spherical to strongly oblate. Experimentally, various scattering measurements [10] have been performed to estimate the quadrupole deformation (β_2) such as (e, e'), (p, p'), (α, α'), although most of these experiments are insensitive to the sign of deformation. These studies reported the β_2 values spanning from $\approx +0.3$ to -1.37 which does not show conclusive evidence for the oblate ground state deformation in ^{12}C predicted in α cluster models.

A Coulomb excitation RE measurement was performed by *Vermeer et al.,* in 1983 [9] to estimate the $Q_s(2_1^+)$ value in ^{12}C. A position sensitive multi-element proportional counter and a magnetic spectrometer were used to analyse the scattered particles and the cross sections were estimated from the particle spectra. This study reported $Q_s(2_1^+)$ = +6(3) efm^2 supporting the oblate ground state deformation in ^{12}C. However, the reported value has a large uncertainty which was due to the poor resolution of the particle detector (see Fig. 1), limited angular resolution of the spectrometer and the contaminations arising from the overlap of inelastic peaks of ^{208}Pb with the ^{12}C. Further, the uncertainty in $Q_s(2_1^+)$ was also due the assumed nuclear polarizability parameter (κ =1) based on the shell model calculations [11]. Thus the determination of precise value of $Q_s(2_1^+)$ in ^{12}C is in order to understand the predicted collectivity in ^{12}C and provide a stringent test of theoretical models. In this proceedings, we are presenting the results of a first particle-γ coincidence data of ^{12}C, aimed to determine the $Q_s(2_1^+)$ value through the RE.

EXPERIMENTAL DETAILS

A safe Coulomb excitation measurement was carried out at the TRIUMF/ISAC II facility [12] in Vancouver, Canada. The first 2^+ state at 4.439 MeV in ^{12}C was excited through the inelastic scattering of ^{12}C beams of 4.97 MeV/u bombarded on a 3 mg/cm^2

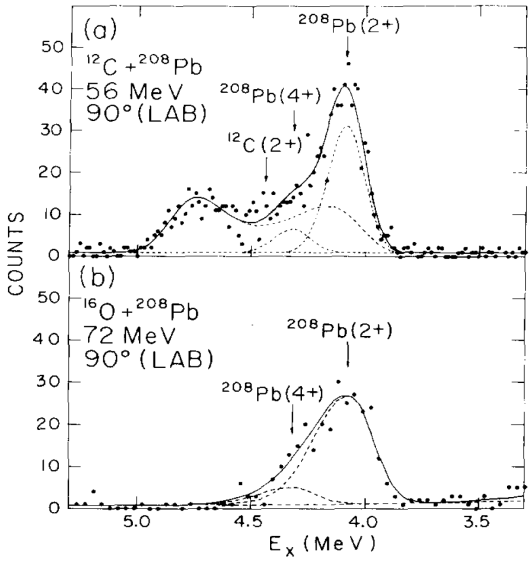

FIGURE 1. Particle spectra showed in Ref. [9] detected using a proportional counter for the reactions with (a) ^{12}C on ^{208}Pb at 56 MeV, with the minimum distance between two nuclear surfaces, S(ϑ) = 5.6 fm, and (b) ^{16}O on ^{208}Pb at 72 MeV and S(ϑ) = 6.0 fm

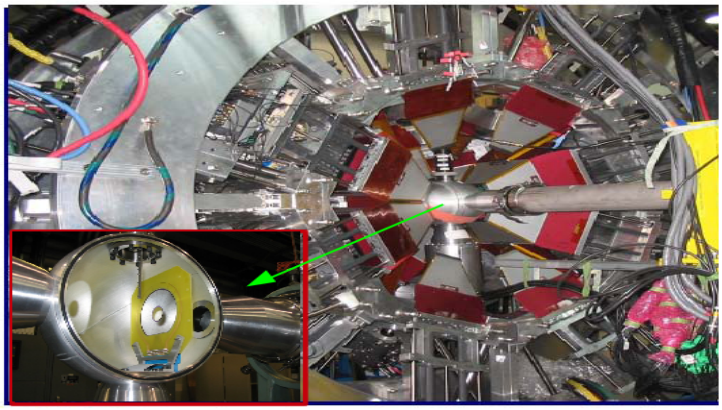

FIGURE 2. The TIGRESS γ-ray array utilised for these experiments. The inset shows the CD-type Silicon detector positioned inside the BAMBINO chamber.

thick ^{194}Pt target. The de-excited γ rays were detected using the highly-efficient and segmented TIGRESS HPGe detector array [13]. During this experiment, this array consisted of 8 TIGRESS clover type HPGe detectors positioned at 15.2 cm from the target and covering $\approx$ 15% of 4π. Each of the TIGRESS detector is 32-fold segmented which output 32 signals from inner core contacts and 32 signal from outer contacts provide information about $\gamma-$ray interactions within the detector, useful for precise Doppler corrections.

Scattered ^{12}C ions were detected in coincidence with γ rays using annular double-sided CD-type silicon detector namely S2 which was placed at 19.4 mm down stream

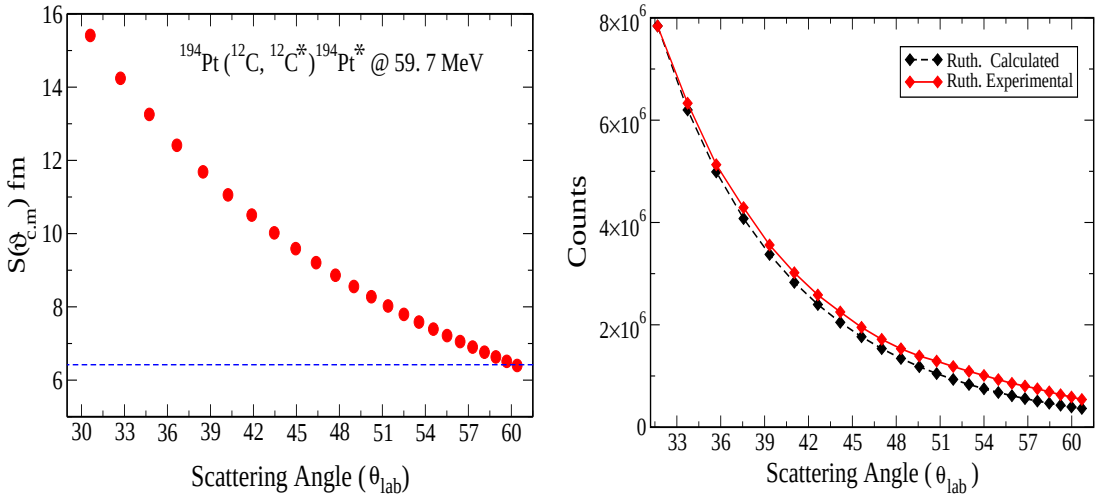

FIGURE 3. Shows (left) the distance between two nuclear surfaces [S($\vartheta_{c.m.}$)] as a function scattering angle (θ) in laboratory frame at a beam energy of 59.7 MeV. Right panel shows the calculated classical Rutherford cross sections normalized with experimental yields and displayed as a function of scattering angle (θ) in laboratory frame.

from the target center and perpendicular to the beam axis. One side of the S2 consists of 48 rings which output 24 electronic signals correspond to each 2 rings, covered laboratory polar angles from 30.7° to 61.0° and the other side of the S2 comprises 16 sectors. The data from individual rings and sectors are important for angular distribution measurements and Doppler corrections, respectively. A picture of the experimental setup with the TIGRESS and S2 detectors is shown in Fig. 2. The ^{12}C beam energy was chosen based on the calculations satisfying the condition of minimum distance between two nuclear surfaces S$(\vartheta_{c.m.})_{min} \approx 6.5$ fm suggested in systematic RE experiments of light nuclei [9, 14, 15, 16] and was calculated using an expression given by Spear [14]

$$S(\vartheta_{c.m.}) = \frac{0.72 Z_1 Z_2}{E}(1+\frac{A_1}{A_2})[1+cosec(\frac{1}{2}\vartheta_{c.m.})] - 1.25(A_1^{1/3}+A_2^{1/3}) \text{ fm} \qquad (3)$$

Figure 3 (right) shows the variation of S$(\vartheta_{c.m.})$ with respect to the scattering angle in the laboratory frame at beam energy of 59.7 MeV for ^{194}Pt(^{12}C, ^{12}C*)^{194}Pt* reaction which indicate S$(\vartheta_{c.m.})$ ranging from $\approx$ 6.5 fm at 60.7° to 15.4 fm at 31.7°, hence satisfying Spear's prescription[14] for all the scattering angle range of the silicon detector, therefore nuclear interference considered negligible. The left panel of Fig. 3 shows the calculated integrated Rutherford cross sections normalised to the experimental integrated Rutherford scattering yields as a function of scattering angle in the laboratory frame, which depict that both the curves follow a classical Rutherford scattering trend supporting the negligible nuclear interference. The Sommerfeld parameter for the present reaction system is $\eta \approx 34$ which validates the semiclassical approximation ($\eta >> 1$).

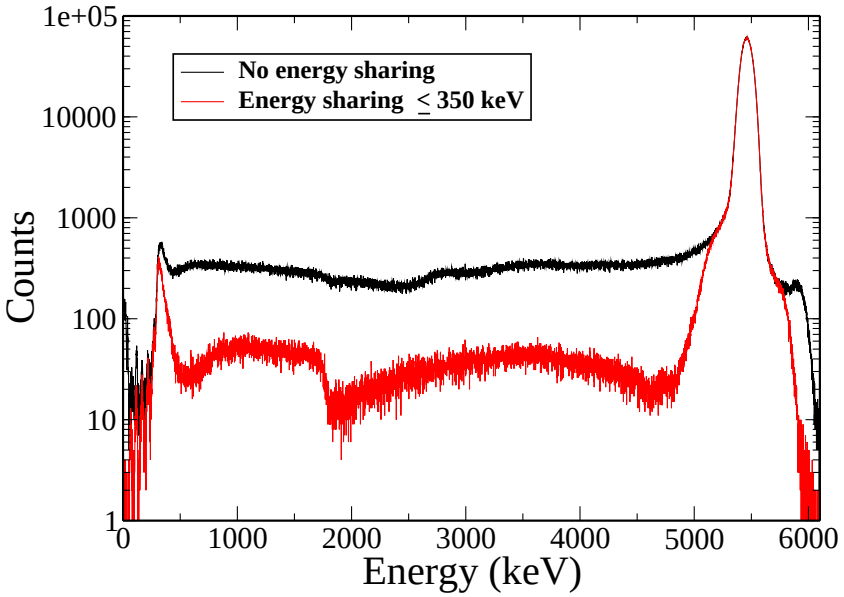

FIGURE 4. Particle energy spectra at 31.7° correspond to the inner most ring of S2 detector generated employing particle-γ coincidence, energy sharing and timing conditions. The spectrum in red (black) color indicates the particle spectrum with (without) energy sharing condition of 350 keV.

DATA ANALYSIS AND RESULTS

Data have been collected online using a high speed (100 MHz) digital data acquisition system. The data was sorted offline using the *sortshell* program [17] and further analysed with MIDAS [18] and RADWARE [19] packages. The energy calibration and relative photopeak efficiency of the TIGRESS array were obtained using ^{152}Eu and ^{56}Co standard radioactive sources. The particle spectra were calibrated using a triple α source (^{239}Pu, ^{241}Am and ^{244}Cm) at low-energies including the energy losses in the 0.3 micron thick Al coating on the silicon strips together with kinematic considerations. GEANT4 simulations of elastic peaks were used at higher energies. Most of the radioactive background γ rays from the experimental area were suppressed from the collected data by employing particle $-\gamma$ coincidence condition such that an event was stored in list-mode for each hit in a TIGRESS detector and a hit in both ring and sector of the silicon detector. Further, random coincidences were minimised keeping a prompt time window of 100 *ns*. The de-excited γ rays from residual nuclei affected by large Doppler shifts due to relatively high velocity of projectile which causes shift in the $\gamma-$ray energy. These Doppler shifts have been corrected using the expression 4

$$E_\gamma = E_{\gamma_0} \frac{\sqrt{1-\beta^2}}{1-\beta cos(\theta_{particle-\gamma})} \tag{4}$$

where E_γ is the Doppler shifted $\gamma-$ray energy relative to the $\gamma-$ray transition energy E_{γ_0} and $\cos(\theta_{particle-\gamma})$ is the angle between direction of moving projectile residue and photon emission. In addition to the Doppler correction and particle-γ coincidence conditions, a particle-energy sharing condition, $\mid E_{ring} - E_{sector} \mid \leq 350$ keV was applied

to clean the background in both the particle and $\gamma-$ray spectrum, which enables a better selection of the inelastic particle gates. The 350-keV restriction was chosen by making sure that the 4439 keV peak counts in the $\gamma-$ ray spectrum were conserved. The effect of the energy sharing condition is shown in Fig. 4, where the particle spectrum with 350 keV energy sharing condition clearly shows the reduction in background which enables a better selection of inelastic particle gates. Fig. 5 is a representative Doppler corrected sum $\gamma-$ray spectrum obtained from the TIGRESS array in coincidence with particles detected in S2 detector including the energy sharing condition and inelastic particle gates. Inset of this figure shows the non-Doppler corrected spectrum. It is evident from the spectrum that the 4439-keV γ energy from the first 2^+ state in ^{12}C is visible with reasonable yields of approximately 1300(50) counts and also the 328 keV peak of 2^+ state in ^{194}Pt. These experimental yields along with the known information of levels in ^{12}C and ^{194}Pt will be utilised to extract the matrix elements $\langle 2_1^+ \,||\, E2 \,||\, 0_1^+ \rangle$ and $\langle 2_1^+ \,||\, E2 \,||\, 2_1^+ \rangle$ in ^{12}C using normalisation procedure. The experimental ratio of the intensities of 4439 keV γ energy in ^{12}C and 328 keV in ^{194}Pt can be calculated using an expression

$$\frac{\sigma_{E2}^T W(\vartheta)^T}{\sigma_{E2}^P W(\vartheta)^P} = \frac{N_\gamma^T}{N_\gamma^P}\frac{\varepsilon_\gamma^P}{\varepsilon_\gamma^T} = \frac{I_\gamma^T}{I_\gamma^P} \tag{5}$$

where I_γ^T (328 keV) and I_γ^P (4439 keV) are the intensities, ε_γ^T (328 keV) = 0.0698(10) and ε_γ^P (4439 keV) = 0.0186(4) are the absolute γ-ray efficiencies calculated for the TIGRESS array with the known radioactive sources. The experimental ratio of yields will be normalised with the theoretical yields to extract the matrix elements which will be calculated using a semiclassical coupled channel Coulomb excitation code GOSIA [20]. This code calculate the integrated yields of γ peaks for the defined scattering angle range (31.7° to 60.7° in the present work) of particle detector by inputting the known information such as lifetimes of levels, transition probabilities, beam energy losses in target and detector material, absorption coefficients, detector geometry etc. The experimental ratio (eq. 5) will be normalised with the calculated integrated yields from GOSIA by fixing the matrix elements $\langle 2_1^+ \,||\, E2 \,||\, 0_1^+ \rangle$ and $\langle 2_1^+ \,||\, E2 \,||\, 2_1^+ \rangle$. Further the Coulomb excitation curve [21] will be generated by varying the $\langle 2_1^+ \,||\, E2 \,||\, 0_1^+ \rangle$ value for a fixed $\langle 2_1^+ \,||\, E2 \,||\, 2_1^+ \rangle$ value such that the experimental and theoretical yields are normalised. This Coulomb excitation curve overlapped with the well known B(E2) value in ^{12}C provide information about the sign and magnitude of spectroscopic quadrupole moment $Q_s(2_1^+)$ of ^{12}C.

In Coulomb excitation theory, the other second order effect such as nuclear polarizability [22] due to virtual electric dipole excitations of states near Giant dipole resonance (GDR) region also influence the sign and magnitude of $Q_s(2_1^+)$. The GOSIA code take this effect into account by considering the nuclear polarizability parameter $[\kappa(2_1^+)] = 1$. However, the value of $\kappa(2_1^+)$ was shown to be significantly different from a value of 1 for the light nuclei in recent studies based on shell model (SM) calculations [23, 24, 25] which have been successful in reproducing the κ parameters for p shell nuclei. In this work we have performed *NCSM* calculations considering large model space and using *CD-Bonn 2000 2N* potential to estimate the value of polarizability parameter (κ) for

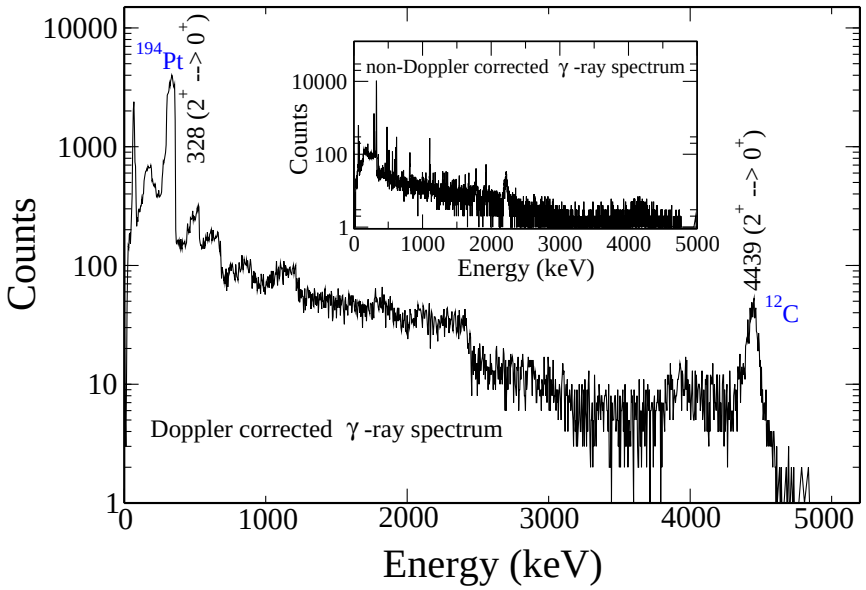

FIGURE 5. A representative Doppler corrected sum γ-ray spectrum generated employing the coincidence and particle energy sharing conditions which illustrate the 328 keV and 4439 keV γ transitions from 2_1^+ state in ^{194}Pt and ^{12}C respectively. The inset shows the non-Doppler corrected spectrum.

2_1^+ state in ^{12}C. The value of κ will serve as a input to GOSIA code to account the 2nd order nuclear polarizability effect and enable accurate estimation of nuclear matrix elements. The full details of the experimental results and *NCSM* calculations will be communicated elsewhere.

SUMMARY AND OUTLOOK

A particle-γ coincidence experiment was performed to determined the spectroscopic quadrupole moment of 2_1^+ state at 4.439 MeV in ^{12}C through Coulomb excitation of ^{12}C beams at 59.7 MeV impinging on a 3 mg/cm^2 thick ^{194}Pt target. The deexcited γ-rays have been detected using the highly efficient TIGRESS detector array and scattered particles were detected with annular double sided silicon detector (S2). The data have been sorted offline employing the conditions of particle-γ coincidence, particle energy sharing and Doppler corrections. The resultant sum γ-ray spectrum corresponds to the 8 TIGRESS clovers shows evidence for the 4.439 MeV γ-ray from first 2^+ state in ^{12}C with reasonable yields. This is the first γ-particle coincidence data obtained for ^{12}C through Coulomb excitation. Further, the no-core-shell-model (NCSM) calculations were performed to estimate the polarizabilty parameter, $[\kappa(2_1^+)]$. The experimental yields, polarizabilty parameter, $\kappa(2_1^+)$ and known information of levels in ^{12}C and ^{194}Pt will be utilised to extract the transitional and diagonal matrix elements of 2_1^+ sate in ^{12}C by normalisation method and GOSIA coupled channel Coulomb excitation code.

ACKNOWLEDGEMENT

We acknowledge the accelerator group at TRIUMF for their excellent support during the experiment. The author (M.K.R) acknowledge financial support from the South African National Research Foundation (NRF) and iThemba LABS for Post-doctoral grant No. 88361 and the NRF grant No. 93500.

REFERENCES

1. K. Alder and A. Winther, *Electromagnetic Excitation*(North-Holland, Amsterdam, 1975).
2. D. Cline, *Ann. Rev. Nucl. Part. Sci.* **36**, 683 (1986).
3. G. Breit, R. L. Gluckstern, and J. E. Russell, *Phys. Rev.* **103**, 727 (1956).
4. M. Freer and H. O. U. Fynbo, *Prog. in Part. Nucl. Phys.* **78**, 1-23 (2014).
5. T. Kibédi, R.H. Spear *Atomic Data and Nuclear Data Tables* **89**, 77-100 (2005).
6. O. Karban *et al., Nucl. Phys. A* **292**, 1 (1977).
7. W. J. Thompson *et al., Phys. Lett. B* **67**, 151 (1977).
8. D. M. Brink, *J. Phys. Conf. Ser.* **111**, 012001 (2008).
9. W. J. Vermeer *et al., Phys. Lett. B* **122**, 23 (1983).
10. J. P. Svenne and R. S. Mackinthosh, *Phys. Rev. C* **18**, 983 (1978).
11. F. C. Barker, *Aust. J. Phys.* **35**, 301 (1982).
12. J. Lassen e*et al., Hyperfine Interact.* **162**, 69 (2005).
13. C. E. Svensson *et al., J. Phys. G.* **31**, S1663 (2005).
14. R. H. Spear, *Phys. Rep.* **73**, 369 (1981).
15. D. L. Disdier *et al., Phys. Rev. Lett.* **27**, 1391 (1971).
16. W. J. Vermeer *et al., Aust. J. Phys.* **35**, 283 (1982).
17. C. J. Pearson, *Private communication*.
18. K. Olchanski S. Ritt, P. Amaudruz, *Maximum Integration Data Acquisition System*, http://midas.psi.ch
19. D. C. Radford, *Nucl. Instrum. Methods A* **361**, 297 (1995).
20. T. Czosnyka, D. Cline, and C.Y. Wu, *Bull. Am. Phys. Soc.* **28**, 745 (1983).
21. J. N. Orce *et al., Phys. Rev. C* **86**, 041303 (R) (2012).
22. J. N. Orce *http://arxiv.org/pdf/1510.04087v2.pdf*
23. O. H¨ausser *et al., Nucl. Phys. A* **212**, 613 (1973).
24. F. C. Barker, *Aust. J. Phys.* **35**, 291 (1982).
25. P. Navrátil *et al., J. Phys. G.* **36**, 083101 (2009).

SESSION

"NUCLEAR REACTIONS (FISSION AND CLUSTERING)"

Conveners: D. Kamanin, S. Mullins

Ternary clusterization of heavy nuclear systems

A.V. Karpov* and A. Adel†

*Flerov Laboratory of Nuclear Reactions, JINR, Dubna, Russia;
Dubna State University, Dubna, Russia
†Physics Department, Faculty of Science, Cairo University, Giza, Egypt

Abstract. Since more than 40 years of theoretical and experimental studies of true ternary fission, we are still quite far from its understanding. The true ternary fission channel, being strongly suppressed by the macroscopic properties of the potential energy, may however be present with a significant probability owing to shell effects. The three-center shell model of deformed nucleus is developed in this paper. The model can be applied for analysis of any ternary as well as binary fission channels. The properties of the potential energy landscape of ^{252}Cf are discussed. The potential energy structures are compared with the experimental observations. We found that the potential energy has pronounced valleys favorable for ternary fission with formation of doubly magic tin as one of the fragments and two other lighter fragments. The positions of the found fission valleys are in good agreement with the experimental data.

Keywords: true ternary fission, three-center shell model, shell effects
PACS: 24.10.-i, 25.85.-w, 25.85.Ca

MOTIVATION

In spite of the fact that a lot of studies of the fission process were performed since its discovery in 1938, the fission physics still offers exciting topics to be explored and understood. One of them is the process of ternary fission. Here one should distinguish two different processes, namely "ternary fission" and "true ternary fission". The ternary fission is the process of formation of a light charged particle (mainly, alpha particles) accompanying fission and emitted with the largest probability in the perpendicular direction to the fission axis. The probability of this process decreases exponentially with the increase of the fragment mass. This supports the idea that the third fragment appears as a fluctuation in the neck region. Nearly complete information on this process can be found in Refs. [1, 2, 3] (see also Refs. [4, 5] for the recent experimental studies).

The term "true ternary fission" is used for a simultaneous decay of a heavy nucleus into three fragments of comparable masses [1]. The true ternary fission is considered as a process similar to the binary fission connected with large-scale evolution of the nuclear shape from the compact shape of the initial nucleus through formation of two necks and final division of a composite system into three fragments.

The true ternary fission of atomic nuclei (below we omit the word "true") has a long history of theoretical and experimental studies. Early theoretical considerations based on the liquid drop model (LDM) [6] showed that for heavy nuclei ternary fission produces a larger total energy release in comparison to binary fission, but the actual possibility of ternary fission is determined, in fact, not by the total energy release, but by the barrier properties. It was found that the LDM ternary fission barriers for oblate (triangular)

deformations are much higher compared to the barriers of prolate configurations [7], and it seems that the oblate ternary fission may be excluded from consideration. However further study of this problem within the more sophisticated three-center shell model [8] showed that the shell effects may significantly reduce the ternary fission barriers even for oblate deformations of very heavy nuclei. Recently [9] the potential energy as well as the tunneling probability were calculated within the three-center shell model for the isotopes of the 120 element. The calculations were performed assuming equal masses of all three fragments (division into three zirconium isotopes). The authors conclude that such process is very improbable due to the high fission barrier.

The experimental information on the true ternary fission is rather limited. First study of the true ternary fission was done by M.L. Muga with colleagues [10] for spontaneous fission of ^{252}Cf and thermal neutron-induced fission of few uranium isotopes. These experiments showed that the ratio of ternary events to the binary ones is about 10^{-6}. The next study was performed by P. Schall et al. [11] for symmetric ternary spontaneous fission of ^{252}Cf. The deduced upper limit for the symmetric ternary to binary fission ratio is 10^{-8} s. The extensive search for a ternary decay channel was performed by the group of D. Kamanin (see Ref. [12] and references therein) for the spontaneous fission of ^{252}Cf as well as for thermal neutron-induced fission of ^{235}U. The process was named "collinear cluster tri-partition" because the decay products fly apart almost collinearly. It was found that the true ternary fission is a rather probable channel with the yield ratio to the binary one of about 10^{-4}. The increased ternary yield is detected in the spontaneous fission of ^{252}Cf for the following combinations with formation of magic or semimagic clusters: Sn+Ge(or Ni)+S(or Ca). Another dedicated experiment has shown that the ternary fission with formation of ^{68}Ni or ^{72}Ni as one of the fragments has an increased yield.

Today it becomes possible to study experimentally the properties and dynamics of formation and decay of superheavy nuclei, for which the true ternary fission could be rather probable. It is well known that for superheavy nuclei the LDM fission barriers are rather low (or vanish at all) and the shell correction to the total deformation energy is very important. First estimations of the binary and prolate ternary fission barriers of the superheavy nucleus ^{298}114, made in Ref. [13] with the approximately calculated shell corrections, demonstrated their closeness within 10%. This result was later confirmed in [14] within the temperature-dependent LDM. The possibility of symmetric true ternary fission and quasifission (with equal outer fragments) was considered recently in Ref. [15] based on the potential energy calculations. It was found that the ternary fission is quite possible for superheavy nuclei, and it is connected with three-body clusterization with the formation of two tin-like fragments and a heavy third fragment in between. For example, in the case of ^{64}Ni+^{238}U reaction one may expect the ternary exit channel like ^{132}Sn+^{38}Ca+^{132}Sn with three magic clusters. Even larger shell effects are predicted for the giant nuclear systems formed in collisions of actinides. Here the fusion-fission process is not possible at all, however the ternary quasifission in U+U collisions with the formation of two lead-like outer fragments is extremely favorable. Note that it is sufficient to detect two coincident lead-like ejectiles (or one lead-like and one calcium-like fragments) in U+U collisions to unambiguously prove the existence of ternary quasifission of the giant nuclear system. Such experiments are planned for the nearest future.

The present work is aimed at the development of a model for the multidimensional potential energy suitable for the future modeling of nucleus-nucleus collisions (binary entrance channel) within a dynamic approach with the possibility to have two as well as three fragments in the exit channel. The potential energy model should provide: (i) a rich enough nuclear shape parametrization reproducing entrance-channel shapes (rather compact contact configuration) as well as elongated scission shapes with pronounced necking; (ii) a smooth variation of nuclear shapes with the growing third fragment (the middle one), including a smooth transition from the binary to ternary fission shapes; (iii) a correct description of the fusion barriers in the entrance channel as well as ground-state properties and fission barriers. Another purpose of the paper is to test the model on the existing experimental data on the true ternary fission. That is possible since all the features seen in the experiment (such as increased yields for a certain combination of fragment masses) should be present in the potential energy as well.

THREE-CENTER SHELL MODEL

One of the most successful models giving the potential energy of binary nuclear reactions is the two-center shell model. The model was first proposed in Ref. [16] and later on developed by the Frankfurt group [17, 18, 19]. In spite of the fact that the standard two-center shell model works well for the ground-state and saddle-point deformations, it (being applied to the whole system) fails in the region of the Coulomb barrier in the entrance channel of the fusion reaction and also in the region of two well-separated nuclei [20, 21, 22]. The standard model can not describe correctly the transition from the potential energy of a mononucleus to the potential energy of separated nuclei. An extended macro-microscopic approach was proposed in Ref. [22] for the simultaneous analysis of deep-inelastic collisions, quasifission, and fusion-fission processes. The mentioned problem of the standard model was solved within this model. The idea was to use the correct properties of the standard macro-microscopical approach for compact nuclear shapes and moderate deformations (typical for fission saddle points), while the potential energy (or mass) of the system at extreme deformations of scission point (or Coulomb barrier) as well as for separated nuclei can be easily calculated as a sum of the interaction potential (folding, e.g.) and two deformation energies of the fragments. In between a smooth transition between these two cases is used.

In the macro-microscopical method, the whole system is characterized by some collective coordinates that determine the system evolution. The basic ingredient in such an analysis is the shape parametrization that depends on several macroscopic degrees of freedom. The generalized coordinates associated with these degrees of freedom vary in time leading to a split of the nuclear system into the separate fragments. The macroscopic deformation energy is calculated within a variant of the liquid drop model. In particular, we use the model called the finite-range liquid drop model [23, 22]. A microscopic potential must be constructed consistently with this nuclear shape parametrization. A microscopic correction (shell correction) is then evaluated using the Strutinsky procedure [24]. The single-particle states required for the shell correction calculation can be obtained by diagonalization of the Hamiltonian of the model on the basis of the chosen wave functions. The problem is significantly simplified if all of the matrix ele-

ments can be calculated analytically; this is achieved by the proper choice of the basis functions.

In the following, we will give the key relations of the developed three-center shell model (T3CSM). The T3CSM is based on the well-known two-center shell model (TCSM) in the most general form proposed in Ref. [19] and our previous work on the nucleus-nucleus potential [22]. An axial symmetric nuclear shape in the T3CSM is obtained by three smoothly joined ellipsoids with semi-axes a_i and b_i ($i = 1,2,3$). The Hamiltonian of the model is

$$\hat{H} = -\frac{\hbar^2}{2m_0}\nabla^2 + V_{\rm osc}(\vec{r}) + V_{LS}(\vec{r},\vec{p},\vec{s}) + V_{L^2}(\vec{r},\vec{l}). \tag{1}$$

Denoting the positions of the three centers by z_1, z_2 (side fragments) and z_3 (middle fragment), the momentum independent part of the potential in cylindrical coordinates $\{z,\rho,\phi\}$ (independent of ϕ owing to the system axial symmetry) may be expressed as

$$V_{\rm osc}(\rho,z) = \frac{1}{2}m_0 \begin{cases} \omega_{z1}^2(z-z_1)^2 + \omega_{\rho 1}^2\rho^2; & z < z_1; \\ \omega_{z1}^2(z-z_1)^2\left[1 + c_1(z-z_1) + d_1(z-z_1)^2\right] + & \\ +\omega_{\rho 1}^2\left[1 + g_1(z-z_1)^2\right]\rho^2; & z_1 < z < z_L; \\ \omega_{z3}^2(z-z_3)^2\left[1 + c_{31}(z-z_3) + d_{31}(z-z_3)^2\right] + & \\ +\omega_{\rho 3}^2\left[1 + g_{31}(z-z_3)^2\right]\rho^2; & z_L < z < 0; \\ \omega_{z3}^2(z-z_3)^2\left[1 + c_{32}(z-z_3) + d_{32}(z-z_3)^2\right] + & \\ +\omega_{\rho 3}^2\left[1 + g_{32}(z-z_3)^2\right]\rho^2; & 0 < z < z_R; \\ \omega_{z2}^2(z-z_2)^2\left[1 + c_2(z-z_2) + d_2(z-z_2)^2\right] + & \\ +\omega_{\rho 2}^2\left[1 + g_2(z-z_2)^2\right]\rho^2; & z_R < z < z_2; \\ \omega_{z2}^2(z-z_2)^2 + \omega_{\rho 2}^2\rho^2; z > z_2. & \end{cases} \tag{2}$$

Here m_0 is the nucleon mass, ω_{zi} and $\omega_{\rho i}$ are the frequencies of the oscillators defined along the symmetry axis and perpendicular to it. They are connected with the semi-axes as

$$\begin{aligned} a_i = R_0\omega_{zi}/\omega_0, \quad b_i = R_0\omega_{\rho i}/\omega_0, \\ R_0 = r_0 A^{1/3}, \quad \hbar\omega_0 = 41/A^{1/3}\ \text{MeV}, \end{aligned} \tag{3}$$

where $r_0 = 1.16$ fm is the nuclear radius parameter and A is the nucleus mass number.

The momentum-dependent part of the potential consists of a spin-orbit coupling term

$$V_{LS}(\vec{r},\vec{p},\vec{s}) = \begin{cases} \left\{-\frac{\hbar\kappa_1}{m_0\omega_{01}}, (\nabla V_{\rm osc}\times\vec{p})\cdot\vec{s}\right\}; & z < z_L; \\ \left\{-\frac{\hbar\kappa_3}{m_0\omega_{03}}, (\nabla V_{\rm osc}\times\vec{p})\cdot\vec{s}\right\}; & z_L < z < z_R; \\ \left\{-\frac{\hbar\kappa_2}{m_0\omega_{02}}, (\nabla V_{\rm osc}\times\vec{p})\cdot\vec{s}\right\}; & z > z_R \end{cases} \tag{4}$$

and an l^2-like term

$$V_{L^2}(\vec{r},\vec{l}) = \begin{cases} -\frac{1}{2}\left\{\frac{\hbar\kappa_1}{m_0^2\omega_{01}^3}, l^2\right\} + \hbar\kappa_1\mu_1\omega_{01}N_1(N_1+3)/2\delta_{if}; & z < z_L; \\ -\frac{1}{2}\left\{\frac{\hbar\kappa_3}{m_0^2\omega_{03}^3}, l^2\right\} + \hbar\kappa_3\mu_3\omega_{03}N_3(N_3+3)/2\delta_{if}; & z_L < z < z_R; \\ -\frac{1}{2}\left\{\frac{\hbar\kappa_2}{m_0^2\omega_{02}^3}, l^2\right\} + \hbar\kappa_2\mu_2\omega_{02}N_2(N_2+3)/2\delta_{if}; & z > z_R. \end{cases} \quad (5)$$

In these formulas $\{A,B\} = AB + BA$ denotes the anticommutator of two quantities and δ_{if} is a purely diagonal operator; κ_i is the spin-orbit interaction constant; μ_i is the adjustable parameter of the Nilsson model; N_i is the oscillator shell number for the side or middle part of the nucleus; $\hbar\omega_{0i} = 41/\tilde{A}_i$ MeV is the energy level spacing of the spherical oscillator, where $\tilde{A}_i$ is the asymptotic mass number of the nuclear fragment, which is defined in [19] as $\tilde{A}_i = a_i b_i^2/r_0^3$. The parameters N_i and $\tilde{A}_i$ are determined in such a way that for the elliptic shape of the initial nucleus, they should be the oscillator shell number and the nuclear mass number, while for the asymptotic state of separated nuclei they are the corresponding values for the fragments.

The nuclear shape is determined by the profile function $\rho_s(z)$ and can be obtained by assigning $V_{\rm osc}(\rho_s,z) = V_0$, where $V_0 = 1/2m_0\omega_0 R_0^2$. It is clear that the parts of the shape, external with respect to z_1 and z_2, are axially symmetric ellipsoids centered at z_i with semi-axes a_i and b_i ($i = 1,2$). The internal part of the shape is more complicated. The shape parametrization (as well as the mean-field potential $V_{\rm osc}$) has 23 free parameters (z_i, a_i, b_i, c_i, d_i, g_i, z_L, and z_R). We assume that $z_3 = 0$. Another 15 parameters can be fixed from the conditions of volume conservation and the continuity of the parametrization and its first derivative at the matching points z_L and z_R. Therefore, the shape parametrization of the T3CSM has 7 independent parameters, that allows us to introduce 7 collective variables: the elongation of the system $R = z_2 - z_1$, which for separated fragments is approximately the distance between the mass centers of the side fragments; the ellipsoidal deformations of the three parts of the system, $\delta_i = a_i/b_i - 1$; two mass-asymmetry parameters $\eta_{21} = (A_2 - A_1)/(A_2 + A_1)$ and $\eta_3 = A_3/(A_1 + A_2 + A_3)$, where A_1, A_2 and A_3 are the mass numbers of the fragments, and the neck parameter ε. This parameter arises owing to the smoothing of the potential $V_{\rm osc}(\rho,z)$ in the region between the oscillator centers and is defined as the ratio of the smoothed and original potentials at the crossing point of the harmonic oscillator potentials (see Fig. 9 of Ref. [22]). Therefore, smaller values of ε correspond to a thicker neck at fixed values of the other parameters.

The basic functions required for the diagonalization of the Hamiltonian (1) are the solutions of the three-center problem

$$\hat{H}_0\psi = E_0\psi, \qquad \hat{H}_0 = -\frac{\hbar^2}{2m_0}\nabla^2 + V_{\rm osc}(\rho,z), \quad (6)$$

where the mean field potential should be taken without smoothing ($c_i = d_i = g_i = 0$). The corresponding Schrödinger equation for the pure three oscillator potentials (6) is separable when $\omega_{\rho_1} = \omega_{\rho_2} = \omega_{\rho_3}$. When solved, this equation produces the basis for further calculation within the three-center shell model. The total single-particle wave function reads

$$\psi(\rho,z,\phi) = \Phi_{n_z}(z)\cdot\chi_{n_\rho}^{|m|}(\rho)\cdot\eta_m(\phi), \quad (7)$$

where

$$\eta(\phi) = \frac{1}{\sqrt{2}} \exp(im\phi), \tag{8}$$

$$\chi_{n_\rho}^{|m|}(\rho) = N_\rho^{-1} k_\rho^{\frac{|m|+1}{2}} \exp\left(-\frac{k_\rho \rho^2}{2}\right) \rho^{|m|} L_{n_\rho}^{|m|}(k_\rho \rho^2) \tag{9}$$

with the normalization constant N_ρ and $k_\rho = \frac{m_0 \omega}{\hbar}$, n_ρ is non-negative integer, $L_n^\alpha(x)$ is the Laguerre polynomial.

The z-dependent function Φ_{n_z} is defined in three regions corresponding to the three nascent fragments

$$\Phi_{n_z}(z) = \begin{cases} N_{z_1}^{-1} U\left(-n_{z_1} - \frac{1}{2}, -\sqrt{2k_{z_1}}(z - z_1)\right), & z < z_L; \\ \\ N_{z_{3U}}^{-1} U\left(-n_{z_3} - \frac{1}{2}, -\sqrt{2k_{z_3}}(z - z_3)\right) + \\ +N_{z_{3V}}^{-1} V\left(-n_{z_3} - \frac{1}{2}, \sqrt{2k_{z_3}}(z - z_3)\right), & z_L \le z \le z_R; \\ \\ N_{z_2}^{-1} U\left(-n_{z_2} - \frac{1}{2}, \sqrt{2k_{z_2}}(z - z_2)\right), & z > z_R \end{cases} \tag{10}$$

with the normalization factors $N_{z_1}, N_{z_2}, N_{z_3U}$ and N_{z_3V}. Here $U(a,x)$ and $V(a,x)$ are the regular and irregular parabolic cylinder functions defined by

$$\begin{aligned} U(a,x) &= \sqrt{\pi} 2^{-\frac{1}{2}a - \frac{1}{4}} {}_1F_1\left(\frac{1}{2}a + \frac{1}{4}; \frac{1}{2}; \frac{1}{2}x^2\right) / \Gamma\left(\frac{1}{2}a + \frac{3}{4}\right) \cdot e^{-\frac{x^2}{4}} \\ &\quad - x\sqrt{\pi} 2^{-\frac{1}{2}a + \frac{1}{4}} {}_1F_1\left(\frac{1}{2}a + \frac{3}{4}; \frac{3}{2}; \frac{1}{2}x^2\right) / \Gamma\left(\frac{1}{2}a + \frac{1}{4}\right) \cdot e^{-\frac{x^2}{4}} \end{aligned} \tag{11}$$

and

$$\begin{aligned} V(a,x) &= \sqrt{\pi} 2^{-\frac{1}{2}a - \frac{1}{4}} \tan\left[\pi\left(\frac{1}{4} + \frac{1}{2}a\right)\right] {}_1F_1\left(\frac{1}{2}a + \frac{1}{4}; \frac{1}{2}; \frac{1}{2}x^2\right) \times \\ &\times \; e^{-\frac{x^2}{4}} / \Gamma\left(\frac{1}{2}a + \frac{3}{4}\right) \Gamma\left(\frac{1}{2} - a\right) - \\ &- \; x\sqrt{\pi} 2^{-\frac{1}{2}a + \frac{1}{4}} \tan^{-1}\left[\pi\left(\frac{1}{4} + \frac{1}{2}a\right)\right] {}_1F_1\left(\frac{1}{2}a + \frac{3}{4}; \frac{3}{2}; \frac{1}{2}x^2\right) \times \\ &\times \; e^{-\frac{x^2}{4}} / \Gamma\left(\frac{1}{2}a + \frac{1}{4}\right) \Gamma\left(\frac{1}{2} - a\right) \end{aligned} \tag{12}$$

whose properties may be found in Ref. [25]. The seven n_{zi} and N_{zi} coefficients can be determined numerically in a standard way by imposing the normalization condition and the condition of smoothness of the wave function and its first derivative at the matching points

$$\begin{cases} \int\limits_{-\infty}^{\infty} \Phi_{n_z}(z) dz = 1, \\ \Phi_{n_{z1}}(z_L) = \Phi_{n_{z3}}(z_L), \qquad \Phi_{n_{z2}}(z_R) = \Phi_{n_{z3}}(z_R), \\ \Phi'_{n_{z1}}(z_L) = \Phi'_{n_{z3}}(z_L), \qquad \Phi'_{n_{z2}}(z_R) = \Phi'_{n_{z3}}(z_R), \\ \omega_{z_1}\left(n_{z_1} + \frac{1}{2}\right) = \omega_{z_2}\left(n_{z_2} + \frac{1}{2}\right) = \omega_{z_3}\left(n_{z_3} + \frac{1}{2}\right). \end{cases} \tag{13}$$

The last equation in Eq. (13) ensures that the eigenvalue $E_0 = \hbar\omega_{zi}(n_{zi} + 1/2) + \hbar\omega_{\rho i}(2n_\rho + 1)$ cannot depend on the space coordinates.

Finally, the eigenvalues and eigenvectors of the initial problem (1) are found by the standard diagonalization procedure with the cut-off energy for the basis functions equal to $12\hbar\omega_0$.

RESULTS AND DISCUSSION

Within the macro-microscopic approaches the potential energy of a deformed nucleus is usually composed of two parts $V_{\mathrm{mac-mic}}(A,Z;R,\delta_i,\eta_{21},\eta_3,\varepsilon) = V_{\mathrm{mac}}(A,Z;R,\delta_i,\eta_{21},\eta_3,\varepsilon) + \delta E(A,Z;R,\delta_i,\eta_{21},\eta_3,\varepsilon)$. The macroscopic part, V_{mac}, smoothly depends on the proton and neutron numbers and may be calculated within the liquid-drop model. The microscopic part, δE, describes the shell effects. It is constructed from the single-particle energy spectra by the Strutinsky procedure [24].

There are too many collective degrees of freedom necessary for proper description of the potential energy of a nuclear configuration consisting of three deformed heavy fragments. As mentioned above, the three-center parametrization has seven degrees of freedom. In order to test the developed model we have restricted the number of collective variables. Instead of three independent deformation parameters δ_i we use a single unified deformation δ_U defined as

$$\begin{aligned} 3\delta_U &= \left(\delta_1 - \tilde{\delta}_1\right) + \left(\delta_2 - \tilde{\delta}_2\right) + \left(\delta_3 - \tilde{\delta}_3\right), \\ C_{\delta 1}\left(\delta_1 - \tilde{\delta}_1\right) &= C_{\delta 2}\left(\delta_2 - \tilde{\delta}_2\right) = C_{\delta 3}\left(\delta_3 - \tilde{\delta}_3\right), \end{aligned} \tag{14}$$

where $\tilde{\delta}_i$ are the deformation parameters providing the minimum of the potential energy for the fixed other collective variables. The second relation in Eq. (14) is, in fact, the balance equation of forces applied to three deformed nuclear fragments. Equation (14) is limited to second-order terms in the expansion of deformation energies into series in the deformation. The rigidity parameters $C_{\delta i}$ can be evaluated using the corresponding relation for the ellipsoid nucleus. In the calculations shown below we assume $\delta_U = 0$ and the neck parameter $\varepsilon = 1$.

First, let us discuss the macroscopic (LDM) part of the potential energy. Figure 1 shows the LDM potentials for ^{252}Cf along with the corresponding nuclear shapes. The potential energy was calculated for the mirror-symmetric division of the nucleus ($A_1 = A_2$) for zero values of the deformation parameters ($\delta_i = 0$). For better visualization we plot the calculated potential energy as a function of $R/R_0\cos(\alpha_3)$ and $R/R_0\sin(\alpha_3)$, where $\alpha_3 = \pi \cdot A_3/100$ and R_0 is the radius of the spherical nucleus. One may see that the potential energy has two barriers. The first one, which is closer to the ground state, is the usual barrier of binary fission. The second one is the barrier of three-body clusterization, that prevents the system from the ternary fission. The obvious feature of this barrier is that it grows with the increase of the mass of the middle fragment. The origin of this effect is quite obvious, it is due to increase of the Coulomb forces. Such behavior of the second barrier has an important consequence that simple exchange of side and middle

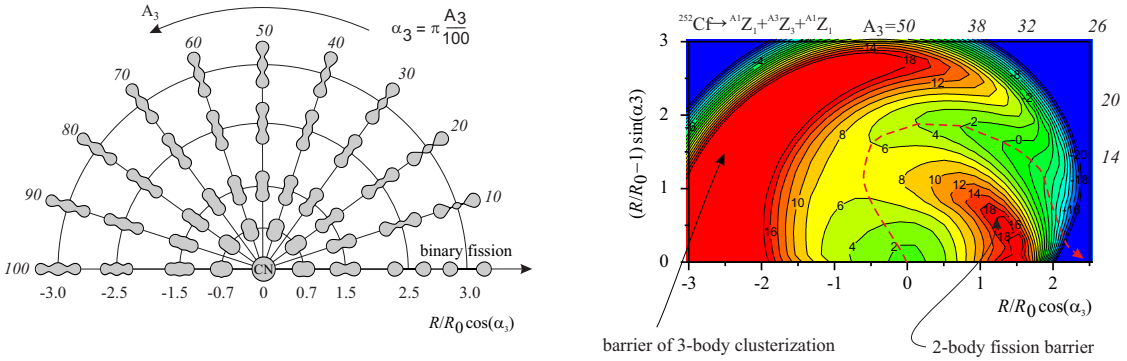

FIGURE 1. Macroscopic part of the potential energy for fission of ^{252}Cf calculated for zero values of the deformation parameters. (right panel) and nuclear shapes (left panel) depending on elongation and mass of third fragment (italic numbers). The contour lines are drawn over 2 MeV. The dashed curve shows one of possible binary fission paths.

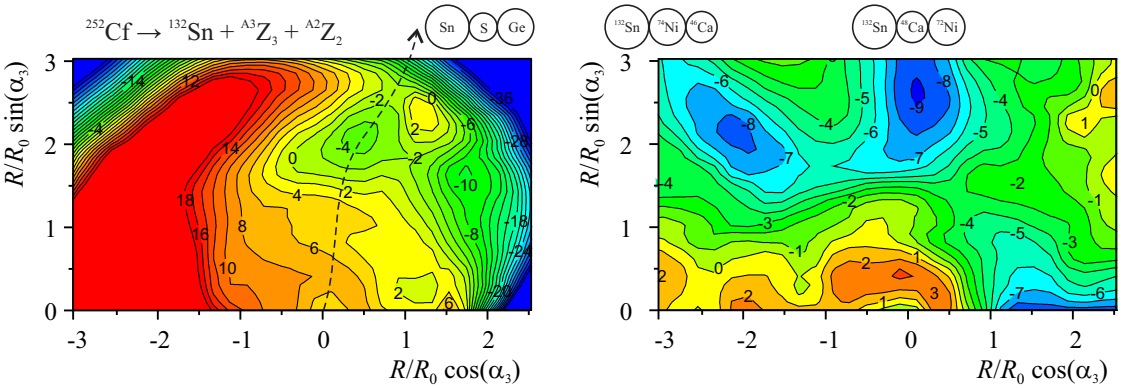

FIGURE 2. Potential energy (left panel) and microscopic shell correction (right panel) for ternary fission of ^{252}Cf depending on elongation and mass of the third fragment calculated for zero value of the unified deformation. One of the side fragments is assumed to be ^{132}Sn. The dashed curve shows schematically the true ternary fission path.

fragments alters the probability of the system decay. A larger probability of the ternary fission should be expected when the middle fragment has a smaller size (see below).

It should be stressed once more that the second barrier on the potential energy landscape has a purely macroscopic nature and its appearance is connected with the formation of the second neck in the nuclear shape on the way to the ternary fission. It is clear that the macroscopic structure of the potential landscape prevents actinides from the ternary decay. Large shell effects for the strongly deformed nuclear system are the only reason for observing a noticeable yield of ternary fission. Such shell effects in the actinide region can be expected for mass-asymmetric fission with the formation of doubly magic tin-like cluster as one of the fragments. In order to test the model on available experimental data [12] we calculated few potential energy surfaces for ^{252}Cf. The first one corresponds to the case when one of the outer fragments is ^{132}Sn. This potential energy along with the corresponding shell correction are shown in Fig. 2. The mass of the second (side) fragment is determined by the mass conservation $A_2 = 252 - 132 - A_3$.

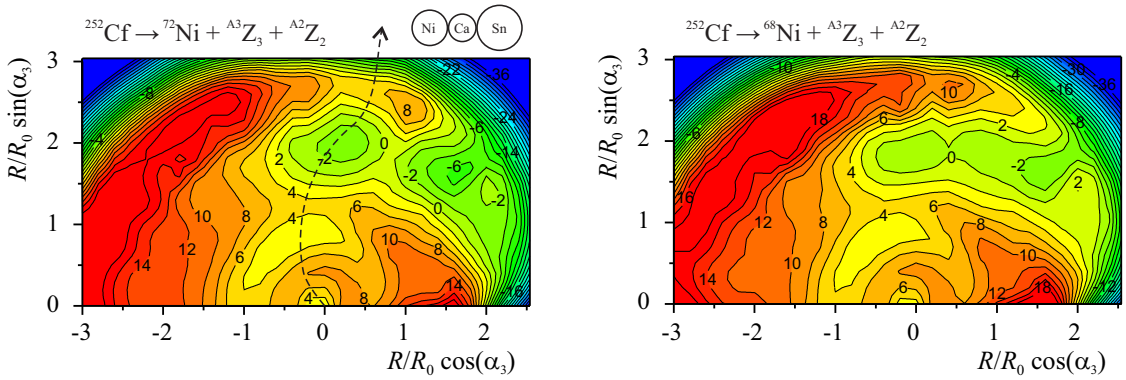

FIGURE 3. The same as in Fig. 2 but with one of the side fragments assumed to be ^{72}Ni (left panel) and ^{68}Ni (right panel).

Three regions of strong shell effects are clearly seen. The first one leads to binary fission with nearly symmetric "tin–cadmium" combination. Other two combinations correspond to the ternary fission with the formation of three magic clusters: tin, calcium, and nickel. The only difference between them is the order of fragments (small difference in the masses of calcium and nickel for these two combinations can be ignored). However, as discussed above, the probability of these two equal (in terms of fragments masses) combinations differs dramatically. One may see a rather well pronounced valley of the potential energy surface corresponding to the formation of three fragments with the masses 132, 40, and 80 ("tin–sulfur–germanium" combination). This valley appears due to strong shell effects for the "tin–calcium-nickel" case. A small shift towards smaller middle fragment (sulfur instead of calcium) is due to macroscopic properties of the ternary barrier. The ternary fission valley is quite well separated by the potential ridge from the binary fission valley. This means that the ternary fission of the ^{252}Cf nucleus into the "tin–sulfur–germanium" combination should be among the most probable true ternary fission channels of this nucleus. This result is in good agreement with the experimental data. The second found ternary combination "tin–nickel–calcium" has negligible probability to be realized owing to large ternary barrier.

The increased ternary fission yield with the formation of ^{68,72}Ni was observed in Ref. [12]. The potential energy surfaces for these two cases are shown in Fig. 3. One may see again a well separated ternary fission valley for the "nickel+calcium+tin" combination (the fragment masses are 72, 48, and 132). However, the potential energy surface calculated assuming ^{68}Ni as the first side fragment does not have a "good" ternary fission valley because of smaller absolute value of the shell correction that cannot "dig" a valley in the second (ternary fission) barrier. Both surfaces shown in Fig. 3 also have well pronounced ternary fission valleys when the middle fragment has mass the around 16 (oxygen). This leads to the "nickel–oxygen-samarium" combination.

To conclude, the three-center shell model of deformed nucleus is developed in this paper. The model is an extension of the well-known two-center shell model and includes it as a special case. The three-center shell model is applied to analyze the general properties of the potential energy landscape on the example of the ternary fission of the ^{252}Cf nucleus. We found that the ternary fission channel, being strongly suppressed

by the macroscopic properties of the potential energy (additional barrier of ternary decay), may however be present with a significant probability owing to shell effects. The potential energy has pronounced valleys favorable for true ternary fission with formation of doubly magic tin as one of the fragments and two other lighter (usually magic or semimagic) fragments. The positions of the found ternary fission fission valleys are in good agreement with the available experimental data.

ACKNOWLEDGMENTS

This work was supported in part by the ARE-JINR Collaboration program. One of us, A.V.K., is indebted to the RSA-JINR Collaboration for support of these studies.

REFERENCES

1. C. Wagemans, *Ternary Fission* in *The Nuclear Fission Process*, edited by Cyriel Wagemans (CRC Press, Boca Raton, 1991), Chap. 12.
2. F. Gönnenwein, M. Wöstheinrich, M. Hesse, H. Faust, G. Fioni, S. Oberstedt, in *Seminar on Fission*, Pont d'Oye IV, Belgium, 1999, edited by Cyriel Wagemans et al., (World Scientific, Singapore, 1999) p. 59.
3. F. Gönnenwein, M. Mutterer and Yu. Kopatch, Europhys. News **36**, 11 (2005).
4. G.M. Ter-Akopian et al., Phys. At. Nucl. **67**, 1860 (2004).
5. A.V. Ramaya, et al., Prog. Part. Nucl. Phys. **46**, 221 (2001).
6. W.J. Swiatecki, Second UN Int. Conf. on the Peaceful Uses of Atomic Energy, Geneva, 1958, p. 651.
7. H. Diehl and W. Greiner, Nucl. Phys. **A229**, 29 (1974).
8. A.R. Degheidy, J.A. Maruhn, Z. Phys. A **290**, 205 (1979).
9. R A Gherghescu and N Carjan, J. Phys. G **36** (2009) 025106.
10. M. L. Muga, C. R. Rice, and W. A. Sedlacek, Phys. Rev. Lett. **18**, 404 (1967).
11. P. Schall, P. Heeg, M. Mutterer, and J. P. Theobald, Phys. Lett. B **191**, 339 (1987).
12. D.V. Kamanin and Yu. V. Pyatkov, *Clusters in Nuclei*, V. 3, ed. by C. Beck, Lecture Notes in Physics 875 (2013) 183.
13. H. Schulheis, R. Schulheis, Phys. Lett. B **49**, 423 (1974).
14. G. Royer, F. Haddad, and J. Mignen, J. Phys. G **18**, 2015 (1992).
15. V.I. Zagrebaev, A.V. Karpov, and Walter Greiner, Phys. Rev. C **81**, 044608 (2010).
16. P. A. Cherdantsev, V. E. Marshalkin, *Bull. Acad. Sci. USSR* **30**, 341 (1966).
17. P. Holzer, U. Mosel, W. Greiner, Nucl. Phys. A **138**, 241 (1969).
18. U. Mosel, J. Maruhn, W. Greiner, Phys. Lett. B **34**, 587 (1971).
19. J. Maruhn, W. Greiner, Z. Phys. A **251**, 431 (1972).
20. W. D. Myers, W. J. Swiatecki, Nucl. Phys. A **601**, 141 (1996).
21. P. Möller, A. J. Sierk, A. Iwamoto, Phys. Rev. Lett. **92**, 072501 (2004).
22. V.I. Zagrebaev, A.V. Karpov, Y. Aritomo, M. Naumenko, W. Greiner, Phys. Part. Nucl. **38** 469 (2007).
23. P. Möller, J. R. Nix, W. D. Myers, W. J. Swiatecki, At. Data Nucl. Data Tables **59**, 185 (1995).
24. V. M. Strutinsky, Nucl. Phys. A **95**, 420 (1967); V. M. Strutinsky, Nucl. Phys. A **22**, 1 (1968).
25. M. Abramowitz and I.A. Stegun, *Handbook of Mathematical Functions*, (New York, Dover Publications 1965).

Many-phonon approach to the mystery of true ternary fission

F. F. Karpeshin

D.I.Mendeleyev Institute for Metrology, Moskovsky pr., 19, St. Petersburg, 190005, Russia

Abstract. The problem of nuclear fission into three comparable fragments is considered. A mechanism of true ternary fission is proposed. In contrast to sequential fission, where the three fragments arise due to two sequential events of binary fission, the mechanism in question relies on a scenario that generically involves fission into three fragments. This mechanism is driven by a hexadecapole deformation of the fissioning nucleus, in contrast to binary fission associated with quadrupole vibrations of the nuclear surface. The estimated fragment-mass ratios are in coincidence with experiment. The dynamics of formation of collinear fragments and their subsequent motion under the barrier in opposite directions is traced. A small number of emitted neutrons is predicted as a critical test of the dynamical picture.

Keywords: true ternary nuclear fission, cold fission, quasiparticle-phonon coupling
PACS: 234.75.+i; 25.85.Ca; 25.85.Ec

INTRODUCTION

Saying fission, people usually undermine traditional binary fission into two fragments, may be not equal, but of comparable size. Ternary fission is called a process of binary fission accompanied with emission of a light charged particle, usually of an α particle. True ternary fission (TTF) was proposed to call tripartition if the third particle has mass close to that of the other two fragments. Another difference as we will see arises due to the angular distribution of the particles. α particle in the ternary fission is emitted perpendicularly to the fission axis. In the case of TTF, the angular distribution is different in principle. A question may arise sometimes what is the third fragment in TTF: fission or emission of a heavy cluster? And may one say that fission is a limiting case of cluster emission [1]?

Let us discuss the problematics if TTF, and about a new physics which it gives chance to discover. This turns out to be a very interesting process from many points of view, including, apart from physics, also general philosophic position and history of science. All the more that story of its study breaks into two eras: before the present experiments performed in Dubna on the FOBOS facility [2], and since them.

Energetically, the TTF is more favorable. From this viewpoint, it is a paradox that during a long time, before the JINR experiments, people did not observe TTF, in spite of many attempts. For a long time, the prevalent opinion was that, at low nuclear excitation energies not exceeding several tens of MeV units, fission into three comparable fragments is highly improbable. Muga et al. [3] found that in interaction of ^{238}U nuclei with thermal neutrons the branching ratio for TTF ξ is less than $\xi \leq 10^{-5}$ [3]. Iver and Coble [4] established the upper bound for TTF in the fission of iridium and gold nuclei by 28

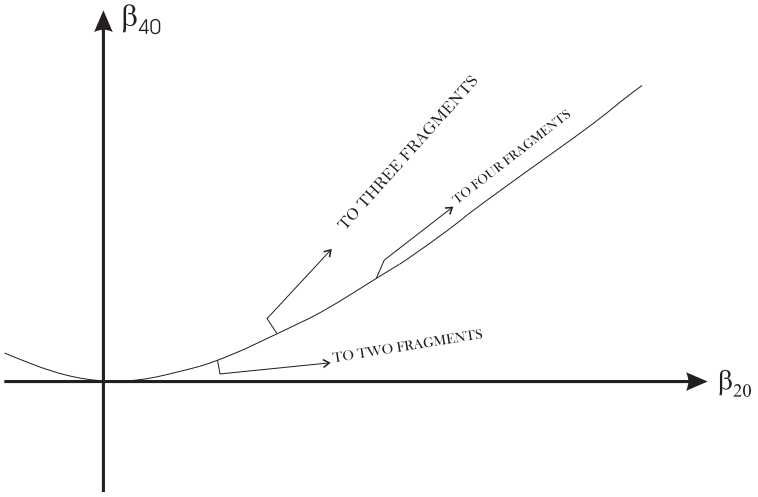

FIGURE 1. Dependence of the fissile nuclear configuration on the deformation parameter of quadrupole or hexadecapole type.

– 150 MeV α particles as $\xi \leq 10^{-8} \div 10^{-5}$. According to Perelygin et al. [5], $\xi \leq 10^{-5}$ in heavy-ion collisions. Theobald *et al.* established the upper bound in spontaneous fission of ^{252}Cf at the level of 10^{-8} [6]. Finally, it was found that in fission of uranium by GeV protons by Solyakin et al. $\xi \leq 10^{-3}$. It can be assumed that ternary fission into comparable fragments that is observed at high energies is caused by a different mechanism — say, fragmentation or sequential fission into three fragments. This seems again surprising since the barrier height for fission into three comparable fragments (about 30 MeV for plutonium) is on the same order of magnitude as the barrier height for ordinary fission — for example, in the case of medium-mass nuclei.

Another paradox is that experiments were aimed at search for TTF under equal angles — so called clover-leaf form. This was in contradiction with the theoretical works which unanimously predicted advantage of linear elongation of the fissile nuclei. Thus, in ref. [7] ternary fission of an atomic sodium cluster of $_{27}Na^{+++}$ into three equal fragments of $_9Na^+$ was considered. The shape of the fissioning cluster was described as that of three equal intersecting spheres. Such a linear shape of fissioning clusters yields in a collinear flight of the three fragments formed. The choice was caused by a very high shell correction, which considerably diminishes the fission barrier. The shell correction is due to the fact that the three final clusters $_9Na^+$ possess closed electronic shells. It was noted, however, that it is not only lower fission barrier which opens a chance of observation ternary fission. TTF is a dynamical process. It was pointed out previously in the literature that playing with hexadecaqpole deformation can lead to a multi-fragment saddle shapes, see Fig. 1. This suggests to relate the

special dynamics of TTF to this mode of deformation of the nuclear surface. Herein we discuss peculiarities of the related dynamics.

MANY-PHONON DOORWAY STATES FOR FISSION

Let us consider first evolution of a fissile nucleus when it undergoes a more usual binary fission. For the sake of simplicity, we assume that the equilibrium shape of the nucleus is spherical. This limitation does not entail radical qualitative changes but renders the ensuing analysis clearer. Many results were obtained within the wall-and-window model. Under strokes of individual nucleons against the nuclear wall, a random deformation is formed. Arising deformation at the beginning of the process can be well described in terms of the quadrupole moment. As the deformation increases the nucleus elongates, the neck is formed, and finally two fragments appear. Its further evolution is conventionally described as a diffusion process under action of a random force. Nucleon strokes against the wall play role of this force. They lead to increase of the deformation, until the neck is formed. The neck becomes thinner and finally ruptures. Exchange with nucleons through the formed window between the fragments forms the final mass and charge distribution of the fragments. As one can see, this is a completely classic physics underlying the method.

Based on these representations, a simple and physically transparent microscopic approach was developed in Ref. [8]. At the equilibrium, the nuclear surface undergoes quadrupole zeroth oscillations (phonons) around the point of equilibrium (Fig. 2). When the nucleus gets excited, e.g. by absorption of a neutron, the energy from individual nucleons is transferred to the collective quadrupole mode, thereby increasing the amplitude of the vibrations. This step can be viewed as a birth, or emission of a phonon. And so on. The initial deformation increases its amplitude step by step, in a diffusion-like process, absorbing (and emitting) elementary quadrupole phonons due to interaction with separate nucleons, up to the top of the barrier is achieved. The coupling between the nucleon modes and the quadrupole phonons is realized by the surface nucleon-phonon interaction, which can be represented in a form (e.g. [9]):

$$H' = \sum_{\lambda\mu pqp'q'} (Q_{\lambda\mu} + Q^{+}_{\lambda-\mu})\alpha^{+}_{pq}\ \alpha_{p'q'} f_{\lambda}(r)\,, \tag{1}$$

where $Q^{+}_{\lambda\mu}$, $Q_{\lambda\mu}$ are, respectively, the creation and annihilation operators for phonons.

Matrix element of this interaction is quite big, of about 50 MeV [10]. Moreover, similar to the classic approach, this interaction is of clearly expressed surface character. According to the Bohr model [11],

$$f_{\lambda}(r) = r\frac{dV(r)}{dr}\,, \tag{2}$$

where $V(r)$ is the mean single-particle field in the nucleus. According to (1), the amplitude and the energy of the surface vibration is quantized. The amplitude and energy of n phonon vibration increases with n according to

$$A_n = \sqrt{n}a_0\,, \tag{3}$$

$$E_n \sim n\hbar\omega_0\,, \tag{4}$$

respectively. Quadrupole phonons are observed in heavy nuclei [12]. n phonon state with $n \approx 8-10$ corresponds to the saddle point. Thus, it can be considered as a doorway state

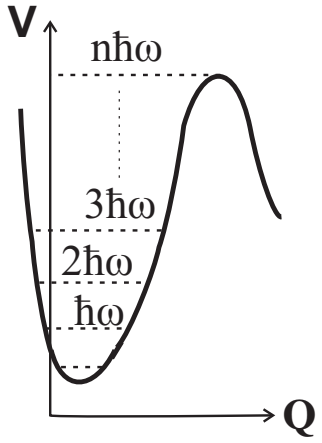

FIGURE 2. Illustration of the microscopic method by Zaretsky and Karpeshin. V — deformation energy, Q — collective coordinate along the fission axis (quadrupole moment).

for fission. It is important to note the self-consistency of the method, that is conditions (3) and (4) are fulfilled simultaneously at the top of the barrier. This is not the case e.g. for the GQR: whereas its energy is of about 10 MeV for an uranium nucleus, its amplitude is only of $\beta_{20} \sim 0.2$. For this reason, there is no direct fission from GQR. At first, its energy dissipates into quasiparticle modes. Then collective mode develops towards fission.

THE DYNAMICS OF THE TTF

A hexadecapole vibration of the nuclear surface is the simplest elementary vibration that could lead to fission into three fragments, see Fig. 1. For such vibrations, the change in the nuclear shape is described by the relation

$$R(\theta,\phi) = R_0(1+\beta_{00}Y_{00}+\beta_{40}Y_{40}(\theta,\phi))\,. \tag{5}$$

The parameter β_{00} is introduced in the expansion in Eq. (5) in order to take into account volume conservation for the nucleus undergoing deformations. This suggests that the dynamical reasons for TTF may be related to the hexadecalpole collective mode of the prefission doorway vibrations of the nuclear shape.

By way of illustration, Fig. 3 shows the calculated

nuclear shape versus β_{40}. The critical value at which the separation of fragments occurs is β_{40}= 1.902. Of course, the final formation of fragment masses proceeds much earlier — at the stage of descent in the fission valley and is due to different factors (viscosity, the shape of the valley with allowance for the shell correction, etc.).

Formation of the two necks is a complex dynamical process. In Fig. 4 lines of the microscopic nuclear flow are shown. In the case of TTF, the initial conditions are such that they naturally form two necks. They are in clear difference with those found in [13], where the ellipsoidal type of the collective motion of an ideal non-viscous incompressible liquid drop was considered. It was specifically shown, that ellipsoidal

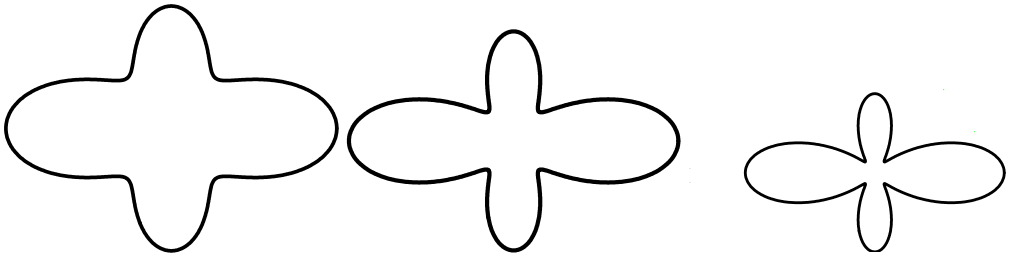

FIGURE 3. Nuclear shapes according to Eq. (1) for various values of the hexadecapole-deformation parameter: β_{40}=0.8, 1.2, 1.7. The mass ratios for the central and one of the edge fragments are 5, 3.14 and 2.13, respectively.

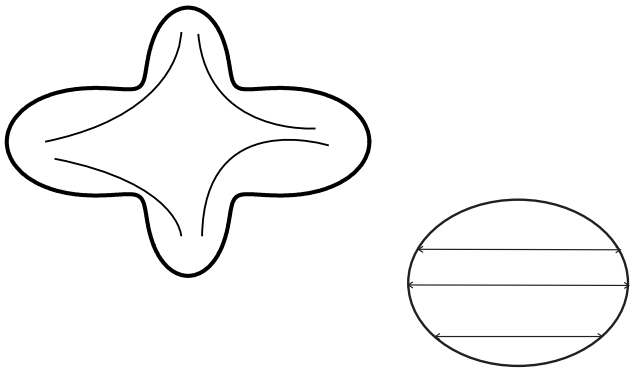

FIGURE 4. Vector lines of the microscopic nuclear flow in the case of hexadecapole (left) and ellipsoidal (right) nuclear shape.

shape preserves during vibration. Therefore, formation of a neck is not a consequence of the initial conditions. There is a dynamic reason which causes beginning of the formation. In the case of TTF, such a reason may be the hexadecapole many-phonon vibration, brought about by the interaction of the quasiparticles with the nuclear surface, as shown above. In this case, the initial conditions are such that they naturally form two necks.

QUALITATIVE ANALYSIS OF THE SCISSION CONFIGURATION

The configuration of the fissile nucleus replies to scission is shown in Fig. 5. We note two characteristic features concerning this configuration.

The critical value at which the separation of fragments occurs β_{40} = 1.902. This corresponds to division into the channel ^{65}Fe + ^{122}Pd + ^{65}Fe. This is in a remarkable agreement with experiment.

There is also another peculiarity worthy of mentioning. Let us consider the initial total potential energy of interaction of the three fragments with one another at scission, Fig. 5. In spite of more compact form at rupture, the Coulomb energy turns out to be smaller as

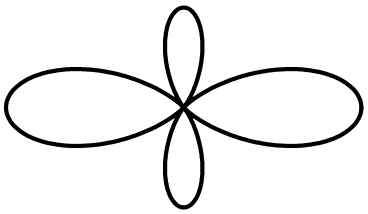

FIGURE 5. Scission configuration of TTF

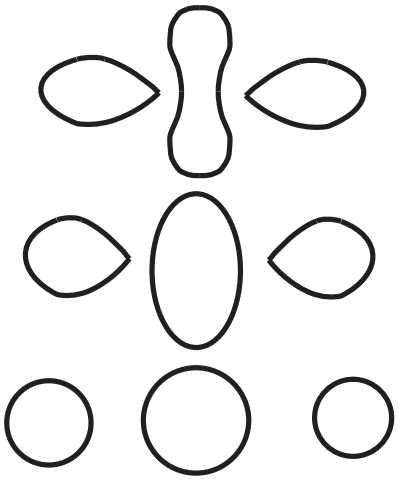

FIGURE 6. Three post-scission consecutive stages of fragment separation under the barrier. The bottom figure corresponds to the moment when both the light fragments get bound of the barrier. All the fragments reach the equilibrium form by this moment.

compared to that of three spherical fragments with of same masses, arranged in line and touching one another, by approximately 25 MeV per each light fragment. This is due to oblate shape of the central heavy fragment and related redistribution of the protons in the direction perpendicular to the fission axis. This condition is critical for comparison of experiment to theoretical models [14]. In our case, this circumstance works in favor of the proposed mechanism.

SIMILARITY OF THE COLD AND TRUE TERNARY FISSION

The mystery of TTF reminds another problem of cold fission, when the TKE is close to the maximal one. This is possible only if the fragments are formed after rupture with the equilibrium form. Final formation of such fragments may only be realized in a subbarier process. Also subbarier is spontaneous or low-energy TTF.

Regarding the TTF, the calculated final mass distribution is in good coincidence with the experimental mass distribution, as shown in section . However, even more important is the right trend caused by the dynamics of the nuclear flow, which is shown in Fig. 4, right. The total repulsive Coulomb energy at the moment of rupture, Fig. 5, remains higher than the final Q value. Therefore, at this moment, the nucleus is in a virtual state

under the barrier. On the next stage, the three pieces of the fissile nucleus shown in Fig. 6 will deploy like a flower bud. Light fragments will advance from their niche, flying away and acquiring their equilibrium shape. Gradual spherization of the fragments in the tunneling will not give rise to their excitation, as distinct to conventional spherization of post-rupture fragments in classically allowed region. But the energy released in spherization will promote the tunneling, increasing its probability. In the end, one may expect that when the fragments reach the turning point at the exit from the barrier, they become spherical and cold. Therefore, the number of emitted neutrons may be expected to be small, if any. This evidence of the dynamics can be checked in experiment as a test of the proposed picture.

CONCLUSION

1) The consideration performed clearly shows that TTF is a dynamical problem of primordial interest. The consideration develops the unique dynamics of this process. The reason is specific nuclear flow, generated by the hexadecapole component of the residual nucleon-nucleon interactions. This kind of flow results in generic formation of the both necks which develop from the very beginning of the TTF process. Collinear tripartion is natural way of realization of this dynamics.

2) TTF may not be explained in terms of fission barrier or final energy balance based on the Q-value. The reason is in the dynamics of the process. Many-phonon doorway states of the hexadecapole type lead to TTF, similar to how the doorway states of the quadrupole type lead to traditional binary fission.

3) Some circumstances were pointed out previously, which lead to better penetration probability in the case of TTF on the basis of the many-phonon picture. These are higher frequency of assaults against the wall, and a shorter path under the barrier. As a result, they may manifest themselves in a qualitative agreement with the experimentally observed TTF probability [15].

ACKNOWLEDGEMENT

The author is grateful to D. Kamanin and Yu. V. Pyatkov for stimulating discussions of the relevant present-day experimental data. He would also like to gratefully acknowledge numerous useful discussions of the problem with G. E. Solyakin. Special thanks are due to J. R. Nix, V. P. Perelygin, V. M. Strutinsky, W.J. Swiatecki, G. V. Valsky and L. F. Vitushkin for their enlightening comments at various stages of this work.

REFERENCES

1. M. Ali Hooshyar, I. Reichstein and F. B. Malik, *Nuclear Fission and Cluster Radioactivity*. (Berlin: Springer), 2005.
2. D. V. Kamanin and Yu. V. Pyatkov 2013 in *Clusters in Nuclei*, Vol. 3, Ed. by C.Beck, Lect. Notes Phys., Vol. 875 (Springer, 2013), p. 183; Yu.V.Pyatkov, D. V.Kamanin, A.A. Alexandrov et al. 2013 in *Proceedings of the International Symposium on Exotic Nuclei EXON-12*, Vladivostok, Russia, Oct. 16, 2012, Ed. by Yu. E. Penionzhkevich and Yu. G. Sobolev (World Sci.), p. 407.

3. M. L. Muga, *Phys. Rev. Lett.* **11**, 129 (1963).
4. Iver and Coble, *Phys. Rev.* **172**, 1176 (1968).
5. V. P. Perelygin, *Nucl. Phys.* A **122**, 577 (1969).
6. M. Mutterer et al., in *Proceedings of the International Conference on 50th Anniversary of Nuclear Fission*, Leningrad, 1989, p. 32; P. Schall, P. Heeg, M. Mutterer, and J. P. Theobald, *Phys. Lett.* B **191**, 339 1987.
7. F. F. Karpeshin, A. Vieira, C. Fiolhais, and J. da Providencia, Jr. 1998 *Europhys. Lett.* **42**, 149
8. F. F. Karpeshin and D. F. Zaretsky, in *Proceedings of the International Conference on Fifty Years Research in Nuclear Fission*, Berlin, 1989; D. F. Zaretsky and F. F. Karpeshin, *Sov. J. Nucl. Phys.* **50**, 959 (1989).
9. V. G. Soloviev, *Theory of complex nuclei.* Pergamon Press, 1976.
10. I. Hamamoto, Phys. Rep., **10**, 63 (1974).
11. O. Bohr, B. Mottelson. The Nuclear Structure. Vol. 2.
12. V. A. Khodel and E. E. Saperstein, Phys. Rep. **92**, No. 5 (1992).
13. F. F. Karpeshin, J. da Providencia, C.Providencia and J. da Providencia jr. *European Phys. J.* D **18**, 319 (2002).
14. Yu. V. Pyatkov, D. V. Kamanin, W. von Oertzen *et al.*, in: Proceedings of the 20th International Seminar on Interaction of Neutrons with Nuclei, Alushta, Ukraine, 21-26 May 2012. Dubna 2013, p. 104.
15. F. F. Karpeshin, *Phys. At. Nucl.,* **. 78**, 548 (2015).

Gas-cell based setup for production and study of heavy neutron rich nuclei

S. Zemlyanoy[*], V. Zagrebaev[*], E. Kozulin[*], Yu. Kudryavtsev[†], V. Fedosseev[**], R. Bark[‡] and Z. Janas[§]

[*] *JINR Dubna, 141980 Dubna, Moscow region, Russia*
[†] *Instituut voor Kern- en Stralingsfysica, Leuven, Belgium*
[**] *CERN, Switzerland*
[‡] *iThemba LABS, Nat. Research Foundation, South Africa*
[§] *Faculty of Physics, University of Warsaw,Warsaw, Poland*

Abstract. The current status of the new GAs cell based Laser ionization and Separation setup (GALS) at Flerov Laboratory for Nuclear Reactions (FLNR) - JINR, Dubna is reviewed. GALS is planned to exploit available beams from the U-400M cyclotron in low energy multi-nucleon transfer reactions to study exotic neutron-rich nuclei located in the "north-east" region of nuclear map. Products from 4.5 to 9 MeV/nucleon heavy-ion collisions, such as ^{136}Xe on ^{208}Pb, are to be captured in a gas cell and selectively laser-ionized in a sextupole (quadrupole) ion guide extraction system.

Keywords: neutron-rich nuclei, multi-nucleon transfer reactions, laser ionization
PACS: 25.60.Je, 28.60.+s, 42.62.Fi

INTRODUCTION

The heavy neutron rich nuclei in the "north-east" part of the nuclide chart are from extremely importance for nuclear physics investigations, especially for the understanding of astrophysical nucleosynthesis and r-process. The closed neutron shell $N = 126$ - the so called last "waiting point" for the r-process - is located just in this region (Fig. 1). Neutron shell $N = 126$ is a classical shell closures for nuclei along the line of stability. However, as one moves away from the line of stability, abrupt changes in nuclear structure can arise. Especially, appearance of new magic numbers and/or disappearance of traditional ones as well as the onset of deformation are expected, as e. g. already observed in the region of lighter nuclei. Study of the structural properties of nuclei along the neutron shell $N = 126$ could contribute to the current discussion about the quenching of shell gaps in nuclei with large neutron excess. A creation and launch of this facility will open a new field of research in low-energy heavy-ion physics, and new horizons in the study of unexplored "north-east" area of the nuclear map. It could be helpful also for finding a new way for the production of heavy and superheavy nuclei.

Experiments at GALS are intended for production of heavy neutron rich nuclei in the above mentioned region by using multi-nucleon transfer reactions. As shown by Zagrebaev and Greiner [1], several tens of new nuclides in the region of $N = 126$ and $Z \sim 75$ can be produced, for example, in the near-barrier collision of ^{136}Xe with ^{208}Pb. Even higher cross sections have been predicted for the production of new neutron rich

nuclei in collisions of ^{198}Pt beam with ^{238}U target. At present this seems to be the only realistically method [1-3] that could fill the "blank spot" of the nuclear map (Fig. 1).

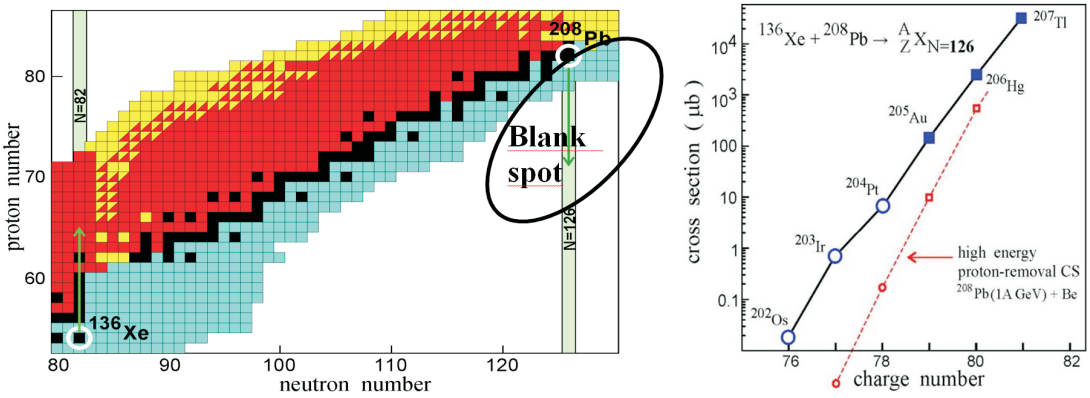

FIGURE 1. Left: upper "north-east" part of nuclear map. Right: cross sections for the formation of heavy nuclei in collisions of ^{198}Pt+^{238}U at center-of-mass energy of 700 MeV. Open circles indicate unknown isotopes [1]. The dashed curve illustrates the yield of the same isotopes in the proton removal reaction from closed shell nucleus ^{208}Pb.

EXPERIMENTAL SETUP

A most suitable experimental method for the purpose of this project is a combined method of Z and A/Q separation. Such method has been proposed in 1992 [4] and subsequently intensively studied (first at LISOL) and developed [5-13]. Known as In-Gas Laser Ionization and Spectroscopy (IGLIS), it is based on stopping of nuclear reaction products in a gas cell and subsequent selective resonance laser ionization [5-13]. Such technique allows extracting nuclei with a given atomic number Z, while a separation of the single-ionized isotopes by their mass number can be done rather easily by a magnetic field. Half-lives of heavy neutron rich nuclei of interest (as a rule, β-decaying), are much longer than the extraction time of ions from a gas cell.

The schematic layout of the proposed facility can be found in [2-3]. Here we present only a brief description of the GALS facility (Fig. 2). Neutron rich isotopes of heavy elements are produced in multinucleon transfer reactions with heavy ions accelerated up to 510 MeV/nucleon (depending on projectile-target combination). The target is a foil of about 300 μg/cm^2 thickness (or larger). It is placed at the window of the gas cell (or inside it). Nuclear reaction products recoiling out from the target as multi-charged ions are thermalized and neutralized by collisions with highly-purified argon or helium buffer gas. Then the atoms of interest (with a given Z) are ionized by means of two or three-step resonance laser irradiation and are extracted by the gas flow through the exit into the vacuum chamber as singly charged ions ($Q = +1$) with low energies of about 0.2 eV. Subsequently, the ions are confined in a radiofrequency ion guide system, which allows pumping out the residual buffer gas while transporting the ions towards the mass separator. Then the ions are accelerated up to $30-60$ keV and selected by the mass-separator. In this way a low-energy beam of singly-ionized ions with a good optical quality (small emittance, energy spread less than 1 eV) is produced. This allows

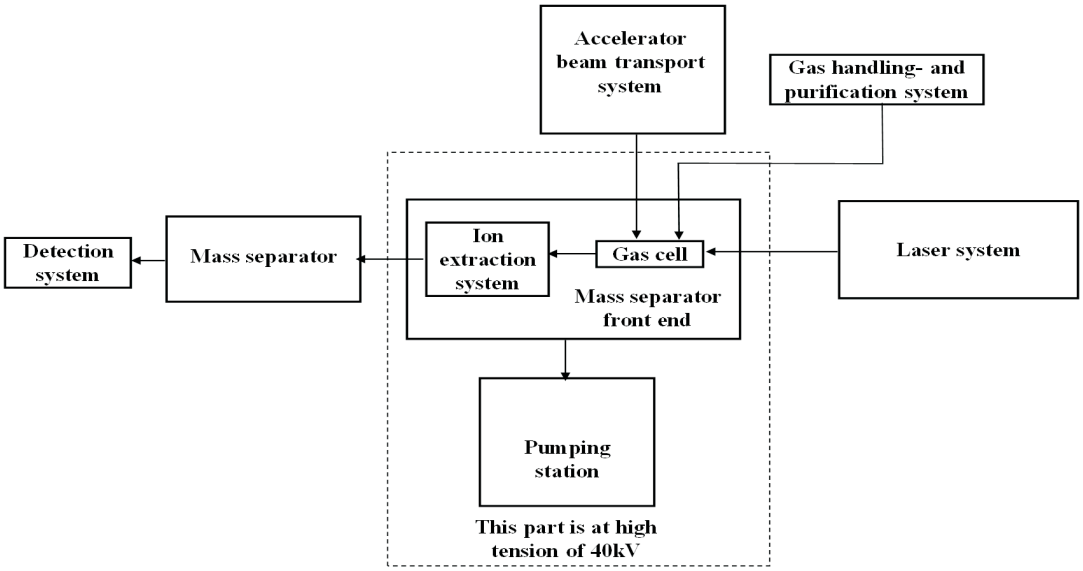

FIGURE 2. Block scheme of GALS-facilities.

obtaining typical mass resolution of 1500 after the dipole magnet. After mass separation a beam of radioactive ions with a definite atomic number and a previously chosen mass value is obtained. The background due to unwanted isobar and isotope admixture is significantly suppressed that leads to an enhanced sensitivity. This gives the possibility to perform subsequently high sensitive analysis of spectroscopic and decay properties of these nuclei, as well as measurements of their spins, magnetic dipole and electric quadrupole moments and charge radii by means of laser spectroscopy. The operation principle of the different parts of the set up can be found in a number of papers (see e.g. [14] and the references therein).

CURRENT STATUS

The GALS project will be realized in stage as determined by the FLNR plans and illustrated in Tab. 1. The ion beams available at FLNR fully satisfy the requirements put from this project: the ions that can be used are quite different depending on the problem to be solved - from ^{16,18}O to ^{238}U, beam energies 4.59 MeV/nucleon (slightly above the Coulomb barrier) and beam intensity up to 10^{13} pps are accessible with a beam size at the target of $3-10$ mm and beam emittance of $20\cdot\pi$·mm·mrad. Different heavy targets, including those of actinides, are expected to be used. Therefore the new facility can be developed and coupled directly to the available U-400M accelerator.

The main parts of the facility to be created and their present status are shown in Tab. 1. Mass separator could be a standard magnet separator similar to GPS at ISOLDE II (see [2, 15]) but nevertheless substantial efforts are needed for its realization. The same refers to the gas purification system. Both, separator and gas purification systems, are in stage of construction and their realization and commissioning will be delayed to the end of 2016. The experimental halls and laser system are in the most advanced stage of

TABLE 1. Status of the project as well as the planned activities in the next two years.

		2015	2016	2017
Laser system	mounting commissioning	yes yes	 yes	Beginning of experiments
Front end system	mounting commissioning	yes	yes yes	
Pump station	mounting commissioning	yes	yes yes	
Gas purification	preparation mounting commissioning	yes	 yes yes	
Separator, detection	preparation mounting commissioning	yes yes	 yes yes	

realization (see Fig. 3).

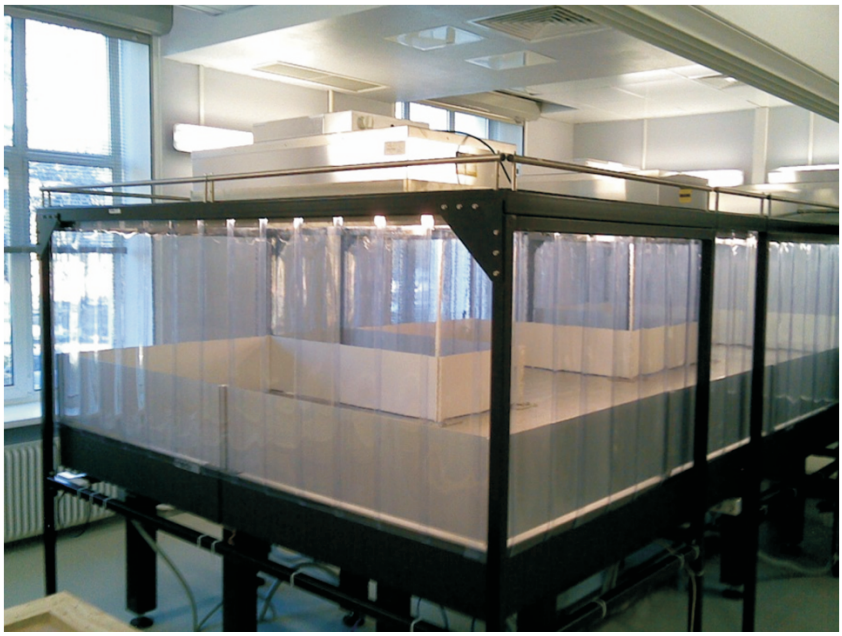

FIGURE 3. Laser laboratory of GALS facility.

The choice of specific laser ionization scheme, the type and number of lasers is determined by the ionization potentials and level schemes of the elements under study. In our case a three-step scheme of ionization looks more favorable. Such a scheme allows choosing more effective optical transitions to increase the yield of resonance-ionized ions, although the use of two-step ionization scheme is as not excluded as well. Dye laser systems pumped by second and third harmonics of Nd:YAG can provide tuning in a broad spectral range: from near UV to near IR [16]. The generation of a Ti:Sapphir lasers, shifted to the red and infrared edge of the spectrum ($680 - 960$ nm), can be also used as complementary to that of the dye lasers. Thus, the installation of two laser-ionization schemes – with dye lasers and Ti:Sapphir laser – would be of a great benefit allowing to meet diverse experimental demands. Such a double RILIS scheme is already

realized in CERN [17]. The parameters of the delivered (and already installed) laser as well as of the ordered ones are summarized in Tab. 2.

TABLE 2. Lasers to be used in multistep ionization. The lasers already delivered are presented in bold.

Type	Output power main&harmonic W (2^{nd}),{3^{rd}, 4^{th}}	Puls frequency, Hz	Puls length, ns	Wave length, nm
Dye laser	**3, (0.3)**	10^4	**10-30**	**213-850**
Ti:Sapphir	2, (0.2), {0.04}	10^4	30-50	680-960
Nd-YAG	**(80-100),** {**20-40**}	10^4	**10-50**	**532**
Matisse system				
Ring dye	0.8-6	cw	cw	540-900
Ti:Sapphir	0.8-6.5	cw	cw	700-1000

At the first stage of our experiments, excitation schemes using 3-step ionization with a non-resonant transition to continuum will be tested with the available lasers: two dye lasers Credo (Sirah) and Nd:YAG. Credo laser has maximal average power of 20 W at fundamental wavelength and 2 W at the second harmonics; its line width is 1.8 GHz at pulse duration about 7 ns. It is an option that allows remote control of wavelength with stabilization to an external laser wavelength meter. The Nd:YAG laser (product of Edge Wave GmbH) generates maximal average power of 90 W and 36 W for the second and third harmonic respectively with repetition rate $10-15$ kHz and pulse duration of $8-10$ ns. The divergence parameter of the green beam is $m^2 = 1.4$. It needs electrical power supply of 3.6 kW including 1.6 kW for the water chiller.

A Matisse series of a ring cw-dye laser and cw-Ti:Sapphir laser pumped by cw-Nd:YAG is planned as a seeding system. Such system has an advantage in the cases when tuning of the laser wavelength is necessary, e.g. for laser spectroscopy.

SUMMARY AND CONCLUSIONS

A new GALS facility at FLNR cyclotron U-400M is in a stage of build-up. GALS will apply the highly selective and efficient technique of stepwise resonant ionization in a gas cell (of the element of interest) with subsequently mass separation. In fact, it is a mass separator from a new type as yet not used in JINR. GALS is addressed to the production and study of new neutron rich nuclei located along the neutron shell $N = 126$. This is the so called "north-east" part of the nuclear map. Nuclei from this region are as yet "terra incognita" but from high fundamental interest mainly due to their large impact of on the astrophysical r-process. The most efficient method to produce such nuclei, as motivated in [1], are the multi-nucleon transfer reactions.

The experimental method is rather universal and allows extracting besides heavy products of multi-nucleon transfer reactions also any other nuclei with half-lives longer than a few tens of milliseconds including neutron rich fission fragments, fusion reaction products and light exotic nuclei. Such studies are already performed at other facilities, for example, in Finland [9], Belgium [10-13], and also using a different approach as that of the hot cavity ion source at CERN [16-17]. The efficiency of such facilities varies from 1% to several tens percent depending on the half-life or the extracted ion.

According to the estimation of the ion yields, at target thickness 0.3 mg/cm^2, ion beam of 0.1 pmA and setup efficiency of 10% we would be able to measure decay properties of 1 new isotope per day.

ACKNOWLEDGEMENT

The authors would like to thank K. Marinova for helpful discussions and advices.

REFERENCES

1. V. Zagrebaev, and W. Greiner, *Phys. Rev. Lett.* **101**, 122701 (2008).
2. V.I. Zagrebaev, S.G. Zemlyanoy, E.M. Kozulin et al., *Hypfine Interacs.* **227**, 181 (2014).
3. V.I. Zagrebaev, S.G. Zemlyanoy, E.M. Kozulin et al., *J. Phys.Conf. Series* **533**, 012025 (2014).
4. P. Van Duppen, P. Dendooven, M. Huyse et al., *Hypfine Interacs.* **74**, 193 (1992).
5. L. Vermeeren, N. Bijnens, M. Huyse et al., *Phys. Rev. Lett.* **73**, 1935 (1994).
6. Y. Kudryavtsev et al., *Nucl. Instrum. Methods Phys. Res. B* **114**, 350 (1996).
7. Y. Kudryavtsev et al., *Nucl. Instrum. Methods Phys. Res. B* **204**, 336 (2002).
8. M. Facina et al., *Nucl. Instrum. Methods B* **226**, 401 (2004).
9. I.D. Moore et al., *J. Phys. G: Nucl. Part. Phys.* **31**, S1499 (2005).
10. Y. Kudryavtsev et al., *Nucl. Instrum. Methods Phys. Res. B* **267**, 2908 (2009).
11. R. Ferrer et al., *Nucl. Instrum. Methods Phys. Res. B* **291**, 29 (2012).
12. R. Ferrer et al., *Nucl. Instrum. Methods Phys. Res. B* **317**, 570 (2013).
13. Y. Kudryavtsev et al., *Nucl. Instrum. Methods Phys. Res. B* **297**, 7 (2013).
14. P. Campbell, I.D. Moore, and M.R. Pearson, *http://dx.doi.org/10.1016/j.ppnp.2015.09.003* (2015).
15. H.L. Ravn, and B.W. Allardyce, *In: Treatise on Heavy-Ion Science* **8**, 363 (1989).
16. V.N. Fedosseev, L.E. Berg, D.V. Fedorov et al., *Rev. Sci. Instrum.* **83**, 02A903 (2012).
17. S. Rothe, B.A. Marsh, C. Mattolat et al., *J. Phys.: Conf. Series* **312**, 052020 (2011).

SESSION

"CONDENSED MATTER PHYSICS"

Conveners: Yu. Shukrinov, A.E. Botha

Breathing chimeras in a stack of intrinsically coupled Josephson junctions

A. E. Botha*, Yu. M. Shukrinov†,** and M. R. Kolahchi‡

*Department of Physics, University of South Africa, Science Campus, Private Bag X6, Florida 1710, South Africa
†Bogoliubov Laboratory of Theoretical Physics, Joint Institute for Nuclear Research, Dubna, Moscow Region 141980, Russia
**Dubna State University, Dubna, Moscow Region, 141980 Russia
‡Department of Physics, Institute for Advanced Studies in Basic Sciences, Zanjan 45195-1159, Iran

Abstract. Preliminary results show that a stack of intrinsically coupled Josephson junctions, as may be realized in a high temperature superconductors, could have the potential to sustain breathing chimera states. The detection of such chimera states in systems of intrinsic Josephson junctions would confirm the expected nonlocal nature of the coupling and could potentially have useful technological and theoretical implications.

Keywords: breathing chimera states, Josephson junctions, nonlocal coupling, inertial coupling, capacitive coupling
PACS: 05.45.Xt; 05.45.Jn; 89.75.Fb

INTRODUCTION

The occurrence of chimera states [1] is a fascinating and relatively new type of synchronization phenomenon. They are found in systems of identical phase oscillators that are coupled nonlocally (most often), globally (less often) or even locally (currently, one known case) [2]. Depending on the exact nature of the coupling and the initial distribution of phases (the initial condition), the oscillators may divide up into two or more spatially distinct groups, as the system evolves. In certain cases the oscillations can produce a spatiotemporal pattern which simultaneously contains domains of coherent and incoherent oscillations – a chimera state. [1, 3].

A very convenient way of characterizing the chimera state is through the real-valued local order parameter,

$$R(t,x) = \left| \sum_{k=1}^{N} G(x - x_k) \exp\left[i\varphi_k(t) \right] \right|. \tag{1}$$

Here φ_k are the phases of the N oscillators, where $k = 1, 2, \ldots, N$. In general the order parameter has a temporal and spatial dependence. The oscillators are typically assumed to be uniformly distributed in a circle, so that the periodic boundary conditions $x_{N+k} = x_k$ apply. If the circumference of this circle is mapped onto the closed interval $[-a, a]$, the positions of the oscillators can be expressed as $x_k = -a + 2ak/N$.

The continuous function $G(x)$ describes the coupling in the system. For example, in Refs. [1, 3], $G(x) = \left[1 + 0.995\cos(x)\right]/(2\pi)$, with $x \in [-\pi, \pi]$, i.e. $a = \pi$. On the other

hand, in Refs. [4, 5] the simplest possible form of nonlocal coupling was chosen, i.e. the top-hat function

$$G(x) = \begin{cases} 1/(2r), & \text{if } |x| \leq r \\ 0, & \text{if } |x| > r \, . \end{cases} \tag{2}$$

In this case $a = 1$, r is the coupling range and the phases evolve according to the nonlocally coupled set of equations, given by

$$\dot{\varphi}_k = -\frac{2}{N} \sum_{j=1}^{N} G(x_k - x_j) \sin(\varphi_k(t) - \varphi_j(t) + \alpha), \tag{3}$$

with the phase lag parameter $\alpha = 1.46$ [5]. By way of example, Fig. 1 shows the local order parameters, as functions of time, for the system described by Eq. (3), at four different system sizes. As was demonstrated in Ref. [4], for finite N the position of the

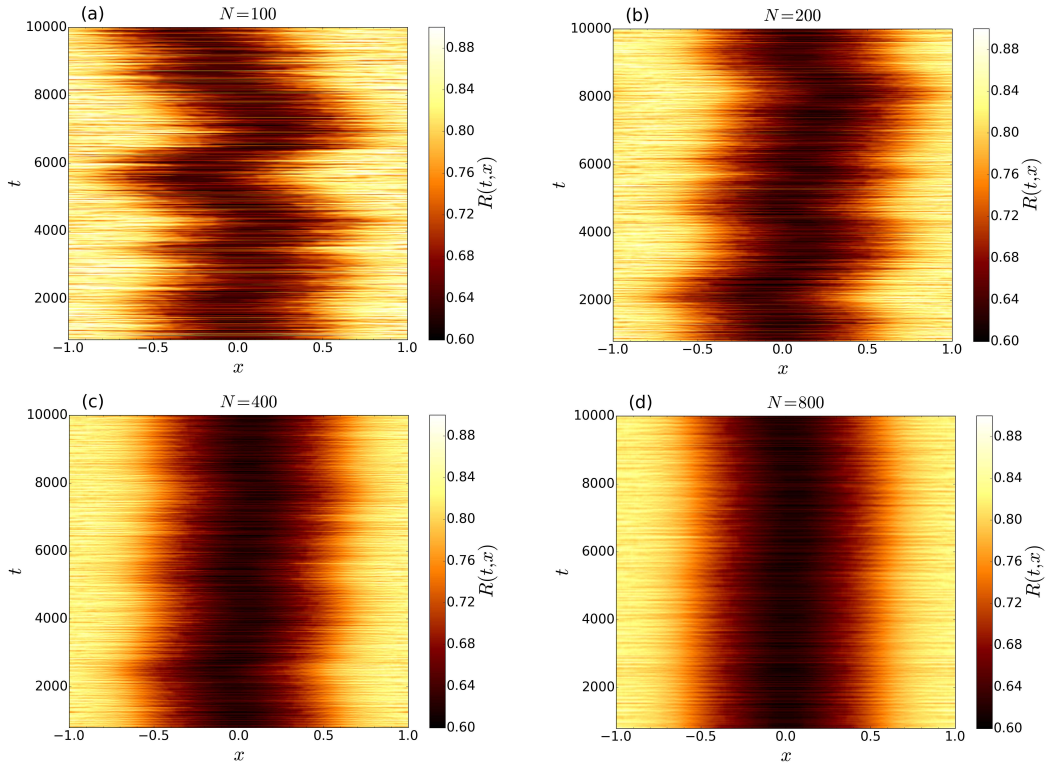

FIGURE 1. Wandering chimera states for the system described by Eq. (3). As the system size approaches the thermodynamic limit ($N \to \infty$), the non-stationary behavior becomes less apparent. This can be seen by comparing the local order parameter $R(t,x)$ for (a) $N = 100$, (b) $N = 200$, (c) $N = 400$, and (d) $N = 800$. As N increases the Brownian motion of the darker (incoherent) region is seen to become increasingly smoother.

incoherently oscillating group, corresponding to darker regions in the figure, meanders chaotically over the circular simulation domain. The successive displacements of the averaged position of the incoherent group are normally distributed, thus giving rise to a Brownian motion. In the limit of infinite N the position of the coherent region is expected to be stationary [4].

In the aforementioned cases [1, 3, 4, 5], the chimera states can all be characterized (at least, in the limit $N \to \infty$) by local order parameters that remain (approximately) constant in time, producing so-called stationary or stable chimeras. However, different studies have revealed several new types of chimeras, including breathing [6], virtual [7], intermittent chaotic [8], travelling [9], and even imperfect chimeras [10]. Imperfect chimera states have recently been observed experimentally in systems of coupled metronomes [10]. Empirically observed (non-stationary) breathing chimera state, which are most similar to the states discussed in the present work have been reported for two subpopulations of oscillators that are globally coupled, both within and between the subpopulations [11]. Such states are characterized by pulsating order parameters [6].

MODEL EQUATIONS AND NUMERICAL METHODS

In the present study the coupling within the CCJJ+DC model [12] will be extended to include nonlocal interaction between the junctions. The modified equations are

$$\frac{\mathrm{d}V_\ell}{\mathrm{d}t} = I + I_\ell^n - \sin\varphi_\ell - \beta\frac{\mathrm{d}\varphi_\ell}{\mathrm{d}t} \tag{4}$$

$$\frac{\mathrm{d}\varphi_\ell}{\mathrm{d}t} = V_\ell + 2\alpha\sum_{m=1}^{N} H_{\ell m}V_m\,, \tag{5}$$

where N is the number of junctions and $H_{\ell m}$ represents the extended coupling. The meaning of the other terms and parameters in Eqs. (4) and (5) has been explained in our previous work [12, 13]. As shown in Fig. 2, for the present case, the matrix elements $H_{\ell m}$ have been obtained from a continuous coupling function at four different coupling ranges.

Abrams and Strogatz [1, 3] have noted that the initial conditions play an important role in setting up a chimera state and generally have to be engineered carefully. Building on their pioneering work, we set the initial phases equal to the randomized symmetric Gaussian distribution: $\varphi_m = r_m \exp\left(-(x_m - x_{N/2})^2/(2\sigma^2)\right)$, where the r_m are random numbers in the range $(-\pi, \pi)$, such that $r_m = r_{N+1-m}$. Initial conditions for the $\dot{\varphi}_m$ were then calculated to correspond to those of single (uncoupled) junctions at the positions φ_m. In practice the calculation of the initial conditions for the $\dot{\varphi}_m$ proceeds as follows. We first consider a single junction at the same dissipation parameter and bias currents as the coupled system. As an initial condition for the single junction we arbitrarily set $\varphi = \pi$ and $\dot{\varphi} = 10$. This initial condition merely ensures that the junction is in a rotating (resistive) state. After allowing a transient time of 1000 dimensionless units, the single junction calculation is then stopped at the desired values of the initial phases. This allows the corresponding initial values for the $\dot{\varphi}$ to be read off from the solution. In this way the initial values set for the $\dot{\varphi}$ ensure that all the junctions in the coupled system initially rotate at approximately the correct frequencies, i.e. they rotate at precisely the frequencies which they would have in the absence of the coupling, i.e. when $\alpha = 0$ and each $\dot{\varphi}_\ell = V_\ell$.

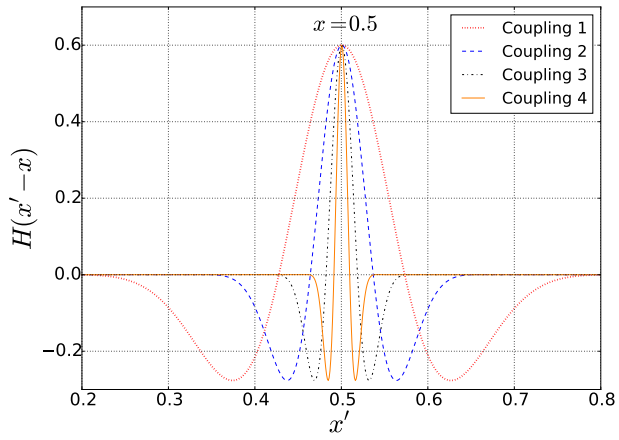

FIGURE 2. Extended coupling at different coupling ranges. Junctions are positioned in a ring (periodic boundary conditions) within the interval [0,1], where x_ℓ is the position of the ℓth junction. For mathematical convenience the coupling is treated as a continuous function: $H_{\ell m} \equiv H(x_\ell - x_m)$. The coupling in the original CCJJ+DC model [12, 13] can be reproduced exactly by the continuous function, $H(x-x') = C\exp(-\frac{(x-x')^2}{2\sigma^2})\left[\cos\left(\frac{2\pi}{\lambda}(x-x')\right) - \delta\right]$, when the coupling range, which is controlled by the parameter σ, is set equal to the separation between junctions.

RESULTS

Figure 3 shows the result of a numerical simulation of Eqs. (4) and (5) for $N = 512$, using the extended continuous Coupling 3.

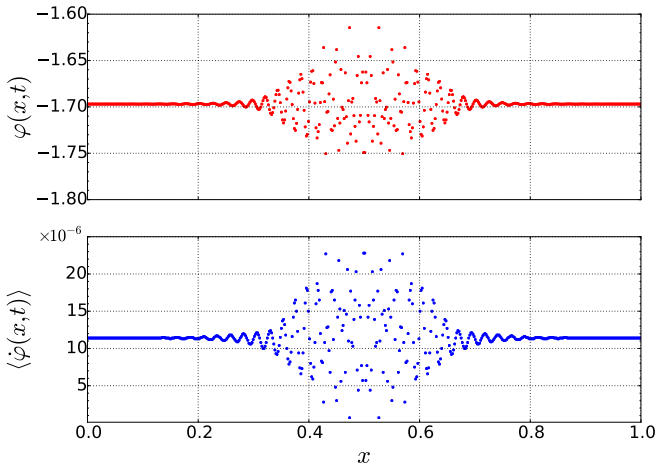

FIGURE 3. Visualisation of the breathing chimera state in a stack of 512 junctions. The top panel shows the instantaneous phase differences for each junction at $t = 10000$. The bottom panel shows the time averaged velocities of the junctions, averaged over the last 1000 dimensionless time units of the simulation. Junctions between about 0.35 and 0.65 are characterized by incoherence among their phases, while those in the remaining region rotate coherently. Note that the scale along the vertical axis of the lower panel runs from 3.990930 to 3.990955, i.e. a range of 25×10^{-6}.

Here we find that the reflection symmetry of the initial condition is retained throughout the entire simulation. Unlike the cases considered by Abrams and Strogatz [1, 3], the symmetric solution appears to be very stable in the present system, and there is no need to impose reflection symmetry artificially [4]. Furthermore, even for the relatively small value of $N = 512$, considered here, the chimera state is stationary, i.e. it does not wander, as discussed previously (see Fig. 1). At this coupling there are three distinct regions seen in the distribution of phases. The outer-most region, ranging from 0 to approximately 0.15 (and from 0.85 to 1) consists of a singly group of oscillators which are rotating almost perfectly in sync. Between about 0.15 and 0.35 the oscillators are also in sync, but for this group the phases are shifted relative to one another in an oscillating pattern. The amplitude of the oscillation increases as one gets closer to the central incoherent region, which is located between about 0.35 and 0.65. Within the central region the phases of the oscillators are scattered, and these oscillators move relative to one another with an almost motion.

Quasi-periodicity within the central group may be easily demonstrated by taking the fast Fourier transforms of the time series for the order parameter $R(t)$, restricted to the central group, as in Ref. [8]. The latter quantity only depends on time and follows from Eq. (1) by setting $G(x) = 1$ and restricting the summation to the oscillators that belong to the central group.

Figure 4 shows that the time series of our $R(t)$ contains one dominant frequency, which is contraindicative to the expected quasi-periodic behaviour that was observed elsewhere.

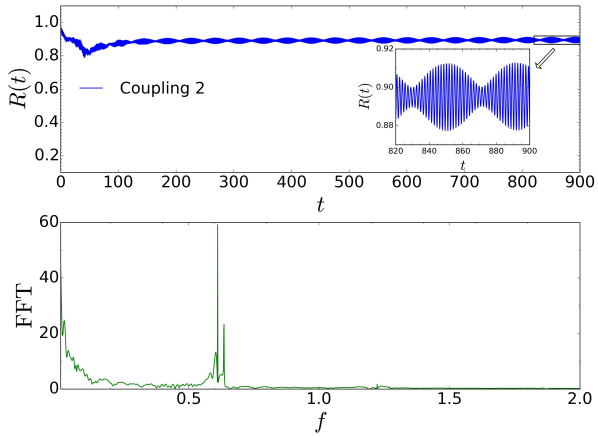

FIGURE 4. Time series of the order parameter $R(t)$ for the chimera state manifested in the case of Coupling 2 (upper panel), and the corresponding FFT spectrum (lower panel), showing that there is only one dominant frequency associated with the (in this case, almost periodic) breathing chimera. The inset in the upper panel shows an enlarged view in which the oscillatory nature of $R(t)$ can be seen more clearly.

CONCLUSION

Chimera states constitute a relatively new class of synchronization phenomena. As mentioned in the introduction, a variety of different types of chimera states have already

been reported in the literature and explored experimentally. Loosely defined, one can conclude that chimera states generally occur due to some innate tendency of identical, identically coupled, oscillators to order themselves into spatially distinct groups, some oscillating coherently; others incoherently. The fact that this ordering is in some way more stable (it appears to be the naturally preferred mode of evolution in such systems) is very intriguing. In a recent review article, Panaggio and Abrams [14] conclude by posing six questions that remain open in connection with chimera states.

In this preliminary report we have extended the coupling range in the well-known CCJJ+DC model of 1-dimensional Josephson junctions. This was done in order to test whether or not such extended coupling may give rise to the interesting phenomenon of chimera states. With the extended coupling, we have demonstrated that the system *is* capable of sustaining a type of breathing chimera state, where the oscillations within the incoherent region appear to be moving almost periodically, relative to one another, rather than quasi-periodically, chaotically or hyperchaotically, as previously reported for other systems with the ineartial-type of coupling, similar to what we have here. OUr result is thus not entirely unexpected, beacause regular breathing chimeras have recently also been reported for a prototype system to which a second order inertial coupling was added [8]. In the present system, however, the second order (capacitive) coupling arises naturally as a result of the dynamic breaking of charge neutrality across junctions. Although the exact range of this coupling is not know precisely for currently available high-T_c materials, it is likely to be nonlocal in nature, as our present explorations anticipate. Furthermore, there may be other ways of achieving the extended non-local coupling; such as, by artificially creating micro-circuits containing Josephson junction elements. Thus, our results support a real possibility for creating chimera states in systems containing intrinsic Josephson junctions, or artificially constructed systems of Josephson junctions. In either case, chimera states created in such systems would be of considerable interest, since they may lead to new insights into this captivating synchronization phenomenon.

ACKNOWLEDGEMENT

M. R. K. thanks F. Osanloo and S. Emadi for helpful discussions related to this work. A. E. B. and Yu. M. S. gratefully acknowledge funding through the JINR-SA agreement – making this work possible.

REFERENCES

1. D. M. Abrams and S. H. Strogatz, “Chimera states for coupled oscillators,” Phys. Rev. Lett. **93**, 174102 (2004).
2. Carlo R. Laing, “Chimeras in networks with purely local coupling," Phys. Rev. E **92**, 050904 (2015).
3. Daniel M. Abrams and Steven H. Strogatz, “Chimera states in a ring of nonlocally coupled oscillators,” Int. J. Bifurcation Chaos 16, 21 (2006).
4. Oleh E. Omel’chenko, Matthias Wolfrum, and Yuri L. Maistrenko, “Chimera states as chaotic spatiotemporal patterns,” Phys. Rev. E 81, 065201(R) (2010).
5. M. Wolfrum, O. E. Omel’chenko, S. Yanchuk, and Y. L. Maistrenko, “Spectral properties of chimera states,” Chaos 21, 013112 (2011).

6. Daniel M. Abrams, Rennie Mirollo, Steven H. Strogatz, and Daniel A. Wiley, "Solvable model for chimera states of coupled oscillators," Phys. Rev. Lett. 101, 084103 (2008).
7. Laurent Larger, Bogdan Penkovsky, and Yuri Maistrenko, "Virtual chimera states for delayed-feedback systems," Phys. Rev. Lett. 111, 054103 (2013).
8. Simona Olmi, "Chimera states in coupled Kuramoto oscillators with inertia," Chaos 25, 123125 (2015).
9. Jianbo Xie, Edgar Knobloch, and Hsien-Ching Kao, "Multicluster and traveling chimera states in nonlocal phase-coupled oscillators," Phys. Rev. E **90**, 022919 (2014).
10. T. Kapitaniak *et al.*, Scientific Reports **4**, 6379 (2014).
11. Mark R. Tinsley, Simbarashe Nkomo, and Kenneth Showalter, "Chimera and phase-cluster states in populations of coupled chemical oscillators," Nat. Phys. **8**, 662 (2012).
12. Yu. M. Shukrinov, F. Mahfouzi, and P. Seidel, Physica C **449**, 62 (2006).
13. A. E. Botha, Yu. M. Shukrinov, S. Yu. Medvedeva, and M. R. Kolahchi, "Structured chaos in 1-d stacks of intrinsic Josephson junctions irradiated by electromagnetic waves," J. Supercond. Novel Magnetism **28**, 349 (2015).
14. Mark J. Panaggio and Daniel M. Abrams, "Chimera states: Coexistence of coherence and incoherence in networks of coupled oscillators," Nonlinearity **28**, R67 (2015).

Numerical study of Josephson nanostructures using parallel computing

I. R. Rahmonov[a,b], Yu. M. Shukrinov[a,d], E. V. Zemlyanaya[c,d], M. V. Bashashin[c,d] and P. Atanasova[e]

[a] *BLTP, Joint Institute for Nuclear Research, Dubna 141980, Russia*
[b] *Umarov Physical and Technical Institute, Dushanbe 734063, Tajikistan*
[c] *LIT, Joint Institute for Nuclear Research, Dubna 141980, Russia*
[d] *Dubna State University, Dubna 141982, Russia*
[e] *Plovdiv University "Paisii Hilendarski", Plovdiv 4003, Bulgaria*

Abstract. We investigate the phase dynamics of the stack of long JJs, the length of which exceeds the Josephson penetration depth λ_J, taking into account the inductive and capacitive couplings between junctions and diffusion current. Numerical simulation of current–voltage characteristics of the stack is based on numerical solution of a system of nonlinear partial differential equations by the fourth order Runge–Kutta method and finite-difference approximation. The calculations are performed using the MPI technique for parallel implementation. The methodical calculations on multiprocessor cluster (LIT JINR) with a different number of parallel MPI-processes are carried out. We have shown that the developed parallel algorithm provides 5-7 time acceleration in comparison with serial simulation.

Keywords: Josephson junction, inductive coupling, capacitive coupling
PACS: 74.20.-z; 74.72.Hs; 02.60.-x

INTRODUCTION

The layered high-Tc superconducting materials such as $Bi_2Sr_2CaCu_2O_{8+\delta}$ (BSCCO) can be considered as a stack of coupled Josephson junctions (JJs) [1]. The interest to the investigation of this system is caused by its rich nonlinear properties. The JJs stack demonstrates a series of interesting properties such as parametric resonance [2, 3, 4], chaotic features [5] and in this system the fluxons [6, 7, 8, 9] and collective excitations [4, 10, 11] can arise. Also, this system is one of the promising objects of superconducting electronics [12, 13]. Coherent terahertz electromagnetic radiation from this system provides wide possibilities for various applications [14]. So, the stack of coupled JJs can be considered as a laboratory for studying nonlinear phenomena in superconducting nanostructures. Therefore, the construction of a model that ensures an adequate description of the properties of the coupled JJs in the high temperature superconductors is one of the topical tasks of modern physics of superconductivity. Also, an actual problem is the construction of effective numerical algorithms for simulation of the phase dynamics of the stack of JJ.

To describe the JJs stack in Ref.[15] a model with inductive coupling between JJs was proposed. Later, Machida and Sakai proposed the model which takes into account both inductive and capacitive couplings [16]. In Ref.[4], we generalized this model with the additional diffusion current [17], whose significance was emphasized.

In this paper, we investigate the effectiveness of a parallel numerical approach for simulation of phase dynamics of stacked JJs taking into account the inductive and capacitive couplings [15, 16] and the diffusion current [18]. Simulation is based on a numerical solution of a system of nonlinear partial differential equations by the fourth order Runge–Kutta method, a finite-difference approximation, and the MPI technique for parallel implementation. The effectiveness of the MPI/C++ code is confirmed by calculations on the multi-processor cluster (LIT JINR, Dubna).

THEORETICAL MODEL AND NUMERICAL APPROACH

Let us consider the layered structure with $N+1$ superconducting and interjacent insulating layers. The x-and y-axes are directed along the length of JJ L and along the width of superconducting layers W, respectively. The z-axis is perpendicular to the superconducting layers. The length of JJ $L > \lambda_J$ and the width $W << \lambda_J$. Each superconducting layer with number l is described by the Ginzburg–Landau order parameter $\Delta_l = |\Delta_0| \exp(i\theta_l)$, where θ_l is the phase of the order parameter. The l-th and $l-1$-th superconducting layers form the l-th JJ and it is described by the gauge–invariant phase difference (1) of the Ginsburg–Landau order parameter [16].

$$\varphi_l = \theta_l - \theta_{l-1} - \frac{2e}{\hbar c} \int\limits_{z_{l-1}}^{z_l} A_z dz. \tag{1}$$

where e - the electrical charge, $\hbar$ - the Plank constant, c - the speed of light in vacuum and A_z is the vector potential. In the framework of this model, due to the presence of capacitive coupling, the AC Josephson relation is generalized and can be written as

$$\frac{\hbar}{2e} \frac{\partial \varphi_l}{\partial t} = D_c V_l + s_c V_{l+1} + s_c V_{l-1}, \tag{2}$$

where $D_c = 1 + (2\lambda_e/d_I)\coth(d_s/\lambda_e)$ is the effective electrical thickness of JJ normalized to the insulating layer thickness d_I, $s_c = -\lambda_e/[d_I \sinh(d_s/\lambda_e)]$ is the capacitive coupling parameter, V_l is the voltage on the lth JJ, d_s is the thickness of superconducting layer, and λ_e is is Debye screening length.

The derivative of phase difference φ_l of lth with respect to the coordinate depends on the magnetic field of the lth JJ and neighbor $l+1$ and $l-1$ junctions.

$$\frac{\hbar c}{2eD_£} \frac{\partial \varphi_l}{\partial x} = B_l + SB_{l+1} + SB_{l-1}, \tag{3}$$

where $S = s_£/D_£$ is the inductive coupling parameter, $s_£ = -\lambda_L/\sinh(d_s/\lambda_L)$, $D_£ = d_I + 2\lambda_L \coth(d_s/\lambda_L)$ is the effective magnetic thickness of JJ, and λ_L is the London penetration depth. The valid values of the inductive coupling parameter S are in the range $S \in (-0.5, 0]$.

The system of equations, which describes the phase dynamics of the coupled long JJs stack in the normalized quantities, can be written as follows:

$$\begin{cases} \dfrac{\partial \varphi_l}{\partial t} = D_C V_l + s_C V_{l+1} + s_C V_{l-1}, \\ \dfrac{\partial V_l}{\partial t} = \displaystyle\sum_{k=1}^{N} \pounds_{lk}^{-1} \dfrac{\partial^2 \varphi_k}{\partial x^2} - \sin\varphi_l + \beta \dfrac{\partial \varphi_l}{\partial t} + I, \end{cases} \tag{4}$$

In this system of equations the voltage is normalized to $V_0 = \hbar\omega_p/(2e)$, where $\omega_p = \sqrt{8\pi d_I e j_c/(\hbar\varepsilon)}$ is the plasma frequency of JJ, j_c is the critical current of JJ, and ε is the dielectric constant of the insulating layer. The time t and coordinate x are normalized to ω_p and λ_J, respectively. Here $\beta = \sigma V_0/(d_I j_c)$ is the dissipation parameter, σ is the conductance of JJ, and I is the bias current normalized to the critical current j_c.

The matrix of inductive coupling $\pounds$ has the form

$$\hat{\pounds} = \begin{pmatrix} 1 & S & 0 & \ldots & & & S \\ & & & & \ldots & & \\ \ldots & 0 & S & 1 & S & 0 & \ldots \\ & & & & & & \\ S & & & & 0 & S & 1 \end{pmatrix},$$

The initial conditions for the system of equations (4) are $\varphi_l(x,0) = 0$ and $V_l(x,0) = 0$. The boundary conditions in the x dirrection given by the external magnetic field $(\hbar c)/(2eD_{\pounds})\partial\varphi_l/\partial x|_{x=0,L} = B_{ext}$. In the z dirrection we use the periodic boundary condition: in the case $l = N$ $\varphi_{l+1} = \varphi_1$, $V_{l+1} = V_1$; in the case $l = 1$ $\varphi_{l-1} = \varphi_N$, $V_{l-1} = V_N$.

SIMULATION OF CURRENT-VOLTAGE CHARACTERISTIC

One of the main electromagnetic properties of the system is current–voltage characteristics (CVC). In order to calculate CVC, we first of all solve numerically the system of partial differential equations (4) for the fixed value of bias current I and obtain the spatiotemporal distribution of the phase difference $\varphi(x,t)$ and voltage $V(x,t)$ of JJs. The details of numerical solution of differential equations are considered in the next section, and here we confine ourselves just to the consideration of the algorithm calculation of CVC. Next, we have averaged the obtained $V_l(x,t)$ with respect to the coordinate x using

$$\bar{V}_l(t) = \frac{1}{L}\int_0^L V_l(x,t)dx \tag{5}$$

and with respect to the time t with expression (6)

$$\langle V_l \rangle = \frac{1}{T_{\max} - T_{\min}} \int_{T_{\min}}^{T_{\max}} \bar{V}_l(t)dt, \tag{6}$$

where $T_{\min}$ is the beginning of the averaging interval. The total voltage of the JJs stack can be calculated using $\langle V \rangle = \sum_{l=1}^{N} \langle V_l \rangle$. Integrals (5) and (6) are calculated using the

Simpson method and the rectangles method, respectively. Then we change the bias current value by ΔI and repeat the above procedure. In our calculations the bias current increases from the starting value $I = 0.01$ to $I = I_{\max}$ and then decreases to $I = 0$.

NUMERICAL SCHEME

In order to solve the system of eq.(4), we introduce the uniform mesh with the stepsize Δx in the coordinate x along JJ and the stepsize Δt in time (Fig.1).

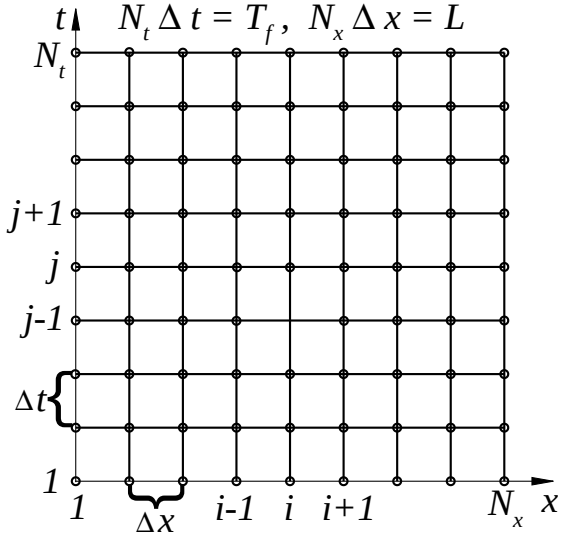

FIGURE 1. The uniform spatiotemporal mesh scheme

We denote the discrete coordinate by $x_i = \Delta x \times (i-1)$, where $i = 1,\ldots,N_x$ and $N_x = L/\Delta x + 1$ - the number of coordinate nodes. The discrete time is denoted by $t_j = \Delta t \times (j-1)$, where $j = 1,2,\ldots N_t$. The $x = 0$ corresponds to x_1; and $x = L$, to x_{N_x}. In the same way, $t = 0$ corresponds to t_1; and $t = T_{\max}$, to t_{N_t}, where $T_{\max}$ is the end of the time domain. We employ the standard second order finite difference approximation in the spatial coordinate x

$$\frac{\partial^2 \varphi_l^1}{\partial x^2} = \frac{2(\varphi_l^2 - \varphi_l^1)}{\Delta x^2} - \frac{2B_{\text{ext}}}{\Delta x}, \quad \frac{\partial^2 \varphi_l^{N_x}}{\partial x^2} = \frac{2(\varphi_l^{N_x-1} - \varphi_l^{N_x})}{\Delta x^2} + \frac{2B_{\text{ext}}}{\Delta x},$$

$$\frac{\partial^2 \varphi_l^i}{\partial x^2} = \frac{\varphi_l^{i+1} - 2\varphi_l^i + \varphi_l^{i-1}}{\Delta x^2}.$$

Then we solve numerically the resulting system of ordinary differential equations for a fixed value of current I by the 4th-order Runge-Kutta (RK) algorithm (here l is the JJ number) in the interval $[0,L]$ by the coordinate and $[0,T_{\max}]$ by time and obtain the $\varphi_l(x,t)$ and $V_l(x,t)$ as functions of x and t. We put $\Delta t = \Delta x/5$ in accordance with the Courant–Friedrichs–Lewy condition in order to provide stability of the numerical scheme.

In order to investigate the collective excitations in the JJs stack like the longitudinal plasma wave [19] or charge traveling wave [20], we need to calculate the electric charge–time dependence in the superconducting layers. In this case, we calculate the electric charge normalized to $Q_0 = \varepsilon V_0/4\pi d_s d_I$ as a function of x and t using the expression $Q_l(x,t) = V_l(x,t) - V_{l-1}(x,t)$ [4]. Then we average the value of $Q_l(x,t)$ with respect to the coordinate x using the Simpson method. For the external current value corresponding to the fluxon states we calculate the magnetic field B in the JJs using the expression $B_l = \sum_{k=1}^{N} \pounds_{lk}^{-1}(\partial\varphi_k/\partial x)$. The magnetic field is normalized to $B_0 = \hbar c/2eD_L\lambda_J$.

PARALLEL IMPLEMENTATION

The parallel algorithm is based on the distribution of calculations in the coordinate nodes x_i between the group of P_m parallel MPI-processes, where $m = 0, 1 \ldots, M$. At each time-step t_j, each process P_m calculates the RK coefficients and $V_l(x_i,t_j)$, $\phi_l(x_i,t_j)$ in the nodes $i_{\min} \le i < i_{\max}$, where $i_{\min} = m \times L_x/M$ and $i_{\max} = (m+1) \times L_x/M$. At each t_j the exchange between neighbor processes is arranged: each process P_m $(m < M-1)$ sends the RK coefficients and values of V and φ at $i = i_{\max} - 1$-th point to the P_{m+1}-process; each P_m process $(m > 0)$ sends the RK coefficients and solutions at $i = i_{\min}$ to the P_{m-1}-process. In order to calculate the average value V_l, the parallel calculation of the integral (5) is performed at each time-step t_j. Each P_m-process calculates the partial sum of elements $V_l(x_i,t_j)$ at each JJ with number l, in accordance with the Simpson quadrature formula. Then the resulting summation is performed in the process P_0. In the P_0-process V_l is averaged in time and in JJs number, and the resulting value is saved to the file. For some values of I the solutions $V_l(x_i,t_j)$ and $\phi_l(t_i,t_j)$ are collected in the process P_0 where they are saved to the file together with the respective physical characteristics.

RESULTS AND DISCUSSION

Let us discuss the effectiveness of the parallel algorithm. The calculations have been performed on the multi-processor cluster (LIT JINR) with a different number of parallel MPI-processes. For these calculations we put the number of JJs $N = 10$ and $N = 5$, the JJ length $L = 5$ and $L = 10$; $\Delta x = 0.05$; $\Delta I = 0.0001$. Figure 2 shows the calculation time (in minutes) of the CVC vs number of parallel processes for the following cases: $N = 10$, $L = 5$; $N = 5$, $L = 10$ and $N = 10$, $L = 5$. For all cases the minimumal calculation time is achieved in the case of 12 processes. The ratio of the calculation time of 1 process and 12 processes for the case of $L = 5$ and $N = 10$ (line 1 in Fig.2) is equal to 5.38. The same ratio for the case of $L = 10$ and $N = 5$(line 2 in Fig.2) is equal to 6.1. In the case $L = 10$, $N = 5$ the speedup is equal to 6.97 (line 3 in Fig.2).

One can see that the developed parallel algorithm provides 5-7 times acceleration (depending on the values of N and L) in comparison with the serial simulation. We should like to note that the good speed up of calculations can be obtained for the cases of big values of JJ length.

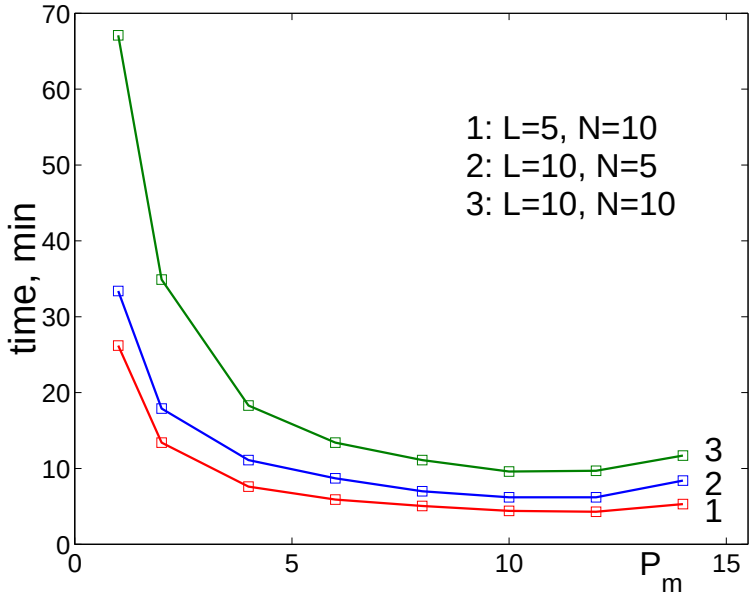

FIGURE 2. The dependence of calculation time on the number of processes.

CONCLUSIONS

In this paper, we have presented the method of numerical simulation of the phase dynamics of the stacked JJs taking into account the inductive and capacitive couplings between junctions and diffusion current. In our investigation, we used the parallel and serial calculations of CVC. The parallel implementation is based on the MPI technique. We showed that the parallel algorithm provides the 5-7 time acceleration in comparison with the serial one.

ACKNOWLEDGEMENT

The study was funded by the RFBR, according to the research project 15–29–01217.

REFERENCES

1. R. Kleiner, F. Steinmeyer, G. Kunkel, P. Müller, *Phys. Rev. Lett.* **68**, 2394 (1992).
2. Yu. M. Shukrinov and F. Mahfouzi, *Phys. Rev. Lett.* **98**, 157001 (2007).
3. Yu. M. Shukrinov, F. Mahfouzi, and M. Suzuki, *Phys. Rev. B* **78**, 134521 (2008).
4. I.R. Rahmonov, Y.M. Shukrinov, A. Irie, *JETP Letters* **99**, 632 (2014).
5. Yu. M. Shukrinov, A. E. Botha, S. Yu. Medvedeva, M. R. Kolahchi and A. Irie, *Chaos* **24**, 033115 (2014).
6. T.A. Fulton and R.C. Dynes, *Solid St. Commun.* **12** 57 (1972).
7. N. F. Pedersen and D. Welner, *Phys. Rev. B* **29**, 2551 (1984).
8. D. W. McLaughlin and A. C. Scott, *Phys. Rev. A* **18**, 1652 (1978).
9. S. Lin, X. Hu, *Phys. Rev. Lett.* **100**, 247006 (2008).
10. R. Kleiner, T. Gaber, G. Hechtfischer, *Phys. Rev. B* **62**, 4086 (2000).

11. Y. Matsuda, M.B. Gaifullin, K. Kumagai, K. Kadowaki, T. Mochiku, *Phys. Rev. Lett.* **75**, 4512 (1995).
12. A.A. Yurgens, *Supercond.Sci.Technol.* **13**, R85 (2000).
13. T.M. Benseman, A.E. Koshelev, K.E. Gray, W.K. Kwok, U. Welp, K. Kadowaki, M. Tachiki, T. Yamamoto, *Phys. Rev. B* **84**, 064523 (2011).
14. L. Ozyuzer, A.E. Koshelev, C. Kurter et al., *Science* **318**, 1291 (2007).
15. S. Sakai, P. Bodin, N.F. Pedersen, *J. Appl. Phys.* **73**, 2411 (1993).
16. M. Machida, S. Sakai, *Phys. Rev. B* **70**, 144520 (2004).
17. Y.M. Shukrinov, F. Mahfouzi, *Physica C* **434**, 6 (2006).
18. Y.M. Shukrinov, I.R. Rahmonov, *JETP* **115**, 289 (2012).
19. Y.M. Shukrinov, F. Mahfouzi, *Phys. Rev. Lett.* **98**, 157001 (2007).
20. Y.M. Shukrinov, M. Hamdipour, *JETP Letters* **95**, 307 (2012).

Simulations of dc SQUIDs with topologically trivial and nontrivial barriers

E. M. Benecha[*], R. Dawood[†], I. R. Rahmonov[**,‡], Yu. M. Shukrinov[**,§] and A. E. Botha[¶]

[*]*College of Graduate Studies, University of South Africa, P.O. Box 392, UNISA 0003, Pretoria, South Africa*
[†]*Department of Physics, Cairo University, Giza 12613, Egypt*
[**]*Bogoliubov Laboratory of Theoretical Physics, Joint Institute for Nuclear Research, Dubna, Moscow Region 141980, Russia*
[‡]*Umarov Physical Technical Institute, TAS, Dushanbe, 734063 Tajikistan*
[§]*Dubna State University, Dubna, Moscow Region 141980, Russia*
[¶]*Department of Physics, University of South Africa, Science Campus, Private Bag X6, Florida 1710, South Africa*

Keywords: dc-SQUID, Josephson junctions, Majorana Fermion, trivial barriers, nontrivial barriers
PACS: 05.45.Xt; 05.45.Jn; 89.75.Fb

INTRODUCTION

The possibility of creating the Majorana quasi-particles [1] in condensed-matter systems has become a focus of intense attention in recent years [2]. Superconducting Quantum Interference Devices (SQUIDs) with Josephson junctions containing topologically nontrivial barriers are among the leading candidates for the detection and manipulation of the Majorana Fermion [3, 4]. The appearance of Majorana bound states in the superconducting junctions enables tunneling of quasi particles with charge e across the junction, instead of $2e$ for cooper pair transport in conventional barriers, resulting in the doubling of the Josephson periodicity of the tunneling current from $I_c = I_0 \sin(\varphi)$ to $I_c = I_0 \sin(\frac{\varphi}{2})$. The doubled periodicity is predicted to lead to a SQUID modulation period of $2\Phi_0$ instead of the usual Φ_0 periodicity, where $\Phi_0 = \frac{h}{2e}$ is the magnetic flux quantum, which in turn doubles the period of the flux dependence of the supercurrent from 2π to 4π [3].

The experimental detection of Majorana Fermions in superconducting junctions containing topologically nontrivial barriers has mainly relied on measurement of zero-bias conductance peak [5, 6, 7] or observation of the 4π periodic dependency of the Josephson supercurrent [8], among other methods [9]. However, the effectiveness of the former set of experiments has been questioned since the expected $\frac{2e^2}{h}$ value of tunneling conductance zero-bias peak may be obscured by resonances from subgap states at nonzero energy as well as the presence of other effects such as magnetic impurities [10]. On the other hand, relaxation to equilibrium states, quantum phase slips, and the large bulk shunt present in contacts with topological insulators may reduce the 4π-periodic dependency. Therefore, there is need to find more definite signatures of the Majorana Fermion in condensed matter systems.

Previously [11], it has been shown that dc-SQUIDs containing trivial barriers exhibit

resonance behavior on their IV-characteristics, while a recent study [8] carried out on SQUIDs with topologically nontrivial barriers has demonstrated that the SQUID parameters β_L and β_c can be used to increase the ratio of Majorana tunneling to standard cooper pair tunneling by more than two orders of magnitude. In this work, we study in detail the behaviour of dc-SQUIDS containing topologically nontrivial barriers in comparison with trivial barriers (where the Josephson junction is typically an ordinary metal or insulator) using the resistively and capacitively shunted Josephson junction (RCSJ) model. We find that the I-V characteristics between the two cases presents significant distinctions which might provide strong signatures in the experimental detection of the Majorana Fermions.

MODEL AND METHODS

Charge transport through a Josephson junction containing a topologically nontrivial barrier is characterised by the standard cooper pair tunneling $[\sin(\varphi)]$ and single electron tunneling by virtue of the Majorana Fermion $[\sin(\frac{\varphi}{2})]$. The relative contribution of these two processess is determined by a factor γ which is connected to the charge carrier $q = \frac{2e}{\gamma}$. In this study, we consider two scenarios where the superconductor is either nontrivial $\gamma = 2$ or topologicaly trivial $\gamma = 1$

When a magnetic field threads a superconducting loop, the flux is quantized according to

$$\frac{\varphi_1 - \varphi_2}{\gamma} + 2\pi\frac{\Phi_t}{\Phi_0} = 2\pi n \tag{1}$$

where $\varphi_1 - \varphi_2$ is the phase drop over the junctions. The total flux Φ_t (normalized to the flux quanta $\Phi_0 = h/2e$) constitutes the sum of the external flux Φ_e and the self-flux induced by the current flowing through the ring, and is given by

$$\frac{\Phi_t}{\Phi_0} = \frac{\Phi_e}{\Phi_0} + \beta_L(\chi_1 - \chi_2) \tag{2}$$

where $\beta_L = \frac{2\pi}{\Phi_0}LI_c$ is a screening parameter which represents the ratio of the magnetic flux generated by the maximum possible circulating current I_c and $\frac{\Phi_0}{2\pi}$. The factor $\chi_{1,2}$ denotes the current dependence on the phase difference of the individual junctions and is given by $\chi_i = \alpha_i \sin(\varphi_i) + (1-\alpha_i)\sin(\varphi_i/2)$ with $\alpha = 0$ for single electron tunneling due to the majorana Fermion (nontrivial case) or $\alpha = 1$ due to cooper pair tunneling (trivial case).

We have modelled the SQUID transport equations using the resistively and capacitively shunted junction (RCSJ) model as shown Figure 1.

Assuming an ideal Josephson junction shunted by a capacitor C and resistor R, the currents through the junctions can be written as $I = C\frac{dV}{dt} + \frac{V}{R} + I_c\chi_{1,2}$, where the voltage is related to the time derivative of the phase by the Josephson relation

$$V = \frac{\gamma\hbar}{2e}\frac{d(\varphi/\gamma)}{dt} = \frac{\hbar}{2e}\frac{d\varphi}{dt} \tag{3}$$

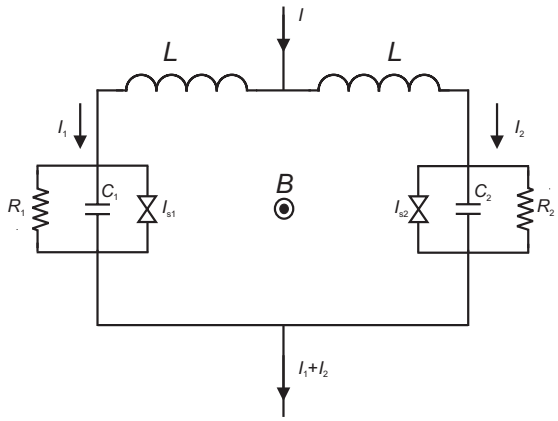

FIGURE 1. SQUID equivalent circuit.

Therefore, the current through each junction can be written as

$$\begin{cases} I_1 = \beta_c \dfrac{d^2\varphi}{dt^2} + \dfrac{d\varphi}{dt} + \chi_1 \\ I_2 = \beta_c \dfrac{d^2\varphi}{dt^2} + \dfrac{d\varphi}{dt} + \chi_2 \end{cases} \tag{4}$$

where $\beta_c = 2\pi I_c R^2 C/\Phi_0$ is the Mc-Cumber parameter. Applying the fluxoid quantization condition (equation 1), the voltage state can be described by the following differential equations which we have solved numerically using the forth order Runge-Kutta method.

$$\begin{cases} \dfrac{\partial\varphi_1}{\partial t} = V_1 \\ \dot{V}_1 = \dfrac{1}{\beta_c}\left\{\dfrac{I}{2} - V_1 - \chi_1 + \dfrac{1}{2\beta_L}\left[2\pi(n-\varphi_e) - \dfrac{1}{\gamma}\left(\sum_{i=1}^{N_1}\varphi_i - \sum_{j=1}^{N_2}\varphi_j\right)\right]\right\} \\ \dfrac{\partial\varphi_2}{\partial t} = V_2 \\ \dot{V}_2 = \dfrac{1}{\beta_c}\left\{\dfrac{I}{2} - V_2 - \chi_2 - \dfrac{1}{2\beta_L}\left[2\pi(n-\varphi_e) - \dfrac{1}{\gamma}\left(\sum_{i=1}^{N_1}\varphi_i - \sum_{j=1}^{N_2}\varphi_j\right)\right]\right\} \end{cases} \tag{5}$$

RESULTS AND DISCUSSION

Figure 2 shows the I-V characteristics of a dc-SQUID with trivial and nontrivial Josephson barriers simulated for an external flux of $\Phi_e = 0$ and $\Phi_e = 1$.

It can be seen that applying an external flux leads to the occurrence of branches in the I-V characteristics, the so called beating solutions. The beating solutions occur when the Josephson frequency equals the frequency of the circuit formed by the loop

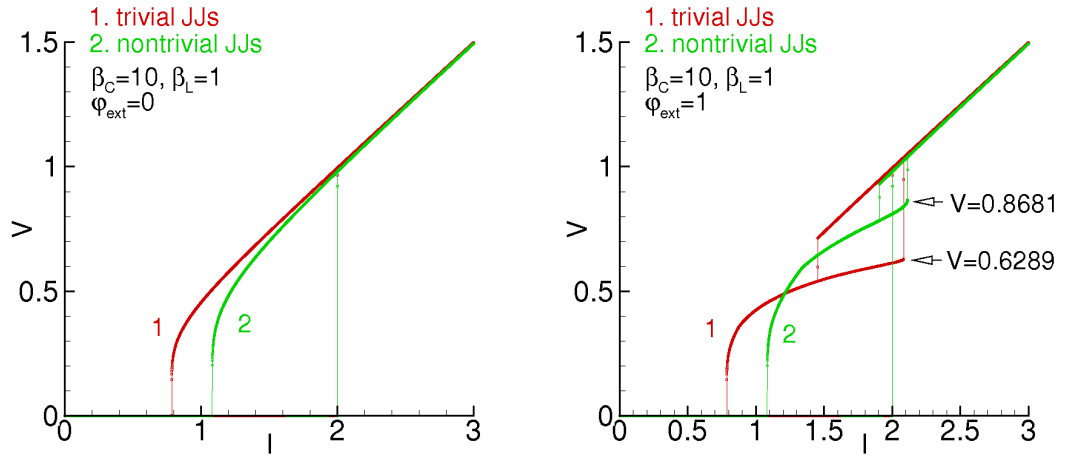

FIGURE 2. Current-voltage characteristics of a DC-SQUID with trivial and nontrivial Josephson barriers simulated for $\varphi_e = 1$; $\beta_c = 10$ and $\beta_L = 1$.

inductance L and the junction capacitance C, in which case the resonance voltage becomes $V_{res} = n\sqrt{\frac{\gamma}{\beta_c \beta_L}}$ (n=1,2,3, ...), where $\gamma = 1$ and $\gamma = 2$ for trivial and nontrivial junctions, respectively. Importantly, we find that V_{res} for SQUIDs with nontrivial barriers is higher by a factor of $\sqrt{2}$ compared to SQUIDS with trivial barriers.

In order to understand the effect of increasing the number of junctions on the behavior of the SQUID, we have simulated the I-V characteristics for a stack of coupled ($\alpha = 0.1$) Josephson junctions on each loop for both trivial and nontrivial cases, and the result is as shown in Figure 3. We find that increasing the number of Junctions reduces the size of the voltage steps, with the effect being more pronounced in the case of nontrivial

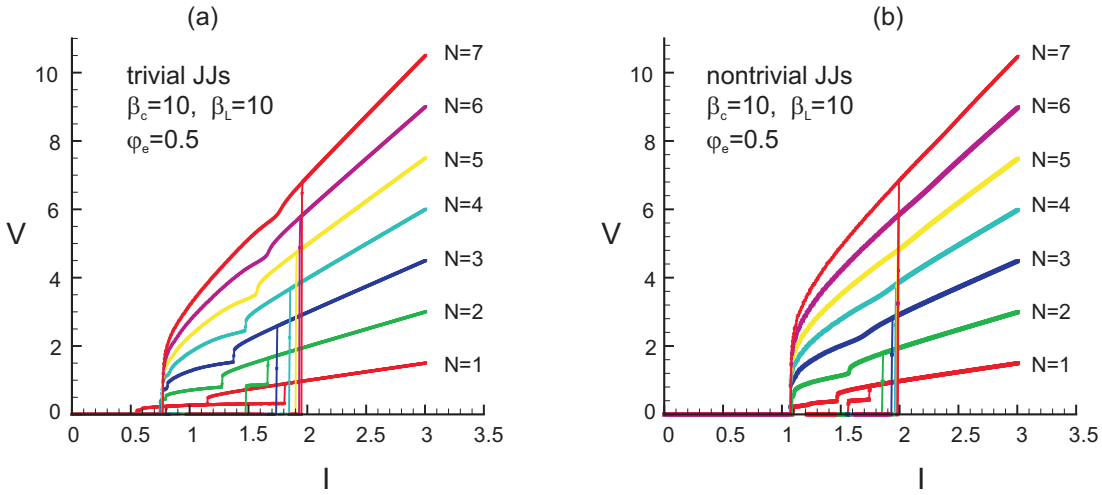

FIGURE 3. I-V characteristics of dc-SQUID with trivial and nontrivial Josephson junctions simulated for different number of coupled junctions, N=1,2,3,...,7. The interjunction coupling parameter is $\alpha = 0.1$

barriers. This observation can be understood from the fact that the total equivalent junction capacitance, given by $\frac{1}{C_{eq}} = \frac{1}{C_1} + \frac{1}{C_2} + \frac{1}{C_3} + ... + \frac{1}{C_N}$, decreases with an increase in number of junctions, and is directly related to the SQUID parameter β_C. Therefore, for a SQUID of N junctions, the resonance voltage becomes $V_{res} = n\sqrt{\frac{2N}{\gamma_j \beta_c \beta_L}}$, which results in the resonance voltage step for nontrivial barriers ($\gamma_j = 1$) becoming smaller by factor of $\sqrt{2N}$ compared to trivial barriers ($\gamma_j = 2$). Since the Junction capacitance is related to β_C, therefore, optimizing the number of junctions N may constitute a convenient way of changing the junction parameter β_C, which can in turn be used be used to optimize the Majorana character of SQUIDS [8].

CONCLUSION

We have carried out a comparative study of the the I-V characteristics of dc SQUIDs containing either conventional (trivial) or topologically nontrivial Josephson junction barriers, and our results demonstrate that the I-V characteristics of the two are significantly different. Topological barriers support Majorana Fermions, which are expected to be used for the realization of quantum gates that are topologoically protected from local sources of decoherence. We find that In both cases, introduction of an external magnetic flux in the SQUID leads to the occurrence of additional branches in the I-V characteristics; however, with different resonance voltages. Importantly, we find that the resonance voltage in SQUIDs containing nontrivial Josephson junction barriers is higher by a factor of $\sqrt{2}$ compared to SQUIDS with trivial Josephson junctions. Further, we find that increasing the number of Josephson junctions N reduces the size of the voltage steps, with the effect being more pronounced in the case of SQUIDs containing nontrivial barriers. Therefore, tuning N constitutes a convenient way of changing the junction parameter β_C, which can in turn be used be used to optimize the Majorana character of SQUIDS [8]. These results are important from the experimental perspective since they provide a way of detecting and manipulating the Majorana bound states.

ACKNOWLEDGEMENTS

The study was funded by the RFBR, according to the research project 15-51-61011. E.M.B. acknowledges financial support from JINR.

REFERENCES

1. E. Majorana, *Nuovo Cimento* **14**, 171 (1937).
2. C. Nayak, S. H. Simon, A. Stern, M. Freedman, and S. Das Sarma, *Rev. Mod. Phys.* **80**, 1083 (2008).
3. L. Fu and C. L. Kane, *Phys. Rev. Lett.* **100**, 096407 (2008).
4. Y. Tanaka, T. Yokoyama, and N. Nagaosa. *Phys. Rev. Lett.* **103**, 107002 (2009).
5. K. Sengupta, I. Zutic, H.J. Kwon , V.M. Yakovenko, and S. Das Sarma, *Phys. Rev. B*, **63** 144531 (2001).
6. C. J. Bolech and E. Demler, *Phys. Rev. Lett.* **98**, 237002 (2007).
7. K.T. Law , P.A. Lee, and T.K Ng, *Phys. Rev. Lett.* **103**, 237001 (2009).

8. M. Veldohorst, C. G. Molenaar, X. L. Wang, H. Hilgenkamp, and A. Brinkman, *Appl. Phys. Lett.* **100**, 072602 (2012).
9. C. W. J. Beenakker, *Annu. Rev. Condens. Matter Phys.* **4**, 113 (2013).
10. E. J. H. Lee, X. Jiang, R. Aguado, G. Katsaros, C. M. Lieber, and S. D. Franceschi, *Phys. Rev. Lett.* **109**, 186802 (2012).
11. W.-D. Schmidt, P. Seidel, and S. Heinemann, *Phys. Stat. Sol.* (a) **91**, K155 (1985).

Influence of barrier on Shapiro Step Features in unconventional junctions

K. V. Kulikov[1,2], M. Maiti[1], Yu. M. Shukrinov[1,2]

[1] *BLTP, JINR, Dubna, Moscow region, 141980, Russia.*
[2] *Dubna State University, Dubna, 141980, Russia*

Abstract. We demonstrate the effect of transmission co-efficient D of a barrier on the Shapiro step features of Josephson junctions which hosts Majorana bound states. We show that the right choice of the values of D can optimize the detection procedure of the Majorana modes in the system and this is associated with the appearance of additional sequence in the staircase structure of Shapiro steps. Changing in the transmission co-efficient of the barrier also leads to the appearance of the " dancing " step structure on the IV-characteristics.

Keywords: Tunneling phenomena; Josephson effect; Superconducting devices; Josephson devices
PACS: 74.50.+r; 85.25.Cp; 85.25.-j

INTRODUCTION

The possibility of realization of Majorana fermions in condensed matter systems has attracted tremendous interest in recent years. In this regard, several suggestions have been put forth regarding systems which can host such fermions [1, 2, 3, 4, 5, 6, 7, 8]. The most promising ones for experimental realization turns out to be those which hosts Majorana fermions as localized subgap states in their superconducting ground state [4, 5, 6, 7, 8]. Typically, the occurrence of such states require unconventional superconducting pairing symmetry such as p- or d-wave pairing [9, 10] which is not accessible easily in naturally available solid-state systems. This hurdle have been circumvented in recent proposals and it was shown that such bound states can occur either at the end of one-dimensional (1D) wire with strong-spin orbit coupling in the presence of magnetic field and a proximate s-wave superconductor [5, 6] or in superconducting junctions atop a topological insulator surface hosting Dirac fermions on the surface of a topological insulators [7]. Those Majorana fermions leave their signature as a midgap peak in tunneling conductance measurement [11] as well through fractional Josephson effect [12].

The effectiveness of the set of experiments involving tunneling conductance in the detection of Majorana fermions has been argued in the community since the midgap peak did not lead to the expected $2e^2/h$ value of the tunneling conductance and their origin can be related to several other effects such as presence of magnetic impurities leading to Kondo effect [13] and impurity induced subgap states [14]. In contrast, the AC Josephson effect which leads to presence even Shapiro steps at $V = n\hbar\omega_J/e$ (and the absence of odd ones at $(2n+1)\hbar\omega_J/2e$ there-off) in Josephson current measurement, where ω_J is the Josephson frequency, n is an integer, and V is the applied external voltage, provide a more definite detection of such fermions since they constitute a

phase sensitive signature which is free of effects of disorder [12]. As a consequence, theoretical studies of AC Josephson effect for unconventional superconductors which hosts Majorana fermions has received a lot of attention lately [15, 16].

It was shown in a recent work [17] that additional *odd* Shapiro steps are found to appear in the CVC of resistively and capacitively shunted Josephson junctions (RCSJ) hosting Majorana bound states subjected to external microwave radiation. These steps occur even in the absence of a 2π-periodic component in the current-phase relation. These odd steps were found to have sub-harmonic nature and hence are qualitatively different from the conventional ones in s-wave Josephson junction [17]. In addition, these Josephson junctions also demonstrated an additional sequence of staircase structure in the current-voltage characteristic.

In this work, we study Josephson junctions described by a RCSJ model, characterised by a transmission co-efficient D and hosts Majorana fermions as bound states in the superconducting ground state. The resultant Josephson junction reflects a 4π-periodicity in the current-phase relationship [12, 17] . We analyze the influence of the value of the transmission co-efficient D on the width of the Shapiro steps.

MODEL AND METHOD

The basic design of the RCSJ circuit which we propose to serve as detector is shown in Fig. 1. The Josephson junction circuit component comprises of two p-wave superconductors separated by a barrier region of thickness d. The transmission co-efficient of the barrier is defined as D and is characterised in terms of the barrier potential V_0 [12]. The thickness r of the superconducting layers are suppose to be greater than the width L, $r \gg L$, so that we can ignore the recombination of Majorana bound states [16]. The RCSJ model, shown in Fig. 1(b), include a resistive component R_0 to take into account dissipative processes into account which may occur, for example, due to quasiparticle tunneling and a shunting capacitance C_0 which takes into account the displacement currents due to possible charge accumulation in the leads [18]. We note at the outset that the present analysis will hold for topological superconductors in 1D wire geometry [5, 6] provided that the transverse dimension L is set to zero.

Josephson junctions shown in Fig. 1, are known to support a pair of localized subgap Andreev bound states which can be obtained as solution of the Bogoliubov-de Gennes (BdG) equations. The Andreev bound states have the following dispersion, [12]

$$E_n = -\Delta_0 \sqrt{D} \cos(\phi/2), \tag{1}$$

where Δ_0 is the amplitude of the superconducting gap, ϕ is the phase difference. The Josephson current can then be obtained as (1)

$$I_J(\phi) = \sum_n \frac{2e}{\hbar} \partial E_n / \partial \phi = \frac{e\Delta_0}{\hbar} \sqrt{D} \sin(\phi/2). \tag{2}$$

Following Ref. [12], we note that the Josephson current has a 4π-periodicity and replacing $\phi \to 2eVt/\hbar$ in Eqn. 2 in the presence of a voltage V will lead to a fractional

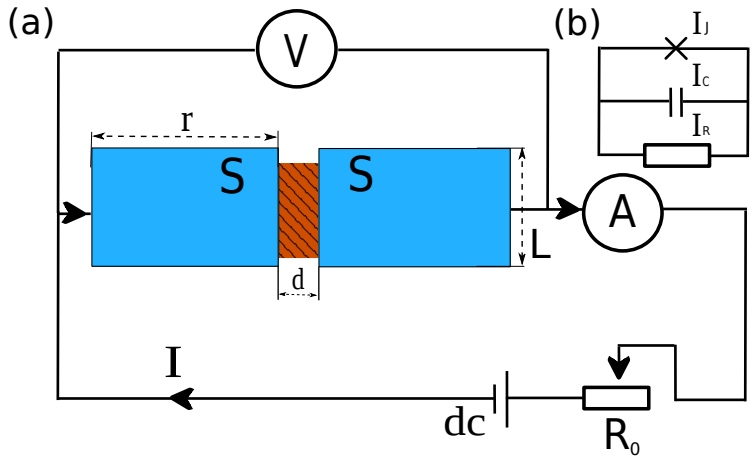

FIGURE 1. (a) Schematic representation of the Josephson junction in the RCSJ circuit (see (b)). The junction has width L in the transverse direction and the barrier region of width d separating the two superconductors. I_J, I_C and I_R are the Josephson current, displacement current and quasiparticle currents respectively.

AC Josephson effect. The normalised current phase-relationship for this model, in the presence of an external radiation, is given by [18, 19]

$$\ddot{\phi} + \beta\dot{\phi} + I_J(\phi) = I + A\sin(\omega t), \tag{3}$$

where A and ω are the amplitude and frequency of external radiation respectively, $\beta = \sqrt{\hbar/(2eI_cR_0^2C_0)}$ is the dissipation parameter. We have normalized I, I_J and A to critical current I_c, $t \to t\omega_p$, where $\omega_p = \sqrt{2eI_c/(\hbar C_0)}$ is the plasma frequency. For the calculation of the current-voltage characteristics we solve the following system of equations numerically by fourth order Runge-Kutta method,

$$\begin{cases} \ddot{\phi} + \beta\dot{\phi} + I_J(\phi) = I + A\sin(\omega t) \\ V = \dfrac{d\phi}{dt}, \end{cases} \tag{4}$$

where V normalized to $V_0 = \hbar\omega_p/2e$.

RESULTS AND DISCUSSION

One of the main difference between the Josephson junction with Majorana states and the conventional one is the emergence of an additional sequence of steps in the staircase structure of Shapiro steps on the CVC. It was shown in Ref.[17], that the sequence of steps that occurs for lower amplitudes of external radiation in the CVC of $p-p$ Josephson junction is reflected by the continued fractions $V = (N \pm 1/n)\omega$ which also appears for the conventional Josephson junction and an additional sequence of steps also

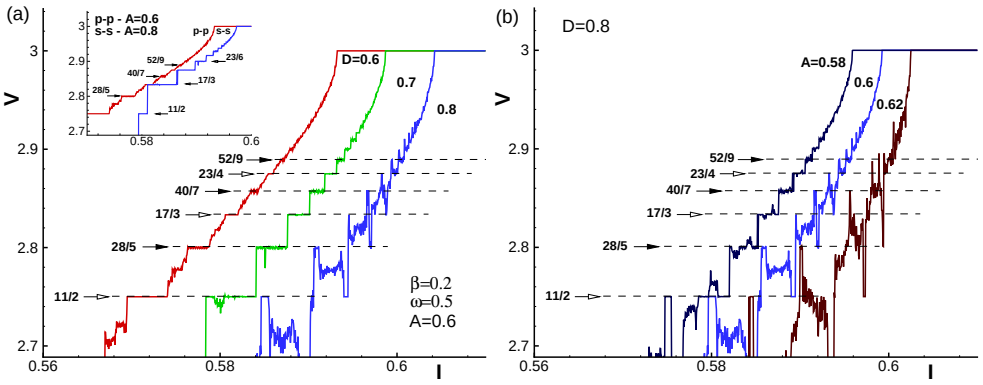

FIGURE 2. Left panel: The enlarged part of the CVC of p-p Josephson junction for $\beta = 0.2, \omega = 0.5, A = 0.6$ and different values of the transmission co-efficient D. The curves are shifted to the right by $\Delta I = 0.05$. The inset shows a comparison of current-voltage characteristics in the staircase structure for the $p-p$ ($D = 0.6$) and $s-s$ ($D = 1$)Josephson junction. Right panel: CVC of $p-p$ junction showing the variation with amplitude of external radiation for a fixed D.

appears which corresponds to the continued fractions $V = (N \pm 2/n)\omega$. The detection of staircase structure with a continuous fractions $V = (N \pm 2/n)\omega$ may serve as a criterion of Majorana fermions in unconventional Josephson junctions. We first discuss the impact of the transmission co-efficient D, which in turn also characterises the barrier transparency, on this staircase structure in $p-p$ junction and refer to Fig. 2 which shows an enlarged part of the CVC with the staircase structure for different values of D for this purpose.

We find that the width of the Shapiro steps decreases with increase in the transmission co-efficient of the barrier (this fact is also corroborated by Eqn. 5, 6 which we derive subsequently in the next part of our analysis). For a fixed amplitude of the external radiation $A = 0.6$, we note that the sub-harmonic steps between the basic and additional sequences starts to disappear when $D = 0.7$. For $D > 0.7$ the "normal" Shapiro step structures are destroyed and a "dancing" step structure appears on the CVC [20]. These structures can be described by regular Shapiro steps whose widths decreases with higher fractions and are separated by chaotic intervals. Thus we find changing D may lead to both the disappearance of steps in the staircase structure and lead the system to chaotic regime. To understand this further, we plot the CVC for a higher value of D with variations in A in the right panel of Fig. 2. We find that the "dancing " step structures appears for a smaller amplitude as we increase the barrier transparency.

We next discuss the effect of the barrier transparency on the width of Shapiro steps. Fig. 3(a) shows the CVC of $p-p$ Josephson junction obtained by solving the Eqns. (4) at $\beta = 0.2$, $D = 0.9$, $\omega = 2$, $A = 2$. In the IV-characteristics, we observe steps corresponding to the voltage $V = 4$ i.e., 2ω even harmonic and corresponding to $V = 2\,\omega$ odd harmonic. In order to assess the impact of the barrier transparency on the properties of these steps, we numerically calculate the amplitude dependence of the width of the Shapiro steps ΔI_n both for the even and odd harmonic corresponding to various values of D. Numerically calculated results for the $2\omega(\omega)$-steps at $D = 0.9, 0.4$ are shown in Fig. 3(b,c) respectively and are marked by circles.

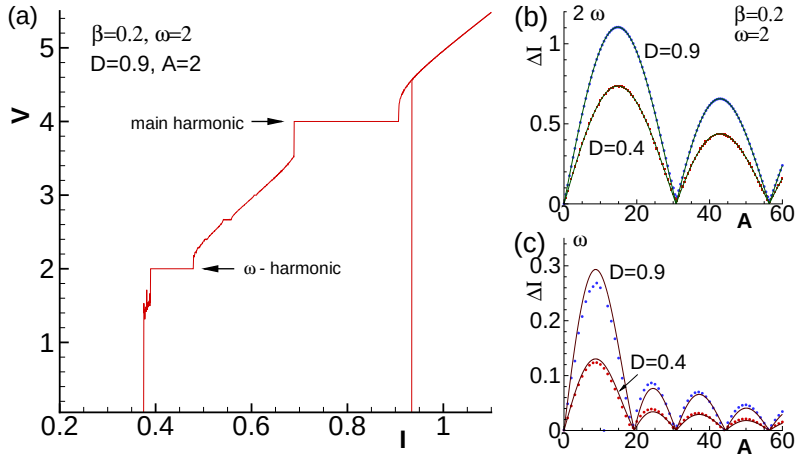

FIGURE 3. (a) CVC of $p-p$ Josephson junction at $\beta = 0.2, \omega = 2, A = 2, D = 0.9$. (b) the amplitude dependence of the width of main (2ω) harmonic of external radiation at $D = 0.9$ and $D = 0.4$. (c) the same as in (b) for sub-harmonics (ω).

The width ΔI_n of the step has a Bessel function dependence of the amplitude of the external radiation A. We further corroborate this fact by comparing the numerical results with analytical results of the step widths for the even and odd harmonics. Following the procedure in Ref. [17] we calculate the dependence of the width of the even and odd Shapiro steps ΔI_n as a function of D and are given as,

$$\Delta I_n^{\text{even}} = \sqrt{D} 2 J_n(x), \tag{5}$$

$$\Delta I_n^{\text{odd}} = \sum_{n_1} \frac{D J_{n_1}(x) J_{2n-1-n_1}(x)}{2[(2n-1-2n_1)\omega]^2/4 + \beta^2}, \tag{6}$$

where $J_n(x)$ is n-th order Bessel function with $x = A/(2\omega\sqrt{\beta^2+\omega^2})$. The results obtained using the Eqns. 5,6 are shown as solid lines in Fig. 3b and Fig. 3c.

We now discuss the main results obtained from the plots in Fig. 3. We note that the amplitude of the maxima of the step width ΔI_n increases with increase in the transparency D for both 2ω and ω steps. These results are in good agreement with the analytical results obtained from Eqn. 5 for 2ω step. The numerical and the analytical (obtained from Eqn. 6) results also has good agreement for smaller D for the odd-steps; however the numerical results tends to deviate from the theoretical predictions as the value of D is increased. To understand this deviation, we note that the main contribution to the width of the sub-harmonics, as in the case of the conventional Josephson junction [21], is from the first term in Eqn. (6) which is plotted as solid line in Fig. 3(c). The deviation of the analytical and numerical data can decreased by taking into account the higher order corrections to the width of the SS for the odd harmonics.

CONCLUSION

We have studied the influence of the transparency of the barrier on Shapiro steps features in unconventional Josephson junctions. Our main results are the following: i) the tuning of the value of D can result in appearance of the chaotic features in the CVC, characterised by "dancing" steps, ii) the amplitude of external radiation for which the "chaotic" features appears is dependent on the transmission co-efficient of the barrier, iii) we obtain an analytical expression for the Shapiro step width both for the even and odd harmonics as a function of the tranmission co-efficient D of the barrier and (iv) the Shapiro step width calculated from high precision numerical simulation demonstrates excellent agreement with theoretical results for a considerable range of the barrier transparency particularly for the even harmonics; for the odd harmonics the deviation between the analytical and numerical result increases as we gradually increase the transmission co-efficient.

We conclude from our results that the choice of the transmission co-efficient D of the barrier of an unconventional Josephson junction is useful in experimental procedure to optimize the procedure of registration of Majorana fermions in $p-p$ Josephson junction. The knowledge of the dependence of the different features of the Shapiro steps on the transmission co-efficient of the barrier is particularly important, because the transmission co-efficient can be modulated by the application of an external gate voltage and very often the source of external radiation is handicapped with fixed amplitude. Thus knowing the dependence of the amplitude of the external radiation with the transmission co-efficient, as we have pointed out in our results, would be beneficial in this regard.

ACKNOWLEDGEMENT

The study was financially supported by RFBR in the framework of a research project # 15–51–61011 Egypt_a.

REFERENCES

1. A. Y. Kitaev, *Physics-Uspekhi* **44**, 131 (2001).
2. G. Moore and N. Read, *Nucl. Phys. B* **360**, 362 (1991); N. Read and D. Green, *Phys. Rev. B* **61**, 10267 (2000).
3. N. B. Kopnin and M. M. Salomaa, *Phys. Rev. B* **44**, 9667 (1991).
4. L. S. Levitov, T. P. Orlando, J. B. Majer, and J. E. Mooij, *arXiv:cond-mat/0108266* (unpublished).
5. R. M. Lutchyn, J. D. Sau, and S. Das Sarma, *Phys. Rev. Lett.* **105**, 077001 (2010);
6. Y. Oreg, G. Refael, and F. von Oppen, *Phys. Rev. Lett.* **105**, 177002 (2010).
7. L. Fu and C. L. Kane, *Phys. Rev. Lett.* **100**, 096407 (2008).
8. L. Fu and C. L. Kane, *Phys. Rev. B* **79**, 161408(R) (2009); J. D. Sau, R. M. Lutchyn, S. Tewari, and S. Das Sarma, *Phys. Rev. Lett.* **104**, 040502 (2010); J. Alicea, *Phys. Rev. B* **81**, 125318 (2010); A. Cook and M. Franz, *Phys. Rev. B* **84**, 201105 (2011); J. D. Sau and S. D. Sarma, *Nat. Commun.* **3**, 10 (2012); A. Das, Y. Ronen, Y. Most, Y. Oreg, M. Heiblum, and H. Shtrikman, *Nature Phys.* **8**, 887 (2012); M. T. Deng, C. L. Yu, G. Y. Huang, M. Larsson, P. Caroff, and H. Q. Xu, *Nano Lett.* **12**, 6414 (2012); A. D. K. Finck, D. J. Van Harlingen, P. K. Mohseni, K. Jung, and X. Li, *Phys. Rev. Lett.* **110**, 126406 (2013); H. O. H. Churchill, V. Fatemi, K. Grove-Rasmussen, M. T. Deng, P. Caroff, H. Q. Xu, and C. M. Marcus, *Phys. Rev. B* **87**, 241401 (2013).

9. D. A. Ivanov, *Phys. Rev. Lett.* **86**, 268 (2001); A. P. Mackenzie and Y. Maeno, *Rev. Mod. Phys.* **75**, 657, (2003).
10. C. R. Hu, *Phys. Rev. Lett.* **72**, 1526, (1994); S. Kashiwaya, Y. Tanaka, *Phys. Rev. Lett.* **74**, 3451, (1995).
11. K. Sengupta, I. Zutic, H-J Kown, V. M. Yakovenko and S. Das Sarma *Phys. Rev. B* **63**, 144531 (2001).
12. H-J Kwon, K. Sengupta and V. M. Yakovenko, *Eur. Phys. Jour. B* **37**, 349 (2004).
13. E. J. H. Lee, X. Jiang, R. Aguado, G. Katsaros, C. M. Lieber and S. D. Franceschi, *Phys. Rev. Lett.* **109**, 186802 (2012).
14. Jie Liu, A. C. Potter, K. T. Law, and P. A. Lee, *Phys. Rev. Lett.* **109**, 267002 (2012); D. Bagrets and A. Altland, *Phys. Rev. Lett.* **109**, 227005 (2012).
15. M. Houzet, J. S. Meyer, D. M. Badiane and L. I. Glazman, *Phys. Rev. B* **111**, 046401 (2013).
16. F. Dominguez, F. Hassler, G. Platero, *Phys. Rev. B* **86**, 140503 (2012).
17. M. Maiti, K. V. Kulikov, K. Sengupta, and Y. M. Shukrinov, *Phys. Rev. B* **92**, 224501 (2015).
18. See for example, *Dynamics of Josephson junctions and Circuits*, K. Likharev, Taylor and Francis, USA (1986).
19. Y. M. Shukrinov, S. Y. Medvedeva, A. E. Botha, M. R. Kolahchi and A. Irie, *Phys. Rev. B* **88**, 214515 (2013).
20. A. E. Botha, Yu. M. Shukrinov, M. R. Kolahchi, *Nonlinear Dynamics* submitted, manuscript No. NODY-D-15-01678R1, 2015
21. V. K. Kornev, T. Y. Karminskaya, Y. V. Kislinskii, P. V. Komissinki, K. Y. Constantinian and G. A. Ovsyannikov, *J. Phys. Conf. Series* **43** 1105 (2006).

SESSION
"NICA"

Conveners: A. Sorin, J. Cleymans

Accelerator complex NICA

Anatoly Sidorin for the NICA team

Veksler and Baldin Laboratory for High Energy Physics, JINR Dubna, 141980 Dubna, Moscow region, Russia

Abstract. The main goal of the NICA (Nuclotron Based Ion collider fAcility) project is to provide ion beams for experimental studies of hot and dense strongly interacting baryonic matter and spin physics. The NICA collider will provide heavy ion collisions in the energy range of $\sqrt{s_{NN}} = 4-11$ *GeV* at average luminosity of $L = 1 \cdot 10^{27}$ $cm^{-2} \cdot s^{-1}$ for Au^{79+} nuclei and polarized proton collisions in energy range of $\sqrt{s_{NN}} = 12-27$ *GeV* at luminosity of $L \geq 1 \cdot 10^{32}$ $cm^{-2} \cdot s^{-1}$.

Keywords: hadron collider, superconducting magnet, beam cooling
PACS: 29.20.-c; 29.20.db; 29.20.+r

INTRODUCTION

The Nuclotron Based Ion collider fAcility (NICA) is a modern accelerator complex which is now under construction at Joint Institute for Nuclear Research (JINR, Dubna) [1], [2]. The NICA project will implement world-leading programs in long base line relativistic nuclear physics and particle spin physics, radiobiology, applied research and education. It will be unique among accelerator facilities worldwide in its flexibility to support multiple research programs based on particle beams of the frontier parameters. The main goal of the project is a study of hot and dense strongly interacting matter in heavy ion (up to *Au*) collisions at centre-of-mass energies up to 11 *GeV*. Two modes of operation are foreseen, collider mode and extracted beams, with two detectors: MPD (MultiPurpose Detector) and BM@N (Baryonic Matter at Nuclotron). An average luminosity in the collider mode is expected as 10^{27} $cm^{-2} \cdot s^{-1}$ for Au^{79+}. Extracted beams of various nuclei species with maximum momenta of 13 GeV/c (for protons) will be available. A study of spin physics with extracted and colliding beams of polarized deuterons and protons at the energies up to 27 *GeV* (for protons) is foreseen with the NICA facility. The proposed program allows to search for possible signs of the phase transitions and critical phenomena as well as to shed light on the problem of nucleon spin structure. The NICA accelerator facility will provide a range of ion beams of wide parameter spectrum. That allows one to perform both applied and fundamental research in different fields of science and technology. Among them one can point out:

– radiobiology and cosmic medicine;

– beam therapy;

– development of accelerator driven reactors (Şenergy generationŤ with subcritical plutonium blankets) and radioactive waste transmutation;

– irradiation tests of electronics.

The facility physics program is suggested to be implemented during three stages:

– At the first stage of the operation it will provide fixed target experiments with heavy

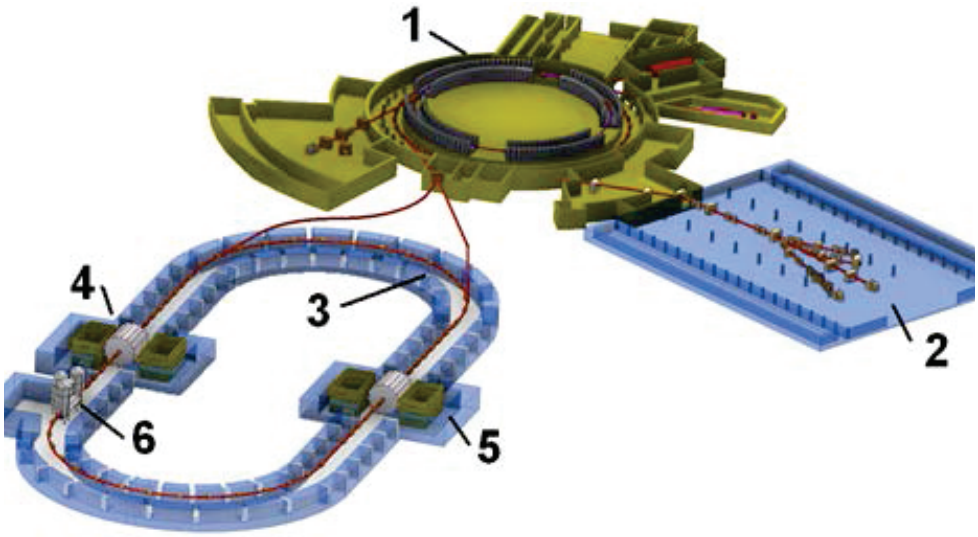

FIGURE 1. Schematics of the NICA layout: 1 – injector facility, Booster and Nuclotron, 2 – existing building for the fixed target experiments, 3 – the collider rings, 4, 5 – MPD and – SPD detectors, 6 – electron cooling system.

and light polarized ions. The heavy ion program at this stage will be realized at BM@N experimental set-up.

– The second stage will be started after completion of the collider construction and dedicated to relativistic nuclear physics researches in heavy ion and light-heavy ion collisions using MPD detector.

– The spin physics program in the collision mode of proton and deuteron beams will be realized at the third stage, when the collider rings will be equipped with required spin control and diagnostic devices.

More detailed information on the NICA experimental program is available at [NICA site].

STRUCTURE OF THE FACILITY

The NICA facility (Fig. 1) will include the existing elements of JINR accelerator complex as well as a few new accelerators and beam transfer lines.

The first stage of the NICA experimental program will be started at existing accelerator facility which is based on injector comprising set of particle sources and existing linac LU-20, that will be equipped with a new RFQ fore-injector. To increase the beam energy and intensity at the exit of the main NICA synchrotron — the existing superconducting Nuclotron — a new injector will be constructed. It consists of ESIS-type ion source providing intensive beam of Au^{31+} ions, heavy ion linac (HILAc) accelerating ions at $A/Z < 6$ up to the energy of 3.2 MeV/u, and Booster-synchrotron housed inside the Synchrophasotron (old weak-focusing JINR synchrotron) yoke. The Booster at circumference of about 211 m and magnetic rigidity of 25 $T \cdot m$ will accelerat Au^{31+} ions up to the energy of about 600 MeV/u. To form required phase volume of the beam the

Booster is equipped with an electron cooling system. After acceleration in the Booster the ions will be fully striped and injected into the Nuclotron providing acceleration of Au^{79+} ions up to the energy of 4.5 GeV/u. The Collider will be constructed in a tunnel with additional buildings for two detectors and HV electron cooler. It will be operated at a fixed energy, also possibility to have slow-rate acceleration of an injected beam is foreseen. To provide required linearity of the field the maximum bending field is chosen to be of 1.8 T. Two collider rings are constructed one above the other and the beam superposition/separation is provided in the vertical plane. The distance between the ring median planes is chosen to be 32 cm. That is achieved with dipole and quadrupole magnets having two apertures in one yoke and a common cryostat. The key issue of the NICA collider is application of sophisticated beam accumulation schemes and both stochastic and electron cooling methods during collisions. Strong space-charge effects in the collider arise a challenge to its optics and application of novel methods of beam stability maintenance. Both new cyclic accelerators of the NICA facility — the Booster and collider will be based on Şsuperferric Ť superconducting magnets developed at JINR during the Nuclotron construction. To provide injection of the beam from the Nuclotron to collider a new beam transport line of the length of about 335 m will be constructed on the basis of conventional dipole and qudrupole magnets operated in a pulse mode.

THE PROJECT STATUS

Project NICA/MPD is a part of the 7-years JINR Roadmap for 2009-2016 and for the new RoadMap 2017-2023. It had been approved by Inetrnational Scientific Council of JINR and The Committee of Plenipotentiaries of JINR in 2009. That is a flagship project of JINR presently.

The NICA project has a special status in Russian Federation and had been included to list of so called megascience projects. This is one of two from the list, which is already supported by State and is under active realization. JINR has made important efforts to reach beyond its traditional community. The construction of NICA and the FAIR/GSI accelerators is in fact tightly linked via a strong collaboration between Germany and JINR on the FAIR project and there is potential for similar close detector collaboration (MPD/SPD/BM@N). The synergy and complementarity of the NICA and of the ESFRI Landmark FAIR and to some extent of the ESFRI Landmark SPIRAL2 make it very desirable to develop a joint coordinated effort for identifying a strong programme and for offering the best opportunities to international nuclear experimental physics. To this end ESFRI encourages these Research Infrastructure both to work closely together and to pay special attention to developing NICA as a Global Research Infrastructure concept.

Now 16 Institutions from Russia and 79 Institutions from 24 foreign countries officially participate in the NICA project.

The NICA construction is provided without termination of the Nuclotron research program. Besides, the Nuclotron beams are used for research in radiobiology and applied research. Moreover, the Nuclotron is very good polygon for testing of the collider equipment and operational regimes, elements and prototypes for the MPD using extracted beams (carbon ions at 3.5 GeV/u and deuterons at 4 GeV/u presently). Particularly, in the run 45 (Feb. 2012) the circulation of 3.5 GeV/u deuteron beam during 1000

seconds was demonstrated. During 2011-2013 the prototype of the NICA stochastic cooling system was designed, constructed and tested at Nuclotron at ion kinetic energy of 3.5 GeV/u with deuteron and carbon ion beams. The segment of the NICA control system based on Tango platform was successfully tested at the Nuclotron, and presently the system is under active development.

The NICA project as a whole has passed the phase of design and is presently in the stage of accelerator elements manufacturing and construction.

The project realization plan foresees a staged construction and commissioning of all major parts and systems of the accelerator complex. The collider commissioning is planned for the end of 2019, beginning of 2020. It is planned to commission so-called NICA start-up version. Nevertheless, this will allow us to start experiments in colliding beamsŠ mode with the test and tuning of the MPD detector and the majority of the accelerators elements at maximum peak luminosity at the level of $5 \cdot 10^{25}\ cm^{-2} \cdot s^{-1}$ at the energy of the Au^{79+} ions in the range of $3 - 4.5\ GeV/u$.

ACKNOWLEDGEMENT

The JINR and the NICA team express their gratitude to JINR member-countries, to the NICA Machine Advisory Committee and to the Ministry of Education and Science of the Russian Federation for support of the project.

REFERENCES

1. G. Trubnikov, et.al. Project of the Nuclotron-based ion collider facility (NICA) at JINR, Proc. of EPAC08, Genoa, Italy.
2. G. Trubnikov, et.al. STATUS OF THE NICA PROJECT AT JINR, Proc. of IPAC2014, Dresden, Germany.

NICA site. http://nica.jinr.ru.

Prospects for dense baryonic matter research at NICA: Status of the MPD

Vadim Kolesnikov on behalf of the MPD team

Veksler-Baldin Laboratory of High Energy Physics, JINR Dubna, 141980 Dubna, Moscow region, Russia

Abstract. The NICA (Nuclotron-based Ion Collider fAcility) project at JINR is aimed in the study of nuclear matter under extreme condistions. The highest baryonic density will be achieved in heavy-ion collisions in the energy range up to $\sqrt{s_{NN}}$=11 GeV. The MultiPurpose Detector (MPD) at NICA is designed to handle high multiplicity events expected in relativistic A+Au interactions. We report on the main physics objectives of the NICA heavy-ion program and ovrview the main detector components. Results of MPD feasibility study for several observables will be also presented.

Keywords: relativistic heavy ion collisions, charged-particle spectroscopy, ionization chambers, calorimeters
PACS: 25.75.Ag;29.30.Ep;29.40.Cs;29.40.Vj

HEAVY-ION PROGRAM AT NICA

The main physics goal of the NICA heavy-ion program is the investigation of the properties of nuclear matter in the region of the maximum baryonic density [1, 2]. Experimental studies of QCD matter under such conditions provides new perspectives to resolve the most fundamental problems of the underlying theory - confinement and chiral symmetry breaking. According to lattice QCD calculations a first order phase transition from the hadronic phase to the quark matter is suggested at large values of baryochemical potential μ_B. Such a phase transition turns into a crossover at small baryon densities (and high T), hence, the critical endpoint (CEP) is expected to exist. However a rigorous proof that such a structure of QCD exists in Nature is not yet available and new reliable experimental data on the nature and properties of the phase transition are needed.

Theory predicts that partial restoration of the chiral symmetry can be happened in heavy-ion collisions at NICA energies [3, 4]. If this will be the case, strong modifications of hadronic spectral functions in central collisions of heavy ions can be observed. The correlated e^+e^- pairs (*dileptons*) from decays of vector mesons (ρ, ω, ϕ) are the best probes for such kind of study since they escape the interaction region unaffected by strong interactions inside the medium. Until now, no dilepton measurements have been performed at center-of-mass energies of several GeV and the dilepton program at NICA is aimed to close this gap. The NICA potential in dilepton study is very high since the effect of modifications of dilepton spectra is sensitive to the baryon density, which has the maximum in central Au+Au collisions within the NICA energy range [5].

At NICA we plan to investigate a wide range of physics phenomena in heavy-ion collisions including phases of nuclear matter, Equation of State (EoS) at high baryon density, properties of the hadron spectral function, features of hyperon-nucleon interac-

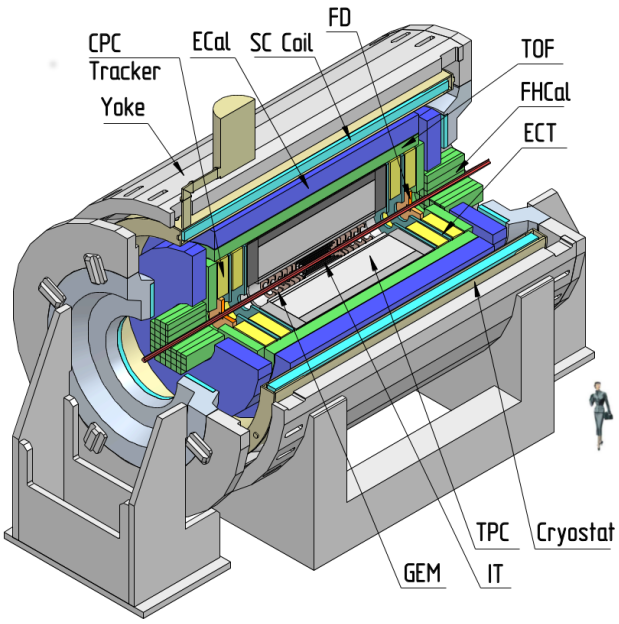

FIGURE 1. A cut-away view of the MPD detector

tion in the medium, and critical behavior of the QCD matter. Our experimental strategy will be in performing a detailed energy and system size scan with an emphasis to the production of hadrons (p, K, π, Λ and their antiparticles) and dileptons, as well as excitation function of event-by-event fluctuations and correlations. Production of composite objects with strangeness (hypernuclei), are of particular interest, since they are a unique tool to probe new nuclear structures or unknown properties of the baryonic interaction, which cannot be seen from the study of ordinary nuclei. The basic element of the NICA facility will be a new heavy-ion collider which will provide ion beams with the design luminosity of $10^{27} cm^{-2} c^{-1}$ (for gold ions) in the energy range from $\sqrt{s} = 4$A to 11A GeV. The experimental setup at the NICA collider (detector) has to be optimized for the study of fluctuations and correlations of bulk event properties and would be capable of unique measurements of heavy-ion collisions including high-precision tracking and particle identification in the full phase-space, as well as very accurate event characterization (centrality and event plane).

MULTIPURPOSE DETECTOR (MPD) AT NICA

The **M**ulti**P**urpose **D**etector (MPD) is designed to fully exploit the NICA physics potential. MPD is a spectrometer with a large uniform acceptance (full azimuth) capable of detecting and identifying hadrons, electrons and gammas at the very high event rate achieved at NICA [6]. MPD design parameters has been determined by characteristics of nuclear collisions at NICA energies and several technical constrains guided by a trade-of of efficient tracking and particle ID against a low material budget. For example, the average transverse momentum $\langle p_r \rangle$ of hadrons produced in central heavy-ion collisions

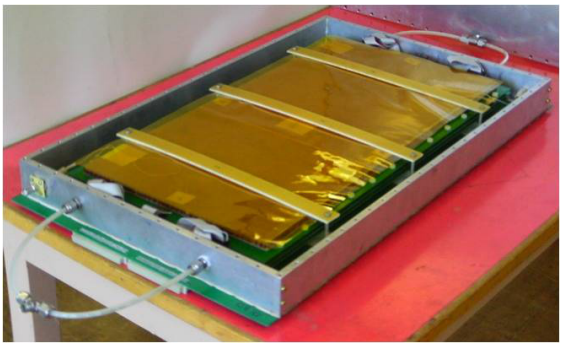

FIGURE 2. A full-scale prototype of a MRPC TOF module.

at NICA energies does not exceed 500 MeV/c at the center-of-mass rapidity. Thus, the detector material budget should be kept at the lowest level in order to be capable to register particles in the full phase-space.

All the elements of the detector (see Fig. 1) are ordered inside a superconducting solenoid generating a magnetic field of up to 0.6 T. Tracking will be performing with a cylindrical Time Projection Chamber (TPC). MPD TPC is required to have a high efficiency and momentum resolution over the pseurapidity range $|\eta| < 2$. TPC will enable particle identification via the specific energy loss dE/dx measurement with a precision better than 8%. At large-η TPC tracking will be supplemented by a multi-layer straw tube tracker (ECT) located just after the TPC end plates. The Inner Tracker (IT) is a four layers of double-sided silicon microstrip detector serving mainly for determination of the position of the primary interaction vertex and secondary decay vertices. The main detector element for hadron identification is the Time-Of-Flight (TOF) system. The TOF detector covers $|\eta| < 3$ and its performance should allow the separation of kaons from protons up to a total momentum of 3 GeV/c. Behind the TOF detector, a high segmented electromagnetic calorimeter (ECal) for electron and gamma identification will be located. Arrays of quartz counters (FD) are meant for fast timing and triggering, and two sets of forward hadron calorimeters (FHCal) covering the large rapidity region ($2.5 < |\eta| < 4$) will measure the forward going energy distribution that is a subject of the off-line centrality and event plane analysis.

MPD PROTOTYPING

Over several years, an extensive R&D program aimed in the detector design and study of the performance of the MPD elements was carried out. These comprehensive efforts resulted in the proposed MPD setup that is uniquely designed such that its basic characteristics are optimized to the conditions of heavy-ion experiment at NICA energies. In this section, selective results of prototyping of the detector elements responsible for particle identification (PID) in MPD will be outlined.

PID in the range of momentum from 0.1 to 3 GeV/c will be performed by means of time-of-flight (TOF) measurements. In order to achieve sufficient particle separation power, the overall timing resolution of better than 100 picoseconds is needed. In ad-

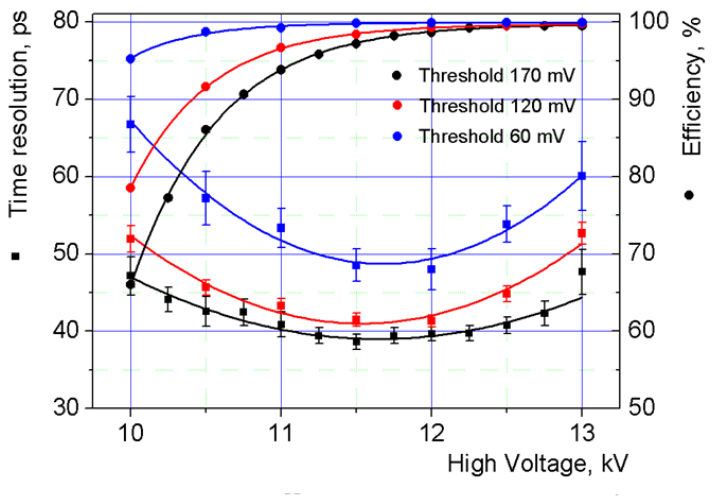

FIGURE 3. Timing resolution (left vertical axes, squares) and efficiency (right axes, circles) as a function of supply voltage for a MRPC TOF prototype.

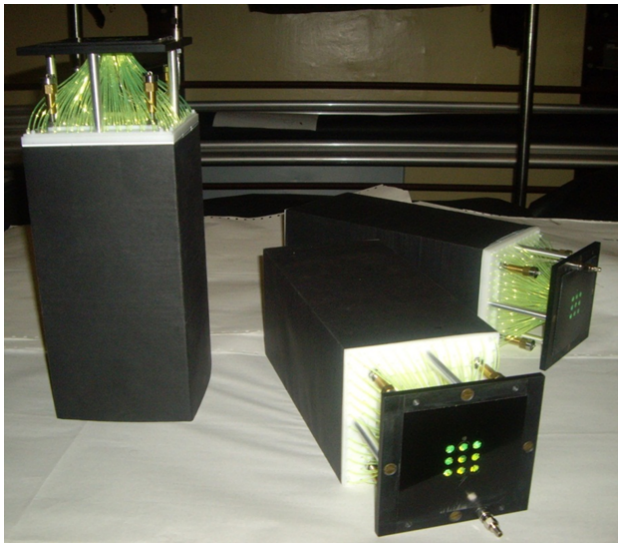

FIGURE 4. Modules of the ECal detector for MPD

dition, the overall area to be covered by the TOF modules is more than 50 m^2, thus a low-cost detector technology is needed. We choose for the basic element of the TOF system Multigap Resistive Plate Chambers (MRPC). In Fig. 2 is shown a photo of a full-scale prototype of the MRPC module for the TOF. Such a technology provides the intrinsic time resolution better than 80 ps and is relatively inexpensive. As the test measurements performed with Nuclotron beams indicate (see Fig. 3), a MRPC prototype has shown an efficiency $>95\%$ and time resolution $\sim$50 ps, that meets our requirements.

The MPD electromagnetic calorimeter (see Fig. 4) is proposed to be built of towers

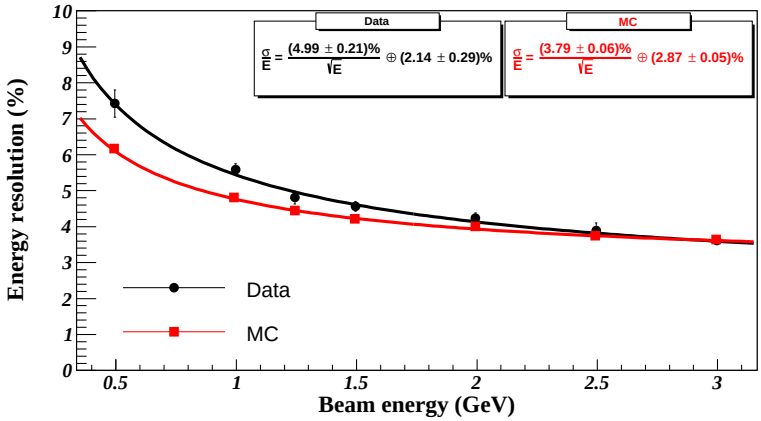

FIGURE 5. Energy resolution for MPD ECal prototype modules as a function of electron energy. Black symbols are the measurements, while red ones indicate the results of Monte Carlo simulations.

of about 3 cm^2 cross section lead-scintillator sampling as basic building elements. Each tower contains 250 alternating tiles of 0.275 mm thick Pb and plastic scintillator of 1.5 mm thickness. The length of each module will be ≈40 cm (18 radiation lengths). The cells of each tower are optically combined by 9 longitudinally penetrating wavelength shifting fibers for light collection. The light collected by these fibers will be read out by avalanche photodiodes (MAPD) units

The energy resolution of MPD ECal prototype modules (shown in Fig. 4) for electrons was studied with electron beams at several energies. The results of these test are demonstrated in Fig. 5 as a function of beam energy. As can be seen, the resolution better than 5% can be achieved at $E_e > 1$ GeV.

With the tracking and PID parameters (momentum, energy, and timing resolutions, as well as efficiencies) achieved for MPD prototypes a comprehensive set of simulation studies was performed aimed in investigations of detector sensitivity to selective physics signals. The results of these studies will be reported in the next section.

RESULTS OF MPD PERFORMANCE STUDY

In addition to the R&D work, an extensive study of detector performance by mean of Monte Carlo simulations has been carried out. All the simulation tasks for MPD were performed in the framework of a dedicated software tool (MPDRoot) comprising interfaces to many event generators, a special program for propagation of particles through material (Geant), and all necessary detector response plus reconstruction algorithms.

In Fig. 6 the results of MPD PID performance study in high multiplicity central Au+Au collisions at $\sqrt{s_{NN}} = 9$A GeV are presented. As can be seen, the basic detector parameters, namely, dE/dx resolution of $\sigma_{dE/dx}$ ≈8% and TOF resolution of σ_{TOF} ≈100 ps, indeed, provide a high degree of selectivity for hadrons at momenta below 2 GeV/c.

MPD performance for dilepton measurements was investigated focusing on determination of the hadron suppression factor of the MPD particle ID system, achieved

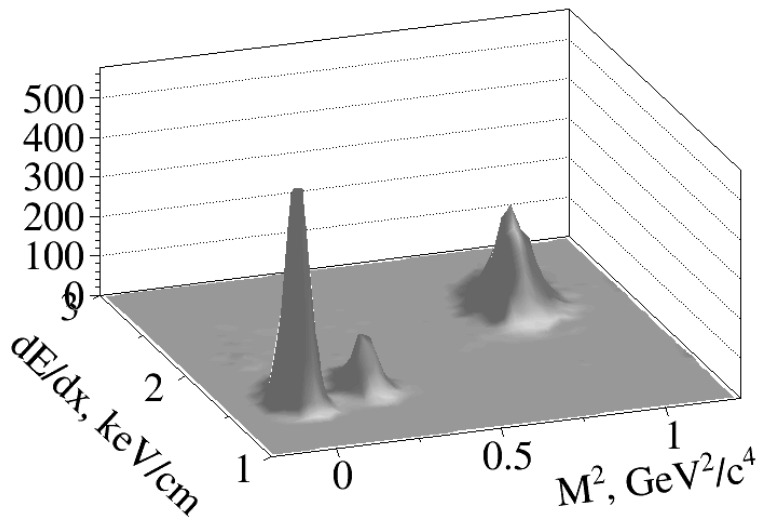

FIGURE 6. A typical distribution (from simulation) of the specific energy loss dE/dx (from TPC) versus mass-squared (from TOF) for π^+, K^+, and protons (from left to right) at p = 1 GeV/c. The results are for realistic MPD simulation of central Au+Au collisions at $\sqrt{s_{NN}} = 9$A GeV.

signal-to-background ratio and invariant mass resolution in the region of masses of vector mesons. A detailed description of the analysis procedure and results can be found in Ref. [7]. Electron identification was achieved by using combined information about the specific energy loss dE/dx from TPC, time-of- flight from TOF and E/p information from EMCal. After applying dedicated quality and PID cuts, the achieved overall hadron rejection factor was found to be of about 3200. The background from conversion pairs was eliminated by an extra set of topological and kinematical cuts. Figure 7 shows invariant mass spectrum of reconstructed electron-positron pairs after background rejection (dots) and that for true dielectrons from the event generator (line). S/B ratio in mass region $0.2 < M_{e^+e^-} < 1.2$ GeV/c^2 was estimated to be of about 10%. Thus, the expected parameters of the MPD setup are among the best over the world.

In order investigate MPD capability for reconstruction of hypernuclei of about $5 \cdot 10^5$ events from the DCM-QGSM event generator (corresponding to about 30 minutes of data taking time at NICA) were used. Employing full event reconstruction, realistic particle ID achieved by combined dE/dx and TOF information, and secondary vertex finding (as described in [8]) we obtained an invariant mass spectra of ^{3}He and π^- candidates as shown in Fig. 8. This result demonstrates a good sensitivity of the MPD setup for hypernuclei: with a typical event rate of 7 kHz for the design NICA luminosity of 10^{27}cm^{-2}c^{-1} we are able to register of about 10^5 hypertritons in a week of data taking. Thus, a detailed study of the production mechanism of single hypernuclei at NICA looks feasible.

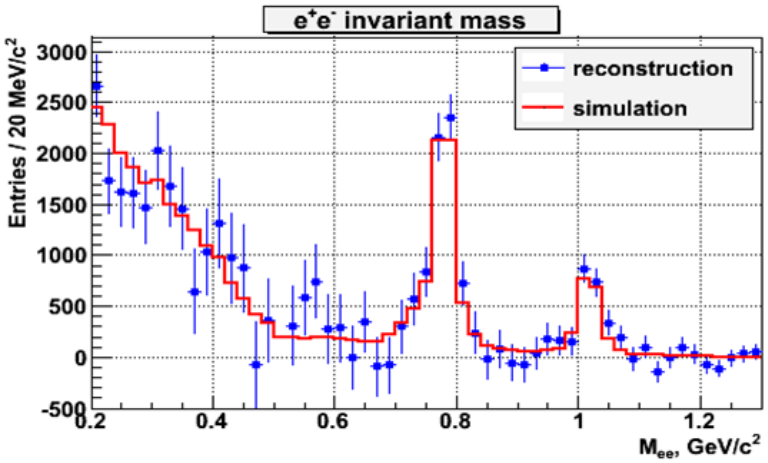

FIGURE 7. Invariant mass of dileptons after background subtraction from central Au+Au collisions in MPD ($2 \cdot 10^7$ simulated events).

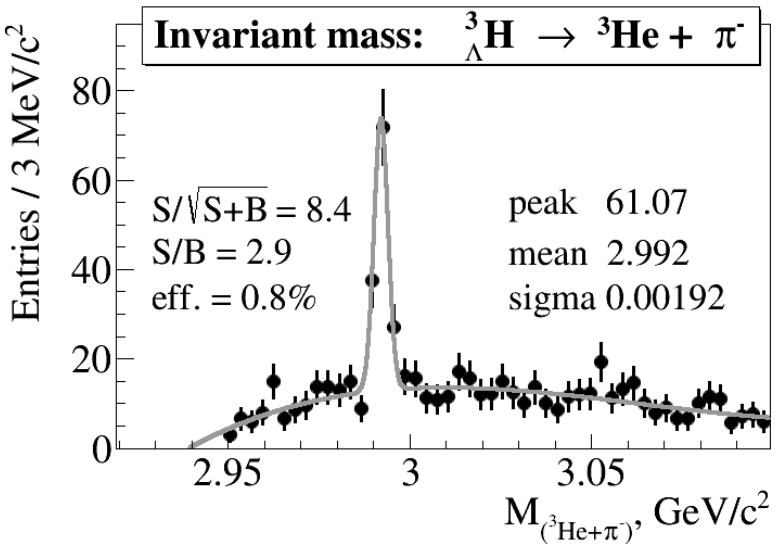

FIGURE 8. Invariant mass of ^{3}He and π^- candidates in central Au+Au at $\sqrt{s_{NN}} = 9$A GeV (10^5 simulated events).

CONCLUSION AND OUTLOOK

The MPD detector has designed to register heavy-ion interactions at the NICA collider. Its parameters allow precise measurements of the hadro-production in high multiplicity events in addition to measure vector meson spectra via lepton decays. The NICA heavy-ion research program after putting the MPD startup into operation in 2019 will open the door to whole set of QCD properties at the highest baryonic density.

REFERENCES

1. G. Trubnikov, A. Kovalenko, V. Kekelidze, I. Meshkov, R. Lednicky, A. Sissakian, A. Sorin, *PoS (ICHEP 2010)*, 523.
2. G. Trubnikov, N. Agapov, V.Kekelidze, A. Kovalenko, V. Matveev, I.Meshkov, R. Lednicky, A. Sorin, *PoS 36th International Conference of High Energy Physics (ICHEP2012)*, July 4-11, Melbourne, Australia.
3. R. Rapp and J. Wambach, *Adv. Nucl. Phys.* **25**, 1 (2000).
4. G.E. Brown and M. Rho, *Phys. Rev. Lett.* **66**, 2720 (1991).
5. J. Randrup and J. Cleymans, *Phys. Rev. C* **74**, 047901 (2006).
6. K.U. Abraamyan et al., *Nucl. Instrum. Meth. A* **628**, 99 (2011).
7. V. Vasendina et al, *Phys. Part. Nucl. Lett.* **10** (2013) 769.
8. M. Ilieva et al., *Phys. Part. Nucl. Lett.* **12** (2015) 618-627.

Experiment BM@N for studies of baryonic matter at the Nuclotron

Mikhail Kapishin

Joint Institute for Nuclear Research, 141980 Russia, Moscow region, Dubna, Joliot Curie 6

Abstract. BM@N (Baryonic Matter at Nuclotron) is the first experiment to be realized at the accelerator complex of NICA-Nuclotron. The aim of the BM@N experiment is to study interactions of relativistic heavy ion beams with fixed targets. The BM@N set-up, results of Monte Carlo simulations and the BM@N experimental program are presented.

Keywords: relativistic heavy ion collisions, baryonic matter, hyperons, hypernuclei
PACS: 25.75.Ag; 29.30.Ep; 29.40.Cs; 29.40.Vj

NUCLOTRON HEAVY-ION PHYSICS PROGRAM

Relativistic heavy ion collisions provide an unique opportunity to study nuclear matter at extreme density and temperature. In the collision, nuclear matter is heated up and compressed for a very short period of time. The ratio of produced mesons to baryons in the fireball increases with the collision energy. A nucleus-nucleus collision at the Nuclotron with kinetic beam energy in the range from 1 to 4.5 GeV per nucleon produces a baryon dominated fireball contrary to higher energies at RHIC or SPS. According to the QGSM transport model calculations [1], at Nuclotron energies the nucleon densities in the collision zone of two gold nuclei exceed the saturation density by a factor of $3 \div 4$. At these densities nucleons start to overlap. It is expected that under such extreme conditions partial restoration of chiral symmetry might occur [2, 3, 4, 5, 6]. It will reveal in in-medium modification of hadrons, in particular, in collisional broadening and dropping mass of vector mesons decaying into di-leptons which are not much effected by final-state interactions.

The relevant degrees of freedom at Nuclotron energies are first of all nucleons and their excited states followed by light and strange mesons. Also the partonic degrees of freedom might show up in small space-time volumes and leave their traces in final hadronic observables. The focus of experimental studies will be on hadrons with strangeness, which are early produced in the collision and not present in the initial state of two colliding nuclei, as nucleons made up from light (u, d)-quarks. The measured production yields of light and strange mesons, as well as of hyperons and anti-hyperons are shown in fig. 1 as a function of the nucleon-nucleon collision energy in c.m.s. The Nuclotron beam energy range corresponds to $\sqrt{s_{NN}} = 2.3 \div 3.5$ GeV. It is well suited for studies of strange mesons and multi-strange hyperons produced in nucleus-nucleus collisions close to the kinematic threshold. These studies and the measurements of collective flows of hadrons provide insights on the equation-of-state (EoS) of strongly interacting matter.

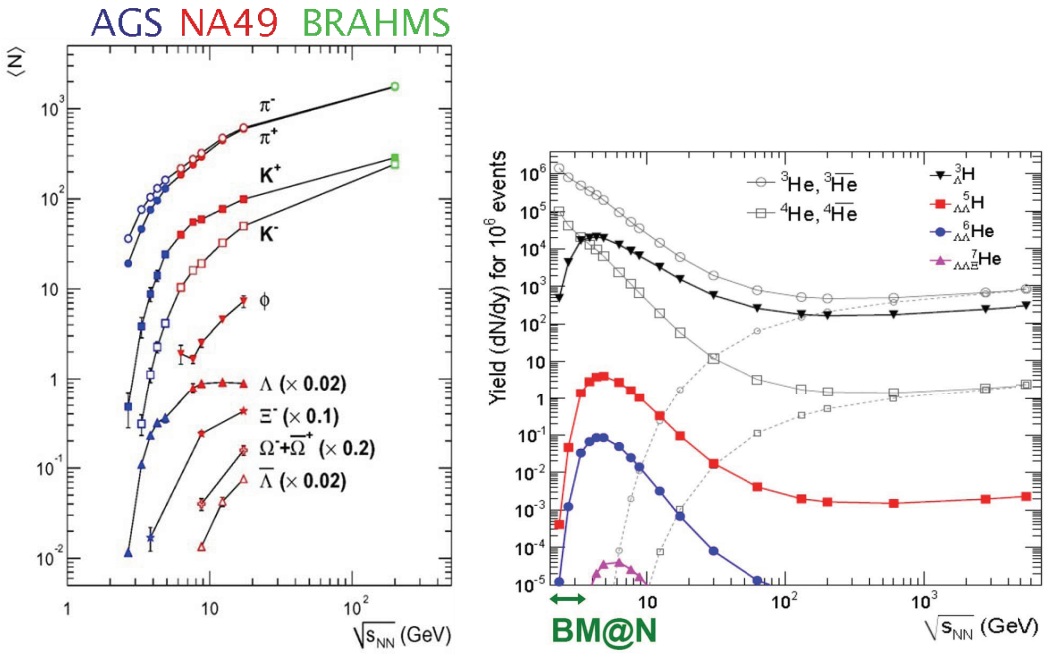

FIGURE 1. Left plot: Yields of mesons and (anti-) hyperons as a function of the nucleon- nucleon collision energy in c.m.s. in Au+Au/ Pb+Pb collisions, taken from [8]. Right plot: Yields of hyper-nuclei as a function of the nucleon-nucleon collision energy in c.m.s. in Au+Au collisions, calculated with a thermal model [9]. The predicted yields of ^{3}He and ^{4}He nuclei are included for comparison. The Nuclotron BM@N beam energy range corresponds to $\sqrt{s_{NN}} = 2.3 \div 3.5$ GeV.

Heavy-ion collisions are a rich source of strangeness, and the coalescence of lambda-hyperons with nucleons can produce a variety of light hyper-nuclei [5, 6]. The study of the hyper-nuclei production is expected to provide new insights into the properties of the hyperon-nucleon and hyperon-hyperon interactions. Figure 1 also presents the yields of hyper-nuclei as a function of the nucleon-nucleon collision energy in c.m.s. in Au+Au collisions, predicted by a thermal model [9]. The maximum in the hyper-nuclei production rate is predicted at $\sqrt{s_{NN}} \sim 4 \div 5$ GeV, which is close to the Nuclotron energy range.

In sum, the research program on heavy-ion collisions at the Nuclotron [7, 10] includes the following topics: investigation of the reaction dynamics and nuclear EoS, study of the in-medium properties of hadrons, production of (multi)-strange hyperons at the threshold and search for hyper-nuclei. In order to interpret experimental data from heavy-ion collisions and to provide a normalization for the measured A+A spectra, a study of elementary reactions (p+p, p+n(d)) is planned.

DETECTOR BM@N

BM@N (Baryonic Matter at Nuclotron) is the first experiment at the accelerator complex of NICA-Nuclotron. The schematic view of the NICA-Nuclotron complex and the position of the BM@N setup are presented in fig. 2. The sources of light and heavy

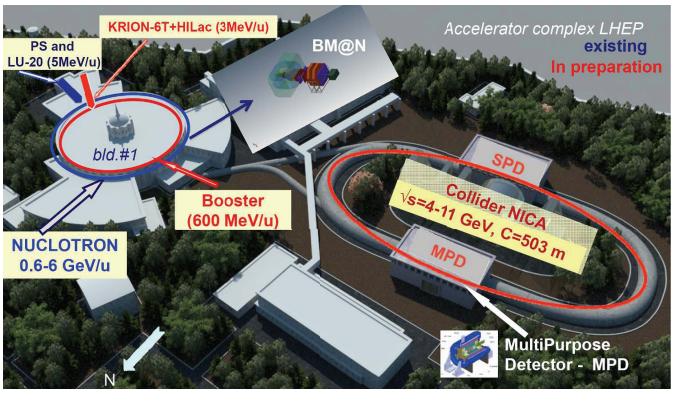

FIGURE 2. Schematic view of the NICA-Nuclotron complex and the existing position of the BM@N setup.

ions, the beam Booster, Nuclotron accelerator and NICA collider are shown. The heavy-ion physics program of the NICA accelerator complex and the MPD experiment planned at the NICA collider are described in [11, 12, 13, 14]. The aim of the BM@N experiment is to study interactions of relativistic heavy ion beams with fixed targets [10]. The Nuclotron will provide variety of beams from protons to gold ions with the kinetic energy of ions ranging from 1 to 6 GeV per nucleon. The maximum kinetic energy for ions with the ratio of the charge to the atomic weight (Z/A) of 1/2 is 6 GeV per nucleon. The maximum kinetic energy for gold ions with the ratio of Z/A $\sim$ 1/3 is 4.5 GeV per nucleon. The maximum kinetic energy of protons is 13 GeV. The existing beam line between the Nuclotron and the BM@N experiment is around 160 meter in length. It comprises 26 elements of magnetic optics: 8 dipole magnets and 18 quadruple lenses. An upgrade program of the beam line is foreseen to minimize the amount of scattering material on the way of heavy ions to the BM@N setup.

The planned intensity of the gold ion beam accelerated and accumulated in the Nuclotron and the Booster and transported to the BM@N experimental zone is up to 10^7 ions per second. The gold ion beam is expected in the beginning of 2019. In the period before 2018 the following ions are foreseen to be accelerated: the polarized deuteron beam in 2016, the carbon, argon and krypton beams in 2017. In this period of operation the planned intensity of the beam interacting with the target inside the BM@N setup is 10^6 ions per second. The proton-proton interactions will be studied after the Nuclotron upgrade planned in 2018 using the proton beam and the liquid hydrogen target. Beam types and intensities are specified in table 1.

Figure 3 shows the diagram of the interaction rates accepted by data acquisition systems of heavy ion experiments running at different energies of colliding nuclei. The beam energy range in the BM@N experiment overlaps partially with that in the HADES experiment. The interaction rate of triggered non-peripheral central and intermediate collisions at the second stage of the BM@N experiment is expected to be around 50 kHz. It is limited by the capacity of the readout electronics and data acquisition system. The second stage of the experiment will be realized in 2020 and later.

A sketch of the proposed configuration of the set-up of the experiment is shown in fig. 4. The experiment combines high precision track measurements with time-of-flight

TABLE 1. Beam parameters and setup at different stages of the experiment

year	2016	2017 spring	2017 autumn	2019	2020 and later
beam	d(↑)	C, Ar	Kr	Au	Au, p
maxim. intensity, Hz	1M	1M	1M	1M	10M
trigger rate, Hz	10k	10k	20k	20k	50k
central tracker status	6 GEM half pl.	8 GEM half pl.	10 GEM half pl.	8 GEM full pl.	12 GEMs or 8 GEMs + Si planes
experim. status	techn. run	techn. run	physics run	stage 1 physics	stage 2 physics

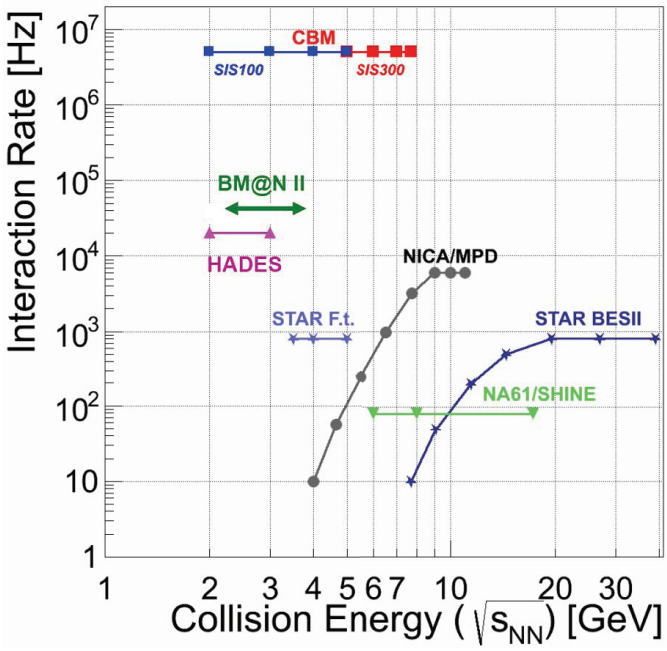

FIGURE 3. Heavy ion experiments: interaction rate and nucleon-nucleon collision energy in c.m.s. The BM@N range is superimposed on the plot taken from [15].

information for particle identification and total energy measurements for the analysis of the collision centrality. The charged track momentum and multiplicity will be measured with the set of twelve planes of GEM (Gaseous Electron Multipliers) detectors with two-coordinate readout located downstream of the target in the analyzing magnet and the drift/straw chambers (DCH, Straw) situated outside the magnetic field. The GEM

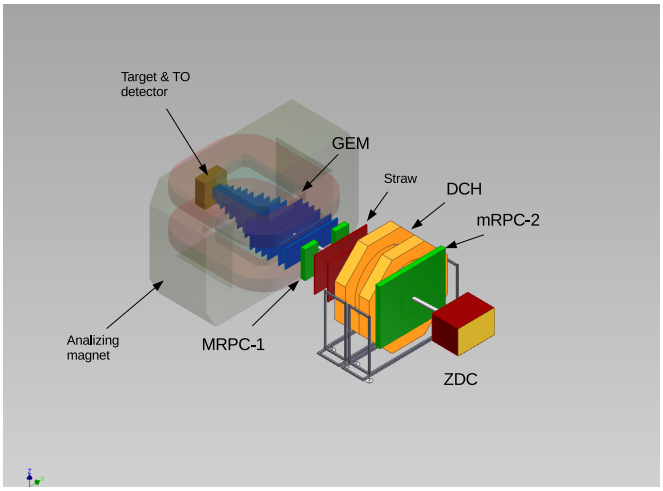

FIGURE 4. Schematic view of the BM@N setup.

detectors sustain high rates of particles and are operational in the strong magnetic field. The gap between the poles of the analyzing magnet is around 1 m. The magnetic field can be varied up to 1.2 T to get the optimal BM@N detector acceptance and momentum resolution for different processes and beam energies. The available drift chambers are suited for reconstruction of interactions of light and medium ion beams. The straw tube detectors will be constructed in addition to the drift chambers to increase the reconstruction efficiency of the outer tracker for heavy ion beams. The design parameters of the time-of-flight detectors based on multi-gap resistive plate chambers (mRPC-1,2) with a strip read-out allow us to discriminate between hadrons (π,K,p) as well as light nuclei with the momentum up to few GeV/c produced in multi-particle events. The zero degree calorimeter (ZDC) is designed for the analysis of the collision centrality by measuring the energy of forward going particles. The T0 detector, partially covering the backward hemisphere around the target, is planned to trigger central heavy ion collisions and provide a start time (T0) signal for the mRPC-1,2 detectors. An electro-magnetic calorimeter will be installed behind the mRPC-2 wall to study processes with electro-magnetic probes ($\gamma, e^{\pm}$) in the final state.

The first technical run of the BM@N detectors was performed with the deuteron and carbon beams in March 2015. The view of the BM@N setup in the run is presented in fig. 5. The experimental data from the drift chambers, time-of-flight detectors, zero degree calorimeter, start time and trigger detectors were readout using the integrated data acquisition system. Meanwhile, the GEM detectors for the BM@N central tracker are being produced at the CERN workshop. The GEM detectors with the maximum size of 200 to 45 cm^2 are foreseen for the BM@N central tracker. Two GEM detectors, fixed around the beam pipe, comprise one full plane.

The minimal configuration of the central tracker in 2016 is based on 6 GEM detectors (half-planes) installed along the beam line. The central tracker will be extended step by step up to eight GEM planes of the full size in beginning of 2019. The factual realization depends on the production capacity of the CERN workshop. The first physics run is

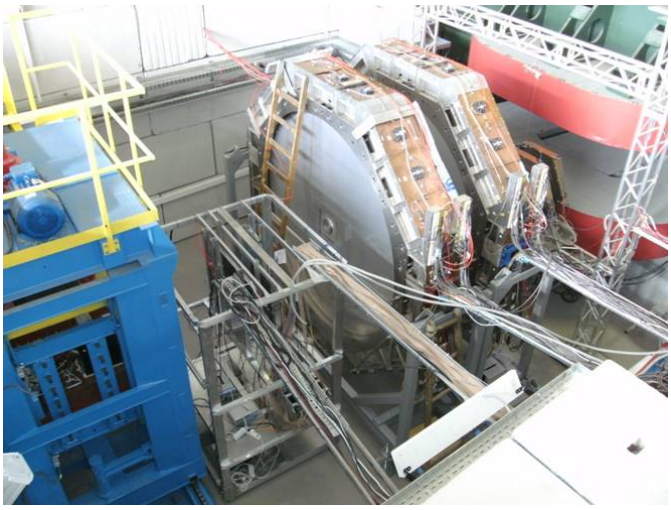

FIGURE 5. BM@N setup behind the analyzing magnet in the first technical run in March 2015. The beam direction is from the right. Two big drift chambers, movable platform with the zero degree calorimeter and elements of mRPC-1,2 time-of-flight detectors are installed.

planned in autumn of 2017 with krypton beam. The full configuration of the central tracker assumes 12 GEM planes. The central tracker configurations at different stages of the experiment are specified in table 1. At the second stage of the BM@N experiment starting in 2020, four planes of two-coordinate silicon strip detectors could be installed instead of four GEM planes situated next to the target to improve the track reconstruction efficiency in Au+Au collisions. Presently, the detectors of this type are being developed for the CBM experiment [16]. The factual realization of the upgrade depends on the time schedule of the silicon tracker program at CBM.

BM@N SIMULATIONS AND FEASIBILITY STUDIES

Activities on the detector and beam line construction are complemented with intensive Monte Carlo simulation studies for optimization of the detector set-up. Special focus is set on the measurement of strange hyperons and hyper-nuclei in Au+Au collisions at the maximal kinetic beam energy of 4.5 AGeV. The simulation of Au+Au collisions is performed using the URQMD [17] and DCM-QGSM [18] models for heavy ion collisions. The products of collisions are transported through the BM@N setup using the GEANT program and reconstructed using the track reconstruction algorithm for multi-particle events [19].

Figure 6 illustrates the distribution of primary protons generated in Au+Au collisions at the kinetic beam energy of 4.5 AGeV in the phase space of the transverse momentum and rapidity in the laboratory frame. The product of the geometrical acceptance and track reconstruction efficiency in 12 stations of the GEM tracker for primary protons for the same phase space is shown on the lower plot. Figure 7 presents the momentum resolution and the vertex impact parameter resolution of charged particles reconstructed in the GEM tracker. The results are presented for the magnetic field in the center of the

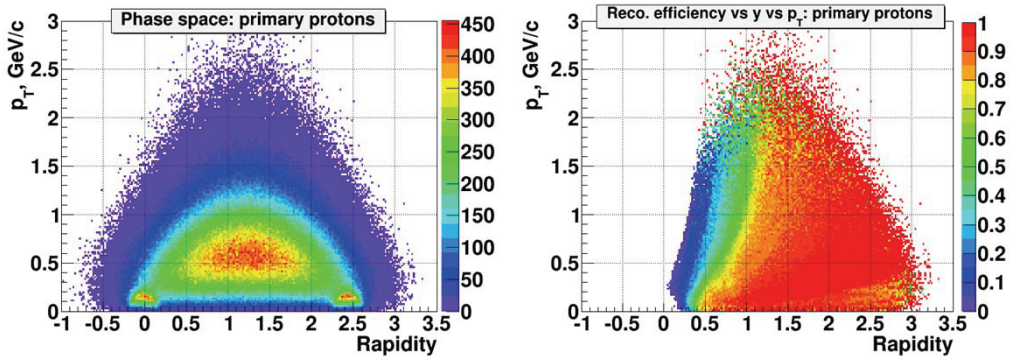

FIGURE 6. Upper plot: distribution of primary protons generated in Au+Au collisions at the kinetic beam energy of 4.5 AGeV in the phase space of the transverse momentum and rapidity in the laboratory frame. Lower plot: product of the geometrical acceptance and track reconstruction efficiency in 12 stations of the GEM tracker for primary protons as a function of the particle transverse momentum and rapidity.

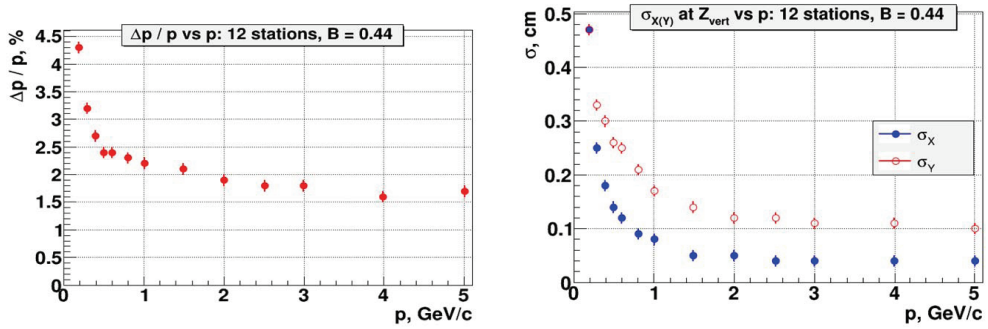

FIGURE 7. Momentum resolution (upper plot) and vertex impact parameter resolution (lower plot) of charged particles reconstructed in 12 stations of the GEM tracker shown as a function of the particle momentum.

magnet of 0.44 T. Figure 8 presents the distributions of the invariant mass of decay products of Λ hyperon, Ξ^- hyperon and hyper-triton ${}^3_\Lambda H$ reconstructed with the GEM tracker in simulated central Au+Au collisions at the kinetic beam energy of 4.5 AGeV. The obtained results indicate that the proposed set-up has a reasonable reconstruction capability for strange hyperons produced in high multiplicity central Au+Au collisions. The signal of Λ hyperon is reconstructed in 10k events of simulated central collisions. At least two Λ hyperons are reconstructed in 30% of central events. The reconstructed signals of Ξ^- hyperon and hyper-triton ${}^3_\Lambda H$ correspond to 0.9M and 2.6M of central collisions, respectively. Taking into account the signal reconstruction efficiency, data acquisition capacity of 20 kHz of triggered central collisions and the duty factor of the Nuclotron beam of 0.5, the expected statistics of Ξ^- hyperons and hyper-tritons ${}^3_\Lambda H$ for a month of the BM@N operation are 7.5M and 8.5M, respectively. The expected statistics is sufficient to perform measurements of strange hyperon and hyper-nuclei production yields and ratios, transverse momentum spectra, rapidity and angular distributions. Studies of fluctuations of event properties and correlations between products of nucleus-nucleus interactions are also feasible.

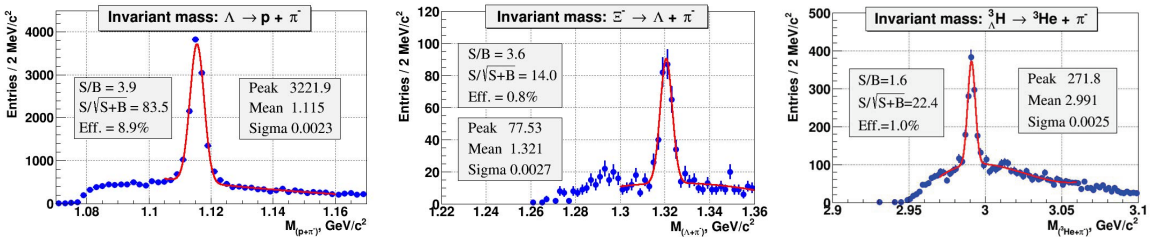

FIGURE 8. Distributions of the invariant mass of decay products of Λ hyperon, Ξ^- hyperon and hypertriton ${}^3_\Lambda H$ reconstructed with 12 stations of the GEM tracker in simulated central Au+Au collisions at the kinetic beam energy of 4.5 AGeV. The statistics of simulated events are given in the text.

REFERENCES

1. B. Friman, W. N*ö*renberg, and V.D. Toneev, Eur. Phys. J. A **3** (1998).
2. R. Rapp, J. Wambach, Eur. Phys. J. A **6**, 415 (1999) .
3. G. E. Brown, Prog. Theor. Phys. **91**, 85 (1987).
4. W. Cassing and E. L. Bratkovskaya, Phys. Rep. **308**, 65 (1999).
5. J. Steinheimer *et al.*, Progress in Particle and Nuclear Physics **62**, 313317 (2009).
6. J. Steinheimer, K. Gudima, A. Botvina, I. Mishustin, M. Bleicher, H. Stocker, Phys. Lett. B **714**, 85 (2012).
7. NICA White Paper, `http://theor0.jinr.ru/twiki-cgi/view/NICA/NICAWhitePaper`
8. C. Blume, J. Phys. G **31**, S57 (2005) .
9. A. Andronic *et al.*, Phys. Lett. B **695**, 203 (2011).
10. BM@N Conceptual Design Report. `http://nica.jinr.ru/files/BM@N/BMN_CDR.pdf`
11. G. Trubnikov, A. Kovalenko, V. Kekelidze, I. Meshkov, R. Lednicky, A. Sissakian, A. Sorin, PoS, ICHEP 2010, July 22-28, Paris, France, p.523.
12. G. Trubnikov, N. Agapov, V.Kekelidze, A. Kovalenko, V. Matveev, I.Meshkov, R. Lednicky, A. Sorin, PoS, ICHEP 2012, July 4-11, Melbourne, Australia, p.411.
13. V. Kekelidze, A. Kovalenko, R. Lednicky, V. Matveev, I.Meshkov, A. Sorin, G. Trubnikov, PoS, ICHEP 2014, July 2-9, Valencia, Spain.
14. V. Kekelidze, Multi-purpose detector (MPD) of the collider experiment, these proceedings.
15. V. Friese, Strangeness Prospects with the CBM Experiment, talk at the SQM-2015 Conference, Dubna, Russia, July 6-11, 2015.
16. J. Heuser *et al.*, Technical Design Report for the CBM Silicon Tracking System, CBM Collaboration, GSI Report 2013-4, `http://repository.gsi.de/record/54798`
17. URQMD model, `http://urqmd.org/`
18. DCM-QGSM model, A.S. Botvina *et al.*, Rhys. Rev. C **84**, 064904 (2011).
19. I. Kisel, Nucl. Instrum. Meth. A **566**, 85 (2006).

The Physics Case for the NICA Project

J. Cleymans

UCT-CERN Research Centre and Physics Department, University of Cape Town, South Africa

Abstract. A short review is presented of the status of the thermal model and chemical freeze-out in relativistic heavy-ion collisions. Some interesting aspects of the physics expected in the energy region covered by the NICA project are emphasized.

Keywords: Heavy Ion Collisions, Thermal Model, LaTeX 2_ε
PACS: 25.75.-q,25.75.Dw

USE OF STATISTICAL CONCEPTS IN HEAVY-ION COLLISIONS

Nuclear collisions at high energies produce large numbers of secondaries. Results from the ALICE collaboration [1] on the pseudo-rapidity distribution of charged particles, reproduced in Fig. 1, show that at mid-rapidity the number of secondary particles is around 1600 for central collisions, which leads to roughly 16 000 charged particles when the full rapidity length is considered or approximately 24 000 when including also neutral particles. In view of this large number it is natural to consider a statistical-thermal model to analyze these. Concepts like temperature T, energy density, pressure, net baryon density etc... are useful and should be used. This has led to a very systematic analysis of yields of identified particles at all beam energies with new insights into particle production in heavy ion collisions. The highly successful analysis of particle yields lead to the notion of chemical equilibrium which is by now a well-established tool in the analysis of relativistic heavy ion collisions, see e.g. [2, 3, 4]. The most recent results from the ALICE collaboration on identified particles have been summarized in [5]. A slightly different way of plotting these results, first proposed in [6], is shown in Fig. 2. The fit is clearly of a high quality and gives support to the notion that a single freeze-out temperature and a single volume are adequate to describe the yields. It can be seen from the figure that the number of pions is underestimated by the model while the number of protons is overestimated but, overall, it can be concluded that chemical equilibrium is a healthy good first approximation to the experimental results.

At lower energies, recent results have been presented by the HADES collaboration. Again these results fit in very well with previous results of the thermal model except for the yield of Ξ which is produced below threshold.

Substantial new knowledge became available in the past decade and now covers almost the complete $T - \mu_B$ curve. A last gap still exists in an energy region to be covered by the Beam Energy Scan at RHIC [7] and by the NA61 [8], FAIR [9] and NICA [10] collaborations. All the results obtained from hadronic yields in heavy ion collisions can be summarized in two figures showing the dependence of the freeze-out temperature on the beam energy and the baryon chemical potential μ_B in Fig. 3

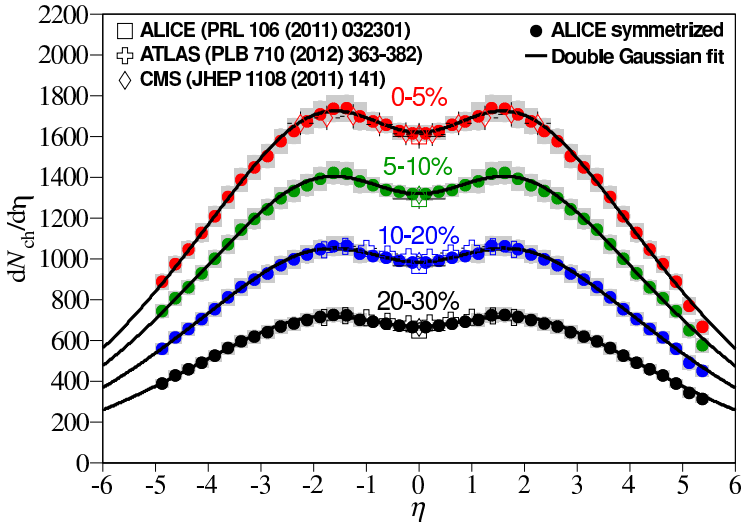

FIGURE 1. Results from the ALICE collaboration [1] on the pseudo-rapidity of charged particles as a function of centrality

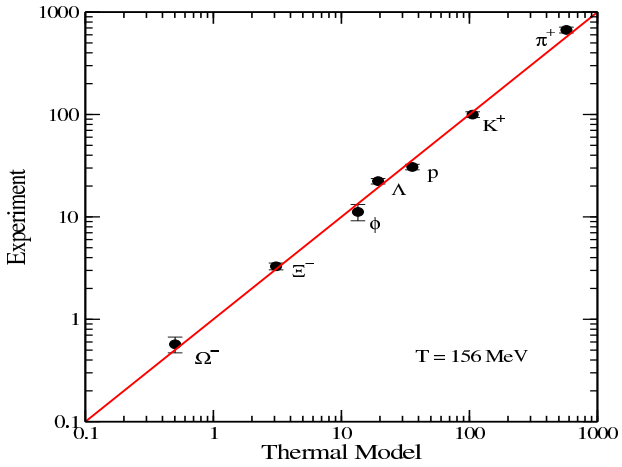

FIGURE 2. Comparison between yields calculated in the thermal model for $T = 156$ MeV and experimental results from the ALICE collaboration [5].

CONSEQUENCES FOR THE NA61/RHIC/FAIR/NICA ENERGY REGION.

The resulting freeze-out curve in the $T - \mu_B$ plane can also be drawn in the energy density vs net baryon density plane as was first done in Ref. [12]. The resulting curve is shown in Fig. 4. The quantities considered are extensive ones and hence they become dependent upon new features like the intrinsic volume of the hadrons. The dependence on this excluded volume is quite important as can be seen from Fig. 4. This feature was first analyzed in detail in [13]. This figure shows that the highest net baryon density will be reached in the beam energy covered by the RHIC/NA61/FAIR/NICA experiments.

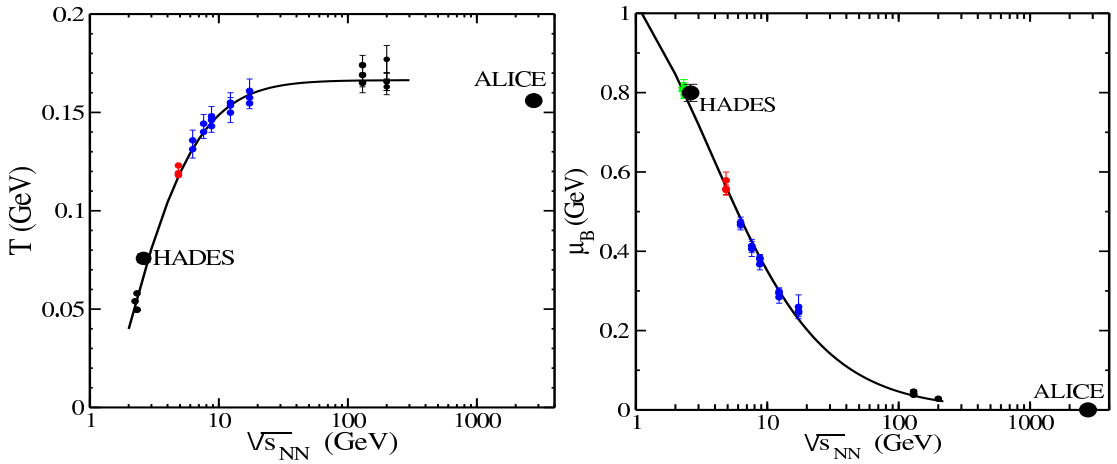

FIGURE 3. Chemical freeze-out temperature T (left panel) and chemical freeze-out baryon chemical potential μ_B (right panel) as a function of the beam energy. The points from ALICE [1] and HADES [11] are indicated. For the other points see [2, 3, 4]

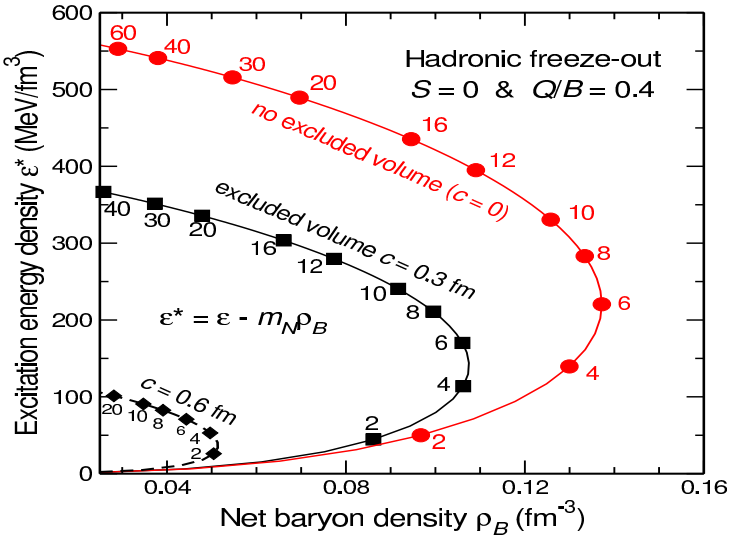

FIGURE 4. The hadronic freeze-out line in the $\rho_B - \varepsilon^*$ phase plane as obtained from the values of μ_B and T that have been extracted from the experimental data in [4]. The calculation employs values of μ_Q and μ_S that ensure $\langle S \rangle = 0$ and $\langle Q \rangle = 0.4 \langle B \rangle$ for each value of μ_B. Also indicated are the beam energies (in GeV/N) for which the particular freeze-out conditions are expected at either RHIC [7], NA61 [8], FAIR [9] or NICA [10].

The corresponding dependence of the temperature and the chemical potential on beam energy is surprisingly smooth [4] as shown in Fig. 3. This however does not imply that the particle ratios as a function of beam energy are also smooth. This can be seen in the $\Lambda/ < \pi >$ ratio, shown in Fig. 5, as well as in th K/π ratio in Fig. 6 where clear maxima are seen. Note that the K^-/π^- ratio does not have a maximum, which is as expected in the thermal model due to the opposite sign for the chemical potential. In the thermal model this maximum has a simple origin, namely, the baryon chemical

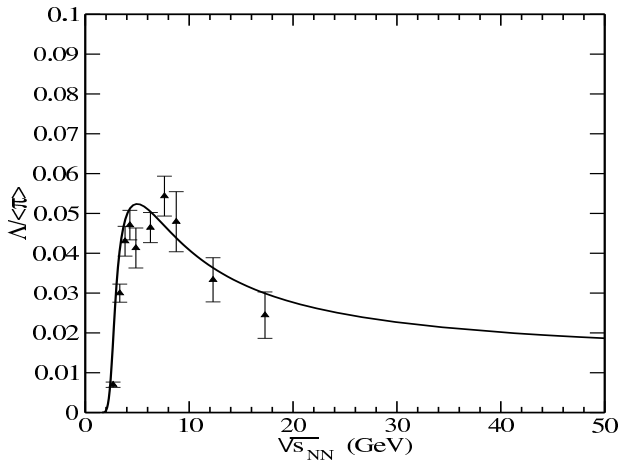

FIGURE 5. Comparison between the thermal model and experimental results for the $\Lambda/ < \pi >$ ratio [14].

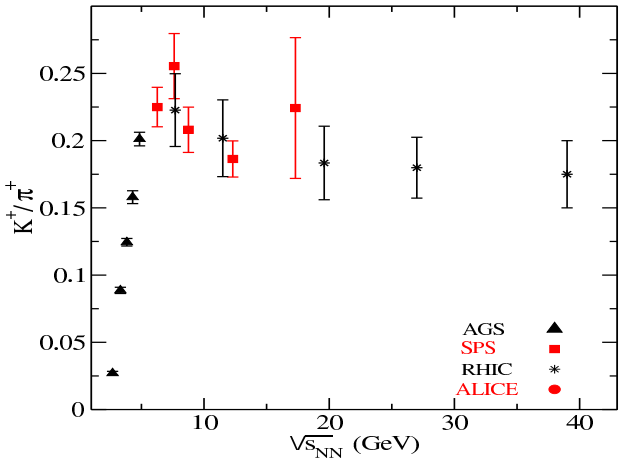

FIGURE 6. The K/π ratios in the energy region covered by the NICA project.

potential decreases continuously with increasing beam energy. At the same time the temperature increases rather quickly until it reaches a plateau which it keeps up to the highest beam energies available. Due to the rapid increase in the temperature with beam energy, ratios like the Λ/π^+ and the K^+/π^+ also increase rapidly. This increase halts when the temperature reaches its limiting value. However, the baryon chemical potential keeps on decreasing. Due to this decrease, the Λ/π ratio also keeps on decreasing, and consequently, also the K^+/π^+ ratio starts decreasing due to strangeness conservation as K^+ are formed in associated production together with a Λ. Note that the K^-/π^- ratio does not have a maximum, which is as expected in the thermal model due to the opposite sign for the chemical potential. The two effects combined lead to a maximum in both ratios, since the baryon chemical potential no longer plays a role at very higher energies and the temperature doesn't change, hence the maxima [14]. In view of the success of chemical freeze-out in relativistic heavy ion collisions, much effort has gone into finding

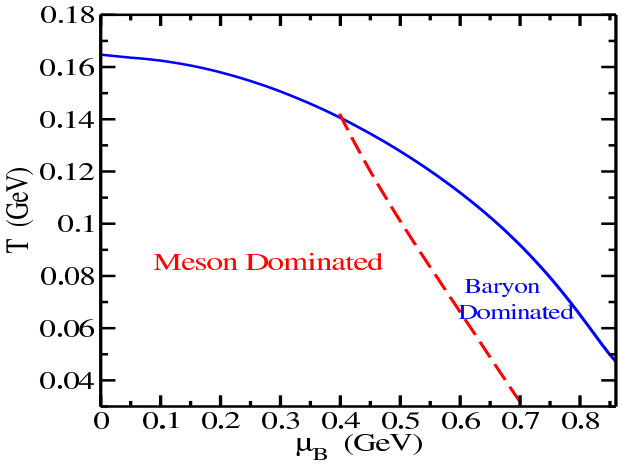

FIGURE 7. The $T - \mu_B$ diagramme showing the chemical freeze-out line as well as the line separating the meson dominated region from the baryon dominated one.

models that lead to a final state in chemical equilibrium, see e.g. curve [15, 16, 17, 14].

To gain more insight in the origin of the changes in the particle ratios, we consider in detail the s/T^3 ratio of the entropy density divided by T^3. It is well-known that when this ratio is fixed to the value 7, it describes fairly well the chemical free-out curve [14]. This has been used to separate the meson-dominated region from the baryon-dominated one as shown in Fig. 7.

CONCLUSIONS

In the thermal-statistical model a rapid change is expected as the hadronic gas undergoes a transition from a baryon-dominated to a meson-dominated gas [14]. The transition occurs at a temperature T = 151 MeV and baryon chemical potential μ_B = 327 MeV corresponding to an incident energy of $\sqrt{s_{NN}}$ = 11 GeV. Thus the strong variation seen in the particle ratios corresponds to a transition from a baryon-dominated to a meson-dominated hadronic gas.

In summary, the transition occurs at a

- temperature $T = 151$ MeV,
- baryon chemical potential $\mu_B = 327$ MeV,
- energy $\sqrt{s_{NN}} = 11$ GeV.

In the statistical model this transition leads to peaks in the $\Lambda/\langle\pi\rangle$, K^+/π^+, Ξ^-/π^+ and Ω^-/π^+ ratios. However, it must be noted that, so far, the experimentally observed ratios appear to be sharper than those calculated in thermal-statistical models.

The theoretical interpretation can only be clarified by covering this energy region in much more detail. In particular the strangeness content needs to be determined with precision, data covering the full phase space (4π) would all be very helpful in determining the parameters of a possible phase transition and the existence of a quarkyonic phase as

has been discussed recently [18]. In summary, in the NICA energy region there is a :

- Maximum in K^+/π^+ ratio,
- Maximum in Λ/π ratio,
- Maximum in the net baryon density,
- Transition from a Baryon dominated system to a Meson dominated.

Need on say more about the interest in the NICA energy region?

ACKNOWLEDGMENTS

The numerous contributions by H Oeschler, J. Randrup, K. Redlich, E. Suhonen and S. Wheaton are gratefully acknowledged.

REFERENCES

1. E. Abbas, et al., *Phys. Lett.* **B726**, 610–622 (2013), 1304.0347.
2. A. Andronic, P. Braun-Munzinger, and J. Stachel, *Nucl. Phys.* **A772**, 167–199 (2006), nucl-th/0511071.
3. F. Becattini, J. Manninen, and M. Gazdzicki, *Phys. Rev.* **C73**, 044905 (2006), hep-ph/0511092.
4. J. Cleymans, H. Oeschler, K. Redlich, and S. Wheaton, *Phys. Rev.* **C73**, 034905 (2006), hep-ph/0511094.
5. M. Floris, *Nucl. Phys.* **A931**, 103–112 (2014), 1408.6403.
6. F. Becattini, *Z. Phys.* **C69**, 485–492 (1996).
7. G. Odyniec, *EPJ Web Conf.* **95**, 03027 (2015).
8. N. Abgrall, et al., *JINST* **9**, P06005 (2014), 1401.4699.
9. I. Augustin, H. H. Gutbrod, D. Kramer, K. Langanke, and H. Stocker, "New Physics at the International Facility for Antiproton and Ion Research (FAIR) Next to GSI," in *4th International Conference on Fission and Properties of Neutron Rich nuclei (ICFN4) Sanibel Island, Florida, USA, November 11-17, 2007*, 2008, URL http://inspirehep.net/record/782515/files/arXiv:0804.0177.pdf, 0804.0177.
10. A. Sorin, V. Kekelidze, A. Kovalenko, R. Lednicky, V. Matveev, I. Meshkov, and G. Trubnikov, *PoS* **CPOD2014**, 042 (2015).
11. M. Lorenz, et al., *J. Phys. Conf. Ser.* **668**, 012022 (2016).
12. J. Randrup, and J. Cleymans, *Phys. Rev.* **C74**, 047901 (2006), hep-ph/0607065.
13. V. V. Begun, M. Gazdzicki, and M. I. Gorenstein, *Phys. Rev.* **C88**, 024902 (2013), 1208.4107.
14. J. Cleymans, H. Oeschler, K. Redlich, and S. Wheaton, *Phys. Lett.* **B615**, 50–54 (2005), hep-ph/0411187.
15. V. Magas, and H. Satz, *Eur. Phys. J.* **C32**, 115–119 (2003), hep-ph/0308155.
16. T. S. Biro, and J. Cleymans, *Phys. Rev.* **C78**, 034902 (2008), 0801.3998.
17. P. Castorina, A. Iorio, and H. Satz, *Int. J. Mod. Phys.* **E24**, 1550056 (2015), 1409.3104.
18. A. Andronic, et al., *Nucl. Phys.* **A837**, 65–86 (2010), 0911.4806.

Vortical structures and strange hyperon polarization in heavy-ion collisions

M. Baznat*, K. Gudima*, A. Sorin† and O. Teryaev†

*Institute of Applied Physics, Academy of Sciences of Moldova, MD-2028 Kishinev, Moldova
†Joint Institute for Nuclear Research, 141980 Dubna, Russia

Abstract.
We study the P-odd effects related to the vorticity of the medium formed in noncentral heavy ion collisions. Using the kinetic Quark-Gluon Strings Model we perform the numerical simulations of the vorticity and hydrodynamical helicity for the various atomic numbers, energies and centralities. We observed the vortical structures typically occupying the relatively small fraction of the fireball volume. In the course of numerical simulations the noticeable hydrodanamical helicity was observed manifesting the specific mirror behaviour with respect to the reaction plane. The effect is maximal at the NICA and FAIR energy range and may lead to the polarization of strange hyperons at the percent level,

Keywords: tire,polarization
PACS: 25.75.-q

INTRODUCTION

The local violation [1] of discrete symmetries in strongly interacting QCD matter is now under intensive theoretical and experimental investigations. The Chiral Magnetic Effect (CME) uses the (C)P-violating (electro)magnetic field emerging in heavy ion collisions in order to probe the (C)P-odd effects in QCD matter.

There is an even more interesting counterpart of this effect, Chiral Vortical Effect (CVE)[2] due to coupling to P-odd medium vorticity leading to the induced electromagnetic and [3] all conserved-charge currents, in particular the baryonic ones.

Another important P-odd observable is the baryon polarizatiion. The mechanism analogous to CVE (known as axial vortical effect, see [4] and Ref. therein) leads to induced axial current of strange quarks which may be converted to polarization of Λ-hyperons [3, 5, 6]. Another mechanism of this polarization is provided [7] by so-called thermal vorticity in the hydrodynamical approach.

The zeroth component of axial current and correspondent axial charge are related to hydrodynamical helicity

$$H \equiv \int dV(\vec{v}\cdot\vec{w}),$$

measuring the (average) projection of velocity $\vec{v}$ to vorticity $\vec{w} = curl\vec{v}$. This quantity is manifesting the recently discovered [6] and confirmed [8] phenomenon of separation, i.e. mirror behavior (same magnitude but different sign) in the half-spaces separated by the reaction plane

The noncentral heavy ion collisions could naturally generate a rotation (global or local, both related to vorticity) with an angular velocity normal to the reaction plane, which is their generic qualitative feature. It is naturally to expect that angular momentum conservation plays an essential role in the defining the quantitative properties of vortical effects. At the same time, it remains to be studied to which extent the particles carrying the main part of angular momentum participate in the collisions.

Here we discuss these problem relying on the extensive numerical simulations [9]. We study in some detail the structure of vorticity field and compare different approaches to polarization calculation. We found the peculiar toroidal "tire-like" structure manifesting themselves in the polarization of hyperons. Very different approaches to polarization calculation lead to qualitatively similar results, while the different rapidity dependence may be used for discrimination between different approaches.

ANGULAR MOMENTUM CONSERVATION IN THE KINETIC MODEL

The natural source of the P-odd observables in heavy-ion collisions is the pseudovector of angular momentum. The question immediately emerges whether it is conserved in the course of evolution governed by Quark-Gluon String Model (QGSM)[10, 11, 12]. To check this we calculated the angular momentum at various moments of collision taking into account both the contributions of participants and spectators.

We found [9] that the participants carry about 20% of angular momentum and that the total angular momentum of participants and spectators is conserved with a rather good accuracy.

LARGE-SCALE STRUCTURES OF VORTICITY FIELDS

We study the qualitative structure of velocity and vorticity fields. Our observation [9] is that while velocity field represent the "small bang" picture, vorticity field form the relatively thin toroidal "tire-like" structures. It is also interesting that the tire survives the averaging over the azimuthal angles. As a result, some effect of the angular momentum, normal to the reaction planes, is still manifested after the average over their orientations.

HYPERON POLARIZATION

We compare two rather distinct methods of determining the hyperon polarization. The first corresponds to earlier suggested[3] and explored [6, 9] relation to induced axial current while the second one follows the procedure [7] based on thermal vorticity. We paid here a special attention to the pseudoscalar characteristics of the vorticity, that is the hydrodynamical helicity mentioned above $H \equiv \int dV(\vec{v}\cdot\vec{w})$ which is related to a number of interesting phenomena in hydrodynamics and plasma physics, such as the turbulent dynamo (providing possibly additional mechanism of magnetic filed generation on the

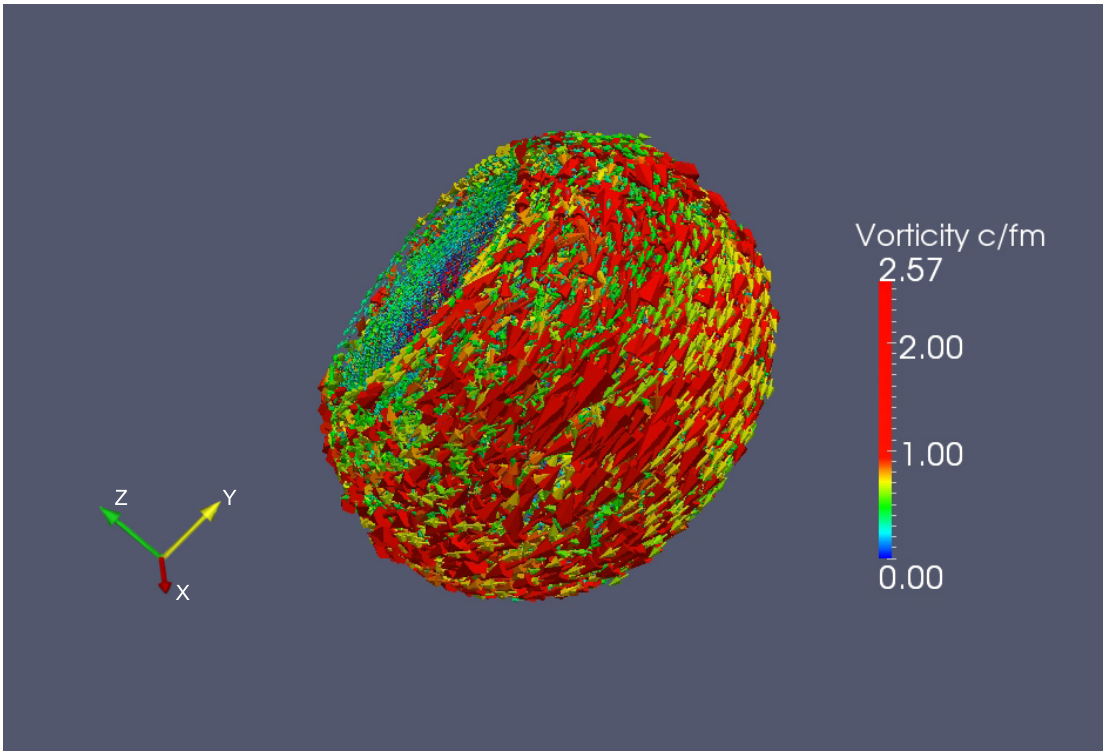

FIGURE 1. Tire-like structure of vorticity field for orientations of reactions plane averaged in the whole 2π region of azimuthal angles

later stages of heavy-ion collisions) and Lagrangian chaos. It might be compared to the topological charge $Q = \int d^3x J^0(x)$ where the current $J^\mu = \varepsilon^{\mu\nu\rho\gamma} u_\nu \partial_\rho u_\gamma$ (as usual, the four-velocity $u_\nu \equiv \gamma\,(1, \vec{v}\,)$) contributes to the hydrodynamical anomaly [13] and the polarization of hyperons [3, 5]. The calculation of the topological charge which is the correct relativistic generalization of the hydrodynamical helicity leads to the extra factor γ^2 in the integrand. Still as the helicity itself is a more traditional quantity, we used it for the numerical calculations.

HELICITY AND POLARIZATION OF HYPERONS

The hydrodynamical helicity should give rise to the polarization of $\Lambda-$hyperons with the sign differing for the particles with "up" and "down" $y-$components of their momenta, so that the hyperons acquire the helicity in the course of their motion transverse to the reaction plane. As we already suggested earlier [3], the effect is pronounced at moderate (NICA) energies due to large (strange) chemical potential. the current investigation shows that, luckily, the helicity at these energies is also noticeable.

For semi-quantitative estimate of this effect one may use the average strange chiral charge produced by the zeroth component of the respective current

$$Q_5^s = \frac{N_c}{2\pi^2}\int d^3x\mu^2(x)\varepsilon^{ijk}u_i\partial_j u_k = \frac{<\mu^2\gamma^2>N_cH}{2\pi^2},$$

where we use the mean value theorem to extract the value of the square of strange chemical potential and Lorentz factor at some point inside the integration region and get the helicity from the remaining integral. Assuming that the strange chirality is carried by the Λ hyperons whose average number in each evemt is $<N_\Lambda>$ one get the estimate for its average polarization as

$$<P_\Lambda> \sim \frac{<\mu^2\gamma^2>N_cH}{2\pi^2<N_\Lambda>}$$

For numerical estimate at NICA energies, we take $H = 30fm^2(c=1)$ and, as a typical values,

$$<\mu^2> = 900MeV^2,\ <N_\Lambda> = 15$$

to get

$$<P_\Lambda> \sim 1\%.$$

This value is not large, but does not exclude the opportunity to measure the effect. Note that it is indirectly supporting the actual calculations of helicity as the obtained expression respects the density matrix positivity [14] limit $P_\Lambda \leq 1$. Should the helicity be much larger, much larger number of hyperons production (and/or K^*-mesons) would be required to preserve the density matrix positivity. This is an example of the situation when the spin-dependent effects may be used [14] to bound the spin-averaged cross-sections from below.

Note also that the polarization in the very different thermal vorticity approach [7] appears to be of the same scale but has the different rapidity dependence [9] which may be used to discriminate different mechanisms.

CONCLUSIONS AND OUTLOOK

We investigated vorticity and hydrodynamical helicity in noncentral heavy-ion collisions in the framework of the kinetic quark-gluon string model. We have observed that the vorticity is predominantly localized in a relatively thin layer ($2\div 3\ fm$) on the boundary between the participant and spectator nucleons. This might be qualitatively understood in the spirit of the core-corona type models [15, 16].

Thus, the gradients of the velocities in the region occupied by the participants are small due to the compensation of momenta between the target and projectile particles in the c.m. frame. As the result the vorticity is substantial only in the thin transition layer between the participant (i.e., core) and the spectator (i.e., corona) regions. We found the novel effect of the helicity separation in heavy-ion collisions when it has the different signs below and above of the reaction plane. We have investigated its dependence on the

type of nuclei and collision energy and observed that it is maximal in the NICA energy range.

This pattern may be compared with the distribution of P-odd correlation of particle momenta, so-called handedness [8] which is manifesting the similar separation phenomenon. The handedness averages to zero when averaged over the whole momentum space and shows mirror pattern in its separate octants.

We used the obtained values of helicity for estimates of Λ hyperons polarization in heavy-ion collisions at NICA energy range due to earlier suggested [3] mechanism. The resulting polarization is bout 1% and may be studied experimentally. Of course, its more detailed theoretical investigations are required.

ACKNOWLEDGMENTS

We are indebted to Jean Cleymans for useful comments and interest in the work,

This work was partially supported by the program of JINR collaboration with South African institutions.

REFERENCES

1. K. Fukushima, D.E. Kharzeev and H.J. Warringa, Phys. Rev. D **78**, 074033 (2008)
2. D. Kharzeev and A. Zhitnitsky, Nucl. Phys. A **797**, 67 (2007)
3. O. Rogachevsky, A. Sorin and O. Teryaev, Phys. Rev. C **82**, 054910 (2010) [arXiv:1006.1331 [hep-ph]].
4. T. Kalaydzhyan, Phys. Rev. D **89**, no. 10, 105012 (2014) [arXiv:1403.1256 [hep-th]].
5. J. -H. Gao, Z. -T. Liang, S. Pu, Q. Wang and X. -N. Wang, Phys. Rev. Lett. **109**, 232301 (2012)
6. M. Baznat, K. Gudima, A. Sorin and O. Teryaev, Phys. Rev. C **88**, 061901 (2013) [arXiv:1301.7003 [nucl-th]].
7. F. Becattini, L. Csernai and D. J. Wang, Phys. Rev. C **88**, no. 3, 034905 (2013) [arXiv:1304.4427 [nucl-th]].
8. O. Teryaev and R. Usubov, Phys. Rev. C **92**, no. 1, 014906 (2015). doi:10.1103/PhysRevC.92.014906
9. M. I. Baznat, K. K. Gudima, A. S. Sorin and O. V. Teryaev, Phys. Rev. C **93**, no. 3, 031902 (2016) doi:10.1103/PhysRevC.93.031902 [arXiv:1507.04652 [nucl-th]].
10. V.D. Toneev, K.K. Gudima, Nucl. Phys. A **400**, 173c (1983).
11. V.D. Toneev, N.S. Amelin, K.K. Gudima, S.Yu. Sivoklokov, Nucl. Phys. A **519**, 463c (1990).
12. N.S. Amelin, E.F. Staubo, L.S. Csernai et al., Phys.Rev. C **44**, 1541 (1991).
13. D.T. Son and P. Surowka, Phys. Rev. Lett. **103**, 191601 (2009)
14. X. Artru, M. Elchikh, J. -M. Richard, J. Soffer and O. V. Teryaev, Phys. Rept. **470**, 1 (2009)
15. J. Aichelin and K. Werner, Phys. Rev. C **79**, 064907 (2009) Erratum: [Phys. Rev. C **81**, 029902 (2010)] doi:10.1103/PhysRevC.79.064907, 10.1103/PhysRevC.81.029902 [arXiv:0810.4465 [nucl-th]].
16. J. Steinheimer and M. Bleicher, Phys. Rev. C **84**, 024905 (2011) doi:10.1103/PhysRevC.84.024905 [arXiv:1104.3981 [hep-ph]].

Quantum transport in the deformation quantization framework

M. I. Krivoruchenko[1,2,3]

[1]*Institute for Theoretical and Experimental Physics, B. Cheremushkinskaya 25, Moscow 117218, Russia*
[2]*Bogoliubov Laboratory of Theoretical Physics, JINR, Dubna 141980, Russia*
[3]*Moscow Institute of Physics and Technology, Dolgoprudny 141700, Russia*

Abstract. The formalism of deformation quantization offers effective techniques for describing the evolution of complex quantum systems. A special role is attributed to phase-space trajectories $u^i(\xi,\tau)$ which are the Weyl symbols of operators of the canonical coordinates and momenta in the Heisenberg picture. The evolution equations for $u^i(\xi,\tau)$ are infinite-order partial differential equations. In the semiclassical expansion these equations turn to a finite system of fist-order ordinary differential equations in an extended phase space.

Keywords: Deformation quantization, star-product, quantum transport, semiclassical expansion
PACS: 03.65.-w; 03.65.Ca; 03.65.Sq

INTRODUCTION

A classical description of the propagation of particles is currently the essential feature of transport models. With a sharp increase in processing power, over the past few decades, going beyond the classical approximation following the path provided by the deformation quantization has become a promising and realistic goal.

Deformation quantization [1, 2] shares many features of the classical Hamiltonian mechanics. The classical Hamilton equations are known to be the characteristics equations of the Liouville equation for the phase-space distribution function. Accordingly, the solutions of the classical Hamilton equations contain all of the dynamic information needed to determine time dependence of the physical observables, including the phase-space density function. The same situation occurs in the deformation quantization framework. The quantum Hamilton equations [3, 4, 5] allow to find quantum trajectories $u^i(\xi,\tau)\in\mathbb{R}^{2n}$ in the phase space with the initial conditions $u^i(\xi,0)=\xi^i$, which possess typical properties of the characteristics [4, 5, 6, 8]. Usually characteristics satisfy a system of first-order ordinary differential equations (ODEs), e.g., the system of the classical Hamilton equations. Characteristics are used further to construct solutions of the first-order partial differential equations (PDEs), such as the classical Liouville equation. In quantum mechanics, the phase-space trajectories obey infinite-order PDEs and they solve the evolution equations that are infinite-order PDEs.

In the Heisenberg representation, the evolution of the Weyl symbol of operator can be written as

$$f(\xi,\tau)=f(\star u(\xi,\tau),0). \tag{1}$$

The relationships of interest, such as the one shown here, are formulated in terms of $\star$-functions that form a special class of functionals. We outline methods for calculating $\star$-functions using the power series expansion in the Planck constant.

The advantage of the deformation quantization is its proximity to the classical picture of the evolution of systems in the phase space. Specific quantum effects, such as coherence and non-localities, appear due to increase in the number of dynamic degrees of freedom upon the semiclassical expansion of the quantum trajectories, or phase-space streamlines $u^i(\xi,\tau)$, around the classical trajectories.

We show that, for any fixed order of the semiclassical expansion, the quantum phase flow defined by $u^i(\xi,\tau)$ can be constructed by solving a finite system of first-order ODEs [5, 8]. This observation makes it possible to approach the evolution problem of complex quantum systems using the standard numerically efficient ODE integrators. The evolution problem thereby reduces to a statistical-mechanics problem of constructing an ensemble of quantum trajectories $u^i(\xi,\tau)$.

PHASE-SPACE QUANTUM TRAJECTORIES

In Hamiltonian formalism, classical systems with n degrees of freedom are described by $2n$ canonical coordinates and momenta $\xi^i = (q^1,...,q^n,p_1,...,p_n) \in \mathbb{R}^{2n}$. The Poisson bracket for these variables takes the standard form $\{\xi^k,\xi^l\} = -I^{kl}$, where

$$I^{kl} = \begin{pmatrix} 0 & -E \\ E & 0 \end{pmatrix},$$

E is the $n \times n$ unit matrix, $I^2 = -1$.

In quantum mechanics, the canonical variables are mapped into operators of the canonical coordinates and momenta acting in a Hilbert space: $\mathfrak{x}^i = (\mathfrak{q}^1,...,\mathfrak{q}^n,\mathfrak{p}_1,...,\mathfrak{p}_n) \in Op(L^2(\mathbb{R}^n))$. These operators obey the commutation relations $[\mathfrak{x}^k,\mathfrak{x}^l] = -i\hbar I^{kl}$. In what follows the operators $\mathfrak{f} \in Op(L^2(\mathbb{R}^n))$ are denoted by Gothic letters, and the functions $f(\xi)$ in the phase space $\mathbb{R}^{2n}$ are denoted by Latin letters.

The Wigner-Weyl correspondence $\xi^i \leftrightarrow \mathfrak{x}^i$ extends to arbitrary functions and operators. The set of operators is a vector space. This space is endowed with the Groenewold basis [1]

$$\mathfrak{B}(\xi) = (2\pi\hbar)^n \delta^{2n}(\xi - \mathfrak{x}) = \int \frac{d^{2n}\eta}{(2\pi\hbar)^n} \exp(-\frac{i}{\hbar}\eta_k(\xi - \mathfrak{x})^k). \qquad (2)$$

Operators $\mathfrak{B}(\xi)$ satisfy useful properties [9, 10]:

$$\begin{aligned}
\mathfrak{B}(\xi)^{\dagger} &= \mathfrak{B}(\xi), && (3)\\
\mathrm{Tr}[\mathfrak{B}(\xi)] &= 1, && (4)\\
\int \frac{d^{2n}\xi}{(2\pi\hbar)^n}\mathfrak{B}(\xi) &= \mathfrak{1}, && (5)\\
\int \frac{d^{2n}\xi}{(2\pi\hbar)^n}\mathfrak{B}(\xi)\mathrm{Tr}[\mathfrak{B}(\xi)\mathfrak{f}] &= \mathfrak{f}, && (6)\\
\mathrm{Tr}[\mathfrak{B}(\xi)\mathfrak{B}(\xi')] &= (2\pi\hbar)^n\delta^{2n}(\xi-\xi'), && (7)\\
\mathfrak{B}(\xi)\exp(-\frac{i\hbar}{2}\mathscr{P}_{\xi\xi'})\mathfrak{B}(\xi') &= (2\pi\hbar)^n\delta^{2n}(\xi-\xi')\mathfrak{B}(\xi'). && (8)
\end{aligned}$$

Here, $\mathscr{P}_{\xi\xi'} = -I^{kl}\frac{\overleftarrow{\partial}}{\partial\xi^k}\frac{\overrightarrow{\partial}}{\partial\xi^l}$ is the Poisson operator.

The Wigner-Weyl association rule $f(\xi)\leftrightarrow\mathfrak{f}$ takes, in the basis $\mathfrak{B}(\xi)$, the simple form [1]

$$\begin{aligned}
f(\xi) &= \mathrm{Tr}[\mathfrak{B}(\xi)\mathfrak{f}], && (9)\\
\mathfrak{f} &= \int \frac{d^{2n}\xi}{(2\pi\hbar)^n}f(\xi)\mathfrak{B}(\xi). && (10)
\end{aligned}$$

The function $f(\xi)$ can be treated as the coordinate of the operator $\mathfrak{f}$ in the basis $\mathfrak{B}(\xi)$, while the right side of Eq.(9) can be interpreted as the scalar product of $\mathfrak{B}(\xi)$ and $\mathfrak{f}$.

Substituting in the place of $\mathfrak{f}$ density matrix $\mathfrak{r}$, we get on the left side of (9) the Wigner function

$$W(\xi) = \mathrm{Tr}[\mathfrak{B}(\xi)\mathfrak{r}]. \quad (11)$$

The normalization condition $\mathrm{Tr}[\mathfrak{r}] = 1$ implies

$$\int \frac{d^{2n}\xi}{(2\pi\hbar)^n}W(\xi) = 1. \quad (12)$$

The set of operators $Op(L^2(\mathbb{R}^n))$ is closed under the multiplication of the operators. Given two functions $f(\xi) = \mathrm{Tr}[\mathfrak{B}(\xi)\mathfrak{f}]$ and $g(\xi) = \mathrm{Tr}[\mathfrak{B}(\xi)\mathfrak{g}]$, one can construct a third function [1]

$$f(\xi)\star g(\xi) = \mathrm{Tr}[\mathfrak{B}(\xi)\mathfrak{f}\mathfrak{g}]. \quad (13)$$

This operation is called $\star$-*product*, its explicit form is given by

$$f(\xi)\star g(\xi) = f(\xi)\exp(\frac{i\hbar}{2}\mathscr{P})g(\xi), \quad (14)$$

where $\mathscr{P} = \mathscr{P}_{\xi\xi}$. The $\star$-product splits into symmetric and skew-symmetric parts

$$f\star g = f\circ g + \frac{i\hbar}{2}f\wedge g. \quad (15)$$

The skew-symmetric part $f \wedge g$ is known under the name of Moyal bracket. It governs quantum evolution in phase space. In classical limit, the Moyal bracket turns to the Poisson bracket: $\lim_{\hbar\to 0} f \wedge g = \{f,g\}$.

The average value of a physical observable described by an operator $\mathfrak{f}$ can be calculated in terms of the Wigner function. If $\mathfrak{f} \leftrightarrow f(\xi)$, then

$$\langle \mathfrak{f} \rangle = \mathrm{Tr}[\mathfrak{f}\mathfrak{r}] = \int \frac{d^{2n}\xi}{(2\pi\hbar)^n} f(\xi) \star W(\xi). \tag{16}$$

The set of operators of the canonical variables is complete in the sense that any operator can be represented as a function of the operators $\mathfrak{x}^i$, i.e., for any $\mathfrak{f}$ one can find $f(\xi)$ such that $\mathfrak{f} = f(\mathfrak{x})$. The function of operators is well defined in the sense of Taylor expansion. The evolution $\mathfrak{f} \to \acute{\mathfrak{f}} = \mathfrak{U}^\dagger(\tau)\mathfrak{f}\mathfrak{U}(\tau)$ under the one-parameter family of unitary operators $\mathfrak{U}(\tau)$ generates transformations of the associated functions in phase space:

$$\begin{aligned} f(\xi) \to \acute{f}(\xi) &= f(\xi,\tau) = \mathrm{Tr}[\mathfrak{B}(\xi)\mathfrak{U}^\dagger(\tau)\mathfrak{f}\mathfrak{U}(\tau)] \\ &= \mathrm{Tr}[\mathfrak{B}(\xi) f(\mathfrak{U}^\dagger(\tau)\mathfrak{x}\mathfrak{U}(\tau))] \\ &= f(\star u(\xi,\tau)). \end{aligned} \tag{17}$$

The $\star$-function $f(\star u(\xi,\tau))$ is the functional of $2n$ functions

$$u^i(\xi,\tau) = \mathrm{Tr}[\mathfrak{B}(\xi)\mathfrak{U}^\dagger(\tau)\mathfrak{x}^i\mathfrak{U}(\tau)]. \tag{18}$$

which are the phase-space quantum trajectories. Equation (1) follows from Eq. (17). Phase-space transformations induced by the unitary operator $\mathfrak{U}(\tau)$ preserve the Moyal bracket and do not preserve the Poisson bracket, so the evolution map $\xi \to u(\xi,\tau)$ is not canonical [4, 7]. Useful examples presenting the formalism for particular quantum systems are discussed in Refs. [5, 7, 11, 12, 13].

SEMICLASSICAL EXPANSION FOR QUANTUM HAMILTON EQUATIONS

Quantum analog of the classical Hamilton equations can be obtained from the Weyl transform of the evolution equations for the Heisenberg operators of canonical coordinates and momenta [4]

$$\frac{\partial}{\partial\tau} u^i(\xi,\tau) = \{\zeta^i, H(\zeta)\}|_{\zeta=\star u(\xi,\tau)}. \tag{19}$$

The right side of the equation is defined in terms of the $\star$-function. Star-function can be calculated with the help of expansion in powers of the Planck constant. Using the cluster-graph method of Refs. [3, 14] one can proceed up to the fourth order in $\hbar$ analytically.

The quantum trajectories can be found using the semiclassical expansion

$$u^i(\xi,\tau) = \sum_{s=0}^{\infty} \hbar^{2s} u^i_s(\xi,\tau).$$

The right side of Eq. (19), $F^i(\zeta) = \{\zeta^i, H(\zeta)\}$, is the $\star$-function of $\zeta = \star u(\xi,\tau)$. We thus expand

$$F^i(\star u(\xi,\tau)) = \sum_{s=0}^{\infty} \hbar^{2s} F_s^i[u(\xi,\tau)].$$

The lowest term gives the classical trajectory $u_0^i(\xi,\tau)$ which satisfies the classical Hamilton equations

$$\frac{\partial u_0^i}{\partial \tau} = F_0^i(u_0) \tag{20}$$

with the initial conditions $u_0^i(\xi,0) = \xi^i$. Given $u_0^i(\xi,\tau)$, the lowest-order correction $u_1^i(\xi,\tau)$ can be found by solving the first-order ODE:

$$\begin{aligned} \frac{\partial}{\partial \tau} u_1^i = u_1^k \frac{\partial F_0^i(u_0)}{\partial u_0^k} &- \frac{1}{16} I^{k_1 l_1} I^{k_2 l_2} J^{i_1}_{0,k_1 k_2} J^{i_2}_{0,l_1 l_2} \frac{\partial^2 F_0^i(u_0)}{\partial u_0^{i_1} \partial u_0^{i_2}} \\ &- \frac{1}{24} I^{k_1 l_1} I^{k_2 l_2} J^{i_1}_{0,k_1} J^{i_2}_{0,k_2} J^{i_3}_{0,l_1 l_2} \frac{\partial^3 F_0^i(u_0)}{\partial u_0^{i_1} \partial u_0^{i_2} \partial u_0^{i_3}} \end{aligned} \tag{21}$$

with initial conditions $u_1^i(\xi,0) = 0$. The functions $J^i_{0,k}$ and $J^i_{0,kl}$ are the generalized Jacobi fields

$$J^i_{r,k_1\ldots k_t}(\xi,\tau) = \frac{\partial u_r^i(\xi,\tau)}{\partial \xi^{k_1} \ldots \partial \xi^{k_t}} \tag{22}$$

with $r = 0$ and $t = 1,2$. The generalized Jacobi fields also satisfy ODE. The lowest order system is

$$\frac{\partial}{\partial \tau} J^i_{0,k} = \frac{\partial F_0^i(u_0)}{\partial u_0^m} J^m_{0,k}, \tag{23}$$

$$\frac{\partial}{\partial \tau} J^i_{0,kl} = \frac{\partial^2 F_0^i(u_0)}{\partial u_0^m \partial u_0^n} J^m_{0,k} J^n_{0,l} + \frac{\partial F_0^i(u_0)}{\partial u_0^m} J^m_{0,kl}. \tag{24}$$

The first of these equations describes the evolution of small perturbations along the classical phase-space trajectories. Being projected onto a submanifold of the constant energy, it becomes the Jacobi-Levi-Civita equation.

The system of equations (20), (21), (23), and (24) is the closed system of equations which allows to find the lowest order quantum correction to the classical trajectory.

Here, we show that, in any fixed order of $\hbar$, we have a finite system of ODEs for $u_r^i(\tau,\xi)$ and $J^i_{r,k_1,\ldots,k_t}(\tau,\xi)$ subjected to initial conditions

$$u_0^i(\xi,0) = \xi^i, \qquad J^i_{0,k}(\xi,0) = \delta^i_k, \qquad J^i_{0,kl}(\xi,0) = 0, \tag{25}$$

$$u_r^i(\xi,0) = 0, \qquad J^i_{r,k_1\ldots k_t}(\xi,0) = 0 \tag{26}$$

for $r \geq 1$ and $t \geq 1$.

Let us consider the effect of the $\star$-product. According to Eq. (14), each power of $\hbar$ is accompanied by differentiation. For order $\hbar^{2s}$, expansion of $F^i(\star u(\xi,\tau)$ contains the

derivatives of order $2s$ at most. Therefore, the Jacobi fields have the highest degree $2s$ ($1 \le t \le 2s$).

This assertion can be strengthened. The number of indices t also depends on the order r of the Jacobi fields $J^i_{r,j_1,\ldots,j_t}(\xi,\tau)$. In Eq. (17), the derivatives of the trajectory $u^i_0(\xi,\tau)$ of order $\le 2s$, the derivatives of the trajectory $u^i_1(\xi,\tau)$ of order $\le 2s\ldots$, and the derivatives of the trajectory $u^i_{s-1}(\xi,\tau)$ of order ≤ 2 survive among all of the derivatives of orders $\le 2s$. The highest-order correction $u^i_s(\xi,\tau)$ has no derivatives. Thus, the maximum number of lower indices of $J^i_{r,j_1,\ldots,j_t}(\xi,\tau)$, involved in the expansion to order $\hbar^{2s}$, depends on r and equals $2s-2r$ ($1 \le t \le 2s-2r$).

Let us consider in more detail the equations of evolution to order $\hbar^{2s}$ for a fixed $r \le s$.

The first part of the ODE system can be written as

$$\frac{\partial}{\partial\tau}u^i_r = F^i_r(u_0,u_1,\ldots,u_r,J_0,J_1,\ldots,J_{r-1}), \tag{27}$$

where the index r takes the values $1,\ldots,s$. In the argument for the function on the right-hand side, we dropped the indices of the trajectories and the Jacobi fields. Note that the time derivative depends on the Jacobi fields of order $r-1$ at most.

The higher-order corrections depend on the lower-order corrections. In the right-hand side of Eq. (27), the Jacobi fields have the following degrees: $J^i_{0,j_1,\ldots,j_t}(\xi,\tau)$ - not more than $2r$, $J^i_{1,j_1,\ldots,j_t}(\xi,\tau)$ - not more than $2r-2$, and so on. In the highest order $\hbar^{2s}$ - term, the maximum degree of $J^i_{r-1,j_1,\ldots,j_t}(\xi,\tau)$, entering the right-hand side, is equal to $2s-2r+2$. The functions $F^i_r(u_0,u_1,\ldots,u_r,J_0,J_1,\ldots,J_{r-1})$ do not depend on the variables with r' for $r<r'$. Equation (27) allows the determination of the trajectories $u_0(\xi,\tau),\ldots,u_s(\xi,\tau)$, provided that the Jacobi fields are known.

We now supplement the resulting system (27) with the equations of evolution of the Jacobi fields.

Consider first Eq. (27) for $r=0$, i.e., the classical Hamilton equations. The right-hand side depends only on $u^i_0(\xi,\tau)$. Differentiating this equation from one to $2s$ times, we obtain evolution equations for the zero-order Jacobi fields of degrees $t=1,\ldots,2s$. Equation (27) for $r=0$ and the $2s$ of the derived equations form a closed system of ODEs whose solutions are well defined.

As a next step we consider Eq. (27) for $r=1$. The right-hand side depends on the trajectories $u^i_0(\xi,\tau)$ and $u^i_1(\xi,\tau)$ and the Jacobi fields $J^i_{0,j_1,\ldots,j_t}(\xi,\tau)$ for $t=1,2$. Differentiating this equation with respect to ξ^i from one to $2s-2$ times, we obtain the evolution equations for the first-order Jacobi fields $J^i_{1,j_1,\ldots,j_t}(\xi,\tau)$ of degrees $t=1,\ldots,2s-2$. After differentiating, the right-hand side depends on the Jacobi fields $J^i_{0,j_1,\ldots,j_t}(\xi,\tau)$ of degrees $\le 2s$ ($=2+2s-2$), while the Jacobi fields $J^i_{1,j_1,\ldots,j_t}(\xi,\tau)$ arising from differentiating $u^i_1(\xi,\tau)$ do not have degrees that are higher than the number of derivatives taken, i.e., not above $2s-2$. Thus, to determine $J^i_{1,j_1,\ldots,j_t}(\xi,\tau)$, additional information about the zero-order Jacobi fields is not required. From these equations, we can find $u^i_1(\xi,\tau)$ and $J^i_{1,j_1,\ldots,j_t}(\xi,\tau)$ of degrees $t \le 2s-2$.

Further arguments are fairly obvious. We are moving in the direction of increasing the order of Jacobi fields. Consider the general case. We take the derivatives of Eq. (27)

from one to $2s-2r$ times and obtain the evolution equations for the order-r Jacobi fields of degrees $t = 1, \ldots, 2s-2r$:

$$\frac{\partial}{\partial \tau} J^i_{r,j_1,\ldots,j_t}(\xi,\tau) = G^i_r(u_0,u_1,\ldots,u_r,J_0,J_1,\ldots,J_r). \tag{28}$$

Consider the right-hand side of Eq. (27). It depends on the Jacobi fields $J^i_{0,j_1,\ldots,j_t}(\xi,\tau)$ of degrees $\leq 2r$. After differentiating from one to $2s-2r$ times, a dependence on the Jacobi fields $J^i_{0,j_1,\ldots,j_t}(\xi,\tau)$ of degrees $\leq 2s$ $(= 2r+2s-2r)$ is acquired. Consequently, for any r, the right-hand side of Eq. (28) depends on the zero-order Jacobi fields of degree $2s$ at most. Furthermore, the right-hand side of Eq. (27) depends on the first-order Jacobi fields of degrees $\leq 2r-2$. After the differentiation, a dependence on the first-order Jacobi fields of degrees $\leq 2s-2$ $(= 2r-2+2s-2r)$ occurs in Eq. (28). The upper value is also independent of r.

For a fixed r, Eq. (27) depends on the h-order Jacobi fields ($h < r$) of degrees $t \leq 2r-2h$. Thus, the evolution equations for the Jacobi fields $J^i_{r,j_1\ldots j_t}(\xi,\tau)$ of degrees $t = 1,\ldots,2s-2r$ contain the trajectory functions $u_0(\xi,\tau),\ldots,u_r(\xi,\tau)$ and the Jacobi fields $J^i_{h,j_1,\ldots,j_t}(\xi,\tau)$ of orders $h = 0,\ldots,r$ and degrees $t = 1,\ldots,2s-2h$.

The truncation of the expansion at any s provides us with the complete system of first-order ODEs for the trajectories and the Jacobi fields. The system is determined by Eqs. (27) and (28) with the initial conditions given in Eqs. (25) and (26).

The above arguments indicate that Eqs. (27) and (28) are sufficient to determine the trajectories and the Jacobi fields for some r, provided that the trajectories and the Jacobi fields of lower orders $< r$ are determined. We have seen that this is true for $r = 0, 1$; therefore, it is true for all r.

CONCLUSIONS

Deformation quantization uses the Wigner-Weyl association rule to establish the one-to-one correspondence between the functions in the phase space and the operators in the Hilbert space. Wigner's function appears as the Weyl symbol of the density matrix. A consistent quantum description of the systems using the Wigner function leads to formalism of the deformation quantization. The evolution of the quantum systems is governed by the Moyal bracket, which represents the quantum deformation of the Poisson bracket. Deformation quantization preserves many features of classical Hamiltonian dynamics.

We discussed applications of the deformation quantization techniques in solving the evolution problem for many-body systems in terms of the semiclassical expansion. We showed that, in any fixed order of $\hbar$-expansion, the evolution problem can be reduced to a statistical-mechanics problem of calculating an ensemble of quantum trajectories in the phase space and their Jacobi fields. In comparison with the corresponding rules of classical statistical mechanics, the rules for computing the probabilities and time-dependent averages of observables are modified. The evolution equations become a finite system of first-order ODEs for quantum trajectories in phase space and the associated Jacobi fields.

A clear gap exists between the classical dynamics of a particle and its quantum dynamics. In the first case, we are dealing with a finite number of degrees of freedom. In the second case, we are dealing *per se* with field theory and infinite number of dynamical degrees of freedom. We see that this gap is filled with the Jacobi fields of higher orders. By increasing the order of $\hbar$-expansion, the number of Jacobi fields is growing rapidly. This provides, in principle, a smooth transition from classical dynamics to quantum dynamics and from mechanics to field theory.

Since appearance of the transport codes in the late 1960s, processing power has increased by about ten orders of magnitude. This dramatic rise in processing power makes it possible to include in transport models the lowest-order quantum effects in the particle propagation.

ACKNOWLEDGEMENT

This work was supported in part by RFBR Grant No. 16-02-01104 and Grant No. HLP-2015-18 of the Heisenberg-Landau Program.

REFERENCES

1. H. J. Groenewold, *Physica*, **12**, 405 (1946).
2. J. E. Moyal, *Proc. Cambridge Phil. Soc.* **45**, 99 (1949).
3. T. A. Osborn, F. H. Molzahn, *Ann. Phys. (N.Y.)*, **241**, 79 (1995).
4. M. I. Krivoruchenko, Amand Faessler, *J. Math. Phys.* **48**, 052107 (2007).
5. M. I. Krivoruchenko, C. Fuchs, Amand Faessler, *Ann. Physik*, **16**, 587 (2007).
6. M. I. Krivoruchenko, B. V. Martemyanov, C. Fuchs, *Phys. Rev. C* **76**, 059801 (2007).
7. N. C. Dias, J. N. Prata, *J. Math. Phys.* **48**, 012109 (2007).
8. M. I. Krivoruchenko, Semiclassical methods of deformation quantisation in transport theory, in: *Some Applications of*
   Quantum Mechanics, Ed. M. R. Pahlavani (InTech, Zagreb, 2012), pp. 67 - 90.
9. M. I. Krivoruchenko, A. A. Raduta, Amand Faessler, *Phys. Rev. D* **73**, 025008 (2006).
10. M. I. Krivoruchenko, *Nonlinear Dyn. Appl.* **13**, 94 (2006).
11. B. R. McQuarrie, T. A. Osborn, G. C. Tabisz, *Phys. Rev. A* **58**, 2944 (1998).
12. S. Maximov *Physica D* **238**, 1937 (2009).
13. M. Blaszak, Z. Domanski, *Phys. Lett. A* **376**, 3593 (2012).
14. M. Cargo, A. Gracia-Saz, R. G. Littlejohn, M. W. Reinsch and P. de M. Rios, *J. Phys. A: Math. Gen.* **38**, 1977 (2005).

SESSION

"PHYSICS AT UNDERGROUND LABORATORY"

Conveners: F. Šimkovic, S. Wyngaardt

JINR Neutrino Program

Dmitry V.Naumov

Laboratory of Nuclear Problems, JINR Dubna, 141980 Dubna, Moscow region, Russia
JINR, Joliot-Curie, 6, Dubna, Russia

Abstract. This paper is a short summary of my plenary talk at 4th SOUTH AFRICA - JINR SYMPOSIUM devoted to "Few to Many Body Systems: Models and Methods and Applications" which was held in Dubna in September 2015. To mark the 60th anniversary of the Joint Institute for Nuclear Research, this paper highlights JINR's contributions to the development of neutrino physics and places special emphasis on the prospects of the JINR neutrino program.

Keywords: neutrino oscillations, neutrino mass, mass hierarchy, CP invariance violation, Majorana neutrino, reactor antineutrino, solar neutrino, atmospheric neutrino, accelerator neutrino, geoneutrino, astrophysical neutrino
PACS: 23.10.-s; 21.60.-n; 23.40.Bw; 23.40.Hc

INTRODUCTION

Systematic experimental research in neutrino physics, weak interactions, rare processes, and astrophysics has been carried out at JINR in the Dzhelepov Laboratory of Nuclear Problems (DLNP). This almost 55-year-long tradition stemmed from the work and ideas of Pontecorvo and his colleagues. Researchers at DLNP have obtained many fundamental results in this field. First of all, the pion beta decay $\pi^+ \to \pi^0 e^+ \nu_e$ was discovered [1], which was direct proof of the vector current conservation in weak interactions, first theoretically predicted by Ya. B. Zeldovich and S. S. Gershtein. Pontecorvo (together with Markov) justified the possibility of the existence of the muon neutrino and in 1959 proposed an experiment to detect this neutrino in high-energy accelerators [2], which was later performed in the USA, where muon neutrinos were actually detected. Pontecorvo and collaborators observed the recoil from the muon neutrino during the capture of negatively charged muons in helium-3, $\mu^- + {}^3\mathrm{He} \to {}^3\mathrm{H} + \nu_\mu$, which enabled imposing an upper bound on the mass of this particle. The experiment confirmed the identity of the muon and the electron in weak interactions (μ-e universality) [3]. The correctness of the vector-axial (V-A) structure of fermionic currents participating in weak interactions with charged $W^\pm$ bosons and the universality of weak interaction were confirmed by measurements of the probability of muon captures by protons, $\mu^- + p \to n + \nu_\mu$ [4].

Vylov and collaborators measured the helicity of electron neutrino in ^{152m}Eu decays using the Ge(Li) detector [5]. In 1957, Pontecorvo put forward the idea of the possible existence of neutrino oscillations, the conversion of one neutrino flavor to another, which is possible in principle only if the neutrino has a nonzero mass [6, 7]. Pontecorvo initiated the first experimental work on the determination of the probability of decays forbidden by the lepton number conservation. At the DLNP, using the ARES (Analyzer of Rare Events) device, a record bound on the $\mu \to 3e$ decay probability was obtained [8]. In 1957, Pontecorvo suggested the possible existence of transitions of muonium (an

atom consisting of two leptons, $M \equiv \mu^+ e^-$) into antimuonium ($\bar{M} \equiv \mu^- e^+$) [6]. In this process, lepton numbers of particles change not by one but by two units, and the transition $\mu^+ e^- \to \mu^- e^+$ is forbidden in the SM. In 1993, using the DLNP phasotron, the upper bound on the $M \to \overline{M}$ transition was established [9, 10].

The development of neutrino physics and particle physics before 1983 can be traced using reviews by Pontecorvo and his colleagues [11, 12, 13, 14, 15, 16, 17, 18], which demonstrated a remarkable simplicity and clarity of many complicated issues, as well as the special role played by JINR in this field.

The first accelerator neutrino experiments, in which JINR physicists played an important role, were carried out with the Neutrino Detector at the High Energy Physics Institute (Protvino) and NOMAD (Neutrino Oscillation MAgnetic Detector) at CERN, which performed a number of important experiments [19, 20, 21, 22, 23, 24, 25, 26, 27, 28, 29, 30, 31, 32, 33].

Presently, studies are carried out in the framework of the neutrino program that has been significantly extended and includes experimental and theoretical research in topical fields of neutrino physics. All projects of the JINR neutrino program are thoroughly justified and have passed through internal and international expertise. The JINR neutrino program is expected to yield advanced results in neutrino physics. The development of experimental devices both in Russia and abroad is a necessary condition for the successful realization of the neutrino program. Here are the three most important avenues. First is the development of the Baikal-GVD experiment. A 1 km^3 neutrino telescope is under construction on Lake Baikal. In 2015, the first cluster of the telescope, called Dubna, was deployed. This experiment is extremely important in connection with the first detection of astrophysical ultra-high-energy neutrinos in the IceCube experiment, which opens up a new area in physical studies – 'neutrino ultra-high-energy astrophysics'. The upgraded Baikal-GVD installation should play an important role in these studies.

Second, a neutrino laboratory successfully operates at the Kalinin NPP. Here, JINR is the principal investigator of the unique experiments GEMMA (measurements of the magnetic moment of antineutrinos), DANSS (search for sterile neutrinos and monitoring of antineutrinos from Kalinin NPP), and νGeN (ν-Ge Nucleus elastic scattering measurement of the neutrino-nucleon coherent scattering cross-section).

Third, JINR considers it necessary to participate in the most ambitious and important international projects in neutrino physics, making significant intellectual and financial contributions into them. Presently, these projects include:

- experiments in the low-background underground laboratories Gran Sasso (Borexino, Dark Side, GERDA) and Modan [EDELWEISS (from French Experience pour Detecter les wimps en site Souterrain) and SuperNEMO (Super Neutrino Majorana Observatory)];
- experiments with reactor antineutrinos (Daya Bay, JUNO);
- experiments with accelerator neutrinos (antineutrinos) (NOνA).

A detailed description of the JINR neutrino program can be found in the JINR Neutrino White Book [34]. Below, we briefly describe the most important results of the neutrino experiments obtained with the active participation of JINR researchers and discuss the expected results and prospects of new projects.

SHORT REVIEW OF NEUTRINO EXPERIMENTS WITHIN JINR NEUTRINO PROGRAM

OPERA experiment

OPERA (Oscillation Project Emulsion-tRacking Apparatus) experiment is a long-distance neutrino experiment aimed at discovering tau neutrinos in a muon neutrino beam. The distance between the neutrino source at CERN and the OPERA detector in Gran Sasso is 730 km. A hybrid detector consisting of two targets was used. Each target was equipped with a muon spectrometer. The target of the OPERA detector consisted of walls filled with 'emulsion bricks', and plastic scintillator detector planes served for targeting purposes. The emulsion bricks consisted of 56 lead layers 1 mm in thickness each, alternating with photoemulsion films providing micrometer accuracy in measuring tracks of charged particles. The OPERA detector contained about 150,000 such bricks. The total mass of the detector was around 1.2 kt. The neutrino beam was directed from CERN to Gran Sasso (CNGS – Cern Neutrino to Gran Sasso) for five years from 2008 to 2012. In total, the target at CERN was bombarded by $17.97 \cdot 10^{19}$ protons, which enabled the detection of 19,505 neutrino interactions in the detector. To date, five ν_τ candidates have been discovered. The expected numbers of the true and background events are respectively 2.64 ± 0.53 and 0.25. The OPERA collaboration reported the discovery of ν_τ in the CNGS beam at the confidence level of five standard deviations [35].

Presently, the OPERA collaboration is completing the data analysis, and the OPERA detector is being dismantled. Part of this detector (targeting detector) will be used in the JUNO experiment.

Daya Bay experiment

The Daya Bay experiment measured the mixing angle θ_{13}, unknown, until recently, which was one of the most significant results in particle physics in 2012. Later, in 2013, the effective difference in the mass squares Δm^2_{ee} was measured. In 2015, the Daya Bay experiment obtained the results [36]:

$$\begin{aligned} \sin^2 2\theta_{13} &= 0.084 \pm 0.005, \\ |\Delta m^2_{\text{ee}}| &= (2.42 \pm 0.11) \times 10^{-3}\ \text{eV}^2. \end{aligned} \tag{1}$$

By 2017, the precision of measurements of $\sin^2 2\theta_{13}$ in the continuing Daya Bay experiment is expected to be around 0.00307. The joint analysis of data obtained by the Daya Bay, Double Chooz, and RENO experiments will allow measurement of $\sin^2 2\theta_{13}$ in the confidence interval ± 0.00282 [37]. The value of Δm^2_{ee} will be determined within the confidence interval $\pm 7 \cdot 10^{-5}$ eV^2 , i.e., to 3% [37]. The location of the Daya Bay detectors relative to the Daya Bay, Ling Ao, Ling Ao II reactors corresponds to nine different 'detector-reactor' distances. This enabled physicists to set new upper bounds on the mixing parameters of the hypothetical sterile neutrino $\sin^2 2\theta_{14}, |\Delta m^2_{41}|$ in the previously unexplored range 10^{-3} eV$^2 \leq |\Delta m^2_{41}| \leq 0.1$ eV^2 [38].

In 2015, the Daya Bay collaboration measured the flux of reactor antineutrinos [39]. The measured flux, which is in agreement with previous data from short-distance experiments, is 0.946 ± 0.02 (0.991 ± 0.023) from the model flux in Huber-Muller [40, 41] (ILL-Vogel [42, 43, 44, 45]). The measured form of the positron spectrum differs by 2 s from the predictions in [40, 41] in all energy ranges by reaching the local significance $4\ \sigma$ in the antineutrino energy range 4 ± 6 MeV. This result is confirmed by the data of the RENO and Double Chooz experiments.

The members of the Daya Bay collaboration jointly with KamLAND, K2K/T2K, Super-Kamiokande, and SNO were awarded the biggest world scientific prize – the 2016 Breakthrough Prize in Fundamental Physics.

Borexino experiment

The international Borexino collaboration has been taking data from a 300 ton LS detector since 2007. Physicists from JINR have been participating in the experiment since 1991. The Borexino detector was designed for real-time studies of low-energy solar neutrinos, first and foremost monoenergetic ones (with the energy 862 keV) from the reaction $^7\mathrm{Be} + e^- \to {}^7\mathrm{Li} + \nu_e$.

The results obtained by the Borexino experiment, in particular, include the direct measurement of the solar neutrino flux from the pp reaction [47] and the first statistically significant observation of geoneutrinos [46]. The Borexino experiment measured the solar beryllium neutrino flux with a 5% accuracy [48], as well as its daily [49] and seasonal [50] variations. In addition to beryllium neutrinos, fluxes of boron neutrinos [52] (this measurement, of course, has a lower accuracy than measurements with large water Cherenkov neutrino detectors, but is the first measurement of the high-energy part of the solar neutrino spectrum by an LS detector), pep neutrinos [51], and pp neutrinos [47] were measured. Thus, neutrino fluxes from all the main reactions of the pp chain were measured for the first time by one detector. Borexino also measured the geoneurino flux from decays of natural radioactive isotopes in Earth [53]; today, this measurement, together with the KamLAND detection, provides unique information on the uranium and thorium content in Earth's interior.

In addition to neutrino flux measurements, the Borexino experiment has searched for rare events beyond the SM according to the program proposed by scientists from Dubna. Presently, the experiment is establishing the best upper bounds on the effective magnetic moment of solar neutrinos[54], on the axion flux from the Sun[55], and on the Pauli principle violation[56]. Constraints on the lifetime of the electron with respect to the decay $e \to \nu + \gamma$: $T_{1/2} \geq 6.6 \cdot 10^{28}$ years [58] were improved by more than two orders of magnitude.

SOX experiment

The Borexino experiment planned measurements with a neutrino source to calibrate the detector, and the antineutrino source $^{90}\mathrm{Sr} - {}^{90}\mathrm{Y}$ was originally proposed. Later, it

was proposed to also use the source of monoenergetic neutrinos based on ^{51}Cr [59]. This source was successfully employed to calibrate the GALLEX experiment. In connection with searches for sterile neutrinos actively discussed in recent years, the idea of measurements with additional neutrino sources is becoming more attractive: due to the large geometric size of the Borexino detector, it is possible to search for oscillations inside it with the characteristic length of about 1 m, which corresponds to $\Delta m^2 \sim 1$ eV^2.

The SOX project [57] planned to carry out measurements using an external ^{51}Cr neutrino source (located 8.25 m from the detector center) with the activity $5-10$ MCi (phase A, or CrSOX) and with the antineutrino source ^{144}Ce (CeSOX) with the activity $50-150$ kCi, installed in a water buffer at a distance of 7.15 m from the detector center (phase B) or in the detector center (phase C).

Baikal-GVD experiment

Pioneering neutrino research in Lake Baikal began more than 35 years ago. Since then, extensive experience was accumulated and important results were obtained. The technology of neutrino registration by large deep-underwater detectors was developed. In 2006-2010, all key elements and units of the GVD detector were designed, manufactured, and tested. A new phase of the experiment began in 2014. The discovery of astrophysical neutrinos by the IceCube detector opened new prospects for neutrino telescopes, because it became clear that telescopes with good angular resolution are required to identify high-energy neutrino sources. The Baikal collaboration optimized the installation and formulated new requirements on the parameters of the new detector [61].

The basic element of the experiment is the optical module (OM) consisting of a 10-inch PMT Hamamatsu-R7081HQE with high quantum efficiency (up to 35%), a high-voltage PMT power supply setup, a controller, a protection system of the PMT from the terrestrial magnetic field, and a calibration system with a photocathode. All elements of the OM are placed into a sealed deep-underwater spherical glass container.

The optical modules are attached to vertical cables forming strings. The main structure unit of a string is the OM section. A section represents a functionally completed detector unit, including blocks of emission registration, signal processing, and data transferring. Data taking from the section enables forming different configurations of optical modules. Individual or pairs of OMs can be placed at different spacings. Several sections can be mounted on each string in different configurations. The configuration of a section, which is presently the base for further projecting, includes 12 optical modules with a 15 m spacing along the string, a central module (CM) of the section located in the middle of the section, and a service module (SM). Analog signals from the OM of a section are transmitted to the CM by identical 100 m coaxial cables. These cables are also used for low-voltage power supply of the OM. In the CM, the analog signals from optical modules are digitized and transmit the information via an Ethernet line. The service module is used for time calibration, determination of the string location, and the power supply of the OM. Electric power supply synchronization and data transmission from sections are combined in the commutation module of the string, which is connected by 1200 m cables with the central control block of the cluster. The data are transmitted using Eth-

ernet technology. The basic cluster configuration includes eight strings, each with 24 OMs (two sections on a string), separated by 60 m from each other. The clusters of the strings are connected to the center of the shore by 6 km combined fiber-optic cables. Each cluster of the telescope represents a functionally completed detector, which can operate either as part of the whole system or autonomously. This provides simplicity in building up the installation and the possibility of starting to operate with individual units during the development of the neutrino telescope. The cluster will observe a volume of the lake comparable to the ANTARES volume. It is expected that the cluster will register one astrophysical neutrino with the energy above 100 TeV a year. The first phase of the construction of the Baikal-GVD experiment should be completed in 2020 with the installation of 12 clusters with 2304 OMs spaced 300 m apart. The instrumental volume of the detector will be 0.4 km^3. The physically observed volume depends on the neutrino energy and increases with energy. By the time of completion, the detector should be able to register 27 events from interactions of astrophysical neutrinos with energies above 100 TeV.

The expected accuracy of the event direction reconstruction is $3.5^o - 5.5^o$ for cascade-generating neutrino interactions and 0.25^o for muon tracks. The Baikal-GVD collaboration plans to further increase the detector volume to an instrumental value of 1.5 km^3. This installation will include 27 clusters of four sections each. The total number of OMs will be 10,368.

GEMMA-II experiment

The main goal of the *GEMMA-II* experiment is to measure or further constrain the value of the neutrino magnetic moment. The new GEMMA-II detector will have better sensitivity to the neutrino magnetic moment than the previous detector GEMMA (Germanium Experiment for measurement of Magnetic Moment of Antineutrino). The new device includes two 3 kg germanium detectors with an effective detection threshold decreased from 2.8 keV to 1.5 keV. The detector is placed inside a NaI crystal with a wall thickness of 14 cm, surrounded by a 5 cm layer of electrolytic copper and a 15 cm layer of lead. The detector, mounted on a mobile platform at a distance of 10 m under the nuclear reactor, is well protected from the hadronic component of cosmic rays by the reactor itself and the technological equipment. The muon flux is reduced by 10 times within the solid angle $\pm 20^o$ near the vertical and by 3 times within the solid angle $\pm(70^o - 80^o)$. Surrounding the detector as mentioned above is passive protection. The remaining muons, by interacting with the detector's protection, produce fast neutrons that interact elastically in the germanium detector and increase the low-energy background. To suppress this background, the detector is surrounded by an additional shield made of a plastic scintillator with an electronic readout, which enables detection of atmospheric muons. This additional protection is active. Additional control of the signal-to-background ratio in the experiment is performed by the mobile platform on which the detector is mounted. The distance between the detector and reactor centers can vary from 10 to 12 m. Special measures are taken to protect the device from noise caused by mechanical vibrations, electric power interference, leakage of radioactive

argon and xenon from the cryostat, and the intrinsic noise of germanium detectors. As a result, systematic uncertainties of measurements were significantly reduced and the detector sensitivity to the neutrino magnetic moment was increased to $1 \times 10^{-11}\mu_B$.

In the future, it is planned to use a new detector with point contacts, which enables the effective detector threshold to be reduced to 300 eV. The use of several detectors with a total mass of 5 kg will allow increasing the sensitivity to the neutrino magnetic moment to $(5-10) \times 10^{-12}\mu_B$ [34].

JUNO experiment

The JUNO experiment will try to measure the neutrino mass hierarchy using an underground LS detector located at a distance of 53 km from the Yangjiang and Taishan nuclear power plants in Guangdong province (China). The experimental chamber with a length of more than 50 m located under a mountain is protected from cosmic radiation by a 700 m granite layer. During six years of operation of the detector, the neutrino mass hierarchy can be measured at the confidence level of $(3-4)\sigma$. To fulfill this task, the antineutrino energy should be reconstructed with a resolution better than 3% for a released energy of 1 MeV with an absolute accuracy of the energy scale better than 1%. In view of the large mass of the detector, when this accuracy in energy reconstruction is attained, it will be possible to measure the $\sin^2\theta_{12}$, Δm^2_{21}, $|\Delta m^2_{\text{ee}}|$ parameters with an accuracy better than 1%.

The multi-purpose JUNO detector can observe neutrinos (antineutrinos) from terrestrial and extraterrestrial sources, including neutrinos from supernovae, diffusion neutrinos from supernovae, geoneutrinos, atmospheric neutrinos, and solar neutrinos, which enables investigating many questions of neutrino physics and astrophysics. JUNO is also sensitive to physics beyond the SM, including sterile neutrinos, neutrinos from dark matter annihilation, and proton decays, as well as nonstandard neutrino interactions and Lorentz-violating and CPT-violating processes.

The central detector of JUNO contains 20 kt of liquid scintillator and around 17,000 PMTs. The expected stable operation time of the detector is more than 20 years. The liquid scintillator will be placed into an acryl sphere 35 m in diameter supported by a stainless steel construction. The requirements to the LS include a light yield and transparency, as well as low radioactive contamination level. A muon veto system will be used to suppress atmospheric muon backgrounds. The muon veto includes a water Cherenkov detector and an upper tracker. The target detector from the OPERA experiment that completed operation will be used as the upper tracker. The water Cherenkov detector consists of a pool filled with purified water and PMTs mounted on the pool walls. The central detector with a liquid scintillator will be placed at the center of the water pool.

PMTs registering scintillation photons from the central detector will be mounted on a spherical surface about 38 m in diameter. To reach the required resolution, they must provide 75% of the total geometric coverage of the sphere. Here, about 17,000 PMTs with a diameter of 508 mm (20 inches) are required. Additionally, about 1600 PMTs are directed aside from the central detector to register Cherenkov photons. The possibility is also being considered of using three-inch PMTs in the free space between

large 20-inch PMTs, two small ones per large one. The use of small PMTs with better time characteristics will enable significant improvement in reconstructing the interaction point inside the detector and hence in the sensitivity.

To reduce the effect of the terrestrial magnetic field on the PMT performance, a system of coils with currents placed around the central detector inside the water pool will be used. The determination of the neutrino mass hierarchy in the experiment is impossible without a careful calibration of the algorithm of the event coordinate and energy reconstruction. The calibrations can be done using different sources (light, γ, e^+, e^-, neutrons, α) imitating interactions inside the detector in the entire energy range of the inverse β-decay. The calibration system should allow placing the source at any point of the central detector. An ultrasound positioning system will enable the source coordinate determination with an uncertainty of less than 3 cm. Several additional calibration subsystems are considered that can overlap different parts of the central detector with different periodicity of their use.

The JUNO electronics include two blocks for the central detector and a veto detector. Their main goals are to read the PMT signal from two subdetectors and to process and transfer data to the data collection system. To avoid data loss during long-distance data transfer, most of the electronics will be located in the water pool near the detectors. The expected data flux is 2 Gb/s. In the case of a supernova explosion at a distance of 10 kpc from Earth, the data flux increases to 10 Gb/s. The experimental data from JUNO will be processed with a dedicated computer including 10,000 cores with a disk memory of 10 Pbyte (10^{16} bytes). The detector is planned to be mounted and filled with a liquid scintillator in 2019, and full-scale data taking will begin in 2020.

NOνA experiment

The NOνA experiment is a multi-purpose experiment. The main goal is to measure the neutrino mass hierarchy and the phase δ responsible for CP-violation in the lepton sector. The NOνA experiment uses two detectors, one near and one far. The near detector is placed at a depth of 100 m at the Fermi National Accelerator Laboratory (Fermilab) (USA) about 1 km away from the target part of the NuMI beam. The mass of the near detector is 0.3 kt. The far detector with a mass of 14 kt is placed at a distance of 810 km from the neutrino source. The basic element of both detectors is a polyvinyl chloride cell 1560 cm $\times$ 4 cm $\times$ 6 cm in size filled with a liquid scintillator. An optical fiber is used inside the cell as the output for the scintillation light produced by charged particles passing through the scintillator. The scintillation light is registered by a 32-channel avalanche photodiode. The cells form the detector layers, whose vertical and horizontal orientations can be used to measure the x and y coordinates of particle tracks. Both NOνA detectors are shifted from the beam axis by the angle of 14 mrad, at which the beam spectrum with a peak energy at 2 GeV is more narrow than that of the on-axis beam. The neutrino mass hierarchy in this experiment manifests itself as different probabilities of oscillations $P(\nu_\mu \to \nu_e)$ and $P(\bar{\nu}_\mu \to \bar{\nu}_e)$.

The oscillation probabilities depend, however, not only on the neutrino mass hierarchy but also on the phase δ and values of $\sin^2 2\theta_{13}$, $\sin^2 2\theta_{23}$. Results of the experiment can

be uncertain due to some parameter degeneracy. For example, if both probabilities turn out to be of the order of $P(\nu_\mu \to \nu_e) \simeq P(\bar{\nu}_\mu \to \bar{\nu}_e) \simeq 0.4$, the NO$\nu$A experiment will be unable to distinguish the normal hierarchy with $\delta = \pi/2$ from the inverted one with $\delta = 3\pi/2$. However, even in the worst case, NOνA will exclude some possibilities (the inverted hierarchy and $\delta = \pi/2$, the normal hierarchy and $\delta = 3\pi/2$).

NOνA plans to accumulate data for six years: three years in the neutrino mode and three years in the antineutrino mode. The experiment started running in the neutrino mode in 2015, and the first results based on 7.6% of the total expected statistics were presented in the summer of 2015 [63]. First of all, the $\nu_\mu \to \nu_\mu$ mode was investigated. The spectrum measured in the near detector was used to reduce systematic errors due to uncertainties in the neutrino-nucleus interaction cross section. In the absence of oscillations, 201 events from ν_μ interactions were expected in the far detector. Only 33 events were detected. This number perfectly fits a neutrino oscillation model with

$$\Delta m^2_{32} = \begin{cases} +2.37^{+0.16}_{-0.15} \cdot 10^{-3}\ \text{eV}^2 & \text{normal hierarchy,} \\ -2.40^{+0.14}_{-0.17} \cdot 10^{-3}\ \text{eV}^2 & \text{inverted hierarchy,} \end{cases} \quad (2)$$
$$\sin^2 2\theta_{23} = 0.51 \pm 0.10.$$

The measurement accuracy attained using such small statistics is only slightly worse than that obtained in the MINOS (Main Injector Neutrino Oscillation Search) and T2K experiments, confirming a significant potential of the NOνA experiment. The next mode explored in NOνA was $\nu_\mu \to \nu_e$. The ν_e identification was performed in two somewhat different ways. The first used the Likelihood IDentification (LID) function, while the second employed the identification of an event most similar to ν_e in the data (Library of Event Matching, LEM). Both methods have a similar efficiency and purity in selecting ν_e events. Both methods predict about one background event in the far detector. The LID (LEM) method predicts 5.62 ± 0.72 (5.91 ± 0.65) signal events, assuming the normal hierarchy with $\delta = 3\pi/2$, and 2.24 ± 0.29 (2.34 ± 0.26) signal events in the case of the inverted hierarchy with $\delta = \pi/2$. These estimates are bounds. The expected number of events for other values of the parameter δ falls within this range.

Six ν_e events were found in the data by the LID method and 11 events by the LEM method. Both methods confirm $\nu_\mu \to \nu_e$ oscillations at 3.3σ (LID) and 5.5σ (LEM). The normal hierarchy with δ around $3\pi/2$ is favored in both methods. So far, the confidence level is not very high, $(1 - 2\sigma)$, but the statistical significance of the final results of the experiment is expected at the 3σ level.

GERDA experiment

The GERDA experiment. Until recently, the claim in [64] of the observation of double inverse beta decay has been neither refuted nor confirmed. Presently, the most sensitive experiments searching for double neutrinoless beta decay include experiments with the ^{136}Xe isotope and the GERDA experiment, which employs germanium detectors enriched to 86% with ^{76}Ge that were taken from HdM and IGEX (International Germanium EXperiment) experiments. Since the matrix elements differ for various isotopes, a

comparison of results of the ^{136}Xe and ^{76}Ge experiments is model-dependent; therefore, only the GERDA experiment can directly confirm (or refute) the claim.

The GERDA experiment is being carried out in several stages. The first stage finished in 2013; its goal was to check the results in [64] with an exposition of 20 kg·year. The data obtained during the first phase of the GERDA experiment did not reveal a peak at the energy $Q_{\beta\beta}$, i.e., the claim about the observation of double neutrinoless beta decay of ^{76}Ge has not been confirmed. Assuming $T_{1/2}^{0\nu}$ from Ref. [64], the expected number of events is 5.9 ± 1.4 in the energy range $\pm 2\sigma_E$ (σ_E is the energy resolution of the detector) near $Q_{\beta\beta}$ with 2.0 ± 0.3 background counts after the pulse shape discrimination. These values should be compared to three events detected in this energy range, all of them falling outside the energy range $Q_{\beta\beta} \pm \sigma_E$. The ($H_1$) hypothesis, which assumes the neutrinoless double beta decay, is in worse agreement than the (H_0) hypothesis, assuming the presence of only the background: the probability ratio of both hypotheses is $P(H_1)/P(H_0) = 0.024$. According to the H_1 model, the probability of a null signal ($N^{0\nu}$=0) is only $P(N^{0\nu} = 0|H_1)$=0.01.

The result of the first phase of the GERDA experiment [65] is compatible with the HdM [66] and IGEX [67] bounds. The likelihood function profile was extended to include the energy spectrum of the HdM experiment (2000-2080 keV) and IGEX experiment (2020-2060 keV). The data processing assumed a homogeneously distributed background for each of five data sets and a Gaussian signal with the same lifetime $T_{1/2}^{0\nu}$.

The experimental parameters (exposition, energy resolution, efficiency) available from the original publications or extrapolations from the GERDA detector data were used. The best fit corresponds to $N^{0\nu} = 0$ and the lifetime upper bound

$$T_{1/2}^{0\nu} > 3.0 \cdot 10^{25} \text{ years} \quad (90\,\%\text{C.L.}). \tag{3}$$

The probability ratio is $P(H_1)/P(H_0) = 2 \cdot 10^{-4}$. Thus, the hypothesis of the observation of double neutrinoless beta decay has a very low probability.

At the next stage (GERDA Phase II), a sensitivity corresponding to $> 10^{26}$ years is expected after an exposure of 100 kg·year with a background rate of $\lesssim 10^{-1}$evt/keV events, the latter being more than an order of magnitude lower than at the first stage of the experiment. To reach such a low background, the collaboration intends to employ about 30 additional BEGe [1] detectors with a total mass of 20 kg of ^{76}Ge with a new geometry of electrodes which improves the differentiation between beta and gamma signals. The new detectors will be placed in liquid argon, which enables detection of scintillation flashes from background radiation sources, thus providing an anti-Compton veto in the regime of coincidence with a signal from germanium detectors.

NEMO-3 experiment

The NEMO-3 experiment in the Modane underground laboratory (Laboratoire Souterrain de Modane – LSM) has sought neutrinoless double beta decay. Measurements of

[1] BEGe: Broad Energy Germanium detectors

several isotopes have been carried out since 2003: ^{48}Ca, ^{82}Se, ^{96}Zr, ^{100}Mo, ^{116}Cd, ^{130}Te and ^{150}Nd. The principal targets were ^{100}Mo with a mass of about 7 kg and ^{82}Se with a mass of 1 kg. The lack of signatures of double neutrinoless beta decay resulted in a 90%-CL upper bound on the probability of this process, and an upper bound on the effective Majorana neutrino mass was obtained. In addition, NEMO-3 precisely measured the two-neutrino decay mode for several isotopes, which is permitted by the SM. Measurements of this process are important in order to decrease the uncertainty in nuclear matrix elements. The period of double beta decay of ^{130}Te was also accurately measured and compared to contradictory results of geochemical experiments.

Super-NEMO is a next-generation experiment employing the same track-calorimetry technique that was successfully used in NEMO-3. Due to the unique capability of watching tracks and indentifying particles, Super-NEMO offers the possibility of both detecting neutrinoless double beta decay and determining its underlying mechanism. In Super-NEMO, as in NEMO-3, the source and detector are separated, and the experiment allows studying several isotopes, including ^{48}Ca, ^{82}Se and ^{150}Nd. The total mass will be around 100-200 kg, enabling the sensitivity longer than 10^{26} years to half-life periods, which corresponds to a Majorana neutrino mass of about 50 meV, depending on the value of matrix elements. The prototype manufacturing was completed in 2015. The international collaboration on the project now faces the following pressing problems: producing sources in the form of thin foil with the required radiation purity, achieving good energy resolution of the calorimeter, and upgrading the construction of the track block of the detector. To control the required high level of radiation purity, several versions of the BiPo detector have been developed [71], one of which is already successfully running at the Canfranc underground laboratory (Spain).

DANSS experiment

The DANSS project plans to develop a relatively compact neutrino spectrometer based on a plastic scintillator, which can be placed near the active zone of a powerful industrial reactor. In the sensitive 1 m^3 zone of the detector, nearly 10,000 inverse beta decay (IBD) reactions a day are expected if placed at the Kalinin NPP at a distance of 10 m from the reactor core. The plastic scintillator segmentation allows the background suppression to 1%. Numerous tests carried out with a simplified prototype DANSSino at the Kalinin NPP under the reactor with a thermal power of 3 GW have demonstrated the performance capability of this concept. Background conditions at the Kalinin NPP have been studied. The general concept of the detector was probed and constructive improvements were implemented. The spectrum of the reactor antineutrinos was measured. Presently, the detector is under assembly. Using a lifting mechanism, the DANSS detector will be able to move, together with a shield, over distances from 9.7 to 12.2 m from the active zone, enabling searches for sterile neutrinos with $\Delta m^2 \simeq 1$ eV^2. The sensitivity estimate (90% CL) of the DANSS experiment in one year of measurements will be enough to exclude all currently available parameter space used to interpret various anomalies in neutrino oscillations as a hint for the sterile neutrino.

νGEN experiment

The reaction of coherent scattering on nuclei $\nu + A \to \nu + A$ has not been experimentally observed so far. Coherent neutrino scattering on a nucleus occurs via the Z^0-boson exchange between the neutrino and all nucleons. The differential cross section of this process is [72]

$$\frac{d\sigma}{d\Omega} = \frac{G_F^2}{4\pi^2} E_\nu^2 (1+\cos\theta) \frac{(N-(1-4\sin^2\theta_W)Z)^2}{4} F^2(Q^2), \tag{4}$$

where E_ν – neutrino energy, G_F – Fermi constant, θ – angle between neutrino arrival direction and direction of scattered nucleus, N, Z – number of neutrons and protons in the nucleus, respectively, θ_W – Weinberg angle, and $F(Q^2)$ – form-factor of the nucleus. The form-factor was not taken into account in [72]. Because the value of $\sin^2\theta_W$ is close to $1/4$, cross section (4) weakly depends on the charge of the nucleus, and after integrating (4) over the angle θ, we obtain the approximate formula

$$\sigma \simeq \frac{G_F^2}{4\pi} N^2 E_\nu^2 \simeq 0.42 \cdot 10^{-44} \mathrm{N}^2 \frac{\mathrm{E}_\nu^2}{\mathrm{MeV}^2}\ \mathrm{cm}^2,$$

which suggests that the more neutrons are contained in a nucleus, the larger the coherent scattering cross section. The mean energy of the recoil nucleus with an atomic mass A is

$$\overline{E}_A = \frac{2}{3A}\left(\frac{E_\nu}{\mathrm{MeV}}\right)^2 \mathrm{keV}.$$

For neutrino energies of about 6 MeV and a germanium nucleus, $\overline{E}_A \simeq 360$ eV. To register such a low energy, detectors with an extremely low energy threshold are needed. The cross section of coherent neutrino scattering on the Ge nucleus is three orders of magnitude higher than that of the inverse beta decay.

Coherent neutrino scattering is especially important from the practical standpoint, because very heavy mass detectors are typically used for neutrino detection. The comparatively large coherent scattering cross section lowers the requirements for the mass of the detector for neutrino registration in this process. It is planned that the νGEN experiment will use low-threshold, low-background HPG (High Purity Germanium) detectors designed by JINR for the device to observe coherent neutrino scattering on Ge nuclei [73].

One of the reactors at the Kalinin NPP will be used as the neutrino source. To separate the coherent scattering contribution, the data accumulated with the reactor switched on and switched off (the differential method) will be analyzed. With a device consisting of 450 g HPGe detectors placed about 10 m from the reactor center, several dozen events a day are expected from coherent scattering with an energy threshold of 300 eV. The sensitivity of the installation can be increased by increasing the mass of the detectors to 5 kg. The unique properties of the proposed HPGe detectors, as well as the high antineutrino fluxes available at the Kalinin NPP, make it highly probable that neutrino-nucleon coherent scattering will be observed in the nGEN experiment for the first time.

SUMMARY

Neutrino physics and astrophysics, together with accelerator physics of ultra-high-energy elementary particles, are the main avenues of modern elementary particle physics. These fields are especially rich in potentially the most fundamental and unexpected discoveries, which can undoubtedly change our knowledge about the world. It can be asserted that neutrino physics started the phase of precision measurements, of systematically solving the fundamental problems on the nature of the neutrino. JINR has a wide and profound Neutrino Program which shall bring us yet new discoveries.

ACKNOWLEDGEMENT

My sincere thanks go all my colleagues from JINR for making this program possible and for their hard work. Also I would like to thank my co-authors V. Bednyakov and O. Smirnov for their permission to adopt our common work [74] for these proceedings.

REFERENCES

1. Prokoshin Yu.D. et al., Diplom N 135 (1973). Prioritet 08.09.1955.
2. Pontecorvo B.M., *ZhETF* **37** 1751 (1959)
3. Pontecorvo B.M. et.al., *ZhETF* **45** 1803 (1963)
4. Dzhelepov V.P. et.al., *ZhETF* 66 **43** (1974)
5. Vylov C.D. et al., Preprint P6-84-148 (Dubna: JINR, 1984).
6. Pontecorvo B.M., *ZhETF* **33** 549 (1957).
7. Pontecorvo B.M., *ZhETF* **34** 247 (1958).
8. Korenchenko C.M. at al., *Yadernaya Fizika* 53 1302 (1991).
9. Savchenko O.V. et al., *Pis'ma ZhETF* **57** 262 (1993).
10. Savchenko O.V. et al., *Pis'ma ZhETF* **59** 565 (1994).
11. Pontecorvo B.M., *UFN* **141** 675 (1983).
12. Bilenky C.M., Pontecorvo B.M., *UFN* **123** 181 (1977).
13. Pontecorvo B.M., *UFN* **120** 705 (1976).
14. Pontecorvo B.M., *UFN* **119** 633 (1976).
15. Pontecorvo B.M., *UFN* **104** 3 (1971).
16. Pontecorvo B.M., *UFN* **95** 517 (1968).
17. Pontecorvo B.M., *UFN* **79** 3 (1963).
18. Dzhelepov V.P., Pontecorvo B.M., *UFN* **64** 15 (1958).
19. Blumlein J et al *Phys. Lett. B* **279** 405 (1992)
20. Baranov S A et al. *Phys. Lett. B* **302** 336 (1993)
21. Anikeev V B et al. *Z. Phys. C* **70** 39 (1996)
22. Bunyatov S A Nefedov Y A *Phys. Atom. Nucl.* **60** 935 (1997) [Yad. Fiz. **60N6**, 1045 (1997)]
23. Sidorov A V et al. [IHEP-JINR Neutrino Detector Collaboration], Eur. Phys. J. C **10** 405 (1999) [hep-ex/9905038]
24. Alekhin S I et al. *Phys. Lett. B* **512** 25 (2001) [hep-ex/0104013]
25. Barabash L S et al., *Instrum. Exp. Tech.* **46** 300 (2003) [Prib. Tekh. Eksp. **46**, 20 (2003)]
26. Samoylov O et al. [NOMAD Collaboration] *Nucl. Phys. B* **876** 339 (2013) [arXiv:1308.4750 [hep-ex]]
27. Kullenberg C T et al. [NOMAD Collaboration]*Phys. Lett. B* **682** 177 (2009) [arXiv:0910.0062 [hep-ex]]
28. Lyubushkin V et al. [NOMAD Collaboration] *Eur. Phys. J. C* **63** 355 (2009) [arXiv:0812.4543 [hep-ex]]

29. Wu Q et al. [NOMAD Collaboration] *Phys. Lett. B* **660** 19 (2008) [arXiv:0711.1183 [hep-ex]]
30. Astier P et al. [NOMAD Collaboration] *Phys. Lett. B* **570** 19 (2003) [hep-ex/0306037]
31. Astier P et al. [NOMAD Collaboration] *Nucl. Phys. B* **621** 3 (2002) [hep-ex/0111057]
32. Astier P et al. [NOMAD Collaboration] *Nucl. Phys. B* **611** 3 (2001) [hep-ex/0106102]
33. Astier P et al. [NOMAD Collaboration], *Nucl. Phys. B* **588** 3 (2000).
34. Bednyakov V A, Naumov D V in *The White Book: JINR NEUTRINO PROGRAM* `http://dlnp.jinr.ru/ru/neutrino-white-book`
35. Agafonova N et al. [OPERA Collaboration], *Phys. Rev. Lett.* **115** 121802 (2015).
36. An F P et al. [Daya Bay Collaboration], *Phys. Rev. Lett.* **115** no. 11 111802 (2015); [arXiv:1505.03456 [hep-ex]].
37. Cao J, Report at TAUP 2015; Jie Zho, private communication.
38. An F P et al. [Daya Bay Collaboration], *Phys. Rev. Lett.* **113** 141802 (2014). [arXiv:1407.7259 [hep-ex]].
39. An F P et al. [Daya Bay Collaboration], arXiv:1508.04233 [hep-ex].
40. Mueller T A et al., *Phys. Rev. C* **83** 054615 (2011).
41. Huber P, *Phys. Rev. C* **84** 024617 (2011).
42. Vogel P et al., *Phys.Rev. C* **24** 1543 (1981).
43. Schreckenbach K et al., *Phys. Lett. B* **160** 325 (1985).
44. Feilitzsch F Von, Hahn A A, Schreckenbach K, *Phys.Lett. B* **118** 162 (1982).
45. Hahn A A et al., *Phys. Lett. B* **218** 365 (1989).
46. Bellini G et al (Borexino Collaboration), *Phys.Lett.* **B687** 299 (2010).
47. Bellini G et al. [BOREXINO Collaboration], *Nature* **512** 7515 383 (2014).
48. Bellini G et al., *Phys. Rev. Lett.* **107** 141302 (2011).
49. Bellini G et al., *Phys. Rev. Lett.* **B707** 22 (2012).
50. Bellini G et al., *Phys. Rev. D* **89** 112007 (2014).
51. Bellini G et al. [Borexino Collaboration], *Phys. Rev. Lett.* **108** 051302 (2012) [arXiv:1110.3230 [hep-ex]].
52. Bellini G et al., *Phys. Rev. D* **82** 033006 (2010).
53. Agostini M et al., *Phys. Rev. D* **92** 031101 (2015).
54. Bellini G et al., *Phys. Rev. Lett.* **101** 091302 (2008).
55. Bellini G et al., *Phys. Rev. D* **85** 092003 (2012).
56. Bellini G et al., *Phys. Rev. C* **81** 034317 (2010).
57. Bellini G et al., *JHEP* **1308** 038 (2013).
58. Agostini M et al. [arXiv:1509.01223 [hep-ex]].
59. Ferrari N, Fiorentini G and Ricci B, *Phys. Lett.* **B 387** 427 (1996).
60. Palazzo A *Mod. Phys. Lett.* **A28** 1330004 (2013).
61. BAIKAL GVD. Scientific Technical Report (2010).
62. Patterson R B [NOvA Collaboration], *Nucl. Phys. Proc. Suppl.* **151** 235 (2013).
63. Patterson R, Fermlilab Seminar, `http://theory.fnal.gov/jetp/` (2015).
64. Klapdor-Kleingrothaus H V et al. *Phys. Lett. B* **586** 198 (2004)
65. Agostini M et al. (GERDA Collaboration), *Phys. Rev. Lett.* **111** 122503 (2013).
66. Klapdor-Kleingrothaus H V et al., *Eur.Phys.J.* **A12** 147-154 (2001).
67. Aalseth et al., *Phys. Rev. D* **65** 092007 (2002).
68. Agostini M et al. (GERDA), *Eur.Phys.J.* **C75** 39 (2015).
69. Mention G et al., *J.Phys.Conf.Ser.* **408** 012025 (2013).
70. Gando A. et al., [arXiv:1312.0896 [physics.ins-det]].
71. Gomez H et al. (SuperNEMO), *NIM* **A718** 52 (2013).
72. Drukier A. and Stodolsky Leo, *Phys. Rev. D* **30** 2295 (1984).
73. Brudanin V B et al., *Instruments and Experimental Techniques* **54** 470 (2011).
74. Bednyakov V.A., Naumov D.V., Smirnov O.Yu., *UFN* **186** 233-263 (2016).

Towards the South African Underground Laboratory (SAUL)

S. M. Wyngaardt*, R. T. Newman*, R. Dawam*, R. Lindsay†, A. Buffler**, R. de Meijer†, P. Maleka‡, J. Bezuidenhout§, R. Nchodu‡, M. van Rooyen* and Z. Ndlovu*

*Department of Physics, Stellenbosch University, Private Bag X1, Matieland, Stellenbosch, 7602
†Department of Physics, University of the Western Cape, Modderdam Road, Private Bag X17, Bellville, 7530
**Department of Physics, University of Cape Town, Rondebosch, 7700, South Africa
‡iThemba LABS, P.O. Box 722, Somerset West, 7129, South Africa
§Military Academy, Private Bag X2, Saldanha, 7395

Abstract. Over the past two years there has been discussion among South African physicists about the possibility of establishing a deep underground physics laboratory to study, amongst others, double beta decay, geoneutrinos, reactor neutrinos and dark matter. As a step towards a full proposal for such a laboratory a number of smaller programmes are currently being performed to investigate feasibility of the Huguenot Tunnel in the Du Toitskloof Mountains near Paarl (Western Cape, South Africa) as a possible sight for the South African Underground Laboratory facility. The programme includes measurements of radon in air (using electret ion chambers and alpha spectroscopy), background gammaray measurements (inside/outside) the tunnel using scintillator (inorganic) detectors, cosmic ray measurements using organic scintillators and radiometric analyses of representative rock samples.

Keywords: double beta decay, nuclear matrix element, QRPA
PACS: 23.10.-s; 21.60.-n; 23.40.Bw; 23.40.Hc

INTRODUCTION

Discussions about an underground research facility in SA started in 2011. As one of the worlds largest producers of gold, South Africa has a number of the worlds deepest gold mines (TauTona Gold Mine 3.9 km). The use of deep mines in the search for neutrino events is not new to the South African Research community. In 1965 the Nobel Prize laureate along with South African Physicist, Friedel Sellschop detected the first atmospheric neutrino events in the Eastrand mine near Johannesburg (South Africa) [1].

Initial focus by the South African nuclear physics community was on establishing an underground facility in one of South Africa's deep gold mines.The alternative is to develop such an underground laboratory inside the Huguenot Tunnel which is located between the towns of Paarl and Worcerster in the Wester Cape Province of South Africa.

The development of the Huguenot tunnel as an underground low level radiation facility holds a number of strategic advantages in for the South African physics communities in the Western Cape. Such a facility located approximately 25 km for Stellenbosch University and 40 km for the iThemba Laboratory of Accelerator Based Sciences and therefore provides quick and easy access to the local research communities. Research

programs done at such a facility will also also support postgraduate training programs in nuclear physics at Stellenbosch University, the University of the Western Cape and the University of Cape Town. Furthermore the research at the SAUL will support national and international research activities in astronomy, nuclear and particle physics, as well as atmospheric and space science linked to the iThemba LABS [2], Square Kilometre Array (SKA) [3], South African Astronomical Observatory (SAAO) [4], the Southern African Large Telescope (SALT) [5], South African National Space Agency [6], and High Energy Spectrospopic System (HESS) [7] in Namibia.

The SAUL facility at Huguenot tunnel will provide a plateform for training and the development of a research footprint for a dedicated facility in the TauTona mine. The preliminary geological and radiation background studies is currently underway.

PRELIMINARY STUDIES

In order to decide on the best course to take in order to develop sensible research programs around the huguenot tunnel facility a number of measurable parameters will have to be known. According to the geological survey which was done during the excava-

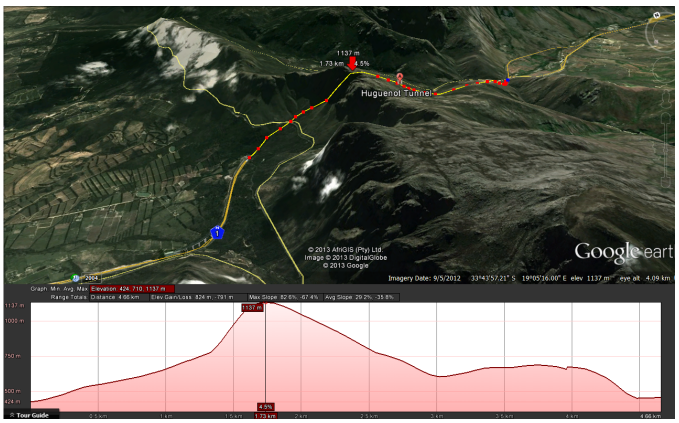

FIGURE 1. Height profile of du Toitskloof mountain range above the Huguenot tunnel.

FIGURE 2. Electrets mounted in groups of 3 on the walls of the tunnel close to the vehicle cross-cuts.

tion period (1973 - 1984) the composition of the mountain range mainly composes of

quarzitic sandstone (also refered to as Tablemountain sandstone). It is therefore expected that radon concentration levels within the tunnel should be insignificant,and should therefore not have any considerable contribution on the background radiation signature. Figure 1 shows the height profile of the du Toitskloof mountain range above the huguenot tunnel.

In April 2013 the environmental radiation groups at Stellenbosch University and iThemba LABS performed a preliminary radon measurements by placing 3 electrets at the three vehicle cross-cut (VCC) areas to monitor the radon in the undeveloped Northern tunnel seen in figures 2 and 3.

FIGURE 3. Vehicle cross-cut area

The radon concentrations at the three measured sites shown in the table in figure 4 confirms that the levels of radon is well below any conciderable levels. Comparison between the radon levels at the three sites also shows a slightly higher level at VCC2 as compared to VCC1 and VCC3.

	Mean	Standard Deviation
location	Air Radon Concentration	Air Radon Concentration
	($Bq.m^{-3}$)	($Bq.m^{-3}$)
VCC1	45.4	0.1
VCC2	**52.7**	**7.1**
VCC3	64.9	5.2

FIGURE 4. Radon levels measured at vehicle cross-cuts

The radon background measurements have been followed up by an accumilated gamma ray measurement with the multi-element detector using a scintillator array (MEDUSA) detection system (see figure 5). The gammaray spectrum from the MEDUSA was then compared to the known gamma energy spectral of ^{40}K, ^{238}U, ^{232}Th, and ^{137}Cs shown in figure 6. This measurement, however, lacks position information which will be included in the next series of measurements.

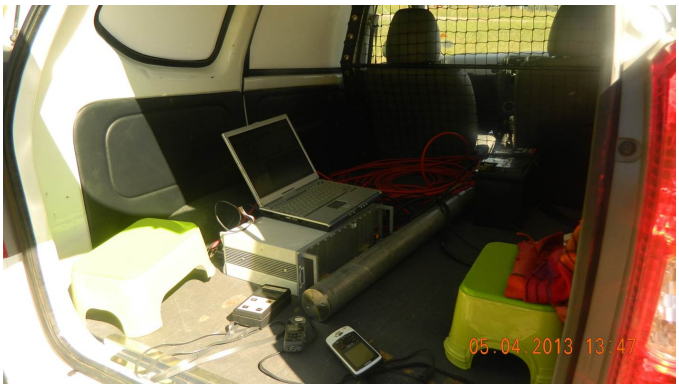

FIGURE 5. The MEDUSA gammaray detector system

FIGURE 6. Gammaray spectrum of tunnel obtained with the MEDUSA detector compared to the gammaray spectra of ^{40}K, ^{238}U, ^{232}Th, and ^{137}Cs

In addition to the gammaray spectra and radon background measurement the collaboration will soon be measuring the muon background within the tunnel. In addition to the background measurements biomonitors were placed at strategic locations within the tunnel in order to measure the air pollution levels within the tunnel as shown in figure 7.

FIGURE 7. Biomonitors placed at locations to monitor air pollution levels in the tunnel.

CURRENT AND FUTURE PROJECTS

The development of the huguenot tunnel as a research facility will be done in two phases. The first phase involves performing a complete survey of the tunnel in order to identify sensible scientific programs and projects which could form the focus of research activities. These programs will form the backbone of the future training programs for postgraduate students with the aim to develop a dedicated underground physics research facility.

The second phase of the project will look into the possibility of establishing an underground research facility in one of South africa's deep gold mines.

ACKNOWLEDGEMENTS

The collaboration would like to acknowledge the financial support from the National Research Foundation through the Knowledge, Interchange and Collaboration fund.

REFERENCES

1. F. Reiner et al., Phys. Rev. Lett. **15**, 428 (1965).
2. www.tlabs.ac.za
3. www.ska.ac.za
4. www.saao.ac.za
5. www.salt.co.za
6. http://www.space-sci.sansa.org.za/
7. http://www.mpi-hd.mpg.de/hfm/HESS/
8. Alburger et al., Earth and Planetary Science Letters **78**, p168-176 (1986).

Neutrino geophysics

Oleg Smirnov

Dzhelepov's Laboratory for Nuclear Problems, JINR Dubna, 141980 Dubna, Moscow region, Russia

Abstract. Geoneutrinos are electron antineutrino accompanying β-decays. Interest in geoneutrino has risen very recently, in parallel with development of large volume detectors, able to detect their tiny fluxes. The main scientific outcomes expected from these measurements are the abundances and distributions of radioactive elements inside the Earth, beyond the reach of direct measurements by sampling. The knowledge of the radioactive content of the Earth's depths is essential for many problems in geoscience.

Keywords: geoneutrino
PACS: 95.55.Vj, 13.15.+g, 14.60.Lm

INTRODUCTION

Geoneutrino is an electron antineutrino accompanying β-decay of nuclear long-lived isotopes present in the Earth. The natural radioactivity of the Earth is a powerful source of heat, influencing the thermal history of the Earth. Radiogenic heat and primordial heat of the Earth constitutes two main contributions to the total energy loss of the Earth. Insignificant amount of heat is produced due to tidal effects, chemical differentiation, crystallization in the D" layer etc. These less important sources produce no more than one percent of the total. The ratio of the radiogenic heat production to the total is called the Urey ratio and is an important quantity characterizing heat production in the Earth.

Analysis of the available measurements of temperature gradients in mines (based on measurements in 22000 mines allover the Earth) gives the total thermal production of 47 ± 2 TW [1]. One should note that these value is not an experimental measurement of heat production but a result of modeling. Thus any independent measurement of total radiogenic heat, that is one of the main contributions to the energetic of the Earth, is by no doubts of huge interest for geophysics.

Geo-neutrino flux measurements do provide experimental evidence for the quantity and distribution of radioactive elements internally heating the Earth, as the direct measurement of the composition of basic regions is possible for the Earth's crust only. Radiogenic heating helps power plate tectonics, hot-spot volcanism, mantle convection, and possibly the geo-dynamo. Information on the extent and location of this heating better defines the thermal dynamics and chemical composition of Earth. Geoneutrinos, if registered with appropriate precision, potentially can help to answer the open questions regarding the natural radioactivity in our planet: what is the radiogenic contribution to terrestrial heat production; how much U and Th the crust contains; how much U and Th the mantle contains; is standard geochemical model (the so called Bulk Silicate Earth model) consistent with geo-neutrino data?

MODELS

Models predicting abundances of radioactive elements in each part of the Earth is required to calculate the geoneutrino signal. The description of the modern system crust+mantle is provided by a model of Bulk Silicate Earth (BSE), which represents a reconstruction of a primitive primordial mantle of the Earth of the base of geochemical arguments. The primitive mantle is the mantle formed immediately after the separation of the core but before the crust differentiation. The composition of the primitive mantle corresponds to the composition of the so called chondritic meteorites, representing the majority of stone meteorites. The composition of chondrite meteorites is practically identical to the chemical composition of the Sun, excluding the light elements, such as hydrogen and helium. It is assumed that chondrites originates from protoplanet matter surrounding the Sun by condensation and accretion of the dust with intermediate heating. Chondrites doesn't show the traces of melting and corresponds to non-differentiated planets (planets without crust), i.e. to the composition of the primitive mantle.

The composition of the mantle and the crust corresponds to another type of meteorites, achondritic ones. These are stone meteorites without chondres. Achondritic meteorites are stone meteorites without chondres close in composition and structure to the Earth's basalts. About 8% of all found meteorites are achondritic ones with traces of melting destroyed the chondres.

The homogeneous composition of seismically differentiated regions is usually assumed in model. The abundances of U/Th in the internal regions is based on the composition of corresponding meteorites in assumption of typical composition of the Earth within the frames of the Solar system. The BSE model provides full amount of U,Th and K in the Earth as these lithophile elements (having affinity to the silicate minerals and melts) should not be present in the Earth's core. The BSE model is in a good agreement with the majority of experimental observations concerning the core and upper mantle. BSE models can be subdivided in different classes depending on the initial assumptions:

- **Geochemical**. This class of models is based on the composition of carbonaceous chondrites (meteorites class, denoted CI, here "C" is for carbon and "I" is a first letter of the Ivuna location, where these class of meteorites was first found) similar to Solar photosphere in content of refractory lithophile elements (having affinity to silicate minerals and melts), siderophile elements (affinity to iron) and volatile elements. An assumption of identical ratios of Th/U masses is of refractory lithophile elements in BSE and carbonaceous chonrtites is used in this class of models. Typical chondritic ratio of Th/U masses id 3.9 and K/U masses $\sim$13000. Variants of the model are presented in [2, 3, 4, 5, 6]. Typical U concentration in these models is (20 ± 4) ppb and corresponding thermal flux is 20 ± 4 TW.
- **Cosmochemical.** Model proposed in [7] is based on the composition of enstatine chondrites having the closest isotopic similarity to the mantle samples and having high enough iron content to explain the metallic core (similarity in oxygen state). Model of impact erosion by O'Neill and Palme [8] belongs to the class. In the impact erosion model early enriched crust can be partially lost in collisions of the Earth with massive external bodies. Both models predicts U concentration of (10 ± 12) ppb and corresponding thermal flux 11 ± 2 TW.

- **Geodynamical.** These models are based on the mantle convection energetics. Parametric model of convection needs more radiogenic heat compared to other models in order to describe the modern thermal flux on the surface of the Earth, which depends on the radiogenic heat and secular cooling (see i.e. [9, 10]). Typical U concentration in these models is (35 ± 4) ppb, and corresponding radiogenic thermal flux is 33 ± 3 TW.

Geoneutrino signal predicted by the models are in approximate agreement between them. The discrepancy of the order of 10% can be explained mainly by different abundances of U and Th in core and upper mantle, and by non-significant differences in mantle model. Mass restrictions following from the BSE model are used in all calculations to predict elements abundances in lower mantle. Using mass balance equations for the calculation of U and Th concentration in different regions of the Earth one can predict distribution of these elements and calculate geoneutrino flux. In the frame of BSE model mass ratios are: M(Th)/M(U) = 3.9, M(K)/M(U)$\approx 10^4$ and U abundance is $2 \cdot 10^{-8}$ (or 0.02 ppm). Calculations in BSE model gives 19 TW for the modern radiogenic heat, mainly from U and Th, roughly half of all the heat generated in the Earth.

Minimal possible amount of radioactive elements in the Earth is defined by the lower bound of measured abundances of the natural radioactive isotopes in the Earth's crust (minimal radiogenic model). On the other hand radiogenic heat shouldn't exceed total observed heat flux of the Earth of 47 TW. This limiting case is called maximal radiogenic model: all the heat in this model is radiogenic and the chondritic ratio of Th/U is assumed. The elements abundances are scaled to provide the total heat generation of 47 TW. The gap between the minimal and maximal models are quite big and can be reduced using geoneutrino data.

Half of the geoneutrino signal is provided by a local contribution from the distances up to some hundredths kilometers. That is why the knowledge of the local geology is of high importance to make model predictions more precise.

Antineutrino spectra expected from ^{238}U and ^{232}Th chain, as well as from ^{40}K, are presented in fig.1 (left). A fraction of antineutrino spectra from ^{238}U and ^{232}Th chains exceeds the threshold of the inverse beta- decay on proton. This makes their detection by liquid scintillator detectors in the reaction $\overline{\nu}_e + p \rightarrow e^+ + n$ (with a threshold of 1.8 MeV). The theoretical spectra from U and Th chains in assumption of the secular equilibrium in the chains and at the chondritic ratio of Th/U masses M(Th)/(U)=3.9 are shown in fig. 1 (right). The visible difference in the spectra makes contributions from U and Th potentially distinguishable.

Detectors and backgrounds.

At present only two collaboration presented results on the geoneutrino observation: KamLAND [11] and Borexino [12]. Both collaborations are using detectors on the base of the liquid organic scintillator.

Principal backgrounds in the geoneutrino search are: reactor antineutrinos, cosmic muons induced backgrounds, including cosmogenic production of (βn)- decaying isotopes and internal radioactive contamination.

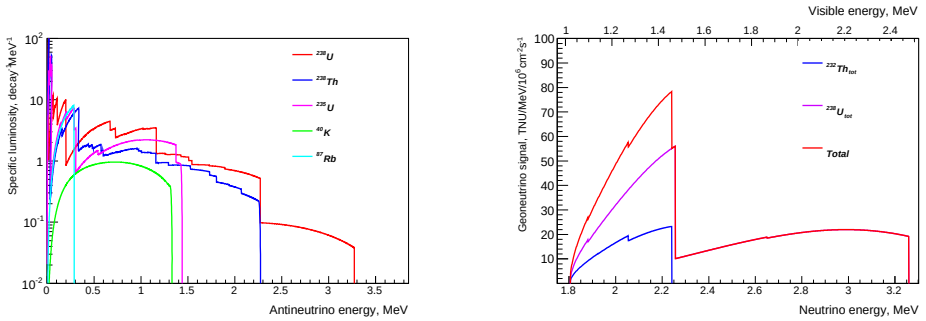

FIGURE 1. Left: theoretical spectra of the geoneutrino from their main sources. Right: theoretical spectra from the U and Th chains in assumption of the secular equilibrium in the chains and at the chondritic ratio of Th/U masses M(Th)/(U)=3.9.

Reactor antineutrinos. For KamLAND measurements they contribute 81% of the total antineutrino signal in KamLAND geo-nu window [0.9-2.6 MeV] and about 36% for the Borexino case. Geo/Reactor antineutrino ratio is 0.23 in KamLAND versus 1.8 in Borexino site (because of the presence of other backgrounds it is different from the signal-to-noise ratio).

Cosmic muons induced backgrounds, including cosmogenic production of (βn)-decaying isotopes. At LNGS (where Borexino detector is placed) the muons flux is of about factor 7 lower than at the Kamioka site (KamLAND detector). A veto of 2 seconds is applied after each muon passing through the detector to remove events caused by short-lived cosmogenic isotopes decaying through (βn) channel. An additional condition on muons is applied in KamLAND - muon should generate a shower, this reduce live time losses to the moderate 4% compared to 10% of the live-time loss in Borexino analysis, despite of the lower muon flux in the Gran Sasso site. The suppression of background from the fast neutrons from buffer is achieved by applying a shorter 2 ms veto (this background is mainly caused by multiple neutron production).

Internal radioactive contamination: contributes through accidental coincidences and (αn)-reaction on ^{13}C, monoenergetic α with energy of 5.4 MeV are produced in ^{210}Po decays. The both backgrounds are much lower in the Borexino. Borexino typical contamination is 3-4 orders of magnitude lower; KamLAND achieved factor 20 on (αn) reduction as reported in [13].

MEASUREMENTS AND COMPARISON TO MODEL

The first indication of the non-zero geoneutrino signal on the data set from 7.09x10^{31} target proton years was reported by KamLAND in 2005 [14], 90% confidence interval for the total number of detected geoneutrinos of 4.5 to 54.2 was found with the U/Th ratio fixed at 3.9.

In April 2010 the first high significance confirmation on the geoneutrino signal come from Borexino [15], the collaboration reported $9.9^{+4.3(15.8)}_{-3.4(8.0)}$ registered geoneutrino events at 68% C.L. (99.73%). . The presence of non-zero geoneutrino signal was

confirmed at the 99.997% level. Though measured with the lower exposition compared to the KamLAND, the result has higher statistical significance due to the much better signal-to-noise ratio.

KamLAND collaboration provided three updates of the initial analysis. The operational troubles at the power reactors after serious earthquake in 2007 caused lower reactor neutrino flux in this period. KamLAND has experienced large known time variation of the background. This helped in extracting constant contribution from geo-neutrinos which can be seen above the estimated reactor neutrino + non-neutrino background in the geo-neutrino energy range, 0.9 - 2.6 MeV. The KamLAND results are summarized in Table 1.

The Borexino results are summarized in Table 2, the last up-to-date measurement was released by Borexino in 2015. The geoneutrino flux measurement was performed with 2056 days data set, which is twice as large as the statistics used in the previous publication. 77 antineutrino candidates were observed in total, with the expected ratio of geoneutrinos to neutrinos from the European reactors of about 1:2 (see 2). Backgrounds from other sources for antineutrino measurement in Borexino are negligible and do not exceed one event for the measurement time. The observed geoneutrino signal is evaluated by fitting the experimental spectrum with the spectral contributions from geoneutrino (with chondritic Th/U mass ratio fixed at M(Th)/M(U)=3.9), reactor neutrino and residual backgrounds. The observed value of $43.5^{+12.1}_{10.7}$ TNU for the geoneutrino flux is totally consistent with the expected one for most of geophysical models (1 TNU, Terrestrial Neutrino Unit, corresponds to 1 event per year for 10^{32} protons in target). The probability of the absence of geoneutrino signal is negligible, namely, 3.6×10^{-9}. Moreover, for the first time in the history of geoneutrino observations, the non-zero contribution from the mantle is confirmed at 98% confidence level. Estimated crust contribution to the total signal is 23.4 ± 2.8 TNU. The statistical difference between the total observed signal and the crust contribution (i.e. the signal from the mantle) is $20.9^{+15.1}_{-10.3}$ TNU, which corresponds to the non-zero contribution from the mantle with 98% probability.

The radiogenic heat contribution calculated for different models is presented in Fig.3. The radiogenic heat is plotted in the x-axis, and the observed signal is presented in the y-axis. The maximal (red line) and the minimal (blue line) signals correspond to two extreme distributions of the radioactive elements in the mantle: homogeneous (maximal) and all the heating elements at the crust/mantle boundary (minimal). The radiogenic contribution to the total Earth heat, corresponding to the signal observed in Borexino, could be from 11 to 52 TW at 68% C.L.. Coloured areas correspond to three classes of the most popular geophysical models, namely, cosmochemical, geochemical and geodynamical ones. With present data the discrimination between these models is still impossible due to the limited precision of the measurement.

FUTURE PROJECTS

SNO+ detector should acquire first geoneutrino data this year (2016). It is located at deep Sudbury mine, at 6010 m.w.e (70 muons a day, for comparison in Borexino there are 4000 muons a day for a smaller detector), and operates 780 tonnes LAB- based liquid scintillator detector. 29 geo-neutrino events per live-year are expected compared

TABLE 1. KamLAND results on the geoneutrino flux measurement (result is presented for the electron antineutrino flux, the total flux is approximately two times higher). Exposition of 1 t·yr in KamLAND corresponds to 8.48×10^{28} protons·yr, and 1 TNU corresponds to 1.1×10^{5} cm^{-2}s^{-1} electron antineutrino flux. Last column presents the probability of the absence of the geo-neutrino signal in the corresponding data set.

Year	Live-time, days	Exposition, protons·yr $\times 10^{31}$	number of candidates	number of geoneutrino	Geoneutrino flux $\times 10^{6}$cm^{-2}s^{-1}	P(H_0)
2005 [14]	749.1	7.09 ± 0.35	152	25^{+19}_{-18}	$5.1^{+3.9}_{-3.6}$	4.6%
2008 [16]	1486	24.4	–	73 ± 27	4.4 ± 1.6	0.45%
2011 [17]	2135	34.9 ± 0.7	841	106^{+29}_{-28}	$4.3^{+1.2}_{-1.1}$	$3 \cdot 10^{-5}$
2013 [18]	2991	49.0 ± 1.0	–	116^{+28}_{-27}	3.4 ± 0.8	—

TABLE 2. Borexino results on the geoneutrino flux measurements.

Year	Live-time, days	Exposition, t·yr	number of candidates	number of geoneutrino	Geoneutrino signal, TNU	P(H_0)
2010 [15]	537.2	256.2	21	$9.9^{+4.1}_{-3.4}$	65^{+27}_{-22}	$3 \cdot 10^{-5}$ (4.2σ)
2013 [19]	1363	613±26	46	14.3 ± 4.4	38.8 ± 12.0	$6 \cdot 10^{-6}$ (4.9σ)
2015 [20]	2056	907±44	77	$23.7^{+6.5}_{-5.7}$	$43.5^{+12.1}_{-10.7}$	$3.6 \cdot 10^{-9}$ (5.9σ)

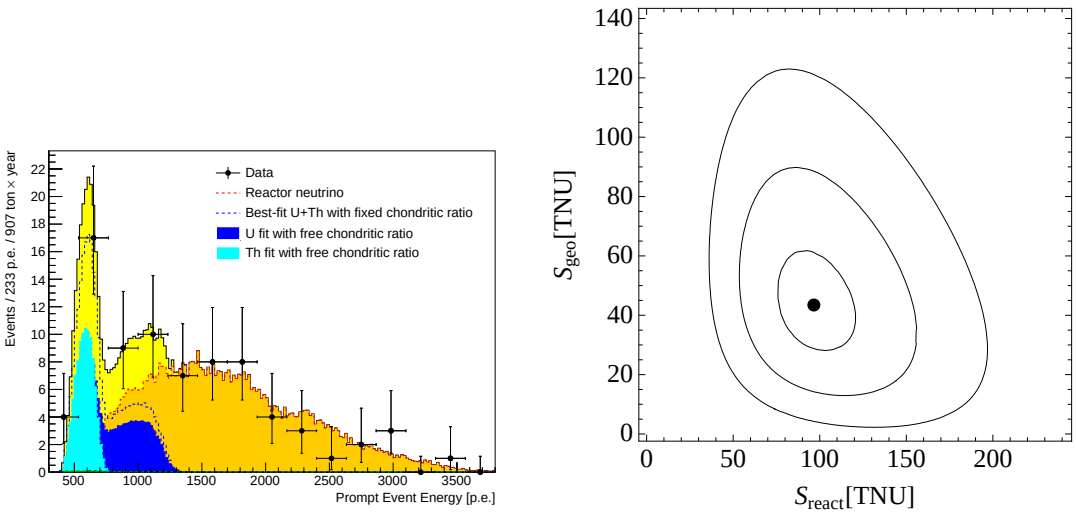

FIGURE 2. Left: Antineutrino spectrum in Borexino for 2056 days of the data taking. 77 antineutrino candidates are observed in total, about 1/3 of which are geoneutrinos. The best-fit shows the geo-neutrino and reactor neutrino spectra (dotted lines) assuming the chondritic ratio of Th to U masses (M(Th)/M(U)=3.9). Colored areas show the result of a separate fit with U (blue) and Th (light blue) set as free and independent parameters. The light yield corresponds to roughly 500 p.e./MeV. Right:Corresponding best-fit contours for 1, 3 and 5 σ's.

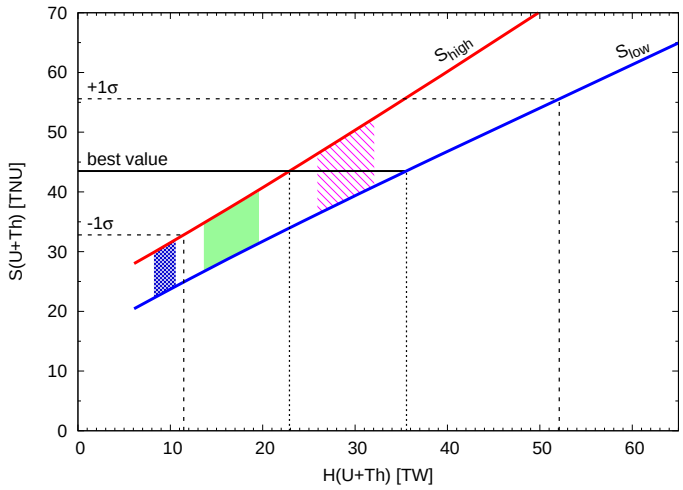

FIGURE 3. Radiogenic heat calculated for different Earth models. The radiogenic heat is plotted in the x-axis, and the observed signal is presented in the y-axis. The maximal (red line) and the minimal (blue line) signals correspond to two extreme distributions of the radioactive elements in the mantle: homogeneous (maximal) and all the heating elements at the crust/mantle boundary (minimal). Coloured areas correspond to three classes of the most popular geophysical models, namely, cosmochemical, geochemical and geodynamical ones.

with 26 events from reactors in the same energy range. The measurement with SNO+ is very promising due to the very low flux of muons, another advantage is also the profound geological studies in the local region (the Sudbury itself is a mine).

LENA is a project of 50 ktonne deep underground multipurpose liquid scintillator detector [21]. About 1500 geoneutrino events per year are expected. Hanohano is another project of underwater 10 ktonne liquid scintillator detector [24]. The Hanohano should be a portable device deployed from the barge. It will be aimed to extract mantle contribution in the total geoneutrino signal, which is very important from the geophysical point of view. About 100 geoneutrino events per year are expected. The combination of data from multiple sites and data from an oceanic experiment would provide valuable information and will help to measure the mantle contribution.

Multitonne detectors of the third generation reactor experiments (JUNO [22], RENO-50 [23]) will be sensitive to the geoneutrino. The expected geo-neutrino signal is $39.7^{+6.5}_{-5.2}$ TNU [25]. Signal from the reactors in the geo-neutrino energy widow will contribute $26.0^{+2.2}_{-2.3}$ TNU with spent near reactors in Taishan and Yangjiang, 10% precision of the geoneutrino signal measurement can be achieved with $\sim$ 100 days of the data taking. After the turning on of the reactors the background will increase up to 354^{+45}_{-41} TNU, making extraction of the geoneutrino signal more difficult. Nevertheless, 10% precision can be achieved with 3 years of the data taking, the same set of data will allow to obtain the contribution of U with 20% precision and of Th with 30% precision [22].

CONCLUSIONS

Geoneutrino existence is confirmed independently by Borexino and KamLAND. The precision of both available measurements (Borexino and KL) is still too low: ~28% and 24% correspondingly for the U+Th signal with fixed mass ratio, and much worse for the unconstrained R(U) and R(Th) measurements. Different geological models for the moment can't be discriminated by existing measurements, more precise measurements are needed. Regional measurements in location of experiments are needed to provide more precision for the models. Independent measurements at various sites are highly desirable to check contributions from crust/mantle. We are expecting more input for the geological models from future detectors.

REFERENCES

1. J. H. Davies, D. R. Davies, *Solid Earth* **115** (2010).
2. W. F. McDonough, S. S. Sun, *Chemical Geology* **120**, 223 (1995).
3. C. J. Allegre et al, *Earth and Planetary Sci. Lett.* **134**, 515 (1995).
4. S. R. Hart, A. Zindler, *Chem. Geol.* **57**, 247 (1986).
5. R. Arevalo, W. F. McDonough , M. Luong, *Earth and Planetary Sci. Lett.* **278**, 361 (2009).
6. H. Palme, H. S. C. O'Neill, *Treatise of Geochemistry. V. 2.* Oxford: Elsevier, 1-38 (2003).
7. M. Javoy, et al. *Earth and Planetary Sci. Lett.* **293**, 59 (2010).
8. H. S. C. O'Neill, H. Palme, *Philos.Trans. Roy. Soc. A: Math., Phys. Engin. Sci.*, **366**,4205 (2008).
9. D. L. Anderson, *New theory of the Earth*, Cambridge University Press, (2007).
10. D. L. Turcotte, G. Schubert, *Geodynamics, applications of continuum physics to 1181 geological problems*, Cambridge University Press, second edition (2002).
11. K. Eguchi, et al., (KamLAND Collaboration), *Phys. Rev. Lett.* **90**, 021802 (2003).
12. G. Alimonti, et al., Borexino Collaboratrion, *NIM A* **600**, 568 (2009).
13. K. Inoue, *Neutrino-2010 conference*, http://www.neutrino2010.gr/.
14. T. Araki T., et al., KamLAND collaboration, *Nature* **436** 499 (2005).
15. G. Bellini, et al., Borexino collaboration, *Phys.Lett. B* **687**, 299 (2010).
16. T. Araki, et al., KamLAND collaboration, *Phys. Rev. Lett.* **100**, 221803 (2008).
17. A. Gando, et al., Kamland Collaboration, *Nature Geoscience* **4** 647 (2011).
18. A. Gando, et al., *Phys. Rev. D* **88**, 033001 (2013).
19. G.Bellini, et al., Borexino Collaboration, *Phys. Lett. B* **722**, 295 (2013).
20. M. Agostini, et al., Borexino Collaboration, *Phys. Rev. D* **92**, 031101 (2015).
21. M. Wurm, et al., LENA Collaboratiom, arXiv:1104.5620 [astro-ph.IM].
22. F. An, at al, JUNO Collaboration, *J. Phys. G* **43** 030401 (2016).
23. Soo-Bong Kim, arXiv:1412.2199 [hep-ex].
24. J. G. Learned, S. T. Dye, S. Pakvasa, arXiv:0810.4975 [hep-ex].
25. V. Strati, M. Baldoncini, I. Callegari, F. Mantovani, W. F. McDonough, B. Ricci, G. Xhixha, arXiv:1412.3324v2 [physics.geo-ph].

Possible alternatives for models of the Galactic Centre

Alexander F. Zakharov[a,b,c,d,e]

[a]*Institute of Theoretical and Experimental Physics, Moscow, 117218, Russia*
[b]*Bogoliubov Laboratory of Theoretical Physics, JINR, Dubna, Moscow region, Russia*
[c]*National Research Nuclear University MEPhI (Moscow Engineering Physics Institute), 115409, Moscow, Russia*
[d]*National Astronomical Observatories of Chinese Academy of Sciences, Beijing, 100012 China*
[e]*North Carolina Central University, Durham, NC 27707, USA*

Abstract. Now there are two basic observational techniques to investigate a gravitational potential at the Galactic Center, namely, a) monitoring the orbits of bright stars near the Galactic Center to reconstruct a gravitational potential; b) measuring a size and a shape of shadows around black hole giving an alternative possibility to evaluate black hole parameters in mm-band with VLBI-technique. At the moment one can use a small relativistic correction approach for stellar orbit analysis (however, in the future the approximation will not be not precise enough due to enormous progress of observational facilities) while now for smallest structure analysis in VLBI observations one really needs a strong gravitational field approximation. We discuss results of observations, their conventional interpretations, tensions between observations and models and possible hints for a new physics from the observational data and tensions between observations and interpretations. We will discuss an opportunity to use a Schwarzschild metric for data interpretation or we have to use more exotic models, for instance, Reissner – Nordström or Schwarzschild – de-Sitter (Kottler) metrics for better fits.

Keywords: Black holes, supermassive black holes, gravitational lensing, the Galactic Center, Large telescopes, VLBI interferometry
PACS: 43.35.Ei, 78.60.Mq

Soon after the discovery of general relativity (GR) [1, 2] a vacuum solution of GR equations has been found [3], however, Albert Einstein was rather skeptical concerning physical applications of the solution, for instance, at the end of the paper he wrote:"...The essential result of this investigation is a clear understanding as to why the "Schwarzschild singularities"[1] do not exist in physical reality..." [6], see also similar opinions in a textbook [7] in spite of the fact that results on maximal masses for white dwarfs [8, 9, 10, 11] and for neutron stars [12] have been known in these times. Moreover, Oppenheimer and Snyder showed an opportunity of black hole formation [13].[2] There were only three famous tests of GR at the beginning, namely, deflection of light, the Mercury anomaly and gravitational redshifts [7], but there is a number of phenomena

[1] According to the wide spread terminology at these times the event horizon was called as Schwarzschild singularity. In fact, the Schwarzschild solution has no singularities but singularities are appeared in the variables chosen in [4], see also [5].
[2] In 1939 Einstein, Oppenheimer, Volkoff and Snyder worked at Institute for Advanced Studies in Princeton, see also other curious issues of an early GR history in a preface written in [14].

where predictions of GR have been checked or they will be checked in the future [15]. An rapid development of black hole physics started since J.A. Wheeler lecture in 1967 and his corresponding article [16], where the term "black hole" has been introduced. In spite of the fact that black hole solutions of Einstein equations are known for almost century there are not too many astrophysical examples where one really need a strong gravitational field approximation but not small relativistic corrections to a Newtonian gravitational field. One of the most important option to test a gravity in the strong field approximation is analysis of relativistic line shape as it was shown [17]. Such signatures of the Fe $K\alpha$-line have been found in the active galaxy MCG-6-30-15 [18]. Analyzing the spectral line shape the authors concluded the emission region is so close to the black hole horizon that one has to use Kerr metric approximation to fit observational data [18]. Results of our simulations of iron K_α line formation are given in [19, 20, 21, 22, 23], where we used our approach [24], see also [25, 26] for more recent reviews on the subject. Supermassive black holes have been found in center of 85 galaxies [27], however, usually astronomers do not use GR approaches for such claims about black hole existence. Around 40 quasars with redshifts $z > 6$ have been found and each quasar has a supermassive black hole with a mass around one billion solar masses $10^9 M_\odot$ and recently [28] found the ultra-luminous quasar SDSS, J010013.02+1280225.8, at redshift $z \sim 6.30$, and the quasar has the black hole with a mass around $1.2 \times 10^{10} M_\odot$. Remarkably, that the initial optical spectroscopy of the quasar was carried out with the Chinese Lijiang 2.4-m telescope (it means that discoveries may be done with relatively modest facilities). Later, spectroscopic observations were conducted for the object with the 6.5-m Multiple Mirror Telescope(MMT) and the twin 8.4-m mirror Large Binocular Telescope (LBT) in the USA and initial estimates of black hole mass and redshift have been confirmed.

Observations of the Galactic Center

The natural way to evaluate a potential gives an analysis of test particle trajectories similarly to the experiment when E. Rutherford got constraints on an atomic potential and showed a presence of nuclei in atoms analyzing paths of α-particles. In the case of massive black holes tracers may be stars, (hot) spots, gas clouds or light trajectories (gravitational lensing). Below we discuss the issues in more details. To evaluate a gravitational potential at the Galactic Center two teams of astronomers observe trajectories of bright stars in the IR band for several years. One group led by A. Ghez (UCLA, USA) uses the twin 10-meter optical/infrared telescopes on Mauna Kea (Hawaii), and according to the Keck Strategic Mission, the first important goal is *high angular resolution astrophysics*[3] and practically it gives an opportunity to be a world leader in the field, see results of the observations of bright stars [29, 30, 31]. Another group led by R. Genzel (ESO, MPE) uses four 8.2-meter VLT telescopes at Paranal (Chile). The European group got very important results [32, 33, 34] which are consistent results presented by

[3] http://www.keckobservatory.org/

US team. The important case of G2 gas cloud is a very useful tracer of the gravitational potential at the Galactic Center [34] (later, the object has been called Dusty S-cluster Object (DSO/G2) since further detailed observations were not completely consistent with the gas cloud model). It occurs that very likely this may be another example of a close peribothron[4] passage of a dust-enshrouded star [36, 37, 38]. The analysis showed that the DSO/G2 is rather a young star than a coreless gas and dust cloud [39]. The ESO and MPE formed a team to construct the GRAVITY, the Very Large Telescope Interferometer for precise astrometry and interferometric imaging. The interferometer will provide precise astrometry of order 10 micro-arcseconds [40, 41]. The GRAVITY equipment should be shipped to the VLT - observatory in Chile in 2015 and commissioning started in October 2015 [41].

Shadows for the black hole at the Galactic Center

Several years ago, a formation of images for supermassive black holes has been simulated [42, 43]. The authors used a toy model for their analysis and they concluded that a strong gravitational field is bent trajectories of photons emitted by accreting particles and an observer can see a dark spot (shadow) around a black hole position. For the black hole at the Galactic Center a size of shadow is around 50 μas. Based on results of simulations, the authors concluded that the shadow may detectable at mm and sub-mm wavelengths, however, scattering may be very significant at cm wavelength, so there are very small chances to observe the shadows at the cm band [42, 43]. Importantly, that results (presented in [42, 43]) are rather general in spite of their specific model. There is a tremendous progress to evaluate a minimal size of spot for the Sgr A^* [44], for instance, the authors evaluated a shadow size as small as 37^{+16}_{-10} μas. Practically, a minimal size of bright spot was evaluated, but a boundary of a dark spot (shadow) has to be bright, a size of bright boundary has been measured. In paper [45], the authors considered different types of shadow shapes for Kerr black holes and different position angles of a distant observer. Moreover, it was shown that for an equatorial plane position of a distant observer, maximal impact parameter $|\beta_{\max}|$ in z-direction (which coincides with a black hole rotation direction) is $\sqrt{27}$, while the corresponding impact parameter in the perpendicular direction for the $\beta_{\max}$ is $\alpha_{\max} = 2a$ [45], if we consider the function $\beta(\alpha)$ for critical impact parameters separating a capture and scattering of photons.

Constraints on black hole parameters

Theories with extra dimensions admit astrophysical objects (supermassive black holes in particular) which are rather different from standard ones. There were proposed tests which may help to discover signatures of extra dimensions in supermassive black holes

[4] The word "peribothron" has been introduced in [35] following W.R. Stoeger's suggestion. Greek bothros means pit or hole. So, the peribothron means the point of least distance of an object orbiting a black hole.

since the gravitational field may be different from the standard one in the GR approach. So, gravitational lensing features are different for alternative gravity theories with extra dimensions and general relativity. Some time ago, Bin-Nun [46, 47] discussed an opportunity that the black hole at the Galactic Center is described by the tidal Reissner–Nordström metric which may be admitted by the Randall–Sundrum II braneworld scenario. Bin-Nun suggested an opportunity of evaluating the black hole metric analyzing (retro-)lensing of bright stars around the black hole in the Galactic Center. Doeleman et al. [44] evaluated a minimal size of a spot for the black hole at the Galactic Center. According to a theoretical consideration and simulations a minimal size of spot practically has to coincide with the shadow size [42, 43]. Measurements of the shadow size around the black hole may help to evaluate parameters of black hole metric [45, 48]. Another opportunity to evaluate parameters of the black hole is an analysis of trajectories of bright stars near the Galactic Center [49, 50]. We derive an analytic expression for the black hole shadow size as a function of charge for the tidal Reissner– Nordström metric. We conclude that observational data concerning shadow size measurements are not consistent with significant negative charges, in particular, the significant negative charge $Q/(4M^2) = -1.6$ (discussed in [46, 47]) is practically ruled out with a very probability (the charge is roughly speaking is beyond 9σ confidence level, but a negative charge is beyond 3σ confidence level). We could evaluate a shadow size for the black hole at the Galactic Center assuming that the black hole mass is about $4 \times 10^6 M_{\odot}$ and a distance toward the Galactic Center is about 8 kpc. In this case a diameter of shadow is about 52 μas for the Schwarzschild metric and about 40 μas for the extreme Reissner–Nordström metric. In paper [44] the authors evaluated a size of the smallest spot near the black hole at the Galactic Center such as 37^{+16}_{-10} microarcseconds at a wavelength of 1.3 mm with 3σ confidence level. Theoretical analysis and observations show that the size of shadow can not be smaller than a minimal spot size at the wavelength [42, 43, 45, 48]. Roughly speaking, it means that a small positive q is consistent with observations but a significant negative q is not. For $q = -6.4$ (as it was suggested in [46, 47]) we have a shadow size 84.38 μas. It means that the shadow size is beyond of shadow size with a probability corresponding to a deviation about 9σ from an expected shadow size. Therefore, a probability to have so significant tidal charge for the black hole at the Galactic Center is negligible. So, we could claim that the tidal charge is ruled out with observations and corresponding theoretical analysis [51, 52]. In Fig. 1 shadow size is given as a function of charge (including possible tidal charge with a negative q and super-extreme charge $q > 1$).

Shadows for a Kottler (Schwarzschild – de-Sitter) black hole

The expression for the Kottler (Schwarzschild – de-Sitter) metric in natural units ($G = c = 1$) has the form, we have

$$ds^2 = -\left(1 - \frac{2M}{r} - \frac{1}{3}\Lambda r^2\right) dt^2 + \left(1 - \frac{2M}{r} - \frac{1}{3}\Lambda r^2\right)^{-1} dr^2 + r^2(d\theta^2 + \sin^2\theta d\phi^2). \quad (1)$$

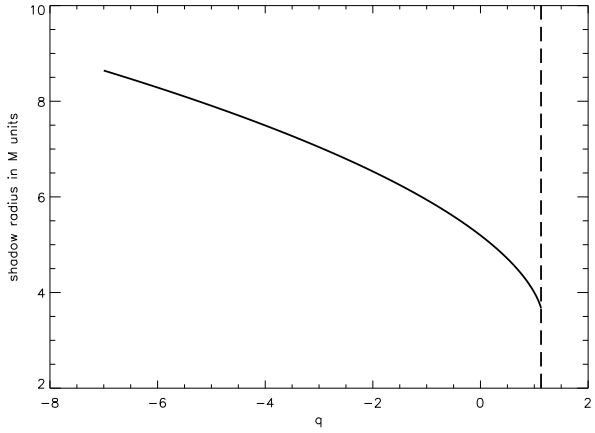

FIGURE 1. Shadow (mirage) sizes M units as a function of q.

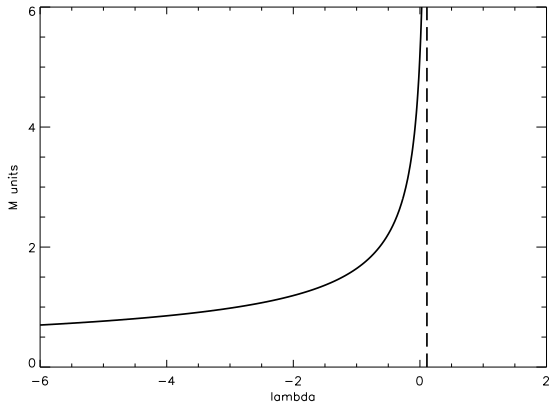

FIGURE 2. Shadow (mirage) radius (solid line) in M units as a function of dimensionless $\lambda = \Lambda M^2$. The critical value $\Lambda = 1/(9M^2)$ is shown with the dashed vertical line.

where use the conventional nomination for the Λ-term. Then we have for shadow size [53] (see also [54])

$$\xi_{\rm cr}^2 = \frac{27}{1 - 9\Lambda M^2}. \tag{2}$$

As one can see from Eq. (2) shadows disappear for $\Lambda > 1/(9M^2)$, and there exist for $\Lambda < 1/(9M^2)$ and for positive Λ its presence decrease shadow dimension while for negative Λ we have an opposite tendency (see, Fig. 2).

Constraints from trajectories of bright stars at the Galactic Center

Constraints on R^n theory

Similarly to the Mercury anomaly [55], dark matter and dark energy problems may be explained by a change of the fundamental gravity law, for instance, one could change Einstein – Hilbert Lagrangian R with a function $f(R)$ and we have $f(R) = R$ for the standard GR [56, 57, 58]. For instance, in the framework of $f(R) = R^n$ (we have GR limit for $n = 1$), one could explain acceleration of Universe without dark energy and rotation curves for spiral galaxies without dark matter, however, we have $n \approx 1$ from Solar system data [59]. One could arrive at the same conclusion from S2 orbit data [60] (see also, [61], where an extended distribution near the Galactic Center has been taken into account).

Constraints on Yukawa gravity theory

In paper [62] the authors constrained parameters of Yukawa gravity from the S2 star trajectory, where it was shown that the Yukawa potential may be a weak gravitational field limit for a wide class of alternative gravitational theories

$$\Phi(r) = -\frac{GM}{(1+\delta)r}\left[1+\delta e^{-\left(\frac{r}{\Lambda}\right)}\right], \tag{3}$$

where Λ is a parameter with a length dimension and δ is a dimensionless constant. The authors obtained the most probable Λ in the case of S2 star, is around 5000 - 7000 AU and that from the current observations it is very hard to obtain the reliable constraints on the universal constant δ. In paper [62] it was found also the same universal constant $\delta = 1/3$ which was successfully applied to clusters of galaxies and rotation curves of spiral galaxies also gives a good agreement in the case of observations of S2 star orbit.

Constraints on massive graviton theory

A version of a Lorentz invariant massive gravity has been introduced by Fierz and Pauli in 1939, however, later people found a number of problems with such theories such as existence of ghosts, vDVZ discontinuity and some other technical problems, however, some of them may be overcame. Assuming a natural modification of the Newtonian potential corresponding to massive graviton theory [15]

$$V(r) = \frac{GM}{r}\exp(-r/\lambda_{\mathrm{g}}). \tag{4}$$

An opportunity to evaluate a graviton mass analyzing a time delay in electromagnetic waves such as supernova or gamma-ray burst has been analyzed [15], moreover, earlier

it was demonstrated an opportunity to constrain a graviton mass from from gravitational wave signal alone [63] ($\lambda_g > 2.8 \times 10^{12}$ km). An analysis of S2 orbit data from VLT and Keck telescopes showed that $\lambda_g > 2950$ AU$= 4.3 \times 10^{11}$ km or $m_g < 1.9 \times 10^{-21}$ eV [64]. Our constraints are consistent with those obtained from a gravitational wave signal GW150914 recently detected by the LIGO collaboration [65] and exceeds the LIGO constraint (1.2×10^{-22} eV) which represents 90% probability limit for distinguishing massless gravitons.

Conclusions

One can conclude that there are tensions between a size of the smallest spot at the Galactic Center and an expected shadow size, therefore one should use Reissner – Nordström or/and the Kottler (Schwarzschild – de-Sitter) metrics or there are systematic effects. Concerning the best fits for trajectories S2 like stars with alternative theories of gravity, one concludes that R^n is practically has to be ruled out with the observational data, there are hints for the Yukawa potential from an analysis of these data, because the Yukawa potential provides a slightly better fit in comparison the Newtonian fit. One needs more precise observations (such as VLBI in mm band, GRAVITY interferometer or/and forthcoming large telescopes (E-ELT and TMT) for more definite claims on the discussed issues. Our graviton mass constraint is consistent with the recent constraint obtained by the LIGO collaboration from the first gravitational wave detection [65].

The author thanks D. Borka, V. Borka Jovanović, F. De Paolis, G. Ingrosso, P. Jovanović, S. M. Kopeikin, A. A. Nucita for useful discussions. A. F. Z. thanks also a senior scientist fellowship of Chinese Academy of Sciences NSF and (HRD-0833184) and NASA (NNX09AV07A) for a partial support.

REFERENCES

1. A. Einstein, Sitzungsberichte der Koniglich Preussischen Akademie der Wissenschaften (Berlin), 844 (1915); see English translation in *The collected papers of Albert Einstein, Volume 6: The Berlin Years: Writings, 1914-1917* (English translation supplement) p. 117 (2005).
2. D. Hilbert, Nachrichten von der Kuniglichen Gesellschaft der Wissenschaften zu Gottingen. Mathematisch-physikalische Klasse, **3**, 395 (1916); English translation in *"100 Years of Gravity and Accelerated Frames The Deepest insights of Einstein and Yang-Mills"* (Advanced series on theoretical physical science; v. 9), edited by J.-P. Hsu and D. Fine, World Scientific, Singapore (2005) p.120, ISBN 978-981-256-335-4.
3. K. Schwarzschild, Sitzungsberichte der Koniglich Preussischen Akademie der Wissenschaften, 189 (1916); see English translation in Gen. Rel. Grav. **35**, 951 (2003).
4. D. Hilbert, Nachr. Ges. Wiss. Gottingen, Math. Phys. Kl., 53 (1917).
5. J. Eisenstaedt, Arch. Hist. Exact Sci. **27**, 157 (1982).
6. A. Einstein, A. 1939, *Ann. Math.*, **40**, 922.
7. P.G. Bergmann, *Introduction to the theory of relativity*, New York, Prentice-Hall, 1942.
8. E.C. Stoner, Philos. Mag. **9**, 944 (1930).
9. S. Chandrasekhar, Astophys. J., **34**, 81 (1931).
10. L. D. Landau, Phys. Z. Sowjetunion, **1**, 285 (1932).
11. S. Chandrasekhar, Observatory **57**, 373 (1934).
12. J. R. Oppenheimer, G. M. Volkoff, *Phys. Rev.*, **55**, 374 (1939).

13. J. R. Oppenheimer, H. Snyder, Phys. Rev. **56**, 455 (1939).
14. A. Ashtekar, in *100 Years of Relativity. Space-Time Structure: Einstein and Beyond*, ed. A. Ashtekar, World Scientific, Singapore, 2005, p. V.
15. C. Will, Living Rev. Relat. **17**, 4 (2014); arXiv:1403.7377v1[gr-qc].
16. J. A. Wheeler, American Scientist **56**, 1 (1968); reprinted in American Scholar **37** 248 (1968).
17. A.C. Fabian, M.J. Rees, L. Stella, N.E. White, Month. Not. R. Astron. Soc. **238**, 729 (1989).
18. Y. Tanaka, K. Nandra, A. C. Fabian et al., Nature **375**, 659 (1995).
19. A.F. Zakharov, S.V. Repin, Astron. & Astrophys. **406**, 7 (2003).
20. A.F. Zakharov, N.S. Kardashev, V. N. Lukash et al., Month. Not. R. Astron. Soc., **342**, 1325 (2003).
21. A.F. Zakharov, S.V. Repin, Advances in Space Res. **34**, 2544 (2004).
22. A.F. Zakharov, S.V. Repin, New Astron. **11**, 405 (2006).
23. A.F. Zakharov, Phys. Atom. Nucl. **70**, 159 (2007).
24. A.F. Zakharov, Month. Not. R. Astron. Soc. **269**, 283 (1994).
25. A.C. Fabian, R.R. Ross, Space Sci. Rev. **157**, 167 (2010).
26. P. Jovanović, New Astron. Rev. **56**, 37 (2012).
27. J. Kormendy, L. C. Ho, Ann. Rev. Astron. Astrophys. **51**, 511 (2013).
28. X.-B. Wu, F. Wang, X.-H. Fan et al., Nature, **518**, 512 (2015).
29. A.M. Ghez, M. Morris, E.E. Becklin, A. Tanner, T. Kremenek, Nature, **407**, 349 (2000).
30. L. Meyer, A. M. Ghez, R. Schödel et al., Science **338**, 84 (2012).
31. M.R. Morris, L. Meyer, A.M. Ghez, Res. Astron. Astrophys. **12**, 995 (2012).
32. R. Schödel, T. Ott, R. Genzel et al., Nature **419**, 694 (2002).
33. S. Gillessen, F. Eisenhauer, S. Trippe et al., Astrophys. J. **692**, 1075 (2009).
34. S. Gillessen, R. Genzel, T.K. Fritz et al., Nature **481**, 51 (2012).
35. J. Frank, M. J. Rees, M.J., Month. Not. R. Astron. Soc. **176**, 633 (1976).
36. K. Phifer, T. Do, L. Meyer, A.M. Ghez et al. Astrophys. J. **773**, L13 (2013).
37. M. Zajaček, V. Karas, A. Eckart, Astron. & Astrophys., **565**, A17 (2014).
38. M. Zajaček, A. M. Eckart, F. Peissker, G.D. Karssen, V. Karas, arXiv:1507.00237v1[astro-ph.GA].
39. M. Valencia-S., A. Eckart, M. Zajaček, F. Peissker et al. Astrophys. J. **800**, 125 (2015).
40. F. Eisenhauer et al., The Messenger **143**, 16 (2011).
41. N. Blind, F. Eisenhauer, S. Gillessen, Y. Kok et al., arXiv:1503.07303 [astro-ph.IM].
42. H. Falcke, F. Melia, E. Agol, Astrophys. J. **528**, L13 (2000).
43. F. Melia, H. Falcke, Ann. Rev. Astron. Astrophys. **39**, 309 (2001).
44. S.S. Doeleman et al., Nature **455**, 78 (2008).
45. A.F. Zakharov, A.A. Nucita, F. De Paolis, G. Ingrosso, New Astron. **10**, 479 (2005).
46. A.Y. Bin-Nun, Phys. Rev. D **81**, 123011 (2010).
47. A.Y. Bin-Nun, Phys. Rev. D **82**, 064009 (2010).
48. A.F. Zakharov, A.A. Nucita, F. De Paolis, G. Ingrosso, Astron. & Astrophys. **442**, 795 (2005).
49. A.F. Zakharov, A.A. Nucita, F. De Paolis, G. Ingrosso, Phys. Rev. D **76**, 062001 (2007).
50. A.A. Nucita, F. De Paolis, G. Ingrosso et al., Proc. Astron. Soc. Pac. **119**, 349 (2007).
51. A.F. Zakharov, A.A. Nucita, F. De Paolis, G. Ingrosso, New Astron. Rev. **56**, 64 (2012).
52. A.F. Zakharov, Phys. Rev. D, **90**, 062007 (2014).
53. A.F. Zakharov, arXiv:1407.2591[astro-ph.GA].
54. Z. Stuchlik, Bull. Astron. Inst. Czechoslov. **34**, 129 (1983).
55. A.F. Zakharov, S. Capozziello, F. De Paolis, G. Ingrosso, A.A. Nucita, Space Sci. Rev. **48**, 301 (2009).
56. S. Capozziello, Int. J. Mod. Phys. D **11**, 483 (2002).
57. S. Capozziello, V.F. Cardone, A. Troisi, J. Cosm. Astropart. Phys. **08**, 1 (2006).
58. S. Capozziello, V.F. Cardone, A. Troisi, Phys. Rev. D **73**, 104019 (2006).
59. A.F. Zakharov, A.A. Nucita, F. De Paolis, G. Ingrosso, Phys. Rev. D, **74**, 107101 (2006).
60. D. Borka, P. Jovanović, V. Borka Jovanović, A.F. Zakharov, Phys. Rev. D **85**, 124004 (2012).
61. A.F. Zakharov, D. Borka, V. Borka Jovanović, P. Jovanović, Adv. Space Res. **54**, 1108 (2014).
62. D. Borka, P. Jovanović, V. Borka Jovanović, A.F. Zakharov, J. Cosm. Astropart. Phys. **11** 050 (2013).
63. C. Will, Phys. Rev. D **57**, 2061 (1998).
64. A.F. Zakharov, P. Jovanović, D. Borka, V. Borka Jovanović, arXiv:1605.00913v1 [gr-qc]; J. Cosm. Astropart. Phys. (accepted).
65. B. P. Abbott et al., (LIGO Scientific Collaboration and Virgo Collaboration), Phys. Rev. Lett., **116**, 061102 (2016).

STUDENT SESSION

Conveners: S. Pakuliak, N. Mkaza

Determining the spectroscopic quadrupole moment (Q_S) of the first 2^+ state in ^{40}Ar

M.J. Mokgolobotho[*], J.N. Orce [*], M. Kumar Raju[*,†], C.V. Mehl [*], N. Erasmus[*,†], S. Triambak[*,†], N. Kheswa[*,†], M. Wiedeking[†], P. Jones[†], E. Lawrie[†], J.C. Lawrie[†], R. Nchodu[†], T.R.S. Dinoko[†], R. Thomae[†], P. Papka[**,†], P. Adsley[**,†], B. Singh[*], N.A. Khumalo[*], L.M. Phuthu[*], S. Noncolela[*,†], J. Easton[*,†], B. Rebeiro[*], L.D. Mavela[*], E.H. Akakpo[*], K.V.J. Abrahams[*], B.V. Kheswa[†] and S. Ntshangase[‡]

[*]*Department of Physics and Astronomy, University of the Western Cape, P/B X17, Bellville ZA-7535, South Africa*
[†]*iThemba LABS, National Research Foundation, P.O. Box 722, Somerset-West 7129, South Africa*
[**]*Stellenbosch University, Private Bag X1, Matieland 7602, South Africa*
[‡]*University of Zululand, Private Bag X1001, KwaDlangezwa, 3886, South Africa*

Abstract. In this work, we aim at measuring the spectroscopic quadrupole moment of the first 2^+ excited state $Q_s(2_1^+)$ in ^{40}Ar through the reorientation-effect in Coulomb excitation (RECE) measurements. The experiment was performed at the iThemba LABS facility using the AFFRODITE array coupled with a segmented CD type silicon detector for coincidence between γ rays and scattered particles. This was the first successful Coulomb excitation experiment at safe energies carried out at the facility.

Keywords: Coulomb excitation, nuclear shapes, nuclear matrix elements
PACS: 25.70.De; 23.20.Lv; 23.40.Hc; 21.60.De

INTRODUCTION

Several experimental investigations have been carried out to study the shape of the 2_1^+ state in 2s-1d nuclei. One of the vital experimental techniques in studying shapes is the Coulomb excitation, which involves the excitation of both projectile and target nuclei through a time-dependent electromagnetic interaction. The excitation process is said to be free of nuclear interactions if the separation between nuclear surfaces in the center-of-mass frame is $S(\vartheta) \geq 6.5$ fm for light nuclei [1], which can be calculated using an expression in eq. 1

$$S(\vartheta) = \frac{0.72 Z_1 Z_2}{E_{max}}(1+\frac{A_1}{A_2})[1+cosec(\frac{1}{2}\vartheta)] - 1.25(A_1^{1/3}+A_2^{1/3})\text{fm}. \quad (1)$$

where E_{max} is the maximum safe energy of a projectile (A_1, Z_1) on a target (A_2, Z_2) with the nuclear radius taken as $1.25\ A^{1/3}$ fm. The shape of the nucleus which undergoes a population from the 0_1^+ ground state to the 2_1^+ state can be directly measured from the $Q_s(2_1^+)$ value which measures the deviation of the charge distribution from sphericity in the laboratory frame. In the rotational model, the $Q_s(2_1^+)$ for an axially symmetric shape with the projection of the angular momentum onto the symmetric axis of the nucleus

vanishing (K = 0), can be related to the intrinsic quadrupole moment Q_0 measured in the body fixed frame as:

$$Q_s(2_1^+) = -\frac{2}{7}Q_0. \tag{2}$$

A positive sign of the $Q_s(2_1^+)$ indicates that the nucleus has an oblate shape, whereas a negative sign of it represents a prolate shape. The sign and magnitude of the $Q_s(2_1^+)$ can be obtained through the RECE which is a second order effect in Coulomb-excitation theory causing hyperfine splitting of the $J^\pi = 2^+$ magnetic substates enhancing the Coulomb-excitation cross section [2, 3, 4]. To date, there is only one RECE measurement of ^{40}Ar carried out through a $^{206}Pb(^{40}Ar,^{40}Ar^*)^{206}Pb^*$ reaction. The de-exciting γ rays where detected using with a NaI counter in coincidence with the scattered particles. This study reported a value of $Q_s(2_1^+) = +1 \pm 4$ e fm^2 (adopted value) [1, 5] indicating large uncertainty in it. This may be due to the poor resolution of γ detector and additional errors due to the assumed $Q_s(2_1^+)\ ^{206}Pb = (0.0 \pm 0.5)|Q^{rot}_{2_1^+}|$ which was used in estimating the $Q_s(2_1^+)$ of ^{40}Ar. However recent results [1, 6] reported the $Q_s(2_1^+)(^{206}Pb) = (0.17 \pm 0.31)|Q^{rot}_{2_1^+}|$. Furthermore the author does not provide information about beam energy and thereby the $S(\vartheta)$ value which are vital to confirm the safe Coulomb-excitation criteria. The purpose of the present work is to measure the $Q_s(2_1^+)$ of ^{40}Ar using safe RECE.

EXPERIMENT

A safe energy of 143.2 MeV ^{40}Ar beam from the iThemba LABS SPC2 cyclotron Accelerator was bombarded on a $1.39\ mg/cm^2$ enriched ^{208}Pb target. The experimental set-up used AFFRODITE array [7] comprised of 8 HPGe clover γ-ray detectors, 5 placed at 90° and 3 placed at 135°, coupled with a segmented CD type S3 charged particle detector consisting of 24 rings (for angular distribution) and 32 sectors (for Doppler correction). The particle detector was placed at 10.05 mm from the target position at backward angles, upstream the beam line covering the angular range $[105° - 131°]$. The chamber set-up is shown in fig. 1.

DATA ANALYSIS AND RESULTS

The data collected through an on-line digital data acquisition system (DDAS) is already being analysed using an MTsort sorting code (MIDAS based) for Coulomb-excitation experiments written by C. V. Mehl. The $0_1^+ \rightarrow 2_1^+$ transition (1461 keV shown in figure 2) was clearly observed after Doppler correction of the γ peaks. Energy sharing condition for dead layers of the S3 detector and time gates for particle-γ coincidence were further incorporated on the code to reduce the background. The data are being further analysed using the Fortran based semi-classical coupled channel Coulomb excitation code GOSIA [8, 9] which calculates theoretical integrated γ-ray yields to be fitted with the experimental γ yields per ring. The GOSIA code calculates theoretical

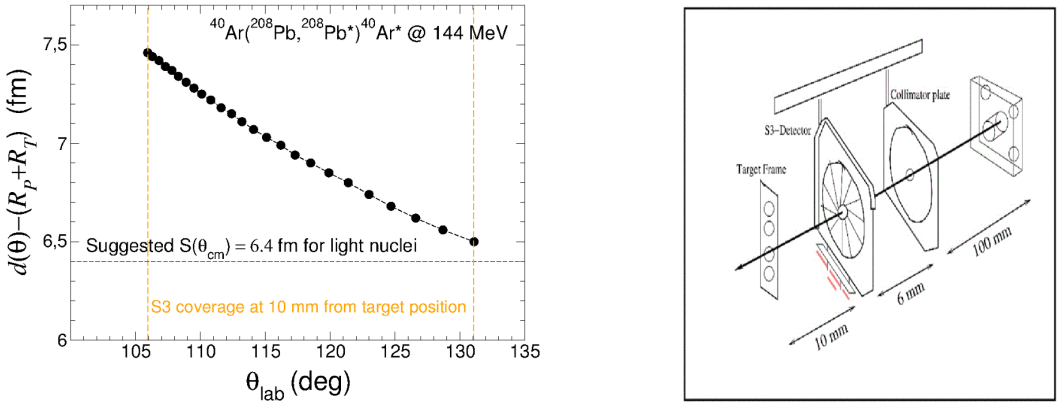

FIGURE 1. Left: Minimum distance of closest approach between the ^{40}Ar and ^{208}Pb nuclei at backward angles at 144 MeV. Right: outline of the set-up inside the reaction chamber showing a Si(Li) particle detector and collimator's (used to avoid direct contact of oncoming beam with detector)

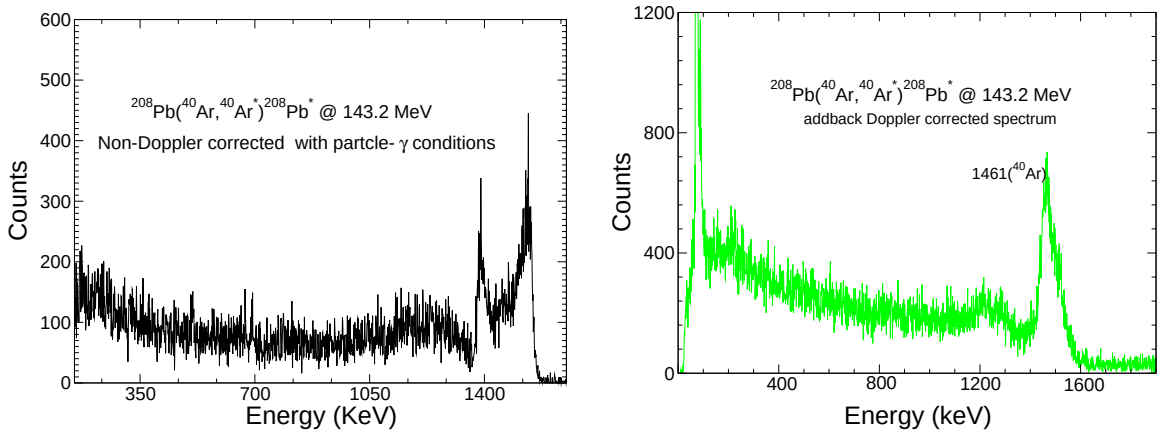

FIGURE 2. Left: Non-Doppler corrected γ ray spectrum showing Doppler shifted with particle-γ coincidence condition. Right: Doppler corrected γ ray spectrum with particle-γ coincidence and timing conditions showing a clearly brought 1461 peak due to the energy loss of the beam

yields which can be related to the experimental data by normalising to the well-known $\langle 2_1^+ \mid\mid \hat{E2} \mid\mid 0_1^+ \rangle$ transitional matrix element in ^{40}Ar and further minimises (locates the χ^2 minima) the data by fitting matrix elements to the experimental data.

The $Q_s(2_1^+)$ will be directly extracted from these matrix elements and will be confirmed by doing and angular distribution of the de-excitation γ rays coming in coincidence with the scattered projectiles.

ACKNOWLEDGEMENT

We acknowledge the iThemba LABS Nuclear physics department, Accelerator group for the selfless work put in to make this experiment possible. The University of the Western Cape (UWC) and the NRF for their exceptional support.

REFERENCES

1. R. H. Spear, Phys. Rep. **73**, 369 (1981).
2. J. de Boer, J. Eichler, Advances in Nuclear Physics (Springer), vol. **1**, 1, (1968).
3. O. Hausser, Nuclear Spectroscopy and Reactions, edited by J. Cerny (1974), Part C, 55.
4. F. K McGowan and P.H stelson, Nuclear Spectroscopy and Reactions, edited by J. Cerny (1974), Part C, 3.
5. K. Nakai, I. L. Quebert, F. S. Stephens and R. M. Diamond, Phys. Rev. Lett. **24**, 903 (1970).
6. A.M.R. Joye, A.M. Baxter, S. Hinds, D.C. Keanand R.H Spear, Phys. Lett. **72B**, 307, (1978)
7. M. Lipoglavsek et al., Nucl. Instr. Meth. Phys. Res., **A557**, 523 (2006).
8. T. Czosnyka, D. Cline, and C.Y Wu. Am. Phys. Soc. **28**, 745 (1983).
9. GOSIA Manual 2012

Developing a sorting code for Coulomb excitation data analysis

C. V. Mehl*, J. N. Orce *, M. Kumar Raju*,†, P. M. Jones†, N. Erasmus*, M. Wiedeking†, E. Lawrie†, S. Triambak*,† and M. Mokgolobotho*

*Department of Physics, University of the Western Cape, P/B X17, Bellville ZA-7535, South Africa
†iThemba LABS, National Research Foundation, P.O. Box 722, Somerset-West 7129, South Africa

Abstract. The sorting code developed in this work was used to process and analyze data acquired from the Coulomb excitation of ^{20}Ne beams at 73 MeV onto a ^{194}Pt target. The detection of γ rays was done using the AFRODITE HPGe clover detector array, which consists of eight clover detectors, in coincidence with ^{20}Ne particles detected with an S3 double-sided silicon detector. The new sorting code includes Doppler-correction effects, charge-sharing, energy and time conditions, kinematics and stopping powers, among others, and can be used for any particle-γ coincidence measurements at iThemba LABS. Results from other Coulomb excitation measurements at iThemba LABS are also presented.

Keywords: Coulomb excitation, spectroscopic quadrupole moment, diagonal matrix elements
PACS: 23.10.-s; 21.60.-n; 23.40.Bw; 23.40.Hc

INTRODUCTION

Coulomb excitation regards the excitation of nuclei solely through the electromagnetic interaction [1, 2]. The simplest nuclear shape that has been investigated in the laboratory frame, using the reorientation effect, RE, in Coulomb excitation studies is the spectroscopic quadrupole moment of excited states in even-A, even-Z nuclei. The spectroscopic quadrupole moment of a nucleus is a measure of the extent to which the shape of the nucleus under investigation deviates from that of a sphere. The relation between the Coulomb excitation probability, σ_{E2}, using the semiclassical approximation to second order, and the spectroscopic quadrupole moment of the first 2_1^+ excitation , $Q_s(2_1^+)$, is given by

$$\sigma_{E2} = \sigma_R K_1(\theta_{cm},\xi) B(E2)(1 + K_2(\theta_{cm},\xi) Q_s(2_1^+)), \quad (1)$$

where σ_R denotes the Rutherford cross section, $B(E2)$ the reduced transition probability, $K_1(\theta_{cm},\xi)$ and $K_2(\theta_{cm},\xi)$ contain the dependence of σ_{E2} on the trajectory of the projectile. The developed sort code was used to analyze data from ^{194}Pt(^{20}Ne, ^{20}Ne*)^{194}Pt* and ^{208}Pb(^{40}Ar, ^{40}Ar*)^{208}Pb* Coulomb excitation reactions. In the case of ^{20}Ne, collective and mean field models such as the shell model and Hartree-Fock-Bogoliubov [1] have not been successful in calculating the $Q_s(2_1^+)$ value at 1.634 MeV in ^{20}Ne. In particular, the magnitude of the calculated values were found to be about 30% less than the one obtained experimentally using the RE [1]. The extent to which nuclear interference is negligible is crucial in these type of measurements. The beam energies for which this condition holds true are often referred as being safe [1].

Prior to the results presented here, only three RE measurements were made prior to 1975 [4, 5, 6]. The inadequacy of these RE measurements arises from the difficulty associated with the production of Ne ion beams in tandem accelerators. In addition, two of the three RE measurements possessed high bombarding beam energies that were associated with unsafe distances of closest approach of about 4 fm. These studies failed to show that the maximum bombarding beam energies utilized could be deemed as safe. The third RE measurement of $Q_s(2_1^+)$ in ^{20}Ne was done by Schwalm et al., and has a rather large uncertainty associated with the gas ^{20}Ne target utilized to make the measurements [5]. In the case of the ^{208}Pb(^{40}Ar^{40}Ar*)^{208}Pb* experiment, the data acquired will be used to provide the first experimental determination of the $Q_s(2_1^+)$ value in ^{40}Ar at safe energies. In RE experiments the quantity that one determines is the diagonal matrix element, which is related to the $Q_s(\,2_1^+)$ value as,

$$Q_s(2_1^+) = 0.75793\langle 2_1^+||\hat{E}2||2_1^+\rangle, \tag{2}$$

where $\langle 2_1^+||\hat{E}2||2_1^+\rangle$ is the measured diagonal matrix element of the electric quadrupole moment, that will be determined by normalizing the γ ray yields in the projectile nucleus to the relative yields in the target nucleus where matrix elements are well-known, or the $B(E2;0_1^+ \rightarrow 2_1^+)$ value of the projectile. In order to extract the $\langle 2_1^+||\hat{E}2||2_1^+\rangle$ matrix element, various conditions have to be used while carrying out the sorting of the data.

The ^{194}Pt(^{20}Ne,^{20}Ne*)^{194}Pt* experiment

A ^{20}Ne^{3+} beam at a laboratory energy of 73 MeV was bombarded onto an enriched ^{194}Pt target of 1.2 mg·cm^{-2} thickness. The ^{20}Ne^{3+} ions were detected with the S3 detector, which was placed at a distance of 30 mm upstream in front of the target and covered a backward angular range of [130.9°, 158.3°]. The AFRODITE array was used to detect γ rays emitted in the de-excitation of states in ^{20}Ne and ^{194}Pt.

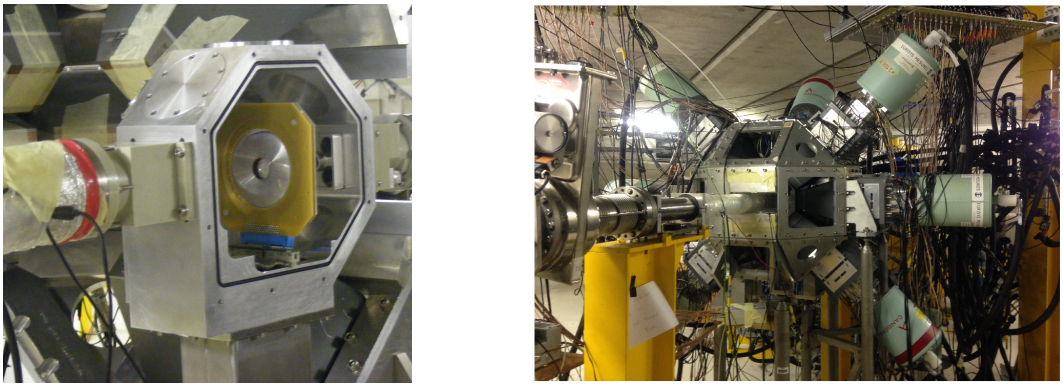

FIGURE 1. The S3 silicon detector (left) and the AFRODITE HPGe array (right).

The requirement for nuclear excitation to be negligible was ensured by having $s(\vartheta) >$ 6.5 fm at all angles, where ϑ is the scattering angle in the center-of-mass frame. The

Sommerfeld parameter for the ^{194}Pt-^{20}Ne system at 73 MeV is $\eta = 70.9$, indicating that the semiclassical approximation is satisfied.

The ^{208}Pb(^{40}Ar^{40}Ar*)^{208}Pb* experiment

A ^{40}Ar^{7+} beam of energy 143.2 MeV was bombarded onto a 1.4 mg·cm^{-2} thick ^{208}Pb target. Again, the AFRODITE array was used to detect the γ rays emitted from the de-excitation of states in the ^{208}Pb and ^{40}Ar nuclei. An S3 detector which had been placed 10 mm upstream from the target was used to detect the scattered ^{40}Ar^{7+} ions at backward angles ranging from 106.1° to 130.0°. The requirement that the effects of nuclear interference could be neglected was ensured by having $s(\vartheta) > 6.5$ fm at all angles. A Sommerfeld parameter of $\eta \simeq 123$ indicates that the semiclassical approximation is valid.

DATA ANALYSIS AND RESULTS

The data analysis of these Coulomb excitation experiments were carried out using a C++ based multi-task program. This program is capable of generating sorting codes for particle-γ coincidence measurements in the *MTsort* language [7]. In the case of the ^{194}Pt(^{20}Ne,^{20}Ne*)^{194}Pt* and ^{208}Pb(^{40}Ar^{40}Ar*)^{208}Pb* experiments, the role of the sorting code was to reduce the background in the γ ray and particle spectra and generate the final Doppler corrected γ ray spectra. This was done so that the peaks corresponding to the 2_1^+ states at 1634 keV and 1461 keV in ^{20}Ne and ^{40}Ar, respectively, could be extracted from the raw γ-ray data. The particle-γ data were calibrated using ^{152}Eu, ^{56}Co and ^{226}Ra radioactive sources together with *GEANT4* simulations of the elastic peaks. Time difference gates between the rings and sectors of the S3 detector, as well as time difference gates between the particles and γ rays were used in conjunction with requiring two simultaneous hits in the S3 detector, one in a ring and one in a sector, to setup a coincidence condition for the acceptance of valid detection events.

The background in the particle and γ-ray spectra was reduced by introducing a broad particle energy gate, covering the energy range of the elastic peaks in the rings. Background events arising when the full energy of a particle is shared between the rings, sectors (active layers) and dead layers of the S3 detector were reduced by adding an additional particle energy condition to the sorting code which required that $|E_{Sector} - E_{Ring}|$ to be less than a given energy. Additional background in the particle-γ spectra was reduced by a inelastic condition on the particle-energy spectra which yield clean γ-ray spectra in coincidence with the particles in the rings. This condition consists of applying particle-energy gates where the inelastic peak is expected to appear. To correct for the shift in energy of the γ rays emitted by the projectile traveling at v $\approx$ 0.08 c, a Doppler correction was applied to the γ-ray spectra. This provided a clear identification of the γ ray of interest. Figure 2 shows the total add-back Doppler corrected γ ray spectra in coincidence with all the rings for the ^{194}Pt(^{20}Ne,^{20}Ne*)^{194}Pt* (left) and ^{208}Pb(^{40}Ar^{40}Ar*)^{208}Pb* (right) experiments.

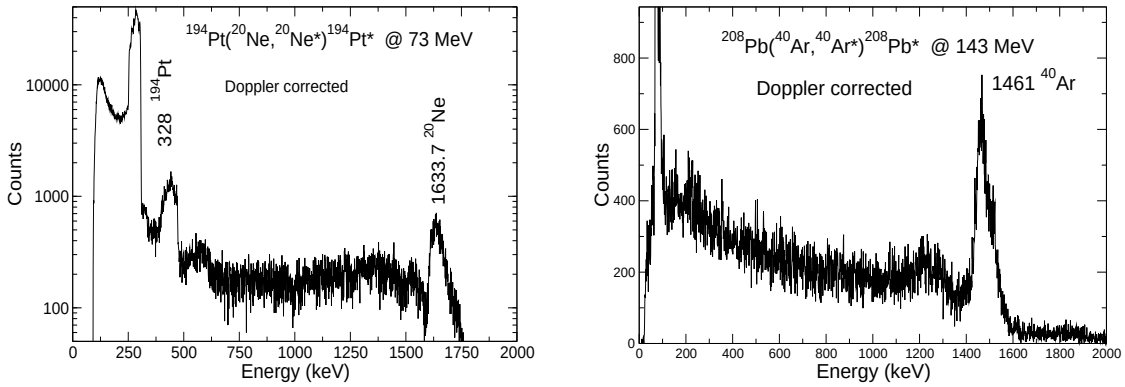

FIGURE 2. Doppler corrected γ-ray spectra.

SUMMARY AND OUTLOOK

Coulomb excitation RE experiments have been carried out at iThemba LABS. The ^{194}Pt(^{20}Ne,^{20}Ne*)^{194}Pt* experiments were primarily aimed at bringing to closure the discrepancies between the predictions of current nuclear mean field models and the experimental determination of $Q_s(2_1^+)$ in ^{20}Ne [1].

The role of this study is the development of sorting codes that can be used to perform the offline and online data analysis in Coulomb excitation experiments carried out using the AFRODITE array in conjunction with double-sided silicon detectors. The task of creating the online and offline sorting codes has been simplified by the creation of a program that can be used to generate similar sorting codes in the MTsort language [7] based on the explicit experimental parameters, such as the beam energy, the atomic masses, charge and mass numbers, excitation energies, together with the geometric details of the experiment. In addition, the program allows the user to select the conditions that should be included in the code. The program then outputs a sorting code that contains the commands to generate required spectra and impose the selected conditions used to reduce the background in the particle and γ ray spectra. The online sorting code allows monitoring of the incoming data during the experiments.

ACKNOWLEDGMENT

We acknowledge the nuclear physics and accelerator group at iThemba LABS, South Africa, for their help during the experiments. The author would like thank the National Research Foundation (NRF) and iThemba LABS for financial support.

REFERENCES

1. R. H. Spear, Phys. Rep. **73**, 369 (1980).
2. D. C. Kean, Lecture Notes in Physics (Springer), Volume **92**, 80 (1976).
3. J. de Boer, J. Eichler, Advances in Nuclear Physics (Springer), **1**, 1-65 (1968).
4. K. Nakai, F. S. Stephens and R. M. Diamond, Nucl. Phys. A **150**, 114-128 (1970).
5. D. Schwalm et al., Nucl. Phys. A **192**, 449-495 (1972).
6. D. K. Olsen, et al., Nucl. Phys. A **220**, 541-568 (1974).
7. J. Cresswell and J. Sampson, *MTsort Language-EDOC033*, http://ns.ph.liv.ac.uk/MTsort-manual/MTsort.html, (2015).

Liquid Metal Ion Source Assembly for External Ion Injection into an ESIS

Matthew Segal[*,†], Robert Bark[*], Rainer Thomae[*], Evgeny E. Donets[**], Evgeny D. Donets[**], Alexey Boytsov[**], Dimitri Ponkin[**] and Alexander Ramsdorf[**]

[*] *iThemba LABS*
[†] *University of Cape Town*
[**] *Joint Institute for Nuclear Research*

Abstract. Research and design of an ion transport beam-line for the injection of Ga^+ ions into the Krion 6-Tesla Electron String Ion Source (ESIS) at JINR in Dubna is currently under way. A focusing system for a liquid metal ion source (LMIS) producing Ga^+ has been tested and characterized at both iThemba LABS in Cape Town and at the JINR. Previously, only neutral atoms from gasses have been charge bred with great efficiency in the ESIS. This work will test the feasibility of charge breeding from singly charged metal ions to higher charge states. This ion injection system currently consists of an LMIS, the focusing elements for the LMIS, and a quadrupole switch-yard for beam bending during injection in a pulse-mode scheme of ESIS operation.

Keywords: Ga^+, Ion Sources, LMIS, Rare Ion Beams, Charge Breeding, Ion Transport
PACS: 37.20.+j

INTRODUCTION

Charged ions have been injected into EBIS (Electron Beam Ion Source) devices before [1]; however this has not yet been performed with an ESIS, which has only charge-bred neutral gasses to higher charge states [2]. The ESIS, and EBIS/T outperform ECRIS (Electron Cyclotron Resonance Ion Source) in reaching these higher charge states, yet also yield a lower number of particles [3]. The ESIS is capable of charge-breeding a narrow spectrum of high charge to mass ratio ions instead of the wider charge to mass spectra expected from EBIS or ECRIS type charge-breeders. It is hypothesized that from already singly charged ions, higher charge state ions can be created more efficiently [4].

LMIS (Liquid Metal Ion Source) are an attractive option for producing a beam of singly positive charged ions for the purposes of injection into an ESIS. In theory, LMIS are good candidates as they have high brightness and intensity, and have long lifetimes at lower power costs. However, LMIS ion beams have a high angular divergence and energy spread and they therefore require a robust electrical optical system to focus the ions [5].

A prototype LMIS assembly has been manufactured at iThemba LABS and underwent an initial testing period with a Gallium 69-long life LMIS which was purchased from AP-TECH [6].

The first testing period was conducted in early 2015 at iThemba LABS in Cape Town,

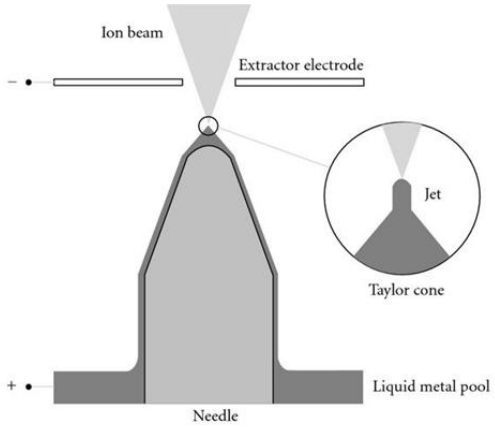

FIGURE 1. Gallium wetted needle tip in a liquid metal ion source and depiction of ion jet formation [8].

South Africa. Further tests with the LMIS and an electrical quadrupole bender from DreEBIT [7] were performed at JINR in Dubna, Russia, later in the year. This "switchyard" allows for the transport of singly-charged ions into the ESIS, and after a charge-breeding cycle, the extraction of highly charged ions (Figure 3).

LIQUID METAL ION SOURCE (LMIS)

A LMIS works on the principal of hydro-electrodynamical equilibrium. A thin needle is wetted by liquid metal or metal-alloy from a nearby reservoir via capillary action. The needle is then held at a positive potential. When the electric field in the vicinity of the needle tip is of the order of $10^{1\ 0}$ N/C, the electrical force breaks the surface tension and charged ions evaporate from the liquid metal at the needle-tip in the form of an ion jet, which can then be focused into an ion beam (see Figure 1). The optimal form of the liquid metal over the wetted needle during operational equilibrium is called a Taylor-Cone [3].

Ga^+ current measurements at iThemba LABS

The LMIS focusing assembly (Figure 2), was setup in the vacuum laboratory at iThemba LABS. These initial investigations served to characterize the ignition conditions, ion current stability and transmission of ion current after bending with a dipole magnet. The LMIS needle tip distance to the emitter electrode plate, *d*, was adjustable between experiments, and three different values were used to study it's influence on the electric field strength. The potential difference between the needle tip *Uex* and emitter plate *Uem* (which along with *d* contribute to electric field strength) were frequently adjusted to find optimal current conditions for ignition, stability and transmission.

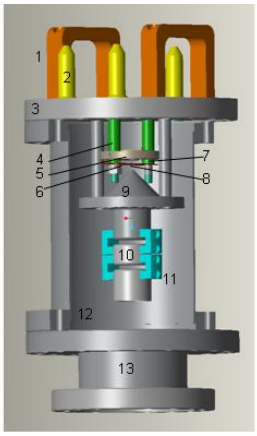

FIGURE 2. Schematic of LMIS and focusing assembly.

TABLE 1. Optimal Ga^+ current conditions for stability at varying extraction electrode distance, d.

d (mm)	Most Stable Current (μ A)	Uex (kV)	Uem (kV)	Longest Stable Time (hours:mins)
0.5	0.31 ± 0.10	0.50	-6.0	1:57
0.3	0.96 ± 0.16	0.41	-5.2	2:27
-0.3	0.61 ± 0.03	0.30	-5.2	2:05

A) Characterization of LMIS

Initially it was made certain that single Ga^+ ions were being produced from the LMIS rather than molecular ions or charged bubbles [9]. This was done by comparing the proton calibration curve of the magnet to the relationship between the LMIS tip potential, *U*ex, with the current, *I*, required for the magnet to bend the ions through 90 degrees. The results agreed with the proton curve, also indicating that the Ga^+ energy is completely characterized by *U*ex.

Comparing biasing settings on *Uex* and *Uem* showed that for a given tip-electrode distance, *d*, there is a minimum threshold to ignite Ga^+ current which is around ΔV = 6.0kV.

B) Stability Measurements

Table 1 summarizes the best results for each distance, *d*. The distance *d* = 0.3mm is a favourable tip-plate distance due to the larger current output and duration of stability. Note that in both table 1 and 2, *d* = -0.3mm, signifies that the needle protrudes into the emitter electrode plate by 0.3mm.

C) Transmission of beam after magnetic bending

Table 2 shows that *d* = 0.3mm is favourable, at both higher ion current output and transmission, which occurs at a large Δ V = 8.4kV. Various values of tip potential *Uex* and emitter plate potentials *U*em were explored, and those yielding highest transmission

TABLE 2. Best Ga^+ transmission after magnetic bending

d (mm)	Transmission %	Ga^+ @ FC2 (μ A)	Uex (kV)	Uem (kV)
0.5	91	1.0	0.55	-6.4
0.3	100	1.6	0.87	-7.5
-0.3	77	1.3	0.50	-5.2

for each *d* were tabulated in table 2.

Ga^+ Measurements with Electrical Quadrupole Deflector in Dubna

The electrical quadrupole switch-yard from Dre-EBIT will form a crucial component in the transport beam-line for injection and extraction with the ESIS (Figure 4). In July/August 2015 tests with the LMIS assembly and the switch-yard were performed at the Veksler and Baldin Laboratory for High Energy Physics at JINR.

A) New Bias Settings

Due to power supply differences at iThemba LABS and at JINR, *Uex* was biased up to 8.0kV and *Uem* was only biased to around -1.3kV. These settings were somewhat opposite to those at iThemba LABS, yet the potential difference required to yield ion current ignition was the same. The electrical quadrupole switch-yard *Ubend* could be biased to $\pm$ 25kV, with a switching frequency of up to 30Hz. For *Uex* = 6kV, *Ubend* is around $\pm$ 5kV to achieve 90 degree bending.

B) Pulse-Mode Settings

Pulsing on the emitter plate was also achieved: 2.6μA Ga^+ was measured for 20ms pulses in 2s intervals which is suitable for over barrier injection into ESIS. Pulsing on *Uem* controls Taylor Cone formation and hence ion production, while not pulsing Uex keeps energy constant and stable - which is favourable for continued use of an LMIS for ion injection into the ESIS.

CONCLUSION

Initial experiments with the Ga^+ LMIS show that LMIS are viable sources for the injection of charged metal ions into an ESIS charge breeder. Experiments conducted in October 2015 at JINR revealed that pulsing could be implemented upon the biasing of the quadrupole switchyard *Ubend* and was preferable to pulsing on the emitter plate

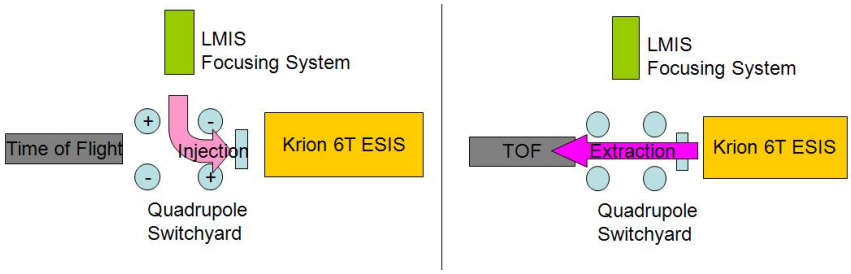

FIGURE 3. Ga^{+} Injection Into ESIS after quadrupole bending, and Extraction of Ga^{n+} after charge breeding in ESIS through un-powered quadrupole.

Uem. The beam focusing of the existing electrical optics was shown to have a wide angular spread which requires improvement.

CURRENT AND FUTURE WORK

Beam quality and profiling measurements were performed in August 2015 through to January 2016. Qualitative beam analysis simulations using simION have been performed throughout this research. Currently a second LMIS assembly with improved focusing is being built and tested at iThemba LABS. 1+ ion injection into the Krion 6-T ESIS using Au^{+} are scheduled for July and later in 2016.

ACKNOWLEDGMENTS

The NRF and SA-JINR collaboration are thanked whole-heartedly for this research opportunity as well as for funding. Thanks also to JINR for their generous hospitality during the various research visits to Dubna.

REFERENCES

1. F. Wenander, J. Instrum. 5, C10004 (2010)
2. E.D. Donets, et al., Rev. Sci. Instrum., Vol. 75, 1543-1545 (2004)
3. A. Thorn, et al., Rev. Sci. Instrum, Vol. 83, No 2, Part 2,02A511 (2012)
4. Van Duppen, P, et al, 1997, An EBIS as Charge State Breeder for the Production of Energetic Radioactive Ion Beams, Physica Scripta. Vol. T71, 199-203, 1997.
5. Wolf, B, 1995, Handbook of Ion Sources, Alton, G, Characterization of Ion Sources, CRC Press, pp257-283
6. `http://www.aptech.com`.
7. `http://www.dreebit.com`.
8. M. Tajmar, and C. A. Scharlemann, *Development of Electric and Chemical Microthrusters*, International Journal of Aerospace Engineering, Cairo, 2011, pp. 3.
9. Colby, B,. Evans, A, 1973, Electrohydrodynamic Ionization Mass Spectrometry, Analytical Chemistry, Vol. 45, No. 11 September 1973

PROGRAM

4th South Africa – JINR Symposium
Few to Many Body-Systems: Models, Methods and Applications
JINR Dubna, September 21-25, 2015

==========

Monday, September 21, 2015
International Conference Hall in Dubna

==========

10:00 Opening the Week of South Africa at the JINR

I. *Words of Welcome:*

JINR Director V.A. Matveev 10-15′
JINR: important events in International activity

Deputy Director general of the Department of Science and Technology Th. Auf der Heide 10-15′
Bird's eye view of the South African National System of Innovation

Deputy Minister of Education and Science of the Russian Federation L.M. Ogorodova 10-15′
To Be Announced

Acting CEO of SKA Rob Adam

Minister-counselor of the Embassy of South Africa in Moscow

II. Reports:

D. Adams 30′
An Overview of the SA-JINR Collaboration: Impact on Human Capital and Research Capacity Development

G. Trubnikov 30′
International large research infrastructure of JINR. NICA megaproject: challenges and perspectives

12:00-12:20 Coffee break

12.20 Excursion to NICA facility

13:30-14:30 Lunch time

14:00-15:00 Registration for the Symposium

15:00 Opening the 4th South Africa – JINR Symposium Few to Many Body-Systems: Models, Methods and Applications (co-chairmen):
Director of the BLTP V.V. Voronov
Director of the SKA Rob Adam

JINR Seminar

chairman: J. Cleymans
15:10 R. Adam (SKA South Africa) 55′+5′
Doing transformational science with the Square Kilometre Array (SKA)

16:10-16:40 Coffee break

Session: Prospects of JINR and South African basic facilities

chairman: J. Cleymans
16:40 V. Aynutdinov (INR RAS) 25′+5′
Baikal GVD experiment
17:10 S. Wyngaardt (Stellenbosch U.) 25′+5′
Towards the South African Underground Laboratory (SAUL)
17:40 M. Shirchenko (DLNP JINR) 25′+5′
Neutrino experiments at the Kalinin Nuclear Power Plant

19:00 Welcome party at the restaurant, hotel "Dubna"

==========

Tuesday, September 22, 2015
Conference Hall
of the Flerov Laboratory of Nuclear Reactions (FLNR)

==========

Session(s): Nuclear Reactions (Fission and Clustering)
Conveners: D. Kamanin, S. Mullins

chairman: A. Karpov
9:00 D. Kamanin (JINR) 18'+2′
Status and prospects of CCT study
9:20 N. Mkaza (Stellenbosch U.) 18'+2′
Programme for LISSA setup in the University of Stellenbosch
9:40 O. Falomkina (Moscow State University/JINR) 18'+2′
Modern mathematical methods in processing of low-statistics data
10:00 A. Yeremin (FLNR) 18'+2′
Spectroscopy of SHE at Dubna: Results and plans
10:20 A. Nasirov (BLTP JINR) 18'+2′
Theoretical study of a possible mechanism of the true ternary fission

10:40-11:00 Coffee break

chairman: A. Popeko
11:00 A. Karpov (FLNR JINR) 18'+2′
Ternary clusterization of heaviest nuclear systems
11:20 F. Karpeshin (Mendeleyev Inst., S-Peterburg) 18'+2′
Many-phonon states and true ternary fission
11:40 Yu. Panebratsev (VBLHEP) 18'+2′
Virtual laboratory of fission
12:00 V. Sargsyan (BLTP, JINR) 18'+2′
Fusion reactions at near and sub-barrier energies
12:20 S. Zemlyanoy
Gas-cell based setup for production and study of heavy neutron rich Nuclei
12:40 L. Grigorenko (FLNR JINR) 18′+ 2′
Theoretical studies of few-body dynamics in the dripline nuclei and recent experimental results

13:00-14:30 Lunch time

Session(s): Few Body Systems
Conveners: A. Motovilov, S. Rakityanski

chairman: S. Rakityansky
14:30 E. Kolganova (BLTP, JINR) 25'+5′
Ultracold atomic clusters and Efimov effect
15:00 L. Lekala (Univ. of South Africa) 25'+5′

Cluster approach for determining spectroscopy for light hypernuclei
15:30 V.S. Melezhik (BLTP JINR) 25'+5′
Ultracold resonant processes in atomic traps

16:00-16:30 Coffee break

Chairman: L. Lekala
16:30 S. Rakityansky (Univ. of Pretoria) 25′+5′
Nuclear fusion d+Li^6 → Be^{8*} induced by X-rays in Lithium-Deuteride crystal
17:00 A. Malykh (BLTP JINR) 25′+5′
Universal description for few two-species particles
17:30 B. Mukeru (Univ. of South Africa) 25'+5′
Coulomb and nuclear breakups in the ^{11}Be and ^{208}Pb
18:00 S. Vinitsky (JINR) 25′+5′
Tunneling of composite particles through repulsive barriers

==========

Tuesday, September 22, 2015
Conference Hall
of the Frank Laboratory of Neutron Physics (FLNP)

==========

Session(s): Applied Nuclear Physics
Conveners: M.Frontasyeva, R. Newman

I.Materials science: radiation stability, materials modifications

Chairman: M.Frontasyeva
9:00 L. Petrik (Western Cape University) 18'+ 2′
Applied Research - new trends in collaboration of SA with JINR
9:20 V. Skuratov (FLNR JINR) 18'+2′
High resolution electron microscopy studies of nuclear ceramics and oxides irradiated with heavy ions of fission fragment energy
9:40 A. Janse van Vuuren (Nelson Mandela Metropoliten U.) 18'+2′
Swift heavy ion irradiation effects on He agglomeration in solids
10:00 A. Nechaev 18'+2′
Sensors for toxic contaminants analyses based on the track membranes with surface enhanced Raman spectroscopy properties as a new activity in frame of RSA-JINR collaboration
10:20 A. Rossouw, (Stellenbosch U.) 18'+2′
Photocatalytic track-etched membranes (A review on MSc studies)

10:40-11:00 Coffee break

II. Environmental studies

Chairman: L. Petrik
11:00 M. Frontasyeva (FLNP JINR) 18'+ 2′
An overview of collaboration with SA for the period of 2010-2015
11:20 D. Pavlov (Inst. of Biology of Inland Waters) 18'+ 2′
Monitoring of trace elements in marine ecosystems: "Mussel Watch" approach
11:40 J. Bezuidenhout (Stellenbosch U.) 18'+ 2′
Results of various element content analyses of invasive black mussels (Choromytilusmeridionalis) in the coastal waters around the industrial port of Saldanha, South Africa
12:00 R. Newman (Stellenbosch U.) 18'+ 2′
Air pollution studies in the Western Cape area. An overview
12:20 Z. Ndlovu (iThemba) 18'+ 2′
Elemental analysis of mosses and lichens from Western Cape (South Africa) using NAA and ICP-MS
12:40 P. Eze (Western Cape U.) 18'+ 2′
Elemental composition of coal flyash: Matla coal power station in the

Mpumalanga province in South Africa case study using nuclear and related analytical techniques

13:00-14:30 Lunch time

Session: Student Session
Conveners: S. Pakuliak, N. Mkaza

Chairman: N. Mkaza

14:30 O. Adeniyi (Western Cape Univ.) 13'+ 2′
Swift heavy ion irradiation of polyester and polyolefin polymeric film for gas separation application

14:45 I. Zinicovscaia (FLNP JINR) 13'+ 2′
Biotechnology of gold And silver nanoparticle production: results of collaborative study with South Africa (necsa).

15:00 Z. Goryainova (FLNP JINR) 13'+ 2′
New results on NAA of mussels from South Africa

15:15 T. Lamula (iThemba) 13'+ 2′
Neutron activation analysis of thin Bi targets with 90 and 140 MeV neutrons.

15:30 K. Kornieieva (FLNR JINR) 13'+ 2′
Structural and micromechanical examination of ODS alloys irradiated with 1-3 MeV/nucleon heavy ions

15:45 R. Rymzhanov (FLNR JINR) 13'+ 2′
Latent tracks and mechanical stresses in Al2O3 irradiated with swift heavy ions

16:00-16:30 Coffee break

16:30 R. Botha (Univ. of Western Cape) 18 ′+ 2′
Radon in-air measurements within wine-cellars of the Western Cape (South Africa) and its associated exposure dosage

16:50 M. Mokgolobotho (Univ. of Western Cape) 13'+ 2′
Determining the spectroscopic quadrupole moment (Q_s) of the first 2^+ state in ^{40}Ar

17:05 C. Mehl (Univ. of western Cape) 13′+2′
Developing a sorting code for Coulomb excitation data analysis

17:20 M. Segal (Univ. of Cape Town/iThemba LABS) 13′+2′
Liquid Metal Ion Source Assembly for External Ion Injection into an Electron String Ion Source (ESIS)

17:35 Discussion of the presentations of young scientists

==========

Wednesday, September 23, 2015

==========

7:30 Excursion to Moscow, Departure from Hotel "Dubna"

==========

Thursday, September 24, 2015

Conference Hall
of the Flerov Laboratory of Nuclear Reactions (FLNR)

==========

Session(s): Nuclear Structure
Conveners: R. Nazmitdinov, W.D. Heiss

Chairman: F. Šimkovic

9:00 R. Nazmitdinov (BLTP, JINR) 25'+5′
Symmetry effects in mesoscopic systems

9:30 V. Nesterenko (BLTP, JINR) 25'+5′
Deformation effects in the dipole and quadrupole giant resonances: Skyrme RPA theory and iThemba experiments

10:00 N. Orce (University of the Western Cape) 25'+5′
Nuclear polarizability: the sleeping beauty of nuclear physics

10:30-11:00 Coffee break

Chairman: R. Nazmitdinov
11:00 P. Schuck (Orsay, France) 25'+5′
Selfconsistent RPA meets Time-Dependent Density matrix
11:30 F. Šimkovic (BLTP, JINR) 25'+5′
QRPA with non-linear operator
12:00 N. Arsenyev (BLTP, JINR) 18'+2′
Complex configuration effects on properties of pygmy resonance
12:20 K. Raju Mukhi (Univ, of Western Cape) 18'+2′
Coulomb excitation reorientation-effect measurements in ^{12}C

13:00-14:30 Lunch time

Session(s): *Physics at Underground Laboratory*
Conveners: F. Šimkovic, S. Wyngaardt

Chairman: F. Šimkovic
14:30 D. Naumov (DLNP, JINR) 25'+5′
Neutrino Physics program at the JINR
15:00 R. Newman (Stellenbosch U.) 18'+2′
Towards SAUL - perspectives, progress and prospects for establishing enhanced low-level radioactivity measurement capability
15:20 O. Smirnov (DLNP, JINR) 18'+2′
Neutrino geophysics
15:40 A. Zakharov (ITEP Moscow) 18'+2′
Possible alternatives for models of the Galactic Centre

16:00-16:30 Coffee break

Session(s): *Condensed Matter Physics*
Conveners: Yu. Shukrinov, A.E. Botha

Chairman: A. Povolotsky
16:30 Yu. Shukrinov (BLTP JINR) 20'+5′
Theoretical Models for Superconducting Nanostructures
16:55 A. E. Botha (Univ. of South Africa) 20'+5′
Chaos and Chimera States in Josephson Junctions.
17:20 I. Rahmonov (BLTP JINR) 20'+5′
Numerical Study of Josephson Nanostructures Using Parallel Computing Based on Cloud Center LIT JINR
17:45 E. Benecha (Univ. of South Africa), R. Dawood (Cairo U.) 20'+5′
Simulation of Topologically Nontrivial DC-SQUID
18:10 K. Kulikov (BLTP JINR) 20'+5′
Josephson junction detectors for Majorana fermions

==========

Thursday, September 24, 2015
Conference Hall
of the Veksler and Baldin Laboratory of High Energy Physics (VBLHEP)

==========

Session: NICA
Conveners: A. Sorin, J. Cleymans

Chairman: A. Sorin
9:00 A. Sidorin (VBLHEP, JINR) 18'+2′
NICA collider complex: challenges and perspectives
9:20 V. Kolesnikov (VBLHEP, JINR) 18'+2′
Prospects for dense baryonic matter research at NICA: Status of the MPD
9:40 M. Kapishin (VBLHEP, JINR) 18'+2′

Prospects for dense baryonic matter research at Nuclotron: Status of the BM@N

10:00 B. Mellado (Witwatersrand) 18'+2′
High-throughput electronics for the NICA complex and the ATLAS Experience

10:20-10:50 Coffee break

Chairman: J. Cleymans

10:50 J. Cleymans (Univ. of Cape Town) 18'+2′
The physics case for the NICA project

11:10 A. Sorin (VBLHEP, JINR) 18'+2′
Vortical structures and strange hyperon polarization in heavy-ion collisions

11:30 A. Muronga (Univ. of Johannesburg) 18'+2′
Relativitic Fluid Dynamics for Heavy Ion Collisions and Astrophysics

11:50 D. Blashke (Univ. of Wroclaw) 18'+2′
Cluster virial expansion for quark/nuclear matter within the 2PI formalism

12:10 A. Trunin (BLTP, JINR) 18'+2′
Equation of State for quark-gluonic matter from Nf=2+1+1 lattice QCD

12:30 M.I. Krivoruchenko (ITEP Moscow/BLTP JINR) 18'+2′
Quantum transport in the deformation quantization framework

12:50 T. Dietel (Univ. of Cape Town) 18'+2′
Online data processing for Multi-Purpose Detector at NICA and experience from ALICE

==========

Friday, September 25, 2015

==========

10:00 Meetings of the working groups of grant holders at laboratories

13:00-14:30 Lunch time

16:00 Round Table discussion at International Conference Hall in Dubna
S.A. Rakityansy (5′)
Few words to the Memory of V.B. Belyaev ans S. Sofianos
F. Šimkovic (5′)
Symposiums: Past, presence and future
A. Popeko, S. Rakytianski, M. Frontasyeva, S. Pakuliak, R. Nazmitdinov, D. Naumov, Yu. Shukrinov, J. Cleymans
Reports for sessions (4′ for each report)

17:00 Closing of the Symposium